

## Carbonation of C-S-H gel and its Effects on the Carbonation Rate in Blended Cement Paste - An Experimental and Modelling Study

Wu, B.

**DOI**

[10.4233/uuid:8dc16e7d-aa56-4927-9077-0e75bdf18514](https://doi.org/10.4233/uuid:8dc16e7d-aa56-4927-9077-0e75bdf18514)

**Publication date**

2023

**Document Version**

Final published version

**Citation (APA)**

Wu, B. (2023). *Carbonation of C-S-H gel and its Effects on the Carbonation Rate in Blended Cement Paste - An Experimental and Modelling Study*. [Dissertation (TU Delft), Delft University of Technology]. <https://doi.org/10.4233/uuid:8dc16e7d-aa56-4927-9077-0e75bdf18514>

**Important note**

To cite this publication, please use the final published version (if applicable). Please check the document version above.

**Copyright**

Other than for strictly personal use, it is not permitted to download, forward or distribute the text or part of it, without the consent of the author(s) and/or copyright holder(s), unless the work is under an open content license such as Creative Commons.

**Takedown policy**

Please contact us and provide details if you believe this document breaches copyrights. We will remove access to the work immediately and investigate your claim.

---

**Carbonation of C-S-H gel and its Effects on the Carbonation Rate in Blended Cement  
Paste - An Experimental and Modelling Study**

Dissertation

for the purpose of obtaining the degree of doctor  
at Delft University of Technology  
by the authority of Rector Magnificus, Prof.dr.ir. T.H.J.J. van der Hagen,  
Chair of the Board for Doctorates  
to be defended publicly on  
Thursday 11 May 2023 at 10.00 o'clock

by

Bei WU  
Master of Engineering, Wuhan University of Technology, China  
born in Jingshan, Hubei, China

---

This dissertation has been approved by the promotor.

Composition of the doctoral committee:

Rector Magnificus,

Prof. dr. ir. K. van Breugel

Dr. G. Ye

chairperson

Delft University of Technology, promotor

Delft University of Technology, promotor

Independent members:

Prof. dr. ir. N. De Belie

Prof. dr. S. Kamali-Bernard

Prof. dr. H. M. Jonkers

Prof. dr. ir. J. Zhou

Dr. M. Nedeljkovic

Ghent University, Belgium

INSA-Rennes, France

Delft University of Technology

Hebei University of Technology, China

Delft University of Technology



Keywords: carbonation, C-S-H, SCMs, microstructure, reaction rate

Printed by: Ipskamp Printing

Cover by: Bei WU

Copyright ©2023 by Bei WU

ISBN: 978-94-6473-112-5

An electronic copy of this dissertation is available at

<https://repository.tudelft.nl/>

---

*To my family*

## Table of Contents

List of Symbols .....	V
List of Abbreviations.....	VIII
Summary .....	X
Samenvatting.....	XII
Acknowledgements .....	XIV
1 .....	1
General Introduction.....	1
1.1 Research background .....	1
1.2 Aim and objectives of this research.....	4
1.3 Strategy of this research .....	5
1.4 Scope of this research.....	5
1.5 Outlines of this thesis .....	6
1.6 References .....	8
2 .....	9
Literature Review and Discussion.....	9
2.1 Introduction .....	9
2.2 Mechanisms of carbonation in Portland cement concrete .....	9
2.3 Carbonation depth prediction models for Portland cement concrete.....	10
2.4 Effects of SCMs .....	12
2.5 Carbonation of C-S-H .....	13
2.6 Effects of C-S-H carbonation on the porosity evolution of concrete .....	15
2.7 Concluding remarks and motivation of the research .....	16
2.8 References .....	18
3 .....	21
Hydration of Portland Cement Blended with Supplementary Cementitious Materials (SCMs).....	21
3.1 Introduction .....	21
3.2 Materials and experiments.....	22
3.2.1 Materials properties.....	22
3.2.2 Sample preparation and experimental procedure .....	26
3.2.3 Test methodology .....	26
3.3 Experimental results and discussions .....	33
3.3.1 Development of amount of portlandite in blended cement paste .....	33
3.3.1.1 Effects of FA on the amount of portlandite in blended cement paste .....	34
3.3.1.2 Effects of BFS on amount of portlandite in blended cement paste .....	37

---

3.3.1.3	Effects of a combination of FA and BFS on the amount of portlandite in ternary blended cement paste.....	40
3.3.2	Development of C-S-H phases in blended cement paste.....	41
3.3.2.1	Stoichiometry of the hydration of OPC.....	42
3.3.2.2	Stoichiometry of the pozzolanic reactions of FA and BFS .....	42
3.3.2.3	Effects of FA on the development of C-S-H phases in blended cement paste .....	43
3.3.2.4	Effects of BFS on the development of C-S-H phases in blended cement paste .....	48
3.3.3	Pore structure evolution of blended cement paste .....	53
3.3.3.1	Effects of FA on the porosity of blended cement paste.....	55
3.3.3.2	Effects of BFS on the porosity of blended cement paste.....	58
3.3.3.3	Situation in OPC-FA-BFS ternary system .....	61
3.4	Conclusion.....	62
3.5	References .....	64
4	.....	67
Accelerated Carbonation of Blended Cement Paste.....		67
4.1	Introduction .....	67
4.1.1	Mixture composition and sample pre-treatment.....	68
4.1.2	Accelerated carbonation test in the lab.....	68
4.1.3	Test methods.....	69
4.2	Experimental results and discussions .....	71
4.2.1	Development of the carbonation depth ( $X_c$ ) .....	71
4.2.2	Phase assemblages in blended cement paste after carbonation .....	73
4.2.3	Profiles of the portlandite and the amounts of $\text{CaCO}_3$ .....	76
4.2.4	Effects of carbonation on the capillary pore-MIP test.....	78
4.2.5	Effects of carbonation on the gel pore-Nitrogen adsorption test.....	83
4.3	Conclusions .....	85
4.4	References .....	87
5	.....	89
Synthesis of C-S-H gel with Different Ca/Si Ratio.....		89
5.1	Introduction .....	89
5.2	Materials and experiments.....	90
5.2.1	Materials.....	90
5.2.2	Synthesis of C-S-H gels .....	90
5.2.3	Characteristic methods of C-S-H gels .....	91

5.3	Experimental results and discussions .....	93
5.3.1	Effects of synthesis time on the formation of C-S-H gels .....	93
5.3.2	Identification of C-S-H gels with different C/S ratio .....	96
5.3.3	Structure of nano-crystalline C-S-H gels .....	104
5.4	Conclusion.....	112
5.5	References .....	113
6	.....	116
Accelerated Carbonation of Synthesized C-S-H gels with Different C/S Ratio .....		116
6.1	Introduction .....	116
6.2	Materials and experiments.....	117
6.2.1	Accelerated carbonation experiment of C-S-H gels.....	117
6.2.2	Test methods of C-S-H gels after carbonation .....	117
6.3	Experimental results and discussions .....	119
6.3.1	Carbonation of C-S-H gels.....	119
6.3.2	Rietveld analysis of XRD test results.....	124
6.3.3	Carbonation rate of C-S-H gels with different C/S .....	129
6.3.4	Carbonation of C-S-H gels in the early stage.....	134
6.4	Conclusions .....	136
6.5	References .....	137
7	.....	138
Implementation.....		138
7.1	Modelling strategy.....	139
7.2	Physicochemical processes involved in carbonation.....	140
7.3	Chemical reactions in blended cement paste.....	140
7.3.1	Hydration reactions in Portland cement and blended cement pastes.....	140
7.3.2	Carbonation reactions in Portland and blended cement pastes.....	142
7.3.3	Pore structure formation and diffusivity – Introductory comments .....	143
7.4	Mathematical model for predicting the carbonation depth.....	143
7.4.1	Mass balance at the reaction front of phases involved in carbonation .....	143
7.4.2	Diffusion coefficient of $\text{CO}_2 - D_{e,\text{CO}_2}^c$ .....	145
7.4.3	Prediction of carbonation depth of Portland and blended cement paste.....	146
7.4.4	Determination of model parameters of prediction formula .....	147
7.4.5	Case study by application of Papadakis' equation .....	154
7.5	Conclusion.....	158

---

7.6	References .....	159
8	.....	160
	Retrospection, Conclusions and Recommendations.....	160
8.1	Retrospection.....	160
8.2	Conclusions .....	161
8.3	Recommendations .....	162
	Curriculum Vitae.....	164



# List of Symbols

$b$	buffering capacity	Kg/m <sup>3</sup>
$[i]$	concentration of constituent $i$	mol/L
$V_i$	molar volume of constituent $i$	cm <sup>3</sup> /mol
$n_i$	molar number of constituent $i$	
$\Delta\phi$	total solid volume changes	cm <sup>3</sup>
$\Delta\phi_{CH}$	solid volume changes due to the carbonation of portlandite	cm <sup>3</sup>
$\Delta\phi_{CSH}$	solid volume changes due to the carbonation of C-S-H	cm <sup>3</sup>
$M_i$	molar weight of constituent $i$	g/mol
$w_{CH}^{binder}$	CH amount described as the weight percentage per 1 g original binder	g/g
$w_h^{CH}$	relative mass percentage of water due to the dehydration of CH	%
$w_{L.O.H}^{total}$	the total weight loss of the raw materials under the TG test condition	%
$f_{cem}$	mass fraction of cement	g/g
$f_{SCMs}$	mass fraction of SCMs	g/g
$w_{L.O.H}^{cem}$	total weight loss of cement after heating at 1050°C	%
$w_{L.O.H}^{SCMs}$	total weight loss of SCMs after heating at 1050°C	%
$\rho_{bulk}$	bulk density of cement paste	g/L
$\rho_i$	density of constituent $i$	g/L
$\phi$	total porosity of the sample	mL/mL
$V_{stem}$	stem volume of penetrometer	ml
$\gamma$	surface tension of mercury	mN/m
$\theta$	contact angle between mercury and the pore surface of the cement paste	°
$d$	pore diameter	μm
$p$	applied pressure in MIP test	MPa
$N_i$	number of atoms of element $i$ at the	

	pixel	
$n_i$	counts of element $i$ at the pixel	
$E_K(i)$	K-shell ionization energy of element $i$	eV
$w_K(i)$	the K-shell fluorescence yield of element $i$	
$Z$	atomic number	
$X_c$	carbonation depth	mm
$t$	time	
$w_c^{\bar{c}}$	the relative weight loss of CO <sub>2</sub> from the decomposition of CaCO <sub>3</sub> in the TG curve	%
$m_{Al_2O_3}(t)$	the weight of Al <sub>2</sub> O <sub>3</sub> in the carbonation products of C-S-H gel after the carbonation time $t$ [day]	g
$m_{cr}(t_0)$	the initial weight of crystal phases identified by XRD in the C-S-H gel	g
$m_{cr}(t)$	the total weight of crystals in the C-S-H gel after carbonation time of $t$ [day]	g
$w_{Al_2O_3}^{rel}(t_0)$	the relative weight percentage of Al <sub>2</sub> O <sub>3</sub> in the crystals at the beginning	g
$w_{Al_2O_3}^{rel}(t)$	the relative weight percentage of Al <sub>2</sub> O <sub>3</sub> after carbonation of $t$ [day]	g
$m_{\bar{c}}^{nor-cr}(t)$	the normalized weight (to the initial crystal weight) of CaCO <sub>3</sub> at exposure time $t$ (day)	g/g
$w_{\bar{c}}^{rel}(t)$	relative weight percentage of CaCO <sub>3</sub> at exposure time $t$ (day)	g/g
$(m_{\bar{c}}(t))/(m_{cr}(t_0))$	the weight normalized to initial total crystal weight	g/g
$(m_{cr}(t_0))/(m_{CSH-cr}(t_0))$	the weight percentage of the crystal portion in C-S-H to the total initial weight of crystal phases identified by XRD	g/g
$(m_{CSH-cr}(t_0))/(m_{CSH}(t_0))$	the weight percentage of the crystal portion in C-S-H to the total initial weight of C-S-H gel	g/g
$w_{CSH-cr}^{rel}(t_0)$	the relative weight percentage of the crystal phases in the initial C-S-H	%

	gel mixed with $\text{Al}_2\text{O}_3$	
$w_{\text{Al}_2\text{O}_3}^{rel}(t_0)$	the relative weight percentage of internal standard $\text{Al}_2\text{O}_3$ in the initial C-S-H gel mixed with $\text{Al}_2\text{O}_3$	%
$w_{\text{Al}_2\text{O}_3}^{abs}(t_0)$	the absolute weight percentage of $\text{Al}_2\text{O}_3$ in the initial C-S-H gel mixed with $\text{Al}_2\text{O}_3$	%
$r_i^h$	hydration rate of constituent $i$	in moles of reactant $i$ , per $[\text{m}^3/\text{s}]$
$r_i^c$	carbonation rate of constituent $i$	in moles of reactant $i$ , per $[\text{m}^3/\text{s}]$
$\varepsilon_0$	the ratio of the volume of mixing water to the total volume of fresh concrete	%
$\Delta\varepsilon_h(t)$	the changes in porosity due to hydration	%
$\Delta\varepsilon_c(t)$	the changes in porosity due to carbonation	%
$d_k$	the Kelvin diameter	$\mu\text{m}$
$f_K$	the volume fraction the pores filled with water	v/v %
$w_T$	thickness of the water film	$\mu\text{m}$
$f_w$	the volume fraction occupied by the film of water	v/v %
$f = f_K + f_w$	the volume fraction of the pores corresponding to the liquid phase	v/v %
$1-f$	the volume fraction of the gas phase.	v/v %
$D_{\varepsilon, \text{CO}_2}^c$	diffusion coefficient of $\text{CO}_2$	$\text{m}^2/\text{sec}$
$S_{SR}$	the degree of saturation of the pore system	%
$\varepsilon^c$	the porosity of total carbonated cement paste.	%

# List of Abbreviations

IEA	International Energy Agency
ETP	Energy Technology Perspectives
Gt	gigatons
WBCSD	World Business Council for Sustainable Development
CSI	Cement Sustainability Initiative
OPC	ordinary Portland cement
SCMs	Supplementary Cementitious Materials
FA	Fly ash
BFS	Blast furnace slag
GGBS	ground granulated blast-furnace slag
C	CaO
S	SiO <sub>2</sub> , quartz
A	Al <sub>2</sub> O <sub>3</sub>
H	H <sub>2</sub> O
$\bar{S}$	SO <sub>3</sub>
$\bar{C}$	CO <sub>2</sub>
C/S	Ca/Si
H/S	H <sub>2</sub> O/Si
$C_3S$	Alite, tricalcium silicate
$C_2S$	Belite, dicalcium silicate
$C_3A$	Aluminate
$C_4AF$	Ferrite
$\bar{C}\bar{S}$	Anhydrite
$\bar{C}\bar{S}H_2$	gypsum
AFt	ettringite, $C_6A\bar{S}_3H_{32}$
AFm	monosulphate aluminate hydrate
$FH_3$	iron hydroxide
$A_2S$	Mullite
$C_2ASH_8$	strätlingit
$C_{1,1}SH_{3,9}$	C-S-H gel produced from the pozzolanic reaction of FA
$C_{7,88}S_{7,39}M_3A$	glass phase in BFS
$C_{1,42}SH_{2,92}A_{0,046}$	C(-A)-S-H gel produced by the reaction of BFS with portlandite

---

$M_{4.6}AH_{19}$	hydrotalcite-like phase produced by the reaction of BFS with portlandite
RRB	the Rosin Rammler Bennett cumulative distribution
C-S-H	calcium silicate hydrate
CH	Portlandite, $Ca(OH)_2$
P100	Portland cement paste
F10	cement paste blended 10% (wt) of fly ash
F30	cement paste blended 30% (wt) of fly ash
B30	cement paste blended 30% (wt) of blast furnace slag
B70	cement paste blended 70% (wt) of blast furnace slag
F10B54	cement paste blended 10% (wt) of fly ash and 54% of blast furnace slag
F30B30	cement paste blended 30% (wt) of fly ash and 30% of blast furnace slag
w/c	water-to-cement ratio
w/b	water-to-binder ratio
Edax	Energy-dispersive X-ray spectroscopy
MIP	mercury intrusion porosimetry
XRD	X-ray diffraction
CIF	crystallographic information file
XRF	X-ray fluorescence spectrometry
ATR	attenuated total reflectance
FTIR	Fourier transform infrared spectroscopy
MS-TGA	thermogravimetric analysis coupled with mass spectrometer
$^{29}Si$ NMR	$^{29}Si$ single pulse magic angle spinning nuclear magnetic resonance
ESEM	environmental scanning electron microscope
BSE	back scattering electron
HOMO	highest occupied molecular orbital
LUMO	lowest unoccupied molecular orbital
MCL	mean silicate chain length
BT	bridging tetrahedra
PT	paired tetrahedra
$Q^0$	a silicon atom with zero connections to another silicon species
$Q^1$	a silicon atom connected to one silicon O-Si species
$Q^2$	a central silicon atom connected to two silicon species
$Q^3$	a central silicon atom connected to three silicon species
$Q^4$	a central silicon atom connected to four silicon species.

---

# Summary

---

Supplementary cementitious materials (SCMs), like fly ash (FA) and blast furnace slag (BFS), are widely used in concrete to partially replace the cement clinker in the production of blended cement or directly replace part of Ordinary Portland cement (OPC) in the concrete. No matter how the SCMs are introduced, they can reduce the cost of concrete and CO<sub>2</sub> emissions during clinker production. From both economic and sustainable development point of view, it is necessary to incorporate more SCMs into concrete. However, the addition of SCMs will affect the cement hydration and bring challenges to the durability of concrete, especially the resistance to carbonation. Carbonation happens when atmospheric CO<sub>2</sub> penetrates inside the concrete and reacts with calcium-bearing phases of the cement paste. The main calcium-bearing phases involving in carbonation of concrete are portlandite (CH) and calcium silicate hydrate (C-S-H). With the addition of SCMs, the amounts of both calcium-bearing phases are reduced due to so-called dilution effects. Moreover, the portlandite is consumed by the pozzolanic reactions of SCMs, to produce C-S-H phases with less Ca/Si ratio. Apparently, the C-S-H phase is now the dominant calcium-bearing phase and is expected to play the key role in the durability of concrete under carbonation. Therefore, it is important to investigate the carbonation mechanisms of C-S-H phases and their effects on the carbonation development in blended cement concrete.

This study aims at a better understanding of the carbonation mechanisms of different types of C-S-H and their effects on the chemistry of the reaction products and microstructure development of cement paste blended with SCMs during carbonation.

Blended cement pastes with different types of SCMs, including FA and BFS, were prepared to study the effects of SCMs on the formation of C-S-H phases with different C/S ratios, and their effects on the amount of portlandite (Chapter 3). The results show that the amount of portlandite in blended cement paste is dramatically reduced compared to that in OPC paste. Other than C-S-H produced from cement hydration, the C-S-H phase with relatively lower C/S ratio is formed from the pozzolanic reaction of FA or BFS, the C/S ratio of which is 1.0 to 1.3 and 1.1 to 1.3 respectively.

In Chapter 4, accelerated carbonation tests were performed on the blended cement pastes studied in Chapter 3. Both the phase assemblage and microstructure of blended cement pastes were determined and compared with values measured for pastes prior to carbonation. Calculation results based on the TGA data show that the dominant amount of CaCO<sub>3</sub> is produced from the carbonation of C-S-H in pastes blended with high amounts of SCMs (pastes B70, F10B54 and F30B30). Meanwhile, porosity measurements (MIP) showed that the porosities of the three mixtures increased after carbonation. This indicates that the carbonation of C-S-H will increase the porosity of blended cement paste after carbonation.

It is expected that the carbonation of C-S-H phases with different C/S ratio develops differently. To figure out this, C-S-H gel with different C/S ratios were synthesized and with target C-S-H phases identified from test data from different measurements (Chapter 5). Accelerated carbonation tests were performed on different C-S-H phases (synthesized over 4 weeks, C/S ratios ranging from 0.66 to 2.0). After carbonation, the carbonated C-S-H phases were tested by different methods to qualify or/and quantify the carbonation rate of C-S-H gel with different C/S ratios. The results showed that C-S-H gel with a higher C/S ratio has a lower carbonation rate.

In Chapter 7, a mathematical model was developed for the prediction of the carbonation depth of Portland and blended cement paste. The parameters in the model were calculated based on data measured in Chapter 3 and 4. Then the model was applied for specified pastes (P100, F30, B70) and compared with measured carbonation depths (Chapter 4). From the comparison it was concluded that the model developed in this study gives accurate predictions of the carbonation depth in both Portland and blended cement pastes.

---

# Samenvatting

---

Aanvullende cementaire materialen (SCMs), zoals vliegashoudend cement (FA) en hoogovenslak (BFS), worden veelvuldig gebruikt in beton om gedeeltelijk de cementklinker te vervangen bij de productie van samengesteld cement, of om rechtstreeks een deel van gewoon Portlandcement (OPC) in het beton. Ongeacht hoe de SCMs worden toegevoegd, kunnen ze de kosten van beton verlagen en de CO<sub>2</sub>-uitstoot tijdens de productie van klinker verminderen. Vanuit zowel economisch als duurzaam oogpunt is het nodig om meer SCMs in beton op te nemen. De toevoeging van SCMs heeft echter invloed op de cementshydratatie en brengt uitdagingen met zich mee voor de duurzaamheid van beton, met name de weerstand tegen carbonatatie. Carbonatatie treedt op wanneer atmosferische CO<sub>2</sub> doordringt in het beton en reageert met calciumhoudende fasen van het cementpasta. De belangrijkste calciumhoudende fasen die betrokken zijn bij de carbonatatie van beton zijn portlandiet (CH) en calciumsilicaathydraat (C-S-H). Met de toevoeging van SCMs wordt de hoeveelheid van beide calciumhoudende fasen verminderd vanwege het zogenaamde verdunningseffect. Bovendien wordt de portlandiet verbruikt door de pozzolanische reacties van SCMs, om C-S-H fasen met een lagere Ca/Si-verhouding te produceren. Het C-S-H fase is nu duidelijk de dominante calciumhoudende fase en wordt verondersteld een sleutelrol te spelen in de duurzaamheid van beton onder carbonatatie. Daarom is het belangrijk om de carbonatatiemechanismen van C-S-H fasen te onderzoeken en hun effecten op de ontwikkeling van carbonatatie in beton met samengesteld cement.

Dit onderzoek heeft als doel een beter begrip te krijgen van de carbonatatiemechanismen van verschillende soorten C-S-H en hun effecten op de chemie van de reactieproducten en de microstructuurontwikkeling van cementpasta gemengd met SCMs tijdens carbonatatie.

Mengsels van cementpasta met verschillende soorten SCMs, waaronder FA en BFS, werden bereid om de effecten van SCMs op de vorming van C-S-H fasen met verschillende C/S-verhoudingen te bestuderen, evenals hun effecten op de hoeveelheid portlandiet (Hoofdstuk 3). De resultaten tonen aan dat de hoeveelheid portlandiet in cementpasta met SCMs drastisch wordt verminderd in vergelijking met die in OPC-pasta. Naast de C-S-H die wordt geproduceerd uit de hydratatie van cement, wordt de C-S-H fase met relatief lagere C/S-verhouding gevormd uit de pozzolanische reactie van FA of BFS, waarvan de C/S-verhouding respectievelijk 1,0 tot 1,3 en 1,1 tot 1,3 is.

In Hoofdstuk 4 werden versnelde carbonatatietesten uitgevoerd op de gemengde cementpasta's die in Hoofdstuk 3 zijn bestudeerd. Zowel de fase-assemblage als de microstructuur van de gemengde cementpasta's werden bepaald en vergeleken met worden die werden gemeten voor pasta's vóór carbonatatie. Berekeningsresultaten op basis van TGA-gegevens tonen aan dat de dominante hoeveelheid CaCO<sub>3</sub> wordt geproduceerd uit de carbonatatie van C-S-H in pasta's die zijn gemengd met hoge hoeveelheden SCMs (pasta's B70, F10B54 en F30B30). Ondertussen toonden porositeitsmetingen (MIP) aan dat de



porositeit van de drie mengsels toenam na carbonatatie. Dit duidt erop dat de carbonatatie van C-S-H de porositeit van de gemengde cementpasta zal verhogen na carbonatatie.

Verwacht wordt dat de carbonatatie van C-S-H fasen met verschillende C/S-verhoudingen zich op verschillende manieren ontwikkelt. Om dit te onderzoeken, werd C-S-H gel met verschillende C/S verhoudingen gesynthetiseerd en werden doelgerichte C-S-H fasen geïdentificeerd aan de hand van testgegevens uit verschillende metingen (Hoofdstuk 5). Versnelde carbonatietesten werden uitgevoerd op verschillende C-S-H fasen (gesynthetiseerd gedurende 4 weken, met C/S verhoudingen variërend van 0,66 tot 2,0). Na carbonatatie werden de gecarbonateerde C-S-H fasen getest met verschillende methoden om de carbonatiesnelheid van C-S-H gel met verschillende C/S verhoudingen te kwalificeren en/of te kwantificeren. De resultaten toonden aan dat C-S-H gel met een hogere C/S verhouding een lagere carbonatiesnelheid heeft.

In Hoofdstuk 7 werd een wiskundig model ontwikkeld voor de voorspelling van de carbonatatediepte van Portland- en gemengd cementpasta. De parameters in het model werden berekend op basis van gegevens die gemeten waren in Hoofdstuk 3 en 4. Vervolgens werd het model toegepast op specifieke pasta's (P100, F30, B70) en vergeleken met gemeten carbonatatedieptes (Hoofdstuk 4). Uit de vergelijking werd geconcludeerd dat het model dat in deze studie is ontwikkeld nauwkeurige voorspellingen geeft van de carbonatatediepte in zowel Portland- als gemengd cementpasta's.

---

# Acknowledgements

---

Finally, I am walking to the end point of this special stage of my life. Life is hard, and I have been lost. I would never have been able to finish my dissertation without those people who gave me help and support. It is to them that I owe my deepest gratitude.

This project was carried out in the Microlab, Civil Engineering and Geosciences, TUDelft and financially sponsored by China Scholarship Council (CSC) and TUDelft. CSC and TUDelft are gratefully acknowledged. I also would like to thank Prof. Xiangguo Li (my sponsor) and Prof. Baoguo Ma, Wuhan University of Technology (WHUT), P.R. China. They supported me in applying for this special PhD position in TUDelft.

I would like to express my deepest appreciation to my promoter Prof. dr. ir. Klaas van Breugel for his excellent guidance, patience, and always providing me with concise comments for my research. Also, he gave me so many valuable comments for writing the manuscript, like language issues and writing logic. He sacrificed tons of time and energy on my thesis revision in the final stage. I really appreciate it.

I would like to give my sincerest acknowledgement to my promotor Assoc. Prof. dr. Guang Ye for his excellent supervision. His advice, patience and encouragement have not only supported me in pursuing my PhD but also in balancing my family over the years. My dissertation will not be finished without his sparkling ideas and patient correction.

I would like to thank my dissertation committee of Prof. dr. ir. N. De Belie, Prof. dr. S. Kamali-Bernard, Prof. dr. H. M. Jonkers, Prof. dr. ir. J. Zhou and Dr. M. Nedeljkovic, for their time and valuable feedback on this thesis.

I am grateful to Ms. Franca Post, assistant project coordinator, Center for International Cooperation and Appropriate Technology (CICAT) for her strong support during my stay in TUDelft.

I would like to thank all the colleagues and former colleagues of Microlab. First of all, I deeply thank Prof. dr. Erik Schlangen for his support. My special thanks go to the kindly technicians, Arjan Thijssen and John van den Berg for their patiently training in test methods and data process, Gerrit Nagtegaal for his selfless assistance in experiments, Maiko van Leeuwen and Ton Blom for their kind help in the materials management and experimental supports. Many thanks to secretaries, Nynke Verhulst, Iris Batterham, Claudia Baltussen, Melanie Holtzapffel and Jacqueline Bergenhenegouwen for their kind help with the daily administration affaires.

Special thanks to Dr. Zhuqing Yu (Dr. Ning Li), they helped me start my life in Delft. Special thanks to Dr. Yong Zhang, for sharing experiences in experiments. Many thanks to Dr. Zhiwei Qian, my roommate, for his insightful discussions and supporting for my stay in the Netherlands. I would like to thank Jiayi Chen (Dr. Wenqin Shi), Xuliang Hou (Ying Yang),

Dr. Huang Dong, Dr. Tianshi Lu, Hao Huang (Niha Naheya), Dr. Peng Gao for those cherished moments and supporting. Special words to CMMB members: Dr. Zhenming Li, Dr. Shizhe Zhang, Dr. Boyu Chen, Yun Chen, Luiz Cezar Miranda de Lima Junior, Albina Kostuchenko, Xuhui Liang, Zhiyuan Xu, Chen Liu, Guilherme Munhoz, Yu Zheng, Hu Shi etc., for knowledge sharing via group meetings. I would like to thank Dr. Branko Savija, Dr. Mladena Lukovic, Dr. Marija Nedeljkovic, Dr. Natalie Mühleisen, Renée Mors, Patrick Holthuizen, Dr. Agus Susanto, Dr. Farhad Pargar for their smile and encouragement. I am also very grateful to my Chinese colleagues, Dr. Ze Chang, Dr. Shi Xu, Dr. Yu Chen, Dr. Shan He.

I would also like to thank my friends: Yin Sun, Yupeng Liu and Lei Zhang in China, for their endless concern and support. Special thanks to Wenqin Zhang (WHUT), for her helps in NMR test.

I am deeply thankful to my parents, for their love, support, and sacrifices. Without them, I cannot finish my dissertation. This last word of acknowledgment I have saved for my dear wife Liqin Wu and my lovely son Yuchen Wu, who shared my tear and happiness, gave me encouragement to finish my PhD work.

Bei Wu (吴 贝)

Delft, the Netherlands,

March 2023

# General Introduction

---

## 1.1 Research background

During the past one and half centuries, a dramatic increase of atmospheric CO<sub>2</sub> concentration [1] is attributed to anthropogenic emissions from fossil-fuel combustion, cement manufacture [2] and land-use changes [3]. Today the CO<sub>2</sub> concentration in the atmosphere has reached 400 ppm, whereas it had been stable at around 270 ppm for thousands of years before the Second Industrial Revolution in the later 19<sup>th</sup> century. As one of the greenhouse gases, the increasing growth of atmospheric CO<sub>2</sub> concentration will increase the global temperature and cause unpredictable climate changes. With the aim to ensure a sustainable future, many efforts have been made to reduce the atmospheric CO<sub>2</sub> concentration. In the Energy Technology Perspectives (ETP) 2008, the International Energy Agency (IEA) has developed 'Blue Map' scenarios for limiting CO<sub>2</sub> emissions and stabilizing CO<sub>2</sub> concentration in the atmosphere at 450 ppm by 2050 [4]. Having in mind that the demand for energy will increase with the increase of world population and the increase of the energy consumption per capita, this goal requires the reduction of annual CO<sub>2</sub> emissions to 50 percent below current levels by 2050. Taking 2007 level as a reference, the global CO<sub>2</sub> emissions will be reduced to 14 Gt (Gt = gigatons) in 2050 (see *Figure 1-1*). Moreover, the IEA has developed specific targets in each sector to realize this Blue Map goal, as well as the costs to reach these goals. Manufacturing industries account for about 25% of total worldwide CO<sub>2</sub> emissions (6.7 Gt), of which 27% comes from non-metallic minerals production. Cement production accounts for approximately 94% of CO<sub>2</sub> emissions from the production of non-metallic minerals [4].

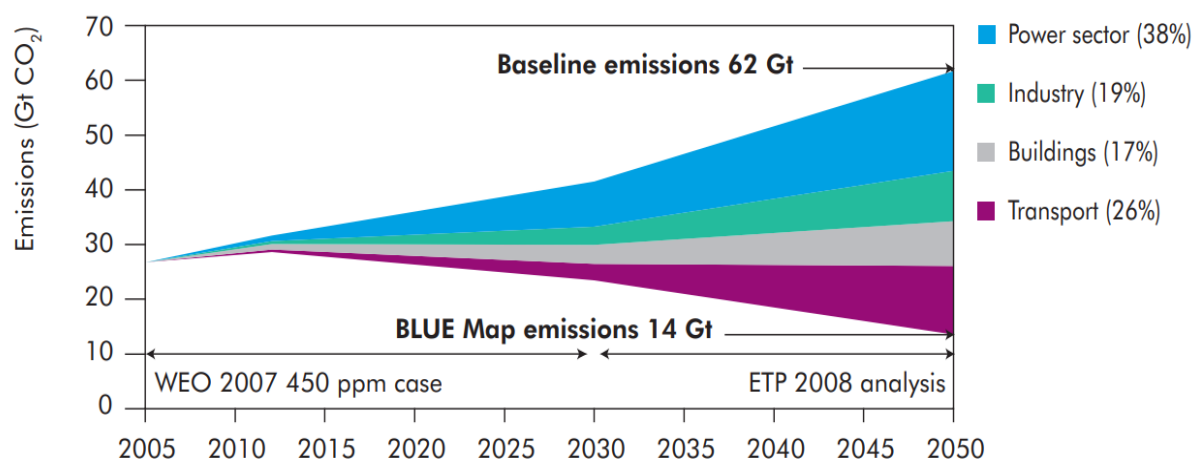


Figure 1-1 Contribution of CO<sub>2</sub> emissions reductions in the BLUE Map Scenario by sector, 2005 - 2050 (World Energy Outlook (WEO) 2007 + ETP 2008)

Cement is the essential ingredient of concrete, which is the most widely used building material for realizing required housing and modern infrastructure. However, the production of cement is responsible for approximately 6.3 of the global CO<sub>2</sub> emissions, calculated based on the above-mentioned data. To meet the Blue Map goal, the cement industry is also expected to contribute to the required reduction of CO<sub>2</sub> emissions. Through the World Business Council for Sustainable Development (WBCSD) and the Cement Sustainability Initiative (CSI), the cement industry and the IEA have worked together to develop a specific roadmap for the cement industry [5]. This roadmap outlines the strategies to achieve the CO<sub>2</sub> reduction targets and establishes a corresponding action plan and timetable. The main techniques identified, and targeted emission reductions are shown in Figure 1-2. The methods include increasing energy efficiency and utilizing alternative fuel like biomass in cement production, clinker substitution and carbon capture and storage in construction.

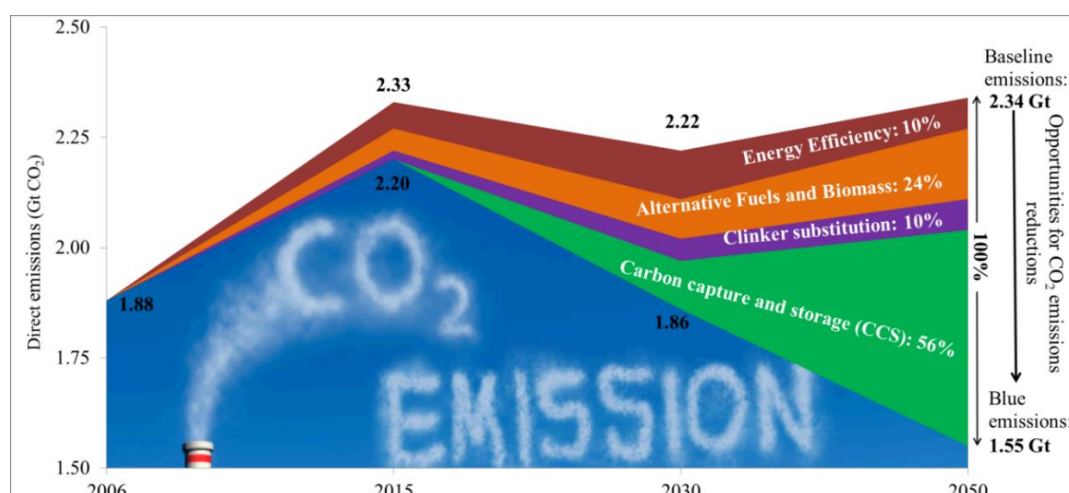


Figure 1-2 Roadmap of CO<sub>2</sub> emissions reductions in cement industry (reproduced from the IEA/WBCSD CEMENT ROADMAP)

Substitution of clinker by alternative binders is a well-known method used in Europe. It is known that ordinary Portland cement (OPC) contains up to 95% clinker. 50% of CO<sub>2</sub> emissions from cement industry is attributed to clinker calcination. Clinker substitution implies partial replacement of clinker by Supplementary Cementitious Materials (SCMs), thus reducing the amount of clinker in the cement and lowering the amount of CO<sub>2</sub> released in the production of concrete. The clinker substitution technology is expected to contribute approximately 10% of the total CO<sub>2</sub> emissions reduction required for the cement industry upon 2050 (see *Figure 1-2*). To reach this goal, increasing amount of SCMs are introduced to produce blended cement.

The use of SCM-based concretes, however, is expected to affect the resistance of the concrete against carbonation. Carbonation happens when atmospheric CO<sub>2</sub> penetrates the concrete and reacts with calcium-bearing phases in the cement paste, as illustrated in *Figure 1-3*. Carbonation is one of the main deterioration processes infrastructure works are exposed to, particularly in situations with high average annual relative humidity. The consequence of carbonation is reduction of alkalinity of the concrete, which makes the reinforcement in the concrete susceptible to corrosion. Therefore, increasing the knowledge on (modelling of) carbonation depth development is of great importance for the service life prediction of Portland cement concrete.

For Portland cement concrete, a well-known square-root relation (see Eq. 1-1) is generally used for estimating the carbonation depth as function of time, which is essentially a solution to Fick's first law of CO<sub>2</sub> diffusion.

$$X_c(t) = A\sqrt{t} \quad \text{Eq. 1-1}$$

in which  $X_c(t)$  is the carbonation depth (m).  $A$  indicates the propagation rate of the carbonation depth (or carbonation front described in *Figure 1-3*). This rate depends on the atmospheric CO<sub>2</sub> concentration near the concrete surface, the amounts of calcium-bearing phases at the start of the carbonation process, as well as the diffusion coefficient of CO<sub>2</sub> in

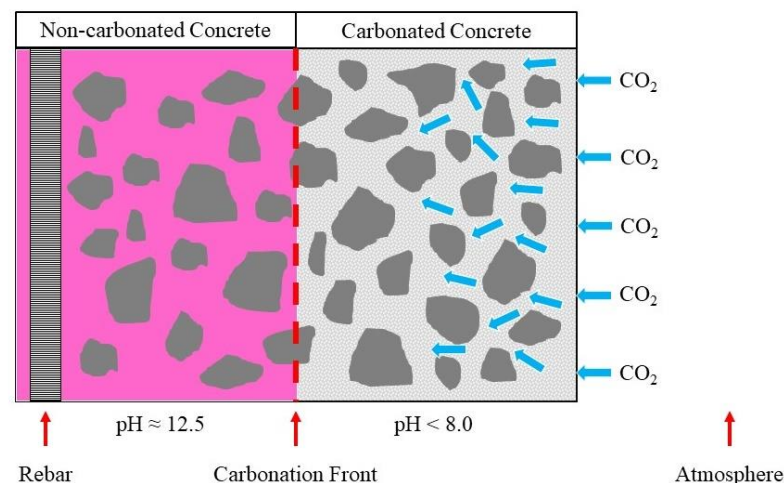


*Figure 1-3 Schematic of an arbitrary stage in the carbonation process in concrete*

carbonated concrete. The diffusion coefficient  $CO_2$  depends on the porosity of the carbonated part, which is determined by the porosity of the concrete before exposure and the total volume changes during the carbonation of calcium-bearing phases. Note that all these parameters are, in fact, a function of the degree of hydration of Portland cement.

In blended cement concrete, different calcium-bearing phases, especially C-S-H with relatively lower Ca/Si (C/S) ratio are produced from the pozzolanic reactions of SCMs. Moreover, both the amounts of calcium-bearing phases and porosity of concrete are changed. These parameters used in predictive formulae are decided, in the end, by the degree of hydration of the OPC and the pozzolanic reactions of SCMs prior to carbonation. Since the situation in blended cement concrete is different from that of Portland cement concrete, an improved relation is needed for predicting the carbonation rate in blended cement concrete.

## 1.2 Aim and objectives of this research

The aim of this research is to study the carbonation mechanism of different types of C-S-H and its effects on the chemistry of the reaction products and microstructure development of cement paste blended with SCMs, such as fly ash (FA) and ground granulated blast-furnace slag (GGBS). Based on the experimental results, a predictive tool has to be developed for predicting the evolution of carbonation profiles. In order to reach this goal, the main objectives are:

1. To figure out the carbonation mechanism of different kinds of C-S-H, including the reaction products and carbonation rates based on the study of the carbonation of synthesized C-S-H phases.
2. To determine the formation of calcium-bearing phases (C-S-H and CH) and the microstructure of cement paste blended with SCMs, considering the type and replacement level of SCMs. Both binary, i.e. OPC blended with either FA or GGBS, and ternary, OPC + FA + GGBS, systems will be studied.
3. To investigate the effects of C-S-H carbonation on the microstructure of blended cement paste by studying the phase transition and microstructure development of blended cement paste.
4. To develop a predictive tool, i.e. formula, to estimate the long-term performance of blended cement paste under carbonation.

Emphasis will be on the objective 1 to 3. In depth modelling of the carbonation process, in which all the investigated mechanisms and interactions are considered, is beyond the scope of this study. The development of a predictive tool, mentioned here as the fourth objective, will mainly consist of an attempt to modify the predictive Eq. 1-1, based on the findings discussed under the objectives 1 to 3.

### 1.3 Strategy of this research

The strategy to reach the goal of this research is as follows.

- Firstly, the main hydration products of blended cement paste are characterized, especially the types of C-S-H and the fractions are identified experimentally. The evolution of the porosity in blended cement pastes is measured as well. Experimental results will be complemented by results of numerical simulations with the hydration model Hymostruc 3D-E [6].
- Secondly, the amounts of carbonation products of cement paste blended with different SCMs are quantified using TGA with mass spectroscopy (MS-TGA). In parallel, porosity changes due to carbonation are evaluated. Effects of carbonation of C-S-H on the phase changes and porosity development of blended cement paste are investigated.
- Thirdly, different C-S-H phases, characterized by their C/S ratio, will be synthesized and characterized by different methods. These artificial C-S-H phases are exposed to an accelerated carbonation test to study the carbonation mechanism of C-S-H phases with different C/S ratio. As a result, the carbonation kinetics of C-S-H with different Ca/Si ratio is obtained.
- In the end, an engineering tool to predict the carbonation rate in cement paste blended with SCMs is proposed that allows for the typical findings regarding the effects of C-S-H type and amount.

### 1.4 Scope of this research

Deterioration of structures made with SCMs-blended concrete can be caused by different factors, such as corrosion, carbonation, sulfate attack or a combination of these factors. The central issue of this research is the carbonation of cement paste blended with SCMs. The SCMs considered in this study are fly ash (FA) and blast furnace slag (BFS), including binary (PC + FA or BFS) and ternary (PC + FA + BFS) system.

In this study the following restrictions do apply:

- Water/binder (w/b) ratio of cement paste was 0.5.
- Prior to the carbonation test the samples were cured in sealed condition at 20°C.
- Accelerated carbonation was applied in a special carbonation chamber. The concentration of CO<sub>2</sub> in the chamber was maintained at approximately 3%. Temperature, relative humidity inside the chamber are 20°C and 75%, respectively.
- Only surface drying of samples was executed before the carbonation test started to prevent the formation of cracks.
- Effects of temperature and relative humidity are not studied in the experimental research part.



The artificial C-S-H with different Ca/Si ratio was synthesized in aqueous solution from CaO and amorphous SiO<sub>2</sub>. The structure of synthesized C-S-H was similar to the C-S-H (I) in cement paste. Ca/Si ratio of synthesized C-S-H was in the range of 0.66 to 2.0. Carbonation of synthesized C-S-H was studied under the same (artificial) carbonation conditions mentioned above.

## 1.5 Outlines of this thesis

As shown in *Figure 1-4*, this thesis consists of 7 chapters. After the Introduction in Chapter 1, Chapter 2 presents a literature survey on existing carbonation depth modelling for OPC concrete, changes of prediction factors brought by the addition of SCMs, especially, microstructure and different C-S-H phases. In the end, it specifies the improvement of carbonation modelling of blended cement paste in this research.

In Chapter 3, MS-TGA is used for quantification of the amount of CH in cement blended with SCMs. Effects of the type and replacement level of SCMs on the amount of CH will be studied. C-S-H phases with different C/S ratios, produced from either hydration of cement or pozzolanic reaction of SCMs, are identified by Energy-dispersive X-ray spectroscopy (Edax). The porosity of blended cement paste is measured by mercury intrusion porosimetry (MIP). Meanwhile, experimental results will be compared with modelling results generated with the numerical simulation program Hymostruc 3D-E developed by P. Gao [25]. Through the above test and modelling results, the effects of SCMs on the amount of CH and types of C-S-H as well as the porosity of blended cement paste can be better understood.

In Chapter 4, the amounts of phases involved in carbonation are analyzed by MS-TGA. Meanwhile, the corresponding evolution of the porosity after carbonation is evaluated by MIP. Based on the experimental results, a more accurate understanding of phase transition and microstructure development of cement paste mixed with SCMs under carbonation is achieved. In particular, the effects of carbonation of C-S-H on the porosity change of blended cement paste after exposure to CO<sub>2</sub> will be studied.

In Chapter 5, C-S-H(I) phases with different C/S ratio, representing those found in blended cement paste and studied in Chapter 3, are synthesized in an aqueous solution by mixing freshly made CaO and fumed silica powder. The products are analyzed by XRD, <sup>29</sup>Si NMR, TGA and FTIR. The crystal structure of synthesized C-S-H phases is discussed as well. The identified C-S-H phases with different C/S ratio will be used for the study on accelerated carbonation, to be dealt with in Chapter 6.

In Chapter 6 the carbonation mechanism of C-S-H with various Ca/Si ratio is investigated. The amount of CaCO<sub>3</sub>, produced from the carbonation of C-S-H, is calculated based on the Rietveld analysis of XRD test results. The carbonation reaction kinetics of different types of C-S-H is calculated based on the formation rate of CaCO<sub>3</sub>. The results in Chapter 6 are used as a reference for the development of a practical engineering tool, i.e. formula, for predicting the rate of carbonation in concrete, as discussed in Chapter 7.

In Chapter 7, a formula for predicting the rate of carbonation in blended cement concrete will be proposed. The starting point is an existing predictive formula, of which modifications are proposed based on the improved understanding of carbonation mechanisms in blended cement mixtures.

From this research, better understanding is gained into the physic-chemical processes of SCMs blended cement paste under carbonation. Additionally, more accurate carbonation profiles in cement paste blended with fly ash and blast furnace slag can be predicted by an envisaged predictive formula.

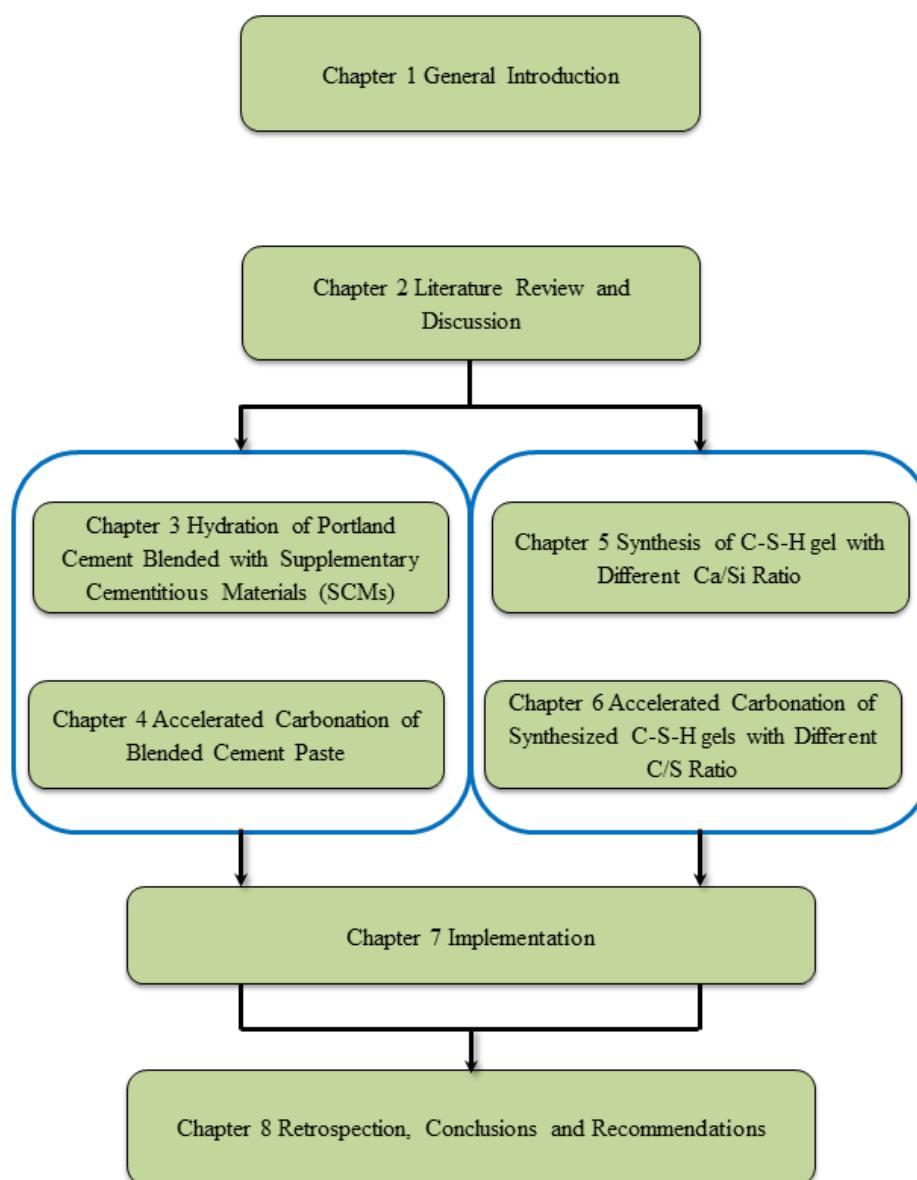


Figure 1-4 Outline of this thesis

## 1.6 References

- [1] T.E. Cerling, M.D. Dearing, J.R. Ehleringer, A history of atmospheric CO<sub>2</sub> and its effects on plants, animals, and ecosystems, Springer 2005.
- [2] G. Marland, T.A. Boden, R.J. Andres, A. Brenkert, C. Johnston, Global, regional, and national fossil fuel CO<sub>2</sub> emissions, Trends: A compendium of data on global change, (2003) 34-43.
- [3] R.A. Houghton, J.L. Hackler, Carbon flux to the atmosphere from land-use changes, TRENDS: a compendium of data on global change, (2002).
- [4] I.E. Agency, Energy Technology Perspectives 2008: Scenarios and Strategies to 2050, OECD/IEA, Paris, 2008.
- [5] I.E. Agency, Cement Technology Roadmap: Carbon Emissions Reductions up to 2050, 2009.
- [6] P. Gao, Simulation of hydration and microstructure development of blended cements, Delft University of Technology, 2018.

## Literature Review and Discussion

---

### 2.1 Introduction

This chapter provides a brief overview of the most important issues related to modelling of carbonation of blended cement concrete. Firstly, some empirical models developed for Portland cement concrete are discussed. Secondly, the decisive factors of carbonation modelling are studied, as well as the changes brought by the introduction of SCMs to the concrete. Thirdly, the importance of C-S-H phases are discussed. Finally, concluding remarks and the intention of new research are made.

### 2.2 Mechanisms of carbonation in Portland cement concrete

This section summarises the chemical reactions occurring during the carbonation of calcium-bearing phases in Portland cement concrete, as well as the diffusion of CO<sub>2</sub> from the concrete surface.

In Portland cement concrete, the term carbonation is defined as the reaction of dissolved CO<sub>2</sub> with calcium ions extracted from calcium-bearing phases in the pore water, or directly with solid calcium-bearing phases. Calcium-bearing phases involved in the carbonation process are hydration products like CH and C-S-H, as well as unhydrated cement clinker components, such as tricalcium silicate (C<sub>3</sub>S), dicalcium silicate (C<sub>2</sub>S) [1-6]. Main physico-chemical processes involved in the carbonation of the cement paste in concrete are:

- Diffusion of atmospheric CO<sub>2</sub> in the gaseous phase of concrete.
- Dissolution of solid calcium-bearing phases in pore water and the diffusion of dissolved calcium-bearing phases in the pore solution.
- Dissolution and transport of CO<sub>2</sub> in pore water and its reaction with dissolved calcium-bearing phases.
- The reduction of pore volume due to the production of solid phases during the hydration and carbonation.
- The condensation of water vapour on the walls of concrete pores.

The main product of the carbonation reactions is calcium carbonate, which can precipitate in three crystalline polymorphs: calcite, aragonite and vaterite, depending on the internal concrete conditions (including temperature, humidity, etc.). The formation of calcium carbonate will release the water that was chemically bound in calcium-bearing phases, leaving changes of the solid volume. These changes can be, volume-wise, positive or negative, depending on the molar volume differences between reactants and products. It has a major impact on the porosity of carbonated area and further affecting the diffusion of CO<sub>2</sub>.

### 2.3 Carbonation depth prediction models for Portland cement concrete

From the discussion of carbonation mechanism, the carbonation depth is always developing with the diffusion of CO<sub>2</sub> but dragged down by the carbonation reactions. In another word, these calcium-bearing phases have buffering effects on the carbonation development. The primary material indicator of carbonation rate could be defined by a single parameter - the effective buffering capacity of the cementitious binder expressed as an equivalent Portland cement content, while other physical properties of concrete are of secondary importance. Based on this assumption, an empirical formula has been developed to predict carbonation depth development [7].

$$d = a + k \cdot \sqrt{t} \quad \text{Eq. 2-1}$$

where  $d$  is the carbonation depth [mm] and  $t$  is the carbonation time [year].

For the carbonation rate  $k$  it holds:

$$k = -4.062 + 2.568 \times (1000/b) \quad (1000/b > 1.5) \quad \text{Eq. 2-2}$$

The total effective buffering capacity  $b$  is calculated with:

$$b = b_1c_1 + b_2c_2 \quad \text{Eq. 2-3}$$

where  $b_1$  is the buffering capacity of the PC component  $c_1$  [kg/m<sup>3</sup>],  $b_2$  is the buffering capacity of the SCMs component  $c_2$  [kg/m<sup>3</sup>]

The effective buffering capacity of PC is calculated from the weight percentage of C<sub>3</sub>A:

$$b_1 = 0.0019(C_3A)^2 - 0.0056(C_3A) + 0.7538 \quad \text{Eq. 2-4}$$

in which  $C_3A$  is the  $C_3A$  content as the weight percentage of cement. The effective buffering capacity of BFS and FA (complying with BS 3892: part 1) is 0.6 and 0.2, respectively.

This prediction model mainly considers the amounts of binders and related buffering capacity factors. It is independent of the diffusion of CO<sub>2</sub>. Apparently, it is a rough estimate, not that suitable for predicting the carbonation depth in concrete.

Considering a series of mass balance of calcium-bearing phases, Papadakis [3] developed an engineering tool for predicting the penetration depth of the carbonation front  $X_c(t)$ , which is assumed to be linearly related with the square root of the exposure time  $t$ , as described with the formula:

$$X_c(t) = \sqrt{\frac{2[CO_2]^0 D_{e,CO_2}^c}{[Ca(OH)_2(s)]^0 + 3[CSH]^0 + 3[C_3S]^0 + 2[C_2S]^0}} \sqrt{t} \quad \text{Eq. 2-5}$$

in which  $[i]^0$  indicates the initial concentrations of constituent  $i$  in the non-carbonated zone in the concrete,  $D_{e,CO_2}^c$  is the effective diffusivity of CO<sub>2</sub> (gas) in the carbonated concrete, depending on the porosity of the concrete.  $[CO_2]^0$  is the atmospheric CO<sub>2</sub> concentration at the concrete surface.

The above empirical equation developed by Papadakis considers the diffusion of CO<sub>2</sub>, while the effective diffusivity is independent of carbonation time. This prediction model is designed for Portland cement concrete. It might need modification when applying for blended cement concrete, because this model does not take into account the effects of carbonation of C-S-H produced from pozzolanic reactions.

Normally, the reactions between unhydrated cement and CO<sub>2</sub> are ignored, because these reactions with CO<sub>2</sub> are negligible compared to the reaction with CH and C-S-H [8]. Therefore, the main carbonation reactions between calcium-bearing phases and CO<sub>2</sub> in the concrete are:



with  $C = CaO$ ,  $H = H_2O$ ,  $S = SiO_2$ , and  $\bar{C} = CO_2$ . The following discussion will focus on the carbonation of CH and C-S-H.

## 2.4 Effects of SCMs

There are lots of SCMs used in cement production all over the world. Two main groups can be distinguished:

1) *Hydraulic SCMs* -- Hydraulic SCMs can set and harden when submerged in water by forming the calcium silicate hydrate (C-S-H) in a hydration reaction. Hydraulic binders, such as blast furnace slag, a by-product of the pig-iron/steel production, and class C fly ash from coal combustion, contain a significant amount of CaO. However, their hydraulic activity is relatively low compared to Portland cement. Normally, hydraulic SCMs are activated chemically to initiate and accelerate the reactions [9, 10]. For example, blast furnace slag can be chemically activated by portlandite (CH) produced from the hydration of Portland cement.

2) *Pozzolanic SCMs* -- Pozzolanic SCMs react with excess calcium hydroxide generated in the hydration of Portland cement. The pozzolanic reactions are slower than hydraulic reactions and generate strength at later ages, beyond 28 days. Some common pozzolanic materials include class F fly ash, silica fume from the production of silicon or ferrosilicon alloys, volcanic ashes, metakaolin and calcined clays. The main difference between Class C and Class F fly ash is the chemical composition of the ash itself. ASTM C618 requires that Class F fly ash contains at least 70% pozzolanic compounds (silica oxide, alumina oxide, and iron oxide), while Class C fly ashes have between 50% and 70% of these compounds. Typically, Class C fly ash also contains significant amounts of calcium oxide - over 20%. Most Class F fly ash contains little calcium oxide.

*Figure 2-1* illustrates the chemical composition and typical variability of the most commonly used groups of SCMs in a CaO-SiO<sub>2</sub>-Al<sub>2</sub>O<sub>3</sub> ternary variation diagram [11]. Alkalis, MgO and Fe<sub>2</sub>O<sub>3</sub> content are ignored in this diagram. Utilization of these SCMs to substitute part of the Portland clinker has both economic and environmental advantages, including a great reduction of CO<sub>2</sub> emission. However, most of the SCMs differ significantly in chemical composition compared to Portland cement (see *Figure 2-1*). They generally have a lower calcium content, but a higher amount of silica and alumina. The use of SCMs in cement will affect the hydration process and microstructure development of cement paste, which might be the consequences for the durability concrete made of blended cement. Among these consequences, the resistance of the concrete against carbonation is the particular topic of this study.

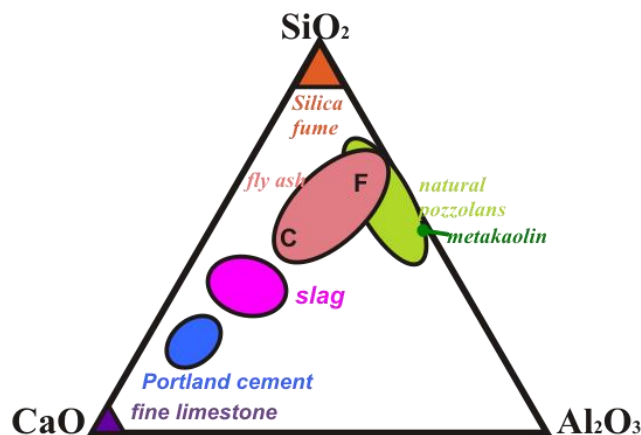


Figure 2-1  $\text{CaO-Al}_2\text{O}_3\text{-SiO}_2$  ternary diagram of cementitious materials (after B. Lothenbach et al, 2011 [11])

In concrete blended with SCMs, the CH content is relatively low compared to ordinary Portland cement concrete due to, first, the dilution effects and, second, the consumption of CH in pozzolanic reactions between SCMs and CH [11]. From the thermodynamic point of view, the reaction kinetic of CH carbonation is initially higher than that of C-S-H [12, 13]. Therefore, in the initial carbonation stage CH is always consumed first. The carbonation of C-S-H will start when all the accessed CH is consumed. In later stage, the only calcium-bearing phase in blended cement concrete is C-S-H, which will play the key role for the long-term durability of concrete under the carbonation attack.

## 2.5 Carbonation of C-S-H

C-S-H is the major product of the hydration of Portland cement, and also the main contributor to the strength of concrete. Carbonation of C-S-H has been studied by many authors [6, 14, 15]. It is a complex decalcification-polymerization process of the C-S-H and the formation of amorphous silica gel (see Eq. 2-7). Carbonation mechanisms, as well as the reaction rates and reaction products, depend on the properties of C-S-H, like Ca/Si (C/S) and  $\text{H}_2\text{O}/\text{Si}$  (H/S). It is more appropriate, therefore, to study the carbonation mechanism of C-S-H based on the C-S-H structure.

The behaviour of different types of C-S-H phases (distinguished per C/S ratio in this discussion) varies in front of carbonation, including the decalcification rate and following influences on the microstructure of concrete. It is widely acknowledged that the C/S ratio of C-S-H gel from cement hydration ranges from 1.50 to 2.0 [16-23]. The C/S ratio of C-S-H gels produced from the pozzolanic reaction of SCMs, such as FA or BFS, varies from 1.0 to 1.60 [24-28]. The C-S-H phases (including all the C-S-H gels mentioned above and natural phases) share a similar layer structure, which can be inferred from the refined structure of  $11\text{\AA}$  tobermorite ( $\text{Ca}_{4.5}\text{Si}_6\text{O}_{16}(\text{OH})\cdot 5\text{H}_2\text{O}$ ) [29]. This refined structure consists of three parts:  $\text{CaO}_2$  sheets, a 'dreierkette' form SiO-chain and interlayer.



C/S ratio of C-S-H in the concrete is normally higher than 0.83. The increase of the C/S ratio in C-S-H gel based on the tobermorite structure can be caused by omission of the bridging tetrahedra and incorporation of additional calcium in the interlayer. If all the bridge tetrahedra are removed, the Ca/Si ratio can increase to 1.25 [30, 31]. Further incorporation of extra  $\text{Ca}^{2+}$  in the interlayer can form the C-S-H with a much higher Ca/Si ratio, the theoretical value of which is 1.50 when all the bridging sites are removed and taken up by extra  $\text{Ca}^{2+}$  [30]. The extra  $\text{Ca}^{2+}$  is normally balanced by the omission of  $\text{H}^+$  or the incorporation of  $\text{OH}^-$  or both. If the amount of extra  $\text{Ca}^{2+}$  continues to increase and achieves a Ca/Si ratio even higher than 1.5, the structure of C-S-H is closer to the C-S-H/CH ‘solid solution’ (T/CH model) [30].

From the above discussion, three types of Ca exist in the C-S-H structure (classification by the position of Ca): Ca in the  $\text{CaO}_2$  sheet layer, Ca in the bridging site and Ca in the interlayer, shown in *Figure 2-2*. The proportions of them vary among C-S-H with different Ca/Si ratio. In the previous statement, the carbonation of C-S-H gel proceeds in steps: removing Ca from different sites in the layer structure and polymerization of SiO chain. Apparently, the removal of Ca from the three above-mentioned chemical sites will need different energy. Moreover, the mean chain length (MCL) of SiO chain also varies in C-S-H phases with different C/S ratio. The MCL of C-S-H gel can be calculated from the  $^{29}\text{Si}$  NMR test results, which has been studied by many researchers and summarized in [32]. Manzano [33] investigated the thermodynamic stability of aluminosilicate chains, which is widely observed in blended cement concrete. The origin of stability in the aluminosilicate chains is analyzed by looking at the gap between the highest occupied molecular orbital (HOMO) and the lowest unoccupied molecular orbital (LUMO). The calculation results indicate that the aluminosilicate chain with less length has a relatively higher HOMO-LUMO energy gap, which means the shorter chain is thermo-dynamically more stable. Considering the variation of both the Ca sites in the layer structure and thermodynamic stability of different SiO chain among different types of C-S-H gels, the decalcification rate of C-S-H phases with different C/S ratio will be different, which has to be taken into account in the study of carbonation of blended cement concrete.

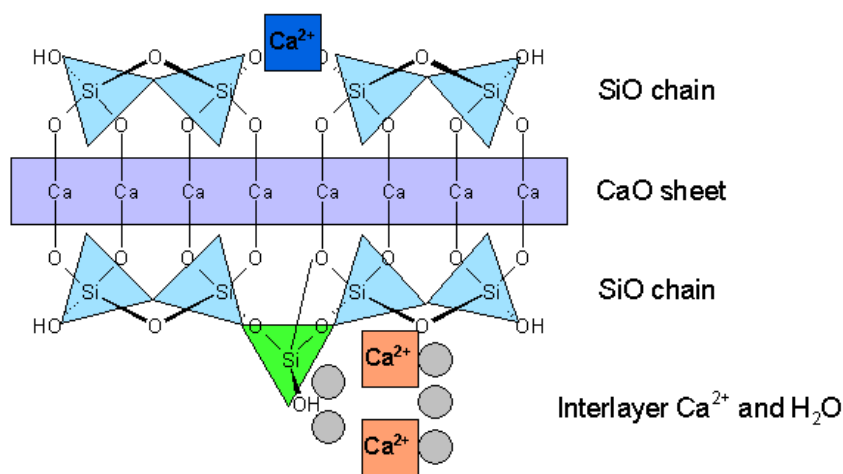


*Figure 2-2 Possible positions of  $\text{Ca}^{2+}$  in the C-S-H layer structure*

## 2.6 Effects of C-S-H carbonation on the porosity evolution of concrete

It is well-known that the carbonation of CH leads to a reduction in porosity which is ascribed to the positive difference of molar volume between CH and the formed  $\text{CaCO}_3$  [34-39]. But if considering the carbonation of C-S-H, the effect of carbonation on the porosity and microstructure of cement paste is still controversial. Carbonation of C-S-H has been studied by many authors [6, 14, 40]. It consists of a complex decalcification-polymerization process of the C-S-H and the formation of amorphous silica gel, see Eq. 2-7. The molar volume change due to the carbonation of C-S-H depends on the properties of C-S-H (like Ca/Si ratio, water content) and the water remained in silica gel.

Based on the Eq. 2-6 and Eq. 2-7, which equations describe the carbonation of CH and C-S-H, the solid volume changes due to carbonation can be obtained with Eq. 2-8 [41]:

$$\Delta\phi = \Delta\phi_{CH} + \Delta\phi_{CSH} = n_{\overline{CC}}^{CH} (V_{\overline{CC}}^{CH} - V_{CH}) + n_{\overline{CC}}^{CSH} \left[ V_{\overline{CC}}^{CSH} + \frac{V_{CSH}(t) - V_{CSH}(t_0)}{(C/S)(t_0) - (C/S)(t)} \right] \quad \text{Eq. 2-8}$$

in which  $V_{\overline{CC}}^{CH} = V_{\overline{CC}}^{CSH} = 36.93 \text{ cm}^3 / \text{mol}$  and  $V_{CH} = 33.08 \text{ cm}^3 / \text{mol}$  are the molar volume of  $\overline{CC}$  and CH respectively.  $n_{\overline{CC}}^{CH}$  and  $n_{\overline{CC}}^{CSH}$  are the molar number of  $\overline{CC}$  contributed by the carbonation of CH and C-S-H.  $(C/S)(t_0)$  and  $(C/S)(t)$  are the Ca/Si ratio of C-S-H before and after carbonation.  $(C/S)(t_0)$  varies from 0.75 – 2.0 and  $(C/S)(t)$  equals to zero.  $V_{CSH}(t)$  is the molar volume of C-S-H after carbonation.  $V_{CSH}(t) = V_{SH_t(gel)}$  is the molar volume of carbonation product  $SH_t(gel)$ , which is in the range of 12-34  $\text{cm}^3 / \text{mol}$  [42].

By applying the above-mentioned parameters, the volume change per 1 mole of  $\overline{CC}$  contributed by the carbonation of C-S-H can be calculated by Eq. 2-9.

$$\Delta\phi_{CSH}^0 (\text{cm}^3 / \text{mol}) = 36.93 - \frac{V_{CSH}(t_0) - V_{SH_t(gel)}}{(C/S)(t_0)} \quad \text{Eq. 2-9}$$

The total volume change due to the carbonation of CH and C-S-H can be calculated by Eq. 2-10.

$$\Delta\phi = \Delta\phi_{CH} + \Delta\phi_{CSH} = 3.85 \times n_{\overline{CC}}^{CH} - \left[ 36.93 - \frac{V_{CSH}(t_0) - V_{SH_t(gel)}}{C/S(t_0)} \right] \times n_{\overline{CC}}^{CSH} \quad \text{Eq. 2-10}$$

Assuming that  $\Delta\phi_{CSH}^0 = 0$ , then:

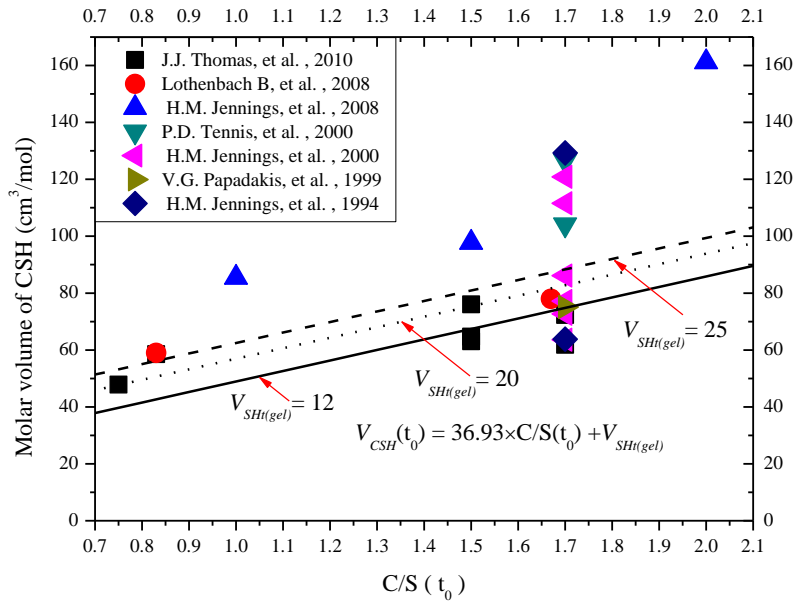


Figure 2-3 Relations between molar volume and Ca / Si ratio of the C-S-H

$$V_{CSH}(t_0) = 36.93 \times C / S(t_0) + V_{SH_t(gel)} \quad \text{Eq. 2-11}$$

The linear relationships between  $V_{CSH}(t_0)$  and  $(C/S)(t_0)$  are drawn in *Figure 2-3*. The value of  $V_{SH_t(gel)}$  is chosen as 12, 20 and 25  $cm^3/mol$ , respectively. The data points in the same figure are the parameter values for C-S-H used in references [43-49].

Calculation of volume changes based on the values of the point above the linear curve will give a negative value of  $\Delta\phi_{CSH}^0 (< 0)$ ; otherwise a positive value. The negative value of  $\Delta\phi_{CSH}^0$  means the carbonation of these types of C-S-H will cause a decrease of the solid volume and the increase of the pore space volume or porosity of the cement paste matrix.

From *Figure 2-3*, carbonation of most of the species of C-S-H will result in an increase of the porosity of cement paste. It should be noticed that the effects of carbonation on the porosity evolution will be different for some types of C-S-H gel in case the value of  $V_{SH_t(gel)}$  will hold.

## 2.7 Concluding remarks and motivation of the research

In this chapter, a brief overview of carbonation mechanisms of concrete is given, and a few prediction tools for estimating the carbonation depth in Portland cement concrete have been mentioned.

Utilization of SCMs in cement production can reduce the clinker content, which makes great contribution to the CO<sub>2</sub> emission reduction. However, the pozzolanic reaction of SCMs

will consume the portlandite during the hydration of blended cement, producing different C-S-H phases, indicated by their C/S ratios. C-S-H phases will replace portlandite to play the key role in the resistance to CO<sub>2</sub> attack.

Current research shows that the reaction kinetics of different C-S-H phases are different during the carbonation. Some C-S-H phases might be more prone to carbonation. Further investigations show that carbonation of C-S-H phases will increase the porosity of carbonated concrete, which is in favor of CO<sub>2</sub> diffusion.

The above-mentioned factors, which may alter the carbonation development trend in the blended cement concrete, are not considered in the existing empirical tools for prediction of the carbonation depth. Therefore, effects of the carbonation of C-S-H on the porosity development of blended cement paste are studied systematically in this thesis. The reaction rate of different types of C-S-H phases is investigated as well by performing accelerated carbonation experiments on synthesized C-S-H. The experimental results will be used for developing an improved empirical equation for the prediction of carbonation depth in blended cement concrete.

## 2.8 References

- [1] J. Young, R. Berger, J. Breese, Accelerated curing of compacted calcium silicate mortars on exposure to CO<sub>2</sub>, *J Am Ceram Soc*, 57 (1974) 394-397.
- [2] V.G. Papadakis, C.G. Vayenas, M. Fardis, A reaction engineering approach to the problem of concrete carbonation, *AIChE Journal*, 35 (1989) 1639-1650.
- [3] V.G. Papadakis, C.G. Vayenas, M.N. Fardis, Fundamental modeling and experimental investigation of concrete carbonation, *Acı Mater J*, 88 (1991).
- [4] K. Garbev, P. Stemmermann, L. Black, C. Breen, J. Yarwood, B. Gasharova, Structural features of C–S–H (I) and its carbonation in air—a Raman spectroscopic study. Part I: fresh phases, *J Am Ceram Soc*, 90 (2007) 900-907.
- [5] P.H. Borges, J.O. Costa, N.B. Milestone, C.J. Lynsdale, R.E. Streatfield, Carbonation of CH and C–S–H in composite cement pastes containing high amounts of BFS, *Cement Concrete Res*, 40 (2010) 284-292.
- [6] A. Morandau, M. Thiery, P. Dangla, Investigation of the carbonation mechanism of CH and CSH in terms of kinetics, microstructure changes and moisture properties, *Cement Concrete Res*, 56 (2014) 153-170.
- [7] P.B. BAMFORTH, G.R. SUMMERS, Carbonation data from 6 year exposure of blended cement concretes in Bahrain, the 5th International Conference on Deterioration and repair of reinforced concrete in the Arabian Gulf, 1997.
- [8] M. Peter, A. Muntean, S. Meier, M. Böhm, Competition of several carbonation reactions in concrete: a parametric study, *Cement Concrete Res*, 38 (2008) 1385-1393.
- [9] M. Regourd, Slags and slag cements, Cement replacement materials. Department of Mechanical Engineering, University of Sheffield, (1986) 73-99.
- [10] E. Lang, Blast furnace cements, *Structure and Performance of Cements*, 2nd ed., Spon, London, (2002) 310-323.
- [11] B. Lothenbach, K. Scrivener, R. Hooton, Supplementary cementitious materials, *Cement Concrete Res*, 41 (2011) 1244-1256.
- [12] F. Glasser, T. Matschei, Interactions between Portland cement and carbon dioxide, *Proceedings of the ICCI Conference*, 2007.
- [13] G.W. Groves, A. Brough, I.G. Richardson, C.M. Dobson, Progressive changes in the structure of hardened C<sub>3</sub>S cement pastes due to carbonation, *J Am Ceram Soc*, 74 (1991) 2891-2896.
- [14] L. Black, C. Breen, J. Yarwood, K. Garbev, P. Stemmermann, B. Gasharova, Structural features of C–S–H (I) and its carbonation in air—a Raman spectroscopic study. Part II: carbonated phases, *J Am Ceram Soc*, 90 (2007) 908-917.
- [15] Z.k. S`auman, Long-term carbonization of the phases 3CaO. Al<sub>2</sub>O<sub>3</sub>. 6H<sub>2</sub>O and 3CaO. Al<sub>2</sub>O<sub>3</sub>. SiO<sub>2</sub>. 4H<sub>2</sub>, *Cement Concrete Res*, 2 (1972) 435-446.
- [16] A. Harrison, An Examination of Some Pore and Composite Portland Cement Pastes Using Scanning Electron Microscopy with X-ray Analytical Capability, *Proceedings of the 8th International Congress on the Chemistry of Cement*, 1986, 1986, pp. 170-175.
- [17] H.F.W. Taylor, A. Turner, Reactions of tricalcium silicate paste with organic liquids, *Cement Concrete Res*, 17 (1987) 613-623.
- [18] G. Groves, P. Le Sueur, W. Sinclair, Transmission Electron Microscopy and Microanalytical Studies of Ion-Beam-Thinned Sections of Tricalcium Silicate Paste, *J Am Ceram Soc*, 69 (1986) 353-356.
- [19] I. Odler, H. Dörr, Early hydration of tricalcium silicate I. Kinetics of the hydration process and the stoichiometry of the hydration products, *Cement Concrete Res*, 9 (1979) 239-248.
- [20] L. SUEUR, Chemical and morphological studies of the hydration of tricalcium silicate, *Proc. Br. Ceram. Soc.*, 1984, pp. 177.
- [21] D.L. Kantro, C.H. WEISE, Hydration of Various Beta-Dicalcium Silicate Preparations, *J Am Ceram Soc*, 62 (1979) 621-626.
- [22] K. Fujii, W. KONDO, Rate and Mechanism of Hydration of  $\beta$ -Dicalcium Silicate, *J Am Ceram Soc*, 62 (1979) 161-167.

- [23] S. Shibata, K. Kishi, K. Asaga, M. Daimon, P. Shrestha, Preparation and hydration of  $\beta$ -C2S without stabilizer, *Cement Concrete Res*, 14 (1984) 323-328.
- [24] H. Uchikawa, S. Uchida, S. Hanehara, Effect of character of glass phase in blending components on their reactivity in calcium hydroxide mixture, 1986.
- [25] T. Sato, I. Furuhashi, Review of the 36th General Meeting, Cement Association of Japan, (1982) 42.
- [26] A. Harrisson, N. Winter, H.F. Taylor, Microstructure and microchemistry of slag cement pastes, *MRS Online Proceedings Library Archive*, 86 (1986).
- [27] R. Snellings, T. Paulhiac, K. Scrivener, The Effect of Mg on Slag Reactivity in Blended Cements, *Waste and Biomass Valorization*, 5 (2014) 369-383.
- [28] J.M. Richardson, J.J. Biernacki, P.E. Stutzman, D.P. Bentz, Stoichiometry of Slag Hydration with Calcium Hydroxide, *J Am Ceram Soc*, 85 (2002) 947-953.
- [29] S. Merlino, E. Bonaccorsi, T. Armbruster, The real structure of tobermorite 11Å normal and anomalous forms, OD character and polytypic modifications, *Eur J Mineral*, 13 (2001) 577-590.
- [30] I. Richardson, Tobermorite/jennite-and tobermorite/calcium hydroxide-based models for the structure of CSH: applicability to hardened pastes of tricalcium silicate,  $\beta$ -dicalcium silicate, Portland cement, and blends of Portland cement with blast-furnace slag, metakaolin, or silica fume, *Cement Concrete Res*, 34 (2004) 1733-1777.
- [31] H. Taylor, J. Howison, Relationships between calcium silicates and clay minerals, *Clay Minerals Bull*, 3 (1956) 98-111.
- [32] B. Wu, G. Ye, Study of carbonation rate of synthetic CSH by XRD, NMR and FTIR, *Heron*, 64 (2019) 21.
- [33] H. Manzano, J. Dolado, A. Ayuela, Aluminum incorporation to dreierketten silicate chains, *The Journal of Physical Chemistry B*, 113 (2009) 2832-2839.
- [34] S.E. Pihlajavaara, Some results of the effect of carbonation on the porosity and pore size distribution of cement paste, *Matériaux et Constructions*, 1 (1968) 521-527.
- [35] S.E. Pihlajavaara, E. Pihlman, Effect of carbonation on microstructural properties of cement stone, *Cement Concrete Res*, 4 (1974) 149-154.
- [36] R.G. Patel, D.C. Killoh, L.J. Parrott, W.A. Gutteridge, Influence of curing at different relative humidities upon compound reactions and porosity in Portland cement paste, *Mater Struct*, 21 (1988) 192-197.
- [37] V.G. Papadakis, C.G. Vayenas, M.N. Fardis, Physical and chemical characteristics affecting the durability of concrete, *Aci Mater J*, 88 (1991).
- [38] V.T. Ngala, C.L. Page, Effects of carbonation on pore structure and diffusional properties of hydrated cement pastes, *Cement Concrete Res*, 27 (1997) 995-1007.
- [39] M.M.Y. Delmi, A. Ai't-Mokhtar, O. Amiri, Modelling the coupled evolution of hydration and porosity of cement-based materials, *Constr Build Mater*, 20 (2006) 504-514.
- [40] V.r.L. Zdeněk Šauman, Long-term carbonization of the phases  $3\text{CaO}\cdot\text{Al}_2\text{O}_3\cdot 6\text{H}_2\text{O}$  and  $3\text{CaO}\cdot\text{Al}_2\text{O}_3\cdot\text{SiO}_2\cdot 4\text{H}_2\text{O}$ , *Cement Concrete Res*, 2 (1972) 12.
- [41] A. Morandea, M. Thiéry, P. Dangla, Impact of accelerated carbonation on OPC cement paste blended with fly ash, *Cement Concrete Res*, 67 (2015) 226-236.
- [42] M. Thiéry, P. Faure, A. Morandea, G. Platret, J.-F. Bouteloup, P. Dangla, V. Baroghel-Bouny, Effect of carbonation on the microstructure and moisture properties of cement-based materials, XII DBMC (12th International Conference on Building Materials and Components, 2011, pp. 1-8.
- [43] J.J. Thomas, H.M. Jennings, A.J. Allen, Relationships between Composition and Density of Tobermorite, Jennite, and Nanoscale  $\text{CaO}-\text{SiO}_2-\text{H}_2\text{O}$ , *The Journal of Physical Chemistry C*, 114 (2010) 7594-7601.
- [44] B. Lothenbach, T. Matschei, G. Möschner, F.P. Glasser, Thermodynamic modelling of the effect of temperature on the hydration and porosity of Portland cement, *Cement Concrete Res*, 38 (2008) 1-18.
- [45] H.M. Jennings, J.W. Bullard, J.J. Thomas, J.E. Andrade, J.J. Chen, G.W. Scherer, Characterization and modeling of pores and surfaces in cement paste: correlations to processing and properties, *J Adv Concr Technol*, 6 (2008) 5-29.
- [46] P.D. Tennis, H.M. Jennings, A model for two types of calcium silicate hydrate in the microstructure of Portland cement pastes, *Cement Concrete Res*, 30 (2000) 855-863.

- [47] H.M. Jennings, A model for the microstructure of calcium silicate hydrate in cement paste, *Cement Concrete Res*, 30 (2000) 101-116.
- [48] H.M. Jennings, P.D. Tennis, Model for the Developing Microstructure in Portland Cement Pastes, *J Am Ceram Soc*, 77 (1994) 3161-3172.
- [49] V.G. Papadakis, Effect of fly ash on Portland cement systems: Part I. Low-calcium fly ash, *Cement Concrete Res*, 29 (1999) 1727-1736.

---

## Hydration of Portland Cement Blended with Supplementary Cementitious Materials (SCMs)

---

### 3.1 Introduction

The chemical composition of calcium-bearing phases and the microstructure of blended cement paste are affected by the types and replacement levels of SCMs. Compared with ordinary Portland cement (OPC), C-S-H, the major calcium-bearing phase in SCMs blended cement paste, originates from the hydration of OPC and pozzolanic reactions. The calcium-bearing phases and the microstructure of cement paste largely determine the concrete's resistance to carbonation. Carbonation in cement paste mainly involves two steps: diffusion of atmospheric CO<sub>2</sub> inside the microstructure of cement paste and chemical reactions between calcium-bearing phases and CO<sub>2</sub>. Therefore, it is very important to figure out the effects of SCMs on the hydration products and microstructure of blended cement paste.

In this chapter the development of hydration products, i.e. portlandite and C-S-H, and the microstructure of cement paste blended with different types of SCMs (FA, BFS) are studied. Influences of the FA or BFS on the amounts of portlandite and C-S-H are discussed, together with the microstructure of blended cement pastes. The characteristics of C-S-H formed from pozzolanic reactions will be investigated as well. The above-mentioned results are input data for Chapter 4 where the phase changes and porosity development due to carbonation are calculated.



## 3.2 Materials and experiments

### 3.2.1 Materials properties

Cement pastes used in this study are made from ordinary Portland cement (OPC) CEM I 425N (classification according to EN 197-1), produced by ENCI in the Netherlands. Two types of SCMs, i.e. fly ash (FA) and blast furnace slag (BFS), are used to replace part of the cement to prepare blended cement paste. The fly ash used is Class F fly ash (ASTM C 618). BFS is produced by ORCEM, Netherlands. The main chemical compositions (in the form of oxides) of the above-mentioned raw materials are determined by X-ray fluorescence spectrometry (XRF). The results are presented in *Table 3-1*. The chemical compositions of raw materials will be used as the input parameters for numerical simulation studies with HYMOSTRUC3D-E proposed by Gao [1], to be explained later in this chapter.

Major crystalline phases of the above-mentioned raw materials were determined by X-ray diffraction (XRD). The X-ray source used is Cu K radiation ( $\lambda = 0.154056$  nm). The scan step size was  $0.03^\circ$ , from  $5^\circ$  to  $70^\circ$  ( $2\theta$ ). Measured XRD patterns of the raw materials are described in *Figure 3-1*.

*Table 3-1 Main chemical composition of raw materials tested by XRF (wt. %)*

Component	Main chemical components [wt. %]								Total
	CaO	SiO <sub>2</sub>	Al <sub>2</sub> O <sub>3</sub>	Fe <sub>2</sub> O <sub>3</sub>	MgO	K <sub>2</sub> O	Na <sub>2</sub> O	SO <sub>3</sub>	
Cement	64.50	18.88	4.48	3.69	2.01	0.51	0.34	4.04	99.993
FA	5.54	50.55	30.74	6.30	1.00	1.11	0.28	0.79	99.982
BFS	41.40	34.02	11.12	0.53	8.28	0.40	0.21	2.43	100.00

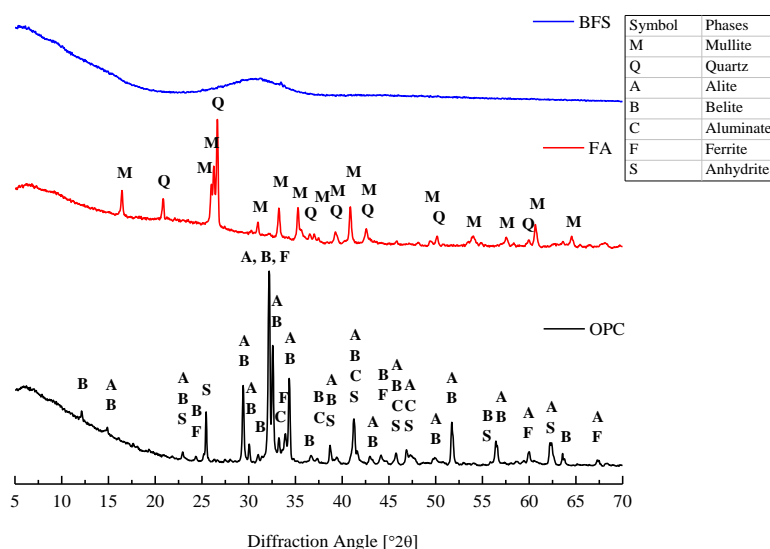


*Figure 3-1 X-ray diffraction pattern of the raw materials*

The major peaks in the XRD pattern of OPC are compared with the characteristic peaks of minerals or crystalline phases in the XRD spectra database to identify the crystals existing in OPC. Main crystalline phases found in OPC are Alite ( $C_3S$ ), Belite ( $C_2S$ ), Aluminate ( $C_3A$ ) and Ferrite ( $C_4AF$ ), together with Anhydrite ( $C\bar{S}$ ). By using the same method, Mullite and quartz are found in FA. Meanwhile, no peaks indicating the diffraction of crystals can be found in the pattern of BFS. This means that BFS is only present in amorphous form. Major crystalline phases of OPC and FA are confirmed by XRD tests and listed in *Table 3-2*.

*Table 3-2 Major crystallographic data of phases identified in raw materials*

Phase name	Abbreviated notation	Composition	Lattice	Space group (ICSD data base [2])
Mullite	$A_2S$	$Al_{4.8}O_{9.6}Si_{1.2}$	Orthorhombic	P2_1/b2_1/a2/m (No. 55)
Quartz	$S$	$SiO_2$	Trigonal	P3_221 (No. 154)
Alite	$C_3S$	$3CaO \cdot SiO_2$	Monoclinic	C1m1 (No. 8)
Belite	$C_2S$	$2CaO \cdot SiO_2$	Monoclinic	P12_1/n1 (No. 14)
Aluminate	$C_3A$	$3CaO \cdot Al_2O_3$	Cubic	P2_1/a-3 (No. 205)
Ferrite	$C_4AF$	$4CaO \cdot Al_2O_3 \cdot Fe_2O_3$	Orthorhombic	I2mb (46)
Anhydrite	$C\bar{S}$	$CaO \cdot SO_3$	Orthorhombic	B2/b2_1/m2/m (No. 63)

Based on the X-ray test results, the amounts of crystalline phases in OPC and FA can be determined by Rietveld method [3]. It is known that only crystalline phases create distinct diffraction patterns, and the amorphous phase is absent in the XRD patterns. By using the Rietveld refinement as shown in *Figure 3-2*, the phase quantifications can be usually reported

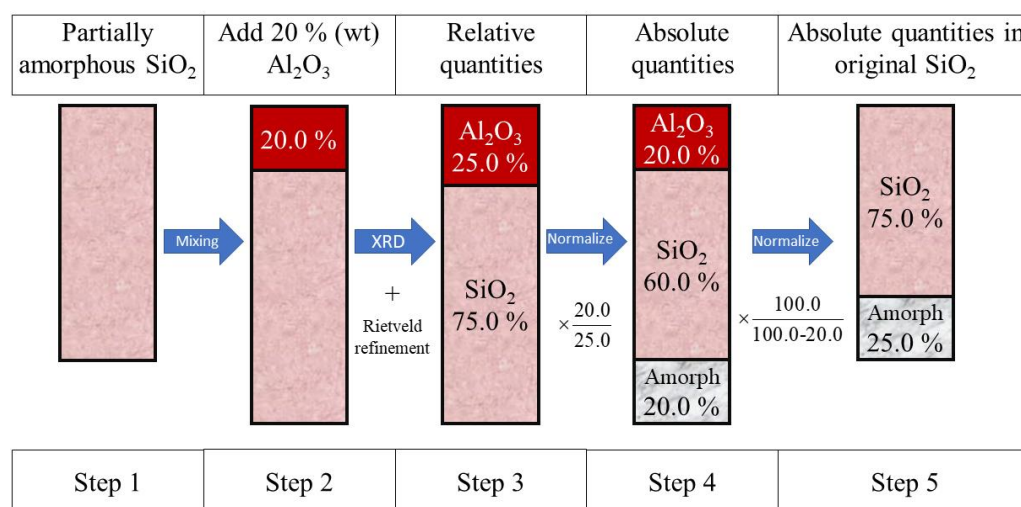


*Figure 3-2 Calculation of the relative and absolute quantities of phases by rietveld refinement with internal standard*

as the relative weight percentage, which is relative to the total weight of all crystalline phases (see Step 3 in *Figure 3-2*). If a crystalline phase with known quantity is added in the sample, the relative quantities can be normalized to absolute values (see Step 4 in *Figure 3-2*).

The crystalline phase added should be stable and inert, which is also known as the internal standard. In this research, the internal standard used is corundum ( $\text{Al}_2\text{O}_3$ ). The weight percentage of  $\text{Al}_2\text{O}_3$  (as per the total amount) in the initial mixture are listed in *Table 3-3*. The procedure of calculating the relative and absolute quantities is performed automatically by the Profex software[4].

*Table 3-3 Weight percentage (%) of the internal standard  $\text{Al}_2\text{O}_3$  added in OPC and FA*

Raw materials	OPC	FA
$\text{Al}_2\text{O}_3$	10.53	10.49

Rietveld refinement was performed on the XRD test results of OPC and FA shown in *Figure 3-1*, in order to calculate the relative amounts of crystalline phases. The crystallographic information files (CIFs) of corundum and other crystalline phases used in the Rietveld refinement are listed in *Table 3-4*.

The amounts of major crystal phases in OPC, recalculated by the above-mentioned method, are listed in *Table 3-5*. The phase composition of OPC will be used as input parameters for numerical simulations hydration processes with HYMOSTRUC3D-E [1]. Meanwhile, the phase composition of fly ash is calculated as well and shown in *Table 3-6*.

*Table 3-4 Crystallographic information file (CIF) of  $\text{Al}_2\text{O}_3$  and other phases in OPC and FA*

Crystal Phases	Corundum	Mullite	Quartz	Alite	Belite	Aluminate	Ferrite	Anhydrite
CIF (ICSD No.) [2]	31546	202159	34636	94742	79550	1841	98837	56107

*Table 3-5 Major crystalline compositions of OPC determined by Rietveld method (wt. %)*

Alite	Belite	Aluminate	Ferrite	Anhydrite	Amorphous
60.1	11.77	4.65	12.59	3.98	6.10

*Table 3-6 Phase composition of fly ash determined by Rietveld method (wt. %)*

Quartz	Mullite	Amorphous
6.99	27.80	65.30

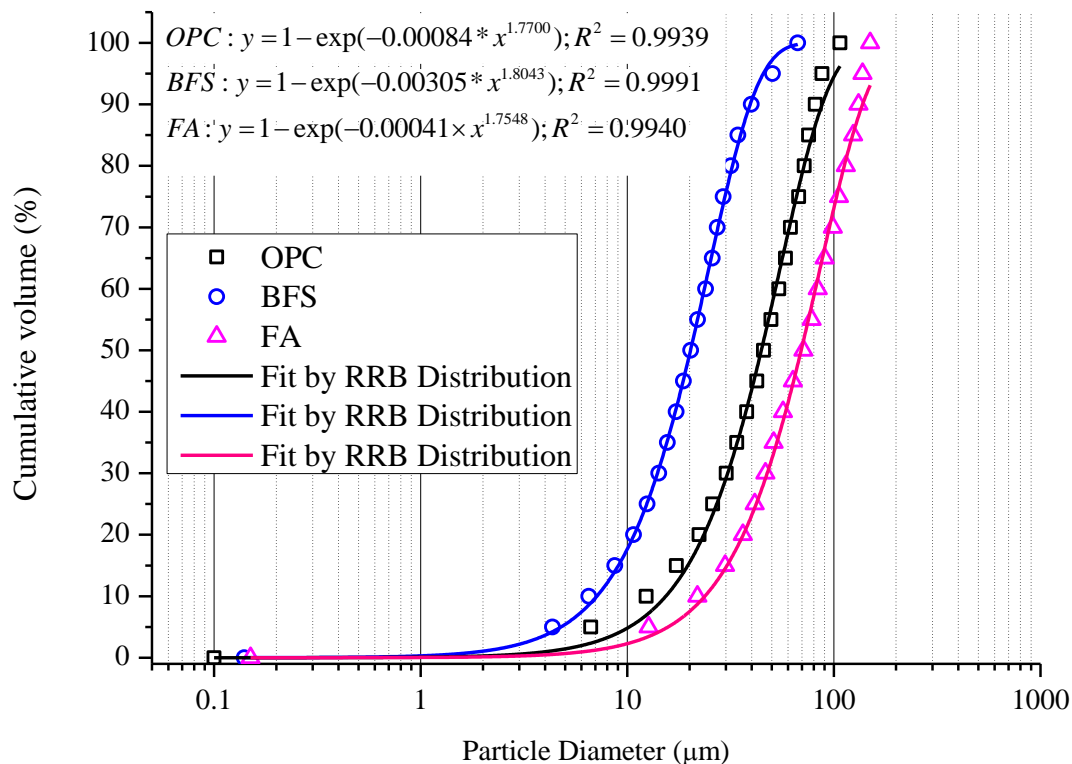


Figure 3-3 Particle size distribution of raw materials (square - PC, triangle - FA, blue cycle - BFS)

Table 3-7 Parameters  $n$  and  $b$  determined for different binders

RRB - parameters	Binders		
	OPC	FA	BFS
$n$	1.7700	1.7548	1.8043
$b$	0.00084	0.00041	0.00305

The particle size distributions of raw materials were analyzed by laser diffraction method. Particle Size Analyzer DIPA-2000 is used for the tests. The results are presented in *Figure 3-3*. As shown in *Figure 3-3*, the particle size distributions of raw binders follow the Rosin Rammler Bennett (RRB) cumulative distribution  $G(d)$ :

$$G(d) = 1 - e^{-bd^n}, \lim_{d \rightarrow \infty} G(d) = 1 \quad \text{Eq. 3-1}$$

where  $d [\mu\text{m}]$  is the particle diameter;  $n$  and  $b$  are fitting parameters. By fitting the test data with RRB equation, the parameters  $n$  and  $b$  are determined for different raw binders, listed in *Table 3-7*.

These parameters will be used as the input data for numerical simulations of reaction processes with HYMOSTRUC3D-E [1].

### 3.2.2 Sample preparation and experimental procedure

Pure Portland cement paste was prepared as the reference sample. In blended cement paste OPC was partly replaced by FA or BFS, including binary (PC + FA or BFS) and ternary mix (PC + FA + BFS). The weight percentages of raw materials in different mixtures are listed *Table 3-8*. The water/binder ratio (w/b) is 0.5.

Cement pastes were prepared in a HOBART mixer at room temperature. The binders were mixed with demineralized water at the low speed for 1 minute and at the high speed for 2 minutes with an interval of 15 seconds. The fresh paste was transferred immediately to the plastic bottles with the diameter of 50 mm. The bottles were filled in 3 steps and vibrated on

*Table 3-8 Mass fraction of raw materials in different mixtures*

Sample ID	PC (g) (wt. %)	FA (g) (wt. %)	BFS (g) (wt. %)	Water (g)
P100	1500			750
F10	1350	150 (10)		750
F30	1050	450 (30)		750
B30	1050		450 (30)	750
B70	450		1050 (70)	750
F10B54	540	150 (10)	810 (54)	750
F30B30	600	450 (30)	450 (30)	750

the vibration table for 10 seconds at each step, in order to remove the air before the bottles were sealed. After sealing the bottles were fixed in the rotation machine at a speed of 5-7 rpm for 24 hours to prevent bleeding. After that sealed curing was performed at 20°C in the fog room for different ages up to 1 year.

After curing for a predefined period, the plastic bottles with cement paste were broken and crushed into small pieces with dimensions of 1-2 cm<sup>3</sup> and immersed into liquid nitrogen for 3-4 min to stop further hydration. After hydration being terminated, the samples were immediately moved into a vacuum freeze-dryer. The temperature and vacuum were maintained at -24°C and 0.1 Pa, respectively [5]. The freeze-drying procedure lasted for at least 4 weeks until the daily weight loss of those specimens was less than 0.1%.

### 3.2.3 Test methodology

As indicated in Eq. 1-1 and discussed in section 1.1 of Chapter 1, the propagation rate of carbonation depth in concrete is mainly determined by the amounts of calcium-bearing phases (CH and C-S-H) and porosity of the concrete. It is known that CH and C-S-H are formed during the hydration of cement clinker in OPC. However, in blended cement concrete, SCMs (FA and BFS) will consume CH to form C(-A)-S-H, which has different properties other than C-S-H found in OPC concrete, i.e. a lower C/S ratio. Therefore, the introduction of SCMs in concrete will affect the resistance of blended cement concrete to carbonation in two ways: affecting the amounts of calcium-bearing phases and changing the porosity of concrete.

To figure out the effects of SCMs on the carbonation resistance of concrete, the amount of main calcium-bearing phases, i.e. CH and C-S-H, and the porosity of blended cement paste have to be determined by different methods. For determining the CH content in different blended cement pastes, thermogravimetric analysis (TGA) is used. The amount of CH is simulated by using HYMOSTRUC3D-E [1] as well, to comparing studied with the data measured by experiments. HYMOSTRUC3D-E is extended from HYMOSTRUC3D, to simulate the hydration and microstructure development of Portland cement blended with blast furnace slag or/and fly ash. HYMOSTRUC, the acronym for HYdration, MORphology and STRUCture formation, is a numerical model of cement hydration proposed by K. van Breugel in 1991[6]. Further incorporated new algorithms by Koenders [7] and Ye [5] respectively, HYMOSTRUC is extended for simulation of 3D microstructure during the cement hydration, so called HYMOSTRUC3D.

Different types of C-S-H phases (classified by C/S ratio in this research) are distinguished and determined based on the further processing of the elemental mapping data, which is carried out by using energy dispersive X-ray analysis (EDAX) under the Backscattered electron (BSE) model. Relative amounts of different types of C-S-H in blended cement paste is supplemented by HYMOSTRUC3D-E [1]. Meanwhile, Mercury Intrusion Porosimetry (MIP) is used to determine the pore size distribution and porosity (including total and capillary porosity) of blended cement paste.

**TGA** -- The amount of CH in the paste is determined by TGA. TGA measurements provide information about the decomposition or dehydration of minerals as a function of



Figure 3-4 Netzsch STA 449 F3 Jupiter instrument used for thermogravimetric analysis

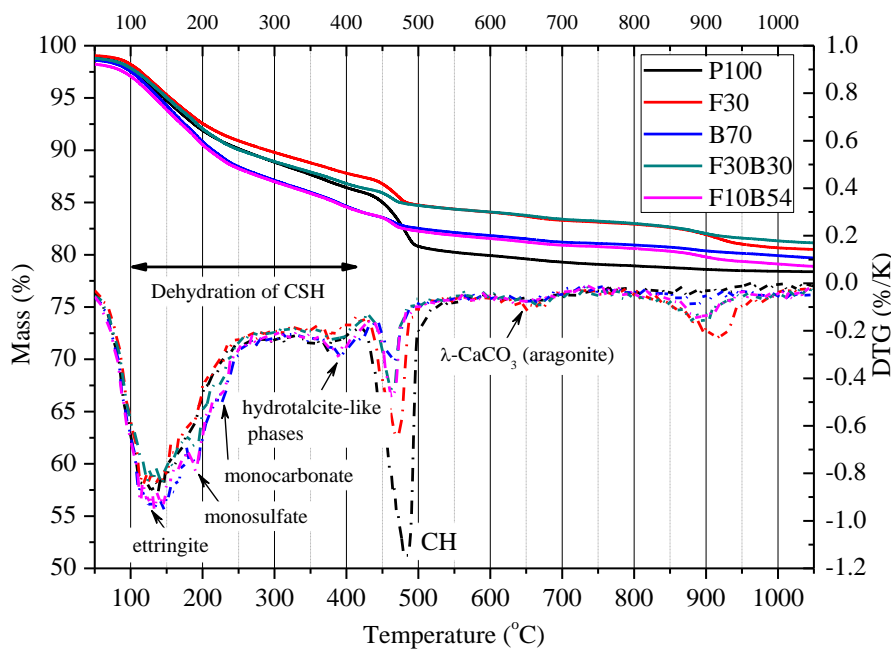


Figure 3-5 Typical TG/DTG curve of freeze-dried cement paste with or without SCMs

temperature. TGA were carried out by the Netzsch STA 449 F3 Jupiter instrument coupled with a mass spectrometer (MS) Netzsch QMS 403 C Quadrupole (see Figure 3-4) under a dry argon atmosphere. With MS, the information of gases released at a certain temperature can be captured by measuring the ion current indicating the relevant gas (e.g. H<sub>2</sub>O or CO<sub>2</sub>), in order to identify the more accurate temperature range related to the emissions of H<sub>2</sub>O or CO<sub>2</sub>. The freeze-dried samples were ground into powder with an average particle size <75 μm. The mass of powder samples used for the measurements was 30-50 mg. The samples were heated at the rate of 10°C/min from 40-1100°C.

Typical TGA-MS results for cement paste hydrated in sealed condition are shown in Figure 3-5. In the DTG curve, the weight loss in the range of 40-400°C is normally related to the dehydration of C-S-H [8, 9], part of the carboaluminate hydrates [10], AFm [11] and AFt [12, 13] phases, monocarbonate [14], hydrotalcite [15, 16], as well as to the emission of physically-bound water [9]. The mass loss related to CH dehydration usually occurs in the range of 450-550°C [9, 17]. The weight loss around 600-650°C is due to the presence of λ-CaCO<sub>3</sub> (aragonite), a metastable calcium carbonate, which indicates the carbonation of cement paste during hydration. The weight loss in the range of 820-900°C is related to the thermal decomposition of anhydrite [18, 19]. It can only be found in the cement paste blended with SCMs.

As discussed above, the dramatic weight loss in the TG curves between 450-550°C is related to the dehydration of CH in the cement paste. Based on the weight loss (amount of water in CH) in this temperature range, the amount of CH can be calculated accordingly. However, from the DTG curves in Figure 3-5 the decomposition temperature of CH varies in different blended mixtures. It is affected by other phases inside the same mixture. In this research, weight loss due to the dehydration of CH is determined by the tangential method [20]. This method makes a correction for the concurrent dehydration of other compounds.

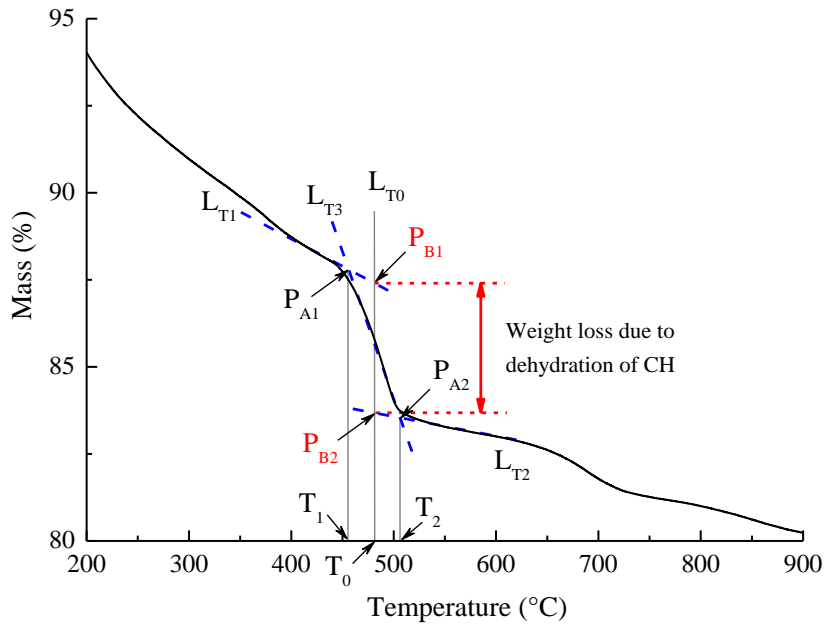


Figure 3-6 Determination of weight loss due to the dehydration of CH - tangential method

The tangential method is illustrated in *Figure 3-6* and the procedure is described as follows:

Step 1: Draw tangent lines  $L_{T_1}$ ,  $L_{T_2}$  and  $L_{T_3}$  to get the two intersection points  $P_{A_1}$  and  $P_{A_2}$

Step 2: From the coordinates of points  $P_{A_1}$  and  $P_{A_2}$ , to find their related temperature values  $T_1$  and  $T_2$ , and calculate the midpoint  $T_0$  of  $T_1$  and  $T_2$  on the  $x$ -axis

Step 3: Draw vertical line  $L_{T_0}$  from  $T_0$ , which will be intersected with the tangent lines  $L_{T_1}$  and  $L_{T_2}$  at point  $P_{B_1}$  and  $P_{B_2}$ , respectively.

The weight loss between  $P_{B_1}$  and  $P_{B_2}$  is indicating the amount of water released due to the dehydration of CH. According to the dehydration reaction formula of CH,



The CH amount described as the weight percentage per 1 g original binder can be calculated with Eq. 3-3.

$$w_{CH}^{binder} = w_h^{CH} \times \frac{M_{CH}}{M_H} \times \frac{1 - w_{L.O.H}^{total}}{w_{1050}} \quad \text{Eq. 3-3}$$

where  $w_h^{CH}$  is the relative mass percentage of water due to the dehydration of CH, calculated by the above-mentioned tangential method (see *Figure 3-6*);  $w_{1050}$  is the relative weight



percentage of the paste at 1050°C in the TG curve.  $M_H$  (g/mol) and  $M_{CH}$  (g/mol) are the molar weights of H<sub>2</sub>O and portlandite, the values of which are 18 and 74 respectively.

$w_{L.O.H}^{total}$  is the total weight loss due to the decomposition of phases in the raw materials under the TG test conditions (heated under the protection of N<sub>2</sub>). The total weight loss of heating (L.O.H) of binders is calculated as follows:

$$w_{L.O.H}^{total} = w_{L.O.H}^{cem} \times f_{cem} + w_{L.O.H}^{SCMs} \times f_{SCMs} \quad \text{Eq. 3-4}$$

where  $f_{cem}$  and  $f_{SCMs}$  are the fractions of OPC and SCMs in the original binder mix, as listed in Table 3-8.  $w_{L.O.H}^{cem}$  and  $w_{L.O.H}^{SCMs}$  are the total weight loss in the temperature range of 40 to 1050°C in TG curve of OPC and SCMs, respectively. The value of  $w_{L.O.H}^{cem}$  is 1.282%, see Figure 3-7. The value of  $w_{L.O.H}^{SCMs}$  for FA and BFS are 2.206% and 0.0%, respectively.

The CH amount described as the volume percentage (ml of CH per ml of cement paste) is determined by Eq. 3-5:

$$[CH](ml/ml) = \frac{w_{CH}^h}{100} \times \frac{M_{CH}}{M_H} \times \frac{\rho_{bulk}}{\rho_{CH}} \quad \text{Eq. 3-5}$$

where  $\rho_{bulk}$  (g/L) is the bulk density of cement paste, calculated from the MIP test result.

$\rho_{CH}$  (g/L) = 2230 is the bulk density of CH.

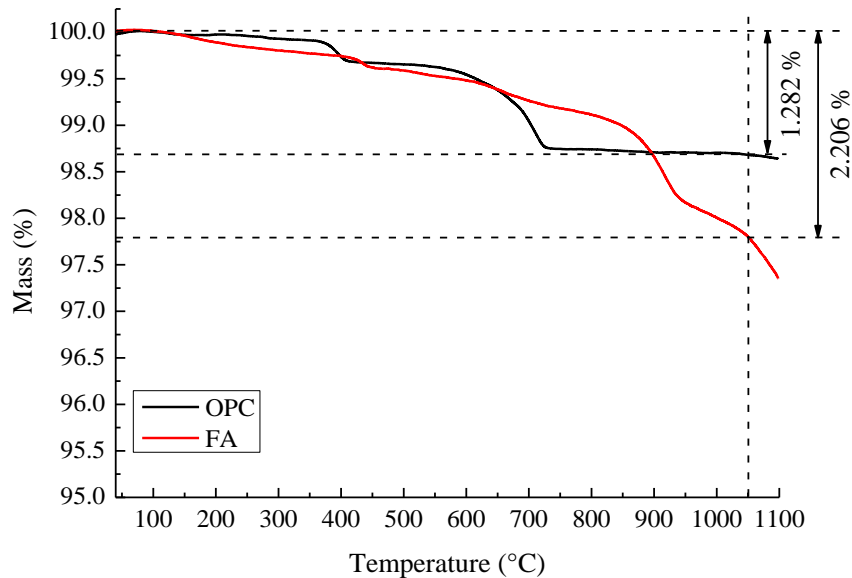


Figure 3-7 TG curves of OPC and FA (raw materials)



Figure 3-8 Polished sample for BSE-EDAX analysis (image from Yu[21])

**BSE-EDAX** -- Elemental mapping is performed by EDAX at the BSE mode with the environmental scanning electron microscope (ESEM). Freeze-dried paste samples are collected in a plastic bottle. Then the bottle with samples is moved into a vacuum chamber and evacuated at 30 mbar for 1 hour. With the running of vacuum pump, the samples are impregnated with epoxy. After impregnation, the paste samples with epoxy are moved to the oven and dried at 40°C for 24 hours. Then the samples were further processed with cutting, grinding, and polishing. After polishing, the sample is ready for the BSE-EDAX test, an example of which is shown in *Figure 3-8*. More details regarding the sample preparation for the BSE test are described in elsewhere [5].

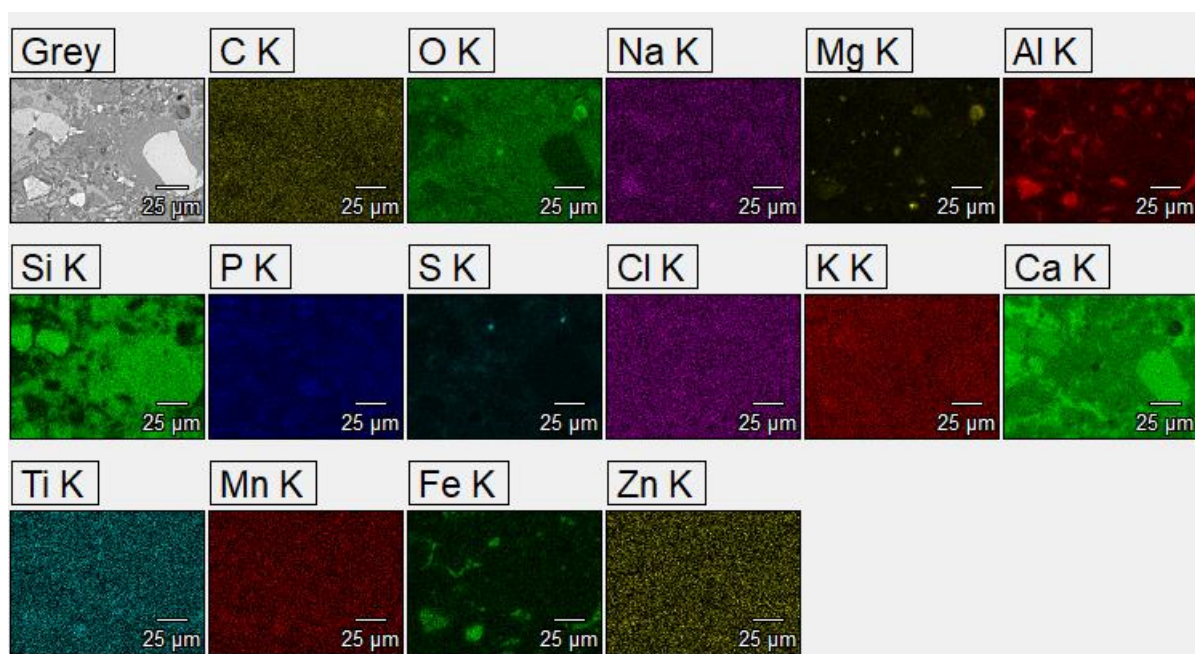


Figure 3-9 Elemental mapping of OPC paste hydrated for 1 year

The BSE images together with EDAX data are collected by a Philips-XL30-ESEM in a gaseous (water vapour, low vacuum) environment. Acceleration voltage of the electron beam is 20 KV. The size of the reference region for the BSE image and related mapping area is 512  $\mu\text{m}$  in length and 384  $\mu\text{m}$  in width. Magnification of the BSE image is  $800 \times$  and the resolution of each image is 0.308  $\mu\text{m}$  / pixel. Typical BSE-EDAX test results are shown in *Figure 3-9*.

**MIP** -- MIP is a widely used method to measure the porosity, pore size and pore size distribution, the density and other porosity-related characteristics of cement paste. Since mercury is non-wetting liquid for cement paste, it can't penetrate the pores spontaneously by capillary force. By the application of external pressure, mercury is pushed into the pores. The equilibrant pressure is inversely proportional to the size of the pores. The pore size in the range of 0.001  $\mu\text{m}$  to 1000  $\mu\text{m}$  can be measured by MIP, depending on the applied pressure.

Micrometrics PoreSizer 9320 was used for the MIP measurement (see *Figure 3-10a*). The maximum pressure that can be achieved is 207 MPa, which limits the effectively measurable pore size to the range of 0.007-500  $\mu\text{m}$ . Each measurement consists of three stages: intrusion at the low pressure running from 0 to 0.170 MPa; intrusion at the high pressure running from 0.170 to 205 MPa, followed by extrusion back to 0.170 MPa. In the test, the MIP instrument will record the cumulative intrusion volume of mercury at each applied pressure.

The appropriate weight of cement paste used for the measurement should be pre-calculated and estimated. To ensure accurate test results, the ratio of the volume of intrusion mercury / the volume of penetrometer stem (see *Figure 3-10b*) should be maintained around 60-90%, according to the regulation of the machine. The intrusion volume equals to the volume of mercury penetrating inside the pores of samples. Therefore, the appropriate sample weight can be estimated by Eq. 3-6:

$$W_{sample} (g) = \frac{\rho_{bulk} \cdot V_{stem}}{\phi} \times (60 \sim 90\%) \quad \text{Eq. 3-6}$$

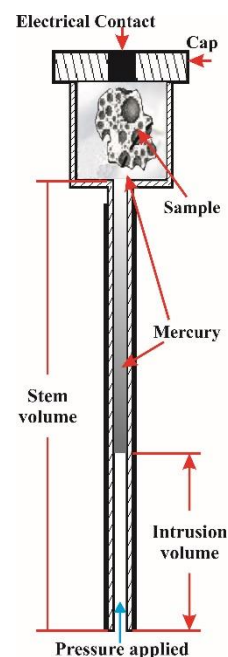
in which  $V_{stem}$  is the stem volume of penetrometer (ml),  $\phi$  is total porosity of the sample. The  $\rho_{bulk}$  varies from 1.4 to 1.6  $\text{g} / \text{cm}^3$ , depending on whether the cement paste is blended with or without SCMs. The paste blended with SCMs has a lower  $\rho_{bulk}$ . It should also be noticed that the carbonation will increase the specific masse of the bulk  $\rho_{bulk}$ .

The pore diameter  $d$  ( $\mu\text{m}$ ) is related to applied pressure  $p$  (MPa), specified by Washburn equation[22] based on a model of cylindrical pores, described as follows in Eq. 3-7.

$$p = - \frac{4\gamma \times \cos \theta}{d} \quad \text{Eq. 3-7}$$



(a) Micrometrics PoreSizer 9320



(b) Penetrometer

Figure 3-10 Micrometrics PoreSizer 9320 and penetrometer used for the measurement of porosimetry

where  $\gamma$  is the surface tension of mercury (mN/m) and  $\theta$  (-) is the contact angle between mercury and the pore surface of the cement paste. The values suggested by Cook were 480 (mN/m) and  $139^\circ$  [23] for the intrusion. The contact angle for extrusion process was  $106^\circ$ , suggested by León [24]. These values were used in this study for the calculation of the pore size. By applying the Washburn equation, MIP test data can be converted into a pore size distribution curve. From the curve, the following parameters can be deduced: porosity (total, inkbottle and capillary); pore size distribution; density ( $\rho_{bulk}$ ,  $\rho_{skeleton}$ ) and “critical” pore diameters [25] etc.. The details of the calculation methods for the above-mentioned parameters were specified elsewhere [5].

### 3.3 Experimental results and discussions

#### 3.3.1 Development of amount of portlandite in blended cement paste

The amounts of portlandite in OPC paste and blended cement paste were calculated following the method mentioned in section 3.2.3. Then the amounts of portlandite in different pastes were compared to study the effects of SCMs on the development of portlandite in blended cement paste.

Firstly, the amount of water released due to the dehydration of portlandite was determined by the tangential method (section 3.2.3), based on the TG curve of the paste. The results are

presented in *Table 3-9*. Then the total weight loss of heating (L.O.H),  $w_{L.O.H}^{total}$ , of binders of different mixtures were calculated with Eq. 3-4. The fractions of different binders, i.e. OPC ( $f_{cem}$ ) and SCMs ( $f_{SCMs}$ ), are taken from *Table 3-8*. The  $w_{L.O.H}^{total}$  of binders of different mixtures are listed in *Table 3-10*.

*Table 3-9 Amount of water released  $w_h^{CH}$  due to the dehydration of portlandite in different pastes, hydrated for different days (wt %)*

Hydration time (days)	$w_h^{CH}$ of different mixtures						
	P100	F10	F30	B30	B70	F30B30	F10B54
28	3.36	3.24	2.36	2.11	0.53	0.92	0.61
105	3.55	3.17	2.11	1.85	0.63	0.91	0.61
365	4.19	3.05	1.8	1.54	0.42	0.79	0.76

*Table 3-10 Total weight loss of heating (L.O.H) ( $w_{L.O.H}^{total}$ ) of binders for different mixtures before hydration (wt %)*

	$w_{L.O.H}^{total}$ of different mixtures						
	P100	F10	F30	B30	B70	F30B30	F10B54
$w_{L.O.H}^{total}$	1.2820	1.3744	1.5592	0.8974	0.3846	1.1746	0.6821

*Table 3-11 Amount of portlandite,  $w_{CH}^{binder}$ , in different pastes, hydrated for different days (wt %)*

Hydration time (days)	$w_{CH}^{binder}$ of different mixtures						
	P100	F10	F30	B30	B70	F30B30	F10B54
28	16.85	16.32	11.55	10.04	2.54	4.49	3.00
105	18.02	15.81	10.49	9.18	3.17	4.51	3.04
365	21.70	15.57	9.05	7.85	2.16	3.96	3.93

Finally, the amounts of portlandite (per 1 g of raw binders) in different pastes hydrated are calculated with Eq. 3-3 for different days. The results are shown in *Table 3-11*.

### 3.3.1.1 Effects of FA on the amount of portlandite in blended cement paste

The amounts of portlandite in the cement paste blended with FA are compared with that in OPC paste, shown in *Figure 3-11*. This figure clearly shows that the amount of portlandite in OPC paste increases with hydration time. However, the amount of portlandite in FA-blended cement pastes F10 and F30 are decreasing with hydration time. Moreover, the partial replacement of cement by FA causes a reduction of the amount of portlandite in F10 or F30 paste compared with the OPC paste at the same hydration age.

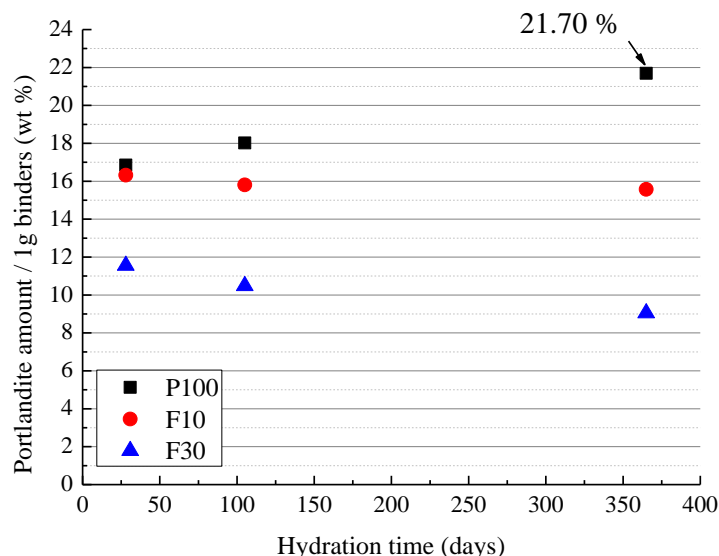


Figure 3-11 Development of the amount of portlandite in cement paste blended with different replacement levels of FA (10% or 30% by weight) determined experimentally

By normalizing the amount of portlandite in F10 and F30 paste to that in OPC paste at the same age, the reduction of the portlandite content in blended cement paste is obvious. The calculated normalized amounts of portlandite in FA-blended cement paste are listed in *Table 3-12*. For the FA replacement level of 10%, the amount of portlandite in F10 paste decreases by approximately 30% at the age of 1 year compared to OPC paste. When the FA replacement level is increased to 30%, the amount of portlandite in F30 is reduced by approximately 60% at the age of 1 year. It means that the use of FA as cement replacement causes a dramatic reduction of portlandite content. This reduction is due to, firstly, the dilution effects and, secondly, consumption of portlandite by pozzolanic reaction [26, 27].

Further study of the effects of FA on the amount of portlandite in the FA-blended cement paste will be performed by numerical simulation. The amounts of portlandite in FA-blended cement paste with different replacement levels are simulated with HYMOSTRUC3D- E [1]. Some input parameters of the simulation program concern the raw materials of the paste, such as the chemical compositions of the binders, and are listed *Table 3-1*.

Table 3-12 Normalized amounts of portlandite in FA blended cement paste (%)

Hydration time (days)	Different blended cement pastes		
	P100	F10	F30
28	100.00	96.84	68.56
105	100.00	87.73	58.18
365	100.00	71.76	41.70

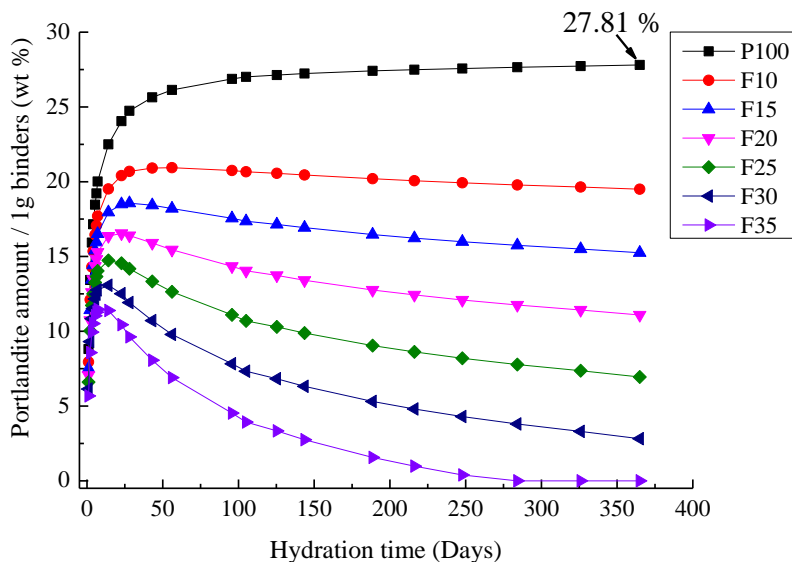


Figure 3-12 Development of amount of portlandite in cement paste blended with different replacement levels of FA (varying from 10% to 35% by weight) determined by numerical simulation with HYMOSTRUC3D-E

The amounts of major minerals in OPC and FA are shown in *Table 3-5* and *Table 3-6*, respectively. Parameters describing the particle size distribution of different binders are listed in *Table 3-7*.

The modelling results of FA blended cement paste are illustrated in *Figure 3-12*. The code 'F35' indicates that the replacement level of FA in this mix is 35% by weight. The other labels in this figure have a similar meaning.

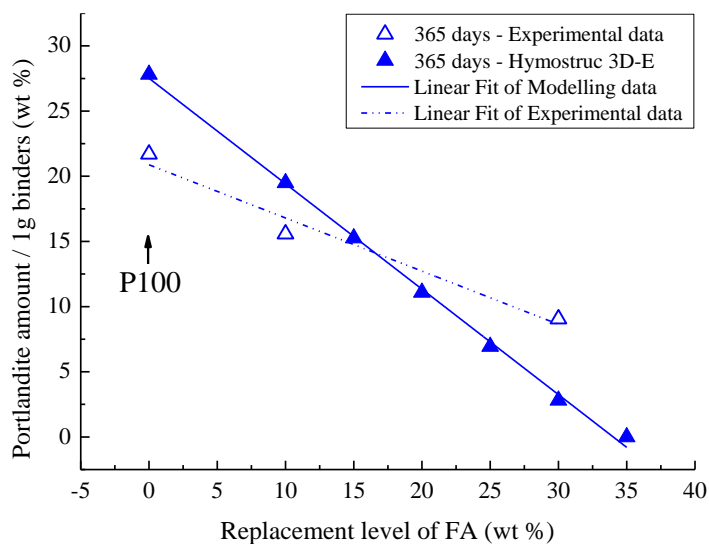


Figure 3-13 Effects of FA on the amount of portlandite in cement pastes hydrated for 1 year, determined experimentally and by numerical simulation with HYMOSTRUC3D-E.

As clearly shown in *Figure 3-12*, the amount of portlandite increases in OPC paste, whereas in the FA blended cement paste this amount decreases after having reached a peak value in the early stage. At the hydration age of 1 year, the amount of portlandite stabilizes. The numerically simulated amounts of portlandite in different pastes hydrated for 1 year are compared with experimental data presented in *Figure 3-11*. The comparative study of the amount of portlandite, affected by FA replacement level, are presented in *Figure 3-13*.

From both experimental data and modelling data, the amount of portlandite in FA blended cement paste has a good negative linear correlation with the replacement level of FA. By fitting the data, the parameters (slope and intercept) to describe this linear relation were determined and listed in *Table 3-13*. It is noticed that the intercept of this linear relation is indicating the amount of portlandite for OPC paste hydrated for 1 year, or which can be considered as the maximum amount of portlandite produced in OPC paste with the same W/C. With this relation, the amount of portlandite in cement paste blended with FA can be estimated based on the amount of portlandite in fully hydrated OPC under the same hydration conditions (W/C, curing temperature and moisture condition).

*Table 3-13 Parameters to describe the linear relation between the amount of portlandite in FA blended cement paste and the FA content.*

	Parameters in: $y = a + b \cdot x$		Amount of portlandite in OPC paste hydrated for 1 year (wt %)
	Slope ( $b$ )	Intercept ( $a$ ) (wt %)	
For experimental data	-0.41	20.88	21.70 (P100 in <i>Figure 3-11</i> )
For modelling data	-0.81	27.52	27.81 (P100 in <i>Figure 3-12</i> )

### 3.3.1.2 Effects of BFS on amount of portlandite in blended cement paste

Amounts of portlandite in the cement paste blended with BFS are compared with that in OPC paste, described in *Figure 3-14*. As illustrated in this figure, the amounts of portlandite in the BFS blended cement paste B30 and B70 are decreasing with the hydration time. Meanwhile, the partial replacement of cement by BFS will also cause a reduction of the amount of portlandite in B30 or B70 paste compared to the amount of portlandite in OPC paste at the same hydration age. Replacement of OPC by either FA or BFS will cause a reduction of the amount of portlandite in cement paste, but for the same replacement level BFS causes a higher reduction than FA, as shown in *Figure 3-14*.

The amounts of portlandite in B30 or B70 paste are normalized to that in OPC paste at the same hydration age. The calculated normalized amounts of portlandite in BFS blended cement paste are shown in *Table 3-14*. With the BFS replacement level of 30%, the amounts of portlandite in B30 paste decreases by approximately 63% at the age of 1 year compared to OPC paste.



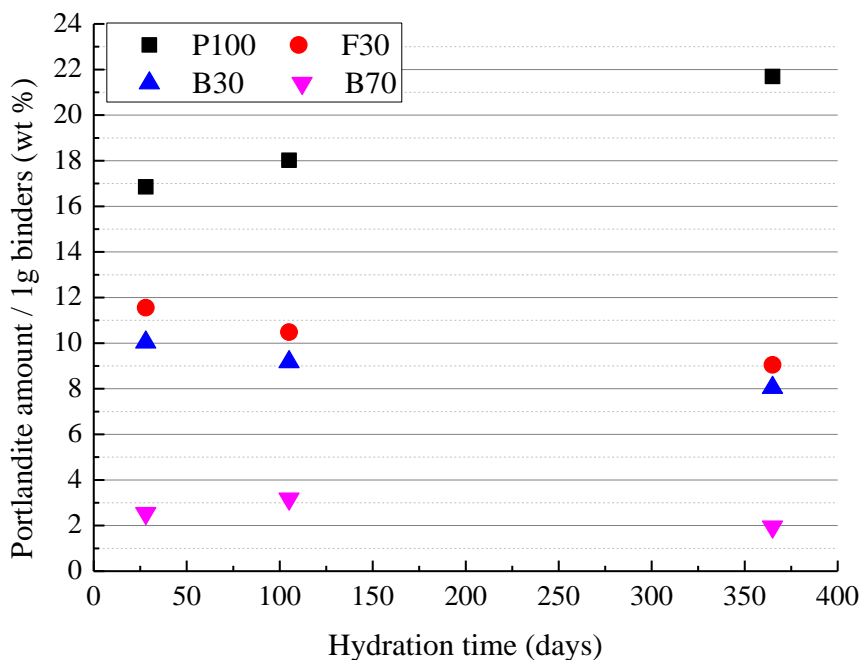


Figure 3-14 Development of amount of portlandite in cement paste blended with different replacement levels of BFS (30% or 70% by weight) determined experimentally

Table 3-14 Normalized amount of portlandite in BFS blended cement paste (%)

Hydration time (days)	BFS blended cement pastes		
	P100	B30	B70
28	100.00	59.57	15.07
105	100.00	50.92	17.60
365	100.00	37.12	9.01

When the BFS replacement level is increased to 70%, the amount of portlandite in B70 is reduced by nearly 90% at the age of 1 year. These values clearly show that the use BFS in concrete mixtures can cause a dramatic reduction of the portlandite content [26, 27].

Similarly, to further study the effects of BFS replacement level on the amount of portlandite in the BFS blended cement paste, more data of the portlandite content in cement paste blended with different replacement levels of BFS are simulated by HYMOSTRUC3D-E [1]. Same input parameters for the numerical simulations as discussed for the FA-blended cement paste are used in the modelling. The modelling results of BFS blended cement paste are illustrated in Figure 3-15. The code 'B10' indicates a mixture with a replacement level of BFS of 10% by weight. The other labels in this figure have a similar meaning.

As clearly shown in Figure 3-15, the amount of portlandite continuously increases in OPC paste, whereas in the BFS blended cement paste this amount decreases after having reached a peak value in the early stage of hardening. In all cases, the amount of portlandite stabilizes at

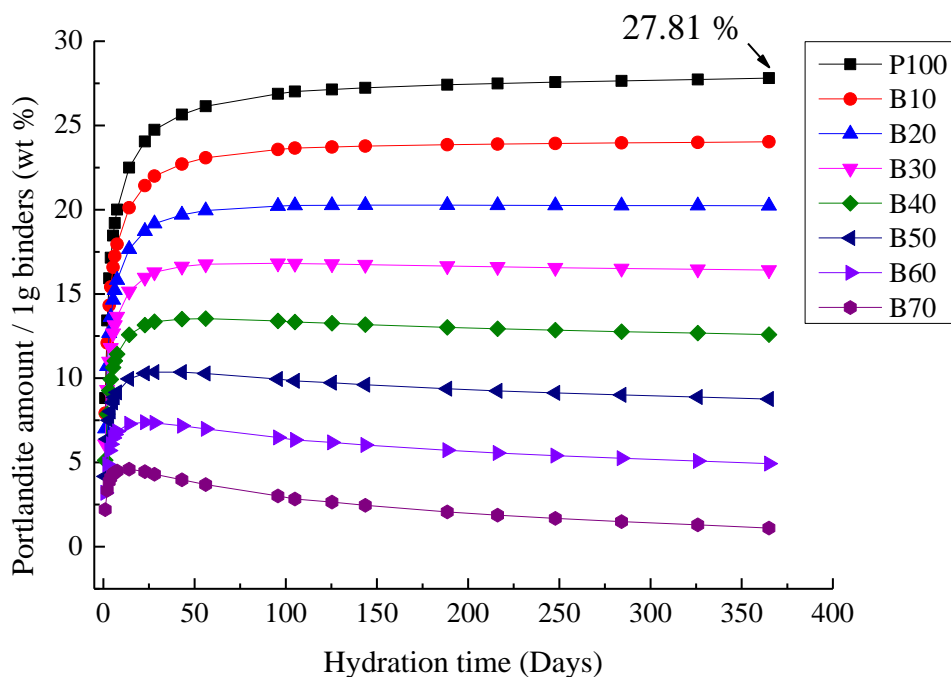


Figure 3-15 Development of the amount of portlandite in cement paste blended with different replacement levels of BFS (varying from 10% to 70% by weight) determined by numerical simulation with HYMOSTRUC3D-E

the hydration age of about 1 year. Therefore, these numerically simulated amounts of portlandite in BFS blended paste hydrated for 1 year are chosen to study the effects of replacement level of BFS on the amount of portlandite in the BFS blended cement paste, regardless of hydration time. The simulation data is compared with the experimental data taken from Figure 3-14, illustrated in Figure 3-16.

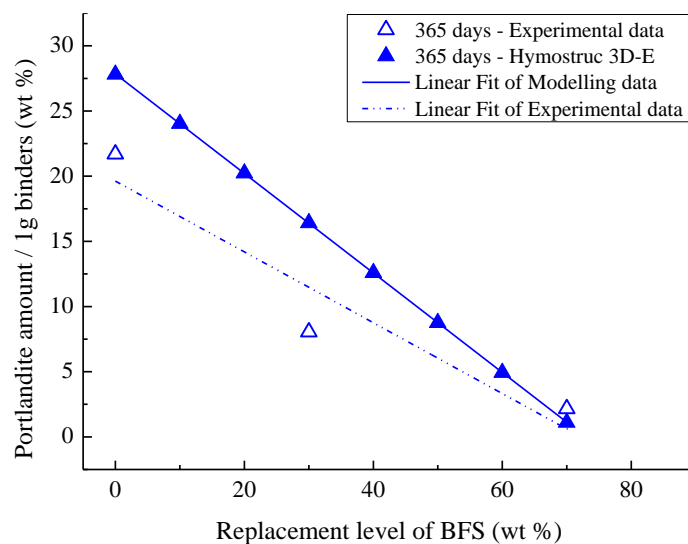


Figure 3-16 Effects of BFS on the amount of portlandite in cement pastes hydrated for 1 year, determined experimentally and by numerical simulation with HYMOSTRUC3D-E.

*Table 3-15 Parameters to describe the linear relation between the amount of portlandite in BFS blended cement paste and the replacement level of BFS*

	Parameters in: $y = a + b \cdot x$		Amount of portlandite in OPC paste hydrated for 1 year (wt %)
	Slope ( $b$ )	Intercept ( $a$ ) (wt %)	
For experimental data	-0.27	19.74	21.70 (P100 in <i>Figure 3-11</i> )
For modelling data	-0.38	27.84	27.81 (P100 in <i>Figure 3-15</i> )

From the modelling data, the amount of portlandite in BFS blended cement paste has a good negative linear correlation with the amount of BFS in the mixture. In the experimental data, the amount of portlandite has not such perfect negative linear correlation with the amount of BFS. But this linear relation can still be used for the prediction of the amount of portlandite in cement paste blended with BFS. By fitting the data, the parameters (slope and intercept) to describe this linear relation were determined and listed in *Table 3-15*.

Similar to what was found for FA blended cement paste, the intercept of this linear relation is close to the amount of portlandite in OPC paste hydrated for 1 year, or which can be considered as the maximum amount of portlandite produced in the OPC paste with the same W/C. With this relation, the amount of portlandite in cement paste blended with BFS can be estimated as well based on the amount of portlandite in fully hydrated OPC under the same hydration conditions (W/C, curing temperature and moisture condition).

### **3.3.1.3 Effects of a combination of FA and BFS on the amount of portlandite in ternary blended cement paste**

Amounts of portlandite in the cement paste blended with FA and BFS are compared with that in OPC paste, described in *Figure 3-17*. As illustrated in this figure, the amounts of portlandite in the ternary blended cement pastes F30B30 and F10B54, and also in B70, are dramatically lower than in OPC paste at the same hydration age. Moreover, the amount of portlandite in ternary blended cement paste mainly depends on the total replacement level of SCMs. It is shown in *Figure 3-17*, that the higher the total replacement level of SCMs, the lower the amount of portlandite compared to the amounts in F30B30 and F10B54 at the same hydration age.

The normalized amounts of portlandite in ternary blended cement paste are calculated and shown in *Table 3-16*. With the total replacement level of SCMs of 60%, the amount of portlandite in F30B30 paste decreases by approximately 75% at the age of 28 days or 105 days compared to OPC paste. When the total replacement level is increased to 65%, the amount of portlandite in F10B54 is reduced nearly 84% at the same age, which is higher than the reduction for F30B30.

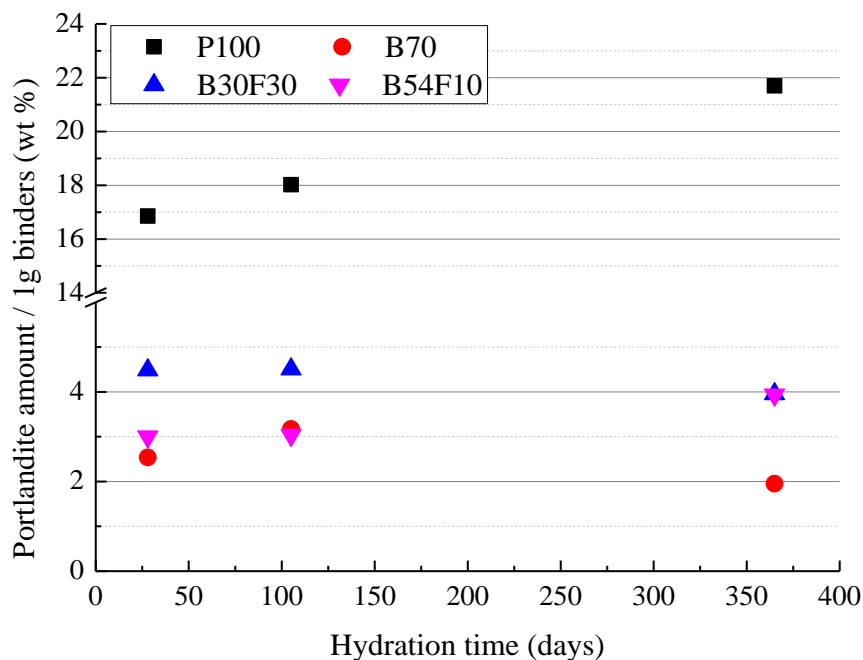


Figure 3-17 Development of amount of portlandite in cement paste blended with both FA and BFS determined experimentally

Table 3-16 Normalized amount of portlandite in ternary blended cement paste (%)

Hydration time (days)	Normalized amounts of portlandite for different mixtures			
	P100	B70	F30B30	F10B54
28	100.00	15.07	26.62	17.81
105	100.00	17.60	25.01	16.84
365	100.00	9.95	18.23	18.13

### 3.3.2 Development of C-S-H phases in blended cement paste

It is widely known that the reactions between portlandite produced by cement hydration and SCMs will cause the reduction of the portlandite content and the formation of C-S-H with a lower C/S ratio or less C(-A)-S-H in the blended cement paste. In section 3.3.1, the effects of SCMs on the amount of portlandite in the blended cement paste has already been discussed based on both experimental data and numerical simulations.

In this section, different types of C-S-H phases (classified by the C/S ratio in this research) are studied and distinguished by further processing the elements data tested by EDAX mapping. Unlike the determination of amount of portlandite, it's hard to calculate the quantities of different types of C-S-H phases in the cement paste based on TG test results, especially in blended cement paste. Therefore, the effects of SCMs on the amounts of different C-S-H phases formed in the blended cement paste will be studied mainly based on the modelling results from HYMOSTRUC3D-E [1]. Before the discussion of the modelling

results, the major chemical reactions involved in the hydration of blended cement, and considered in the simulation model HYMOSTRUC3D-E, will be briefly summarized.

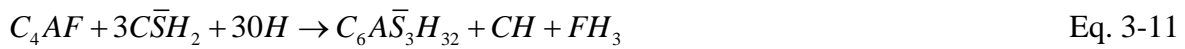
### 3.3.2.1 Stoichiometry of the hydration of OPC

In HYMOSTRUC3D-E [1], the chemical composition of C-S-H is assumed to be  $C_{1.7}SH_4$ , which is produced by the hydration of  $C_3S$  and  $C_2S$  [28-30] shown in Eq. 3-8 and Eq. 3-9.

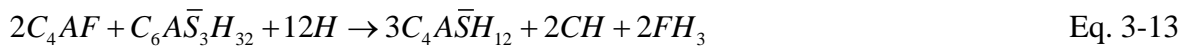


The hydration reactions of other two major minerals  $C_3A$  and  $C_4AF$  in cement clinker, are determined by the actual amounts of gypsum ( $C\bar{S}H_2$ ) and ettringite ( $C_6A\bar{S}_3H_{32}$ ) in the system [29, 30], described as follows:

1. *If gypsum is present in the system:*



2. *If gypsum is totally consumed and ettringite is present in the system:*

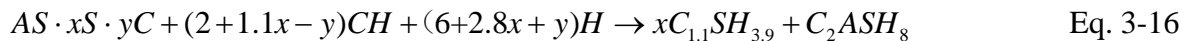


3. *If both gypsum and ettringite are used up in the system:*



### 3.3.2.2 Stoichiometry of the pozzolanic reactions of FA and BFS

The stoichiometry of pozzolanic reaction of FA is described in Eq. 3-16, mentioned by Bentz [31].

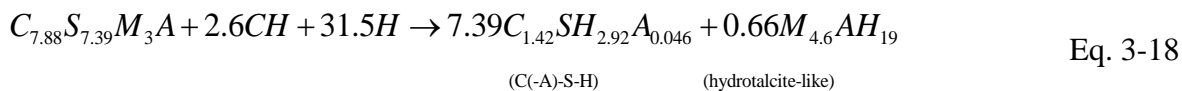


in which  $AS \cdot xS \cdot yC$  is the chemical formula of FA.  $x$  and  $y$  are stoichiometry coefficients, which can be calculated from the chemical composition of FA. For the chemical compositions of FA listed in *Table 3-1*, the values of  $x$  and  $y$  are 1.80 and 0.33, respectively. The pozzolanic reaction of FA is accordingly rewritten as follow:



where  $C_{1.1}SH_{3.9}$  and  $C_2ASH_8$  are the C-S-H gel and strätlingite produced from the pozzolanic reaction of FA.

The stoichiometry of the reaction between BFS and portlandite in the pore solution is from the research of Richardson [32], described in Eq. 3-18:



where  $C_{7.88}S_{7.39}M_3A$  is indicating the glass phase in BFS.  $C_{1.42}SH_{2.92}A_{0.046}$  and  $M_{4.6}AH_{19}$  are the C(-A)-S-H gel and hydrotalcite-like phase produced by the reaction of BFS with portlandite.

### 3.3.2.3 Effects of FA on the development of C-S-H phases in blended cement paste

#### 3.3.2.3.a C-S-H gels in cement paste blended with FA - Experimental

The elemental mapping and BSE image of F30, hydrated for 1 year, are compared in *Figure 3-18*. The BSE image shows unhydrated cement grains and unreacted FA particles in the blended cement paste even after 1 year hydration. The portlandite confirmed by TGA is found in the BSE image as well. C-S-H phases exist close to the side of unhydrated cement grains or in between FA particles and portlandite. Unfortunately, from only the BSE image analysis it is not possible to identify whether the C-S-H gel is produced from the cement hydration or from the pozzolanic reaction of FA.

The elemental mapping images show the distribution of different elements in the same scanning area as the one selected for the BSE image shown in *Figure 3-18*. The mapping data are processed further to calculate the mean C/S ratio of C-S-H gels. Based mainly on the C/S ratio, the C-S-H gels produced from different reactions are determined.

As illustrated in *Figure 3-19*, the rectangle area is selected firstly, which covers the FA particle, cement grain together with the hydration or pozzolanic reaction product in between. The size of the selected area is 20 pixels in height and 57 pixels in length, starting from FA particle and ended in the cement grain. In the elemental mapping data file, each pixel has coordinates in the mapping area. It contains the counts of the characteristic X-ray as well as those of different elements detected.

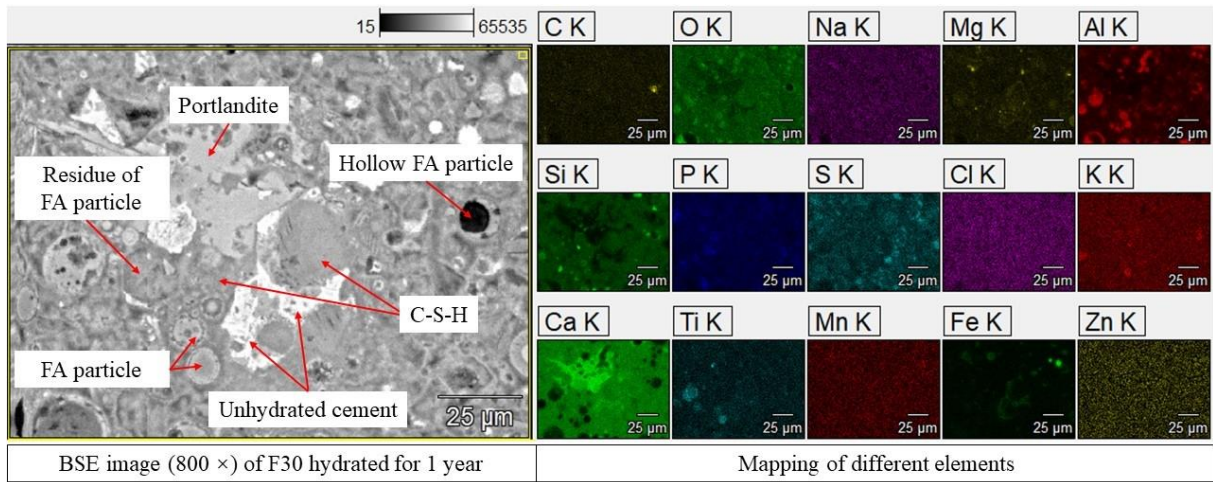


Figure 3-18 BSE image and related elemental mapping of F30 hydrated for 1 year

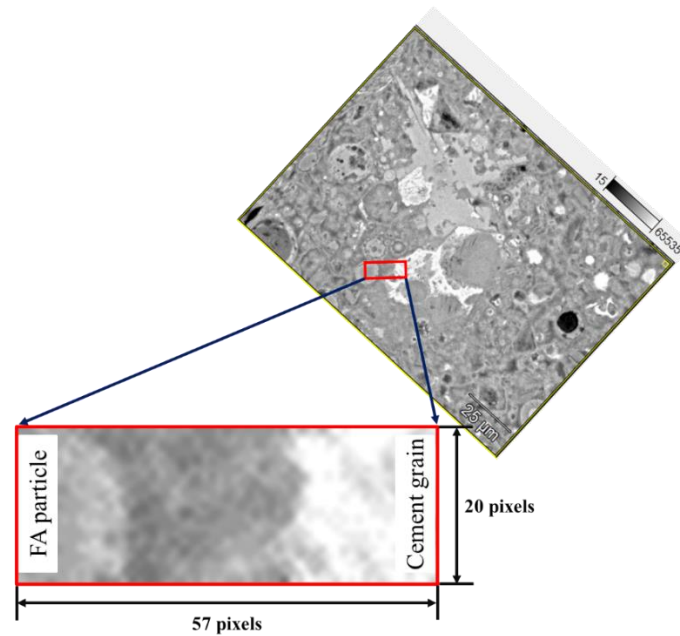


Figure 3-19 Selecting area for the calculation of mean C/S of phases between FA and cement particles

Based on the counts of element Ca and Si, the C/S ratio at each pixel is calculated by following the equation of Castaing [33], described in Eq. 3-19:

$$\frac{N_B}{N_A} = \frac{n_B}{n_A} \times \frac{w_K(A)}{w_K(B)} \times \frac{E_K(B)}{E_K(A)} \quad \text{Eq. 3-19}$$

where the subscripts  $A$  or  $B$  indicate the elements  $A$  or  $B$ .  $N_A$  is the number of atoms of element  $A$  at this pixel;  $n_A$  is the counts of the element  $A$  at this pixel, recorded in the

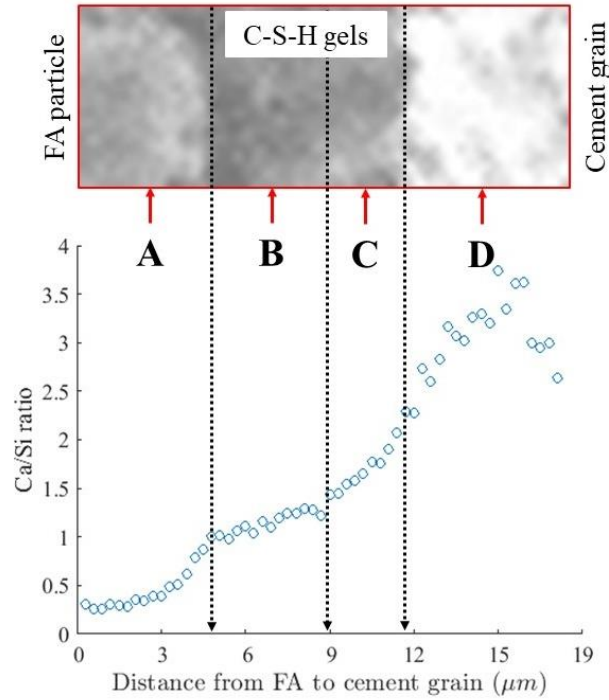


Figure 3-20 Mean C/S of phases located from FA to cement particles (A: FA particle; B: C-S-H gel produced from pozzolanic reaction of FA; C: C-S-H gel produced from cement hydration; D: cement grain)

elemental mapping data file;  $E_K(A)$  is K-shell ionization energy of element  $A$ ;  $w_K(A)$  is the K-shell fluorescence yield of element  $A$ . The value of  $w_K$  is calculated by the semi-empirical equation of Laberrigie-Frolov and Radvanyi [34] as follows.

$$w_K = \frac{1}{1 + (-0.0217 + 0.03318 \times Z - 0.00000114 \times Z^3)^{-4}} \quad \text{Eq. 3-20}$$

in which  $Z$  is the atomic number.

By substituting Eq. 3-20 in Eq. 3-19, the C/S at each pixel is calculated separately. As illustrate in *Figure 3-19*, there are 20 pixels (height of the selected area) in total with the same distance measuring from the start point in FA particle. The mean C/S ratio is calculated based on the values of these 20 pixels. Afterwards, the mean C/S ratio is plotted against the distance between the FA particle and the cement grain, which is measured from the FA particle. The changes of the mean C/S ratio of phases from FA to cement grain are illustrated in *Figure 3-20*.

As shown in *Figure 3-20*, the average C/S ratio of phases located in between the FA particle and the cement grain are increasing from approximate 0.25 inside the FA particle to 3.70 inside the cement grain. Considering rims of the FA and the cement particles in the BSE image, the selected analyzed area can be divided into four sub-areas as follows:



- A: FA particle
- B: C-S-H gel in the relicts of dissolved FA
- C: C-S-H gel near to the rim of cement grain
- D: Cement grain

Inside the FA particle (area A), the measured average C/S ratio is around 0.25. It should be noticed that the overall C/S ratio of the FA particle is approximate 0.12, calculated from the chemical composition of FA listed in *Table 3-1*.

At the other side, in area D, the measured mean C/S ratio is ranging from approximately 2.50 to 3.70, the maximum value of which is quite close to that overall value of 3.44 of the cement grain, calculated from the chemical composition of OPC as listed in *Table 3-1* as well.

In area B, the mean C/S ratio of C-S-H gel measured near the rim of the FA particle is around 1.0. Then the C/S ratio slightly increases up to 1.30, indicating that the C/S ratio of remains of dissolved FA. This part must be the C-S-H gel produced from the pozzolanic reaction of FA, with a C/S ratio ranging from 1.0 to 1.30. This value is in good agreement with the results published by other researchers. Uchikawa reported the formation of C-S-H with the C/S ratio of 1.01 in cement paste blended with 40% FA, hydrated for 4 years [35]. Sato and Furuhashi [36] found a C-S-H gel with a C/S ratio of 1.1-1.2 close to the FA particles in a 10-year-old mortar blended material. It should be noticed that the theoretical C/S ratio of C-S-H gel produced by the reaction of FA is normally 1.10 (see in Eq. 3-17).

In area C, the average C/S ratio of C-S-H gel increases from approximately 1.50 and ending at 2.30 near to the rim of the cement grain. In this area, the C-S-H gel is mainly produced from the hydration of the cement grain. Therefore, the C/S ratio of C-S-H gel produced by cement hydration is ranging from 1.50 to 2.30, which is in agreement with values found by other researchers. Harrisson reported a C/S ratio of 1.82 to 2.20 in the C-S-H gel found in OPC paste ( $W/C = 0.5$ ) hydrated for 14 months [37]. In a 25-year-old sealed paste ( $W/C = 0.45$ ) hydrated from  $C_3S$  phase, Taylor found C-S-H gel with a C/S ratio of 1.81 [38]. By using the TEM coupled with microanalysis, Groves found C-S-H gel in  $C_3S$  paste with a C/S ratio ranging from 1.66 to 1.93 [39]. Odler studied the early hydration kinetics and products of  $C_3S$  [40]. He observed C-S-H gel and measured the C/S ratio by two methods. The C/S ratio of C-S-H measured by TG was approximately 1.99, whereas the value measured by extraction method was around 1.60. Sueur also found a C/S ratio of 1.70 or 1.80 in the C-S-H gel of mature  $C_3S$  paste [41]. As for the C-S-H gel produced by the hydration  $C_2S$ , the C/S ratio was found of 1.80 or 2.0 [42-44].

There seems to be a dramatic gap between C/S ratios measured for C-S-H gels in area B and C. As shown in *Figure 3-20*, the mean C/S ratio of C-S-H gel is jumping from 1.30 in the relicts of dissolved FA to 1.50 measured for the C-S-H gel produced from cement hydration. Clearly, there is a boundary between C-S-H gel produced by the pozzolanic reaction of FA and that formed from the hydration of cement grains. This difference can be considered as an appropriate tool to distinguish C-S-H gels produced from different sources in the cement paste blended with FA.

### 3.3.2.3.b Amounts of C-S-H gels in the cement paste blended with FA - Simulation

As discussed in section 3.3.2.3.a, the C-S-H gel produced by the pozzolanic reaction of FA can be distinguished from that produced by the hydration of cement. However, it is still not easy to measure the amounts of these two types of C-S-H gel, tagged by their C/S ratio, experimentally. Therefore, the effects of FA on the amounts of different types of C-S-H gels formed in FA blended cement paste will be discussed based on the modelling results with HYMOSTRUC3D-E [1].

In HYMOSTRUC3D-E, the amounts of different phases are calculated based on the stoichiometry of different reactions involved, as discussed in section 3.3.2.1 and 3.3.2.2. The input data include the related chemical properties listed in *Table 3-1*, together with the amounts of different binders. Modelling results represent the final products of the hydration of cement and pozzolanic reactions of FA, as illustrated in *Figure 3-21*. The figure shows the paste composition as function of the FA percentage, by weight, in the paste.

Firstly, the amount of portlandite is decreasing with increasing of replacement level of cement by FA, which is in line with the experimental results in section 3.3.1.1. Meanwhile, the amount of C-S-H gel ( $C_{1.7}SH_4$ ) produced from the hydration of cement decreases as well when the amount of FA increases from 0 to 50%. On the contrary, the amount of C-S-H gel ( $C_{1.1}SH_{3.9}$ ) produced by the pozzolanic reaction of FA increases a lot. Volume percentages of different types of C-S-H gels to the total amount of C-S-H are calculated based on the above-mentioned data, together with the volume ratio of different types of C-S-H gels. These volume percentages and ratios are plotted against the replacement level of FA, illustrated in *Figure 3-22*.

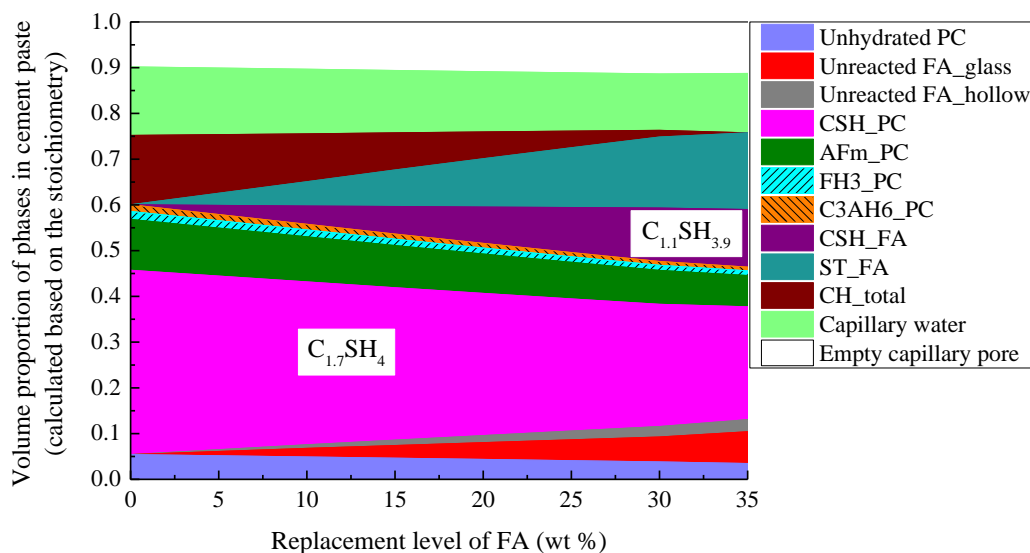


*Figure 3-21 Effects of FA on the amounts of different phases in the cement paste blended with FA simulated with HYMOSTRUC3D-E (w/b = 0.5; Note: AFm\_PC, CSH\_PC, FH3\_PC, C3AH6 are the AFm, CSH, FH<sub>3</sub>, C<sub>3</sub>AH<sub>6</sub> produced by the hydration of PC, respectively. CSH\_FA, ST\_FA are the CSH, C<sub>2</sub>ASH<sub>8</sub> produced by the pozzolanic reaction of FA, respectively.)*

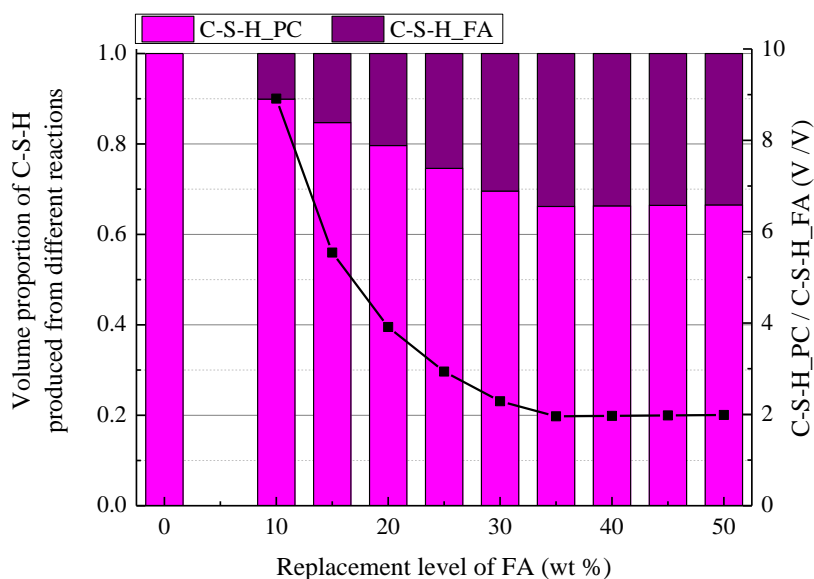


Figure 3-22 Effects of FA on the amounts of different C-S-H gels in the cement paste blended with FA

The volume ratio of C-S-H gel (with higher C/S) produced by the cement hydration to the C-S-H gel (with lower C/S) decreases dramatically from approximate 9.0 to 2.0, when the FA content is increased from 5 to 35%. This drastic change shall be taken into account when studying the carbonation of concrete blended with a high amount of FA. As indicated in the modelling results shown in *Figure 3-21*, there is also a dramatic reduction of portlandite (one of the calcium-bearing phase) in the blended cement paste. The C-S-H gels produced from different sources are the major calcium-bearing phases to resist carbonation of the concrete. It must be emphasized that different types of C-S-H gels, with different C/S ratio, may exhibit different resistance against carbonation attack.

### 3.3.2.4 Effects of BFS on the development of C-S-H phases in blended cement paste

#### 3.3.2.4.a C-S-H gels in the cement paste blended with BFS – Experiments

The elemental mapping and BSE image of B70 hydrated for 1 year are shown in *Figure 3-23*. After 1-year hydration, both the unhydrated cement and BFS particle can be identified in the BSE image. However, portlandite is rarely shown in the BSE image. C-S-H phases exist at the rim of unhydrated cement grains or BFS particles. Unfortunately, from only the BSE image analysis it is not possible to determine whether the C-S-H gel is produced from cement hydration or from the pozzolanic reaction of BFS.

For the selected area of the BSE image shown in *Figure 3-23*, the elemental mapping is performed to show the distribution of different detected elements. The mapping data are processed further in the same way as outlined in section 3.3.2.3.a for determining the mean C/S ratio of C-S-H gels in FA blended cement paste.

A rectangular area is selected as shown in *Figure 3-24*, which covers the BFS particle, a cement grain and hydration or pozzolanic reaction product in between. The size of selected

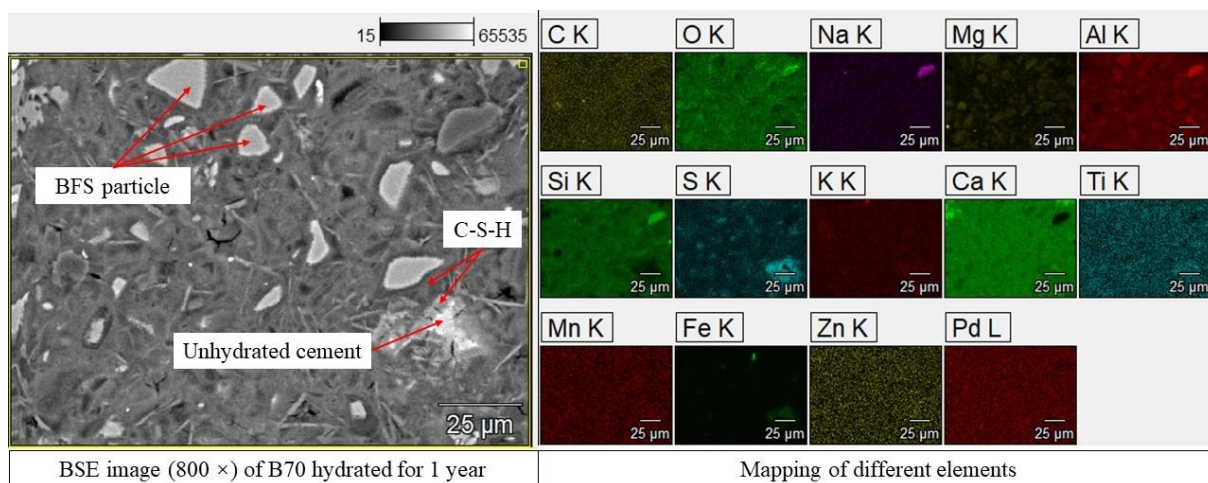


Figure 3-23 BSE image and related elemental mapping of B70 hydrated for 1 year

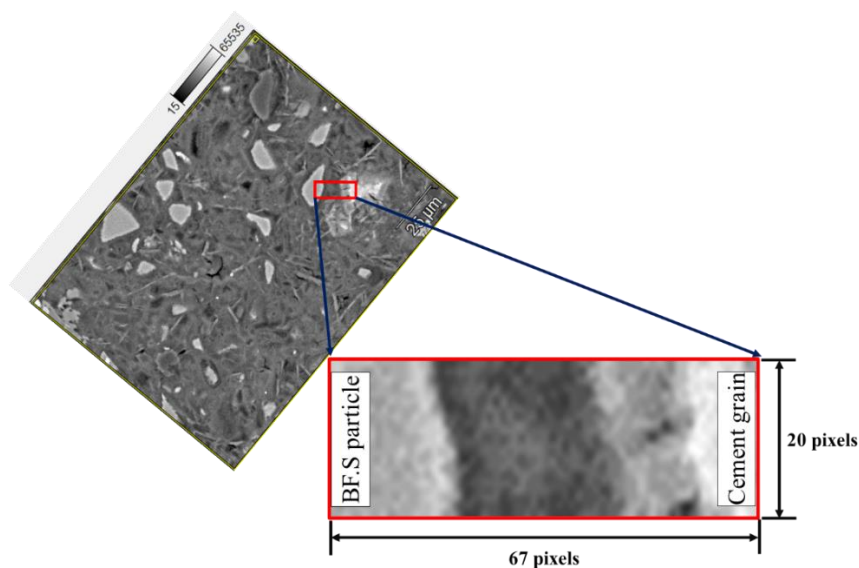


Figure 3-24 Selecting area for the calculation of mean C/S of phases between BFS and cement particles

area is 20 pixels in height and 67 pixels in length, starting from BFS particle and ending in the cement grain.

According to Eq. 3-19 and Eq. 3-20 the C/S ratio at each pixel can be calculated based on the counts indicating element Ca and Si recorded in the elemental mapping data file. Then the mean C/S ratio will be calculated based on the values of 20 pixels in the vertical direction shown in Figure 3-24. Afterward, the mean C/S ratio is plotted against the distance between BFS particle and cement grain, which is measured from the selected start point in BFS particle. The changes of the mean C/S ratio of phases from the BFS particle to the cement grain are shown in Figure 3-25.

As shown in *Figure 3-25*, the average C/S ratio of phases located in between the BFS particle, and the cement grain increases from approximately 0.80 inside the BFS particle to 3.50 inside the cement grain. Considering the rims of BFS and cement particles observed in the BSE image, the selected analyzed area can be divided into four sub-areas as follows:

- A: BFS particle
- B: C-S-H gel near to the rim of BFS particle
- C: C-S-H gel near to the rim of cement grain
- D: Cement grain

Inside the BFS particle (area A), an average C/S ratio is measured between 0.70 to 1.0, which is in good agreement with values found by other researchers [32]. In area D, in contrast, the measured mean C/S ratio is ranging from approximately 2.30 to 3.50, the maximum value of which is quite close to the overall C/S ratio of 3.44 of cement grains calculated based on the chemical composition of OPC as listed in *Table 3-1*. Unlike what is observed in *Figure 3-20*, the C/S ratio of C-S-H gel increases continuously in C-S-H gel produced by the pozzolanic reaction of BFS to the C-S-H gel produced by the hydration of cement grains. There is no clear boundary between these two types of C-S-H gels.

In area B, the mean C/S ratio of C-S-H gel is approximately 1.10, measured near to the rim of the BFS particle. Then the C/S ratio increases slightly up to 1.30. This part must be the

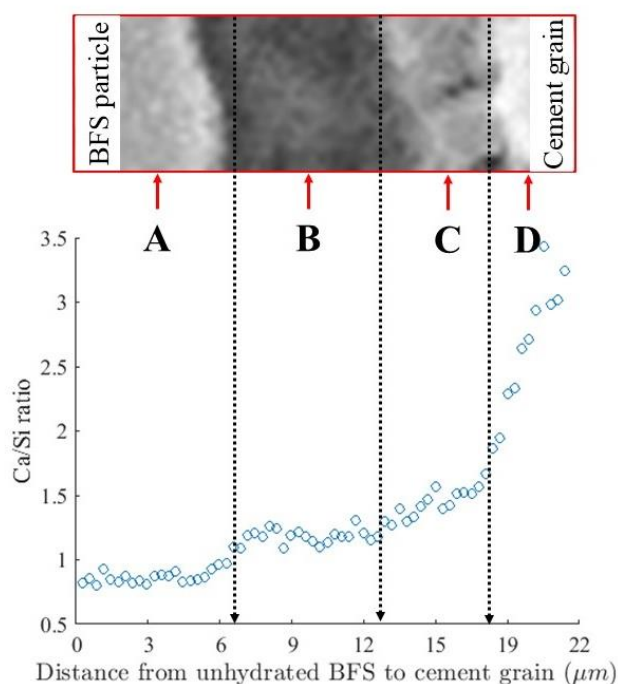


*Figure 3-25 Mean C/S of phases located from BFS to cement particles (A: BFS particle; B: C-S-H gel produced from pozzolanic reaction of BFS; C: C-S-H gel produced from cement hydration; D: cement grain)*

C-S-H gel produced from the pozzolanic reaction of BFS, with a C/S ratio varying from 1.10 to 1.30. Harrison reported that a C/S ratio of C-S-H gel at the rim of slag and relicts of fully reacted slag.

In the same paste, the C/S ratio of C-S-H gel far from the BFS particle is around 1.79. Moreover, the author also found that the hydration time had no effect on the composition of the particles of proximately 1.62 [45]. The measurements were performed on cement paste blended with 40% (wt) BFS. The w/b ratio is 0.5. The hydration time varied from 28 days to 14 months. individual phases in the slag cement pastes studied. Ruben [46] measured the C/S ratio of C-S-H gel formed in cement pasted blended with 30% BFS (w/b = 0.4), but hydrated for only 28 days. The C/S ratio of the inner and outer product around the slag particle were approximately 1.64 and 1.56, respectively. In the reference OPC paste, the measured C/S ratio of C-S-H gel was around 1.72 [46]. As reported by Richardson [32], the C/S ratio of C-S-H gel around slag grains in cement paste blended with 30% BFS is approximately 1.53, while that of C-S-H gel around cement grains is 1.67. The paste he tested had the w/b of 0.55 and hydrated for 32 days under 35°C.

As concluded by Harrison [39], none of the individual phases in the slag cement pastes showed significant compositional variation with time from 28 day to 14-month. Therefore, the hydration time of the paste will not be considered as a relevant parameter when comparing the C/S ratio of C-S-H gel formed by the reaction of BFS and measured in this research, with C/S ratios found by other researchers.

Obviously, the C/S ratio of C-S-H gel produced from the reaction of BFS is much lower than those reported in the above-mentioned literatures. Since the hydration time has no effect on the C/S ratio, another possible reason for different C/S ratios is the *replacement level* of BFS. Richardson [47] measured C/S ratios of C-S-H gel in cement pastes blended with different amounts of BFS. These pastes had the same w/b of 0.40 and were hydrated for 14 months at 20°C. The replacement level of BFS varied from 0 to 100%. He found that the C/S ratio of C-S-H gel around the BFS grain is reduced dramatically with increasing replacement level of BFS, as illustrated in *Figure 3-26*.

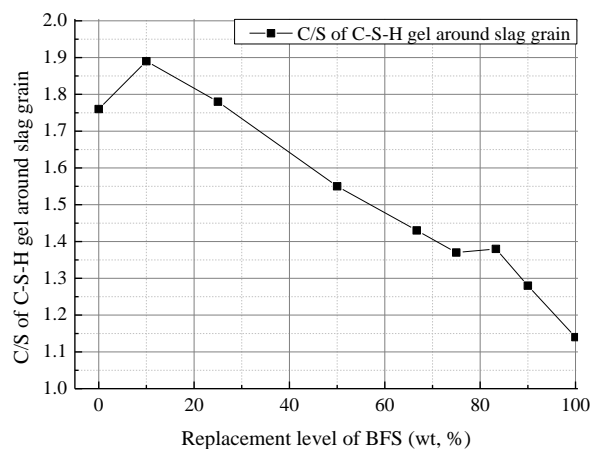


*Figure 3-26 Effects of BFS amount on the C/S value of C-S-H gel produced by the reaction of BFS (after Richardson [47])*

As shown in *Figure 3-26*, the C/S ratio of C-S-H gel produced by the reaction of BFS decreases from 1.78 to 1.55 when the replacement level of BFS is increased from 25% to 50%. This range is exactly covering the values reported in the above-mentioned literatures [32, 45, 46]. Meanwhile, the C/S ratio of C-S-H gel around slag grains are 1.43 and 1.37, respectively, when the amounts of BFS are 66.7% and 75%. The replacement level of BFS is 70% in this study, for which percentage the measured C/S ratio of C-S-H gel around the slag particle varies from 1.10 to 1.30. These values are close to the values measured by Richardson. Therefore, it makes sense to measure and calculate the C/S ratio of C-S-H gels in blended pastes by further processing of EDAX mapping data, proposed in this research.

In area C, the average C/S ratio of C-S-H gel is continuously increasing from approximately 1.30 to 2.00 near to the rim of cement grain. In this area, the C-S-H gel is mainly produced from the hydrating cement grain. Therefore, the C/S ratio of C-S-H gel produced by cement hydration is ranging from 1.50 to 2.00 in slag-blended paste, which is also found by other researchers [32] [38] [45] [46].

#### 3.3.2.4.b Amounts of C-S-H gels in the cement paste blended with BFS - Simulations

Like FA blended case, it is hard to measure the amounts of C-S-H gels produced from different reactions in slag-blended cement paste experimentally. Therefore, the effects of BFS on the amounts of different types of C-S-H gels formed in cement paste blended with BFS will be analyzed using simulation results obtained with HYMOSTRUC3D-E [1].

The input data for numerical simulations concern chemical properties of the binders, as listed in *Table 3-1*, together with the amounts of different binders. Simulation results are the final products of the hydration of cement and pozzolanic reactions of BFS, as illustrated in *Figure 3-27*. This figure shows, firstly, that the amount of portlandite decreases with the increase of replacement level of BFS. This is in line with the experimental results presented in section 3.3.1.2. When the replacement level of BFS is increased to 70%, portlandite is almost absent in the fully hydrated blended cement paste. Meanwhile, the amount of C-S-H gel ( $C_{1.7}SH_4$ ) produced from the hydration of cement decreases dramatically when the amount of BFS is increased from 0 to 70%. In contrast, the amount of C-S-H gel ( $C_{1.4}SH_{2.92}A_{0.046}$ ), produced from the pozzolanic reaction of BFS, increases. Volume percentages of different types of C-S-H gels to the total amount of C-S-H are calculated based on the above-mentioned data, together with the volume ratio of different types of C-S-H gels. These volume percentages and ratio are plotted against the replacement level of BFS, as illustrated in *Figure 3-28*.

The volume ratio of C-S-H gel (with high C/S ratio) produced by the cement hydration to the C-S-H gel (with lower C/S ratio) decreases dramatically from approximate 9.0 to 0.33, when the BFS content increases from 10 to 70%. This drastic change must be considered seriously when studying the carbonation of concrete blended with high amounts of BFS. As indicated in the modelling results shown in *Figure 3-27*, there is also a dramatic reduction of portlandite (one of the calcium-bearing phase) in the blended cement paste. The C-S-H gels produced from different sources are the major calcium-bearing phases to resist carbonation. Moreover, different types of C-S-H gels (with different C/S ratio), produced from either

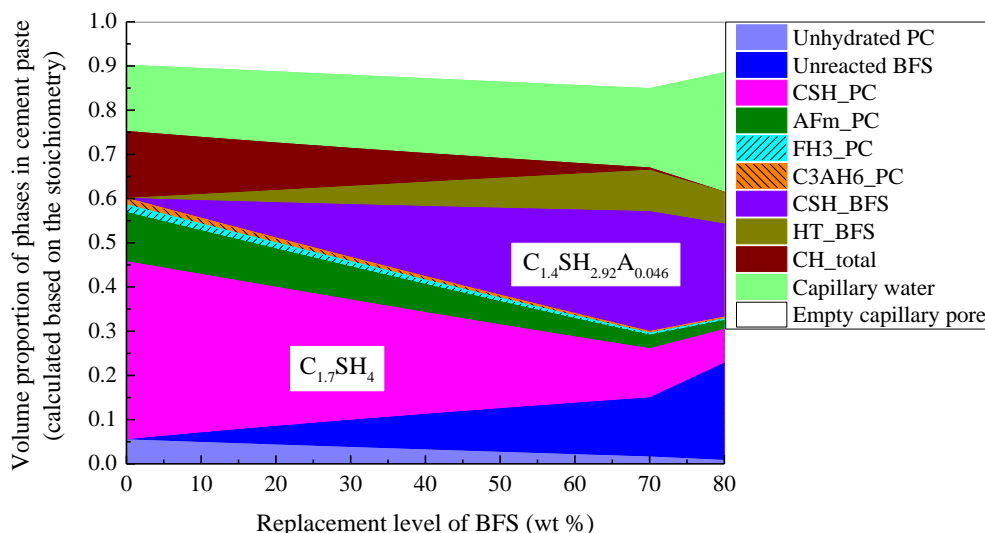


Figure 3-27 Effects of BFS on the amounts of different phases in the cement paste blended with BFS, simulated with HYMOSTRUC3D-E ( $w/b = 0.5$ ; Note: AFm\_PC, CSH\_PC, FH3\_PC, C3AH6 are the AFm, CSH, FH<sub>3</sub>, C<sub>3</sub>AH<sub>6</sub> produced by the hydration of PC, respectively. CSH\_BFS, HT\_BFS are the CSH, M<sub>4.6</sub>AH<sub>19</sub> produced by the pozzolanic reaction of BFS, respectively.)

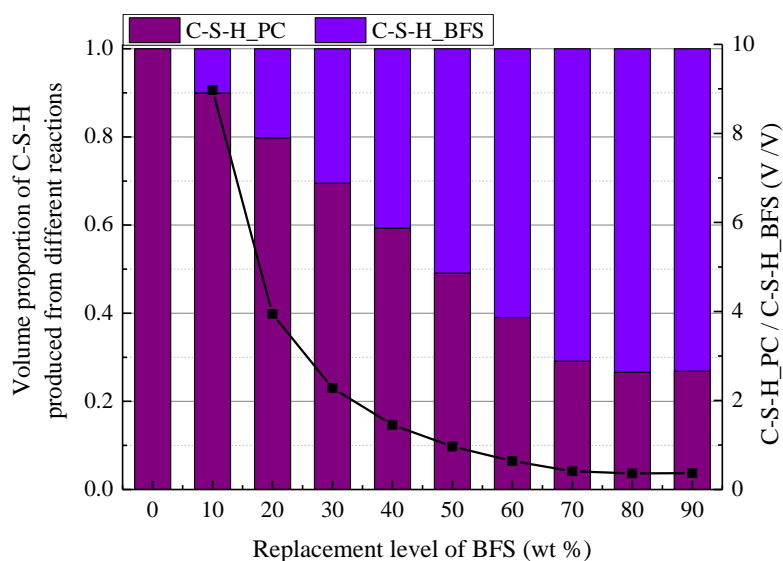


Figure 3-28 Effects of BFS on the amounts of different C-S-H gels in the cement paste blended with BFS

cement hydration or pozzolanic reaction of BFS, may provide different resistance against carbonation attack.

### 3.3.3 Pore structure evolution of blended cement paste

MIP tests normally consist of two steps: mercury intrusion and mercury extrusion. Typical MIP test results of cement pasted are shown in Figure 3-29 and Figure 3-30. The intrusion and extrusion curves in Figure 3-29 provide information about the pore size distribution of cement paste measured in two different stages. The *total* porosity and *effective* porosity can be



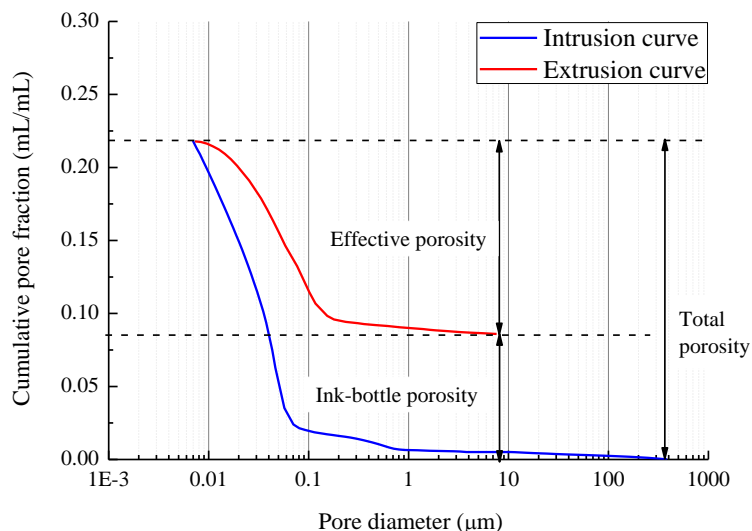


Figure 3-29 Pore size distribution of cement paste measured by the mercury intrusion and extrusion (P100, hydrated for 28 days)

determined accordingly. The difference between intrusion and extrusion curve represents the so-called ink-bottle porosity.

The related differential curves are shown in *Figure 3-30*. The peaks in the curves are named “threshold”, “critical” or “percolation” pore diameters [25]. In cement paste, the first peak, between 0.1  $\mu\text{m}$  to 1  $\mu\text{m}$ , is generally considered to correspond to the large capillary porosity, according to the classification of pores by Mindess and Young [48]. The second peak, between 0.01  $\mu\text{m}$  to 0.1  $\mu\text{m}$ , corresponds to the medium capillary porosity. For example, in *Figure 3-30*, the first peak corresponds to a diameter of 0.526  $\mu\text{m}$  and the second peak to 0.0432  $\mu\text{m}$ .

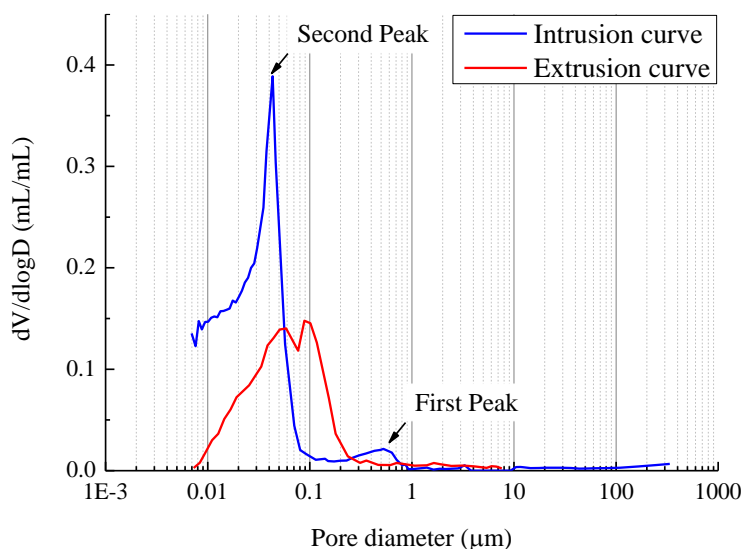


Figure 3-30 Pore size distribution differential curves of cement paste measured by mercury intrusion and extrusion (P100, hydrated for 28 days)

The intrusion and extrusion hysteresis, including the definitions of total, effective and ink-pore structure evolution of blended cement paste will mainly focus on the effects of SCMs on the total porosity and capillary porosity.

### 3.3.3.1 Effects of FA on the porosity of blended cement paste

Pore size distributions of OPC paste (P100) and FA blended paste (F30) are illustrated in *Figure 3-31* and *Figure 3-32*, respectively. The ages of the pastes vary from 28 days to 1 year.

As observed from *Figure 3-31a* and *Figure 3-32a*, the total pore volume decreases with hydration time for both P100 and F30. These pores are (partly) filled with water. In fact, the capillary water is the only water available for hydration of cement or pozzolanic reaction of SCMs [49]. With continuous hydration, more and more capillary water is consumed by the reactions of the binder and is converted into hydration products. These products will precipitate in the capillary pores and reduce the connectivity of the pore structure of the paste. Thus, increasing hydration results in reduction of total pore volume of both OPC paste and FA blended paste [5, 25, 50, 51].

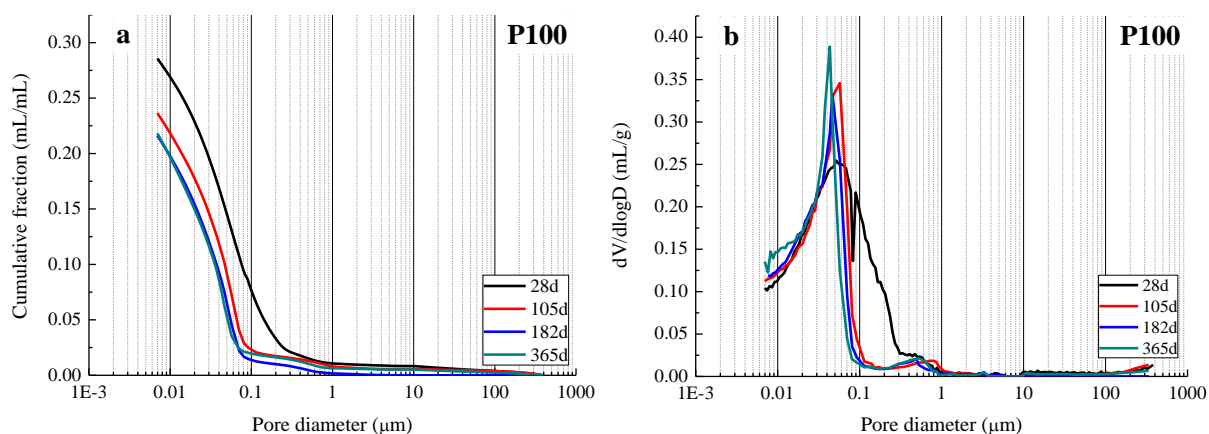


*Figure 3-31* Pore size distribution of P100 hydrated for from 28d up to 1 year

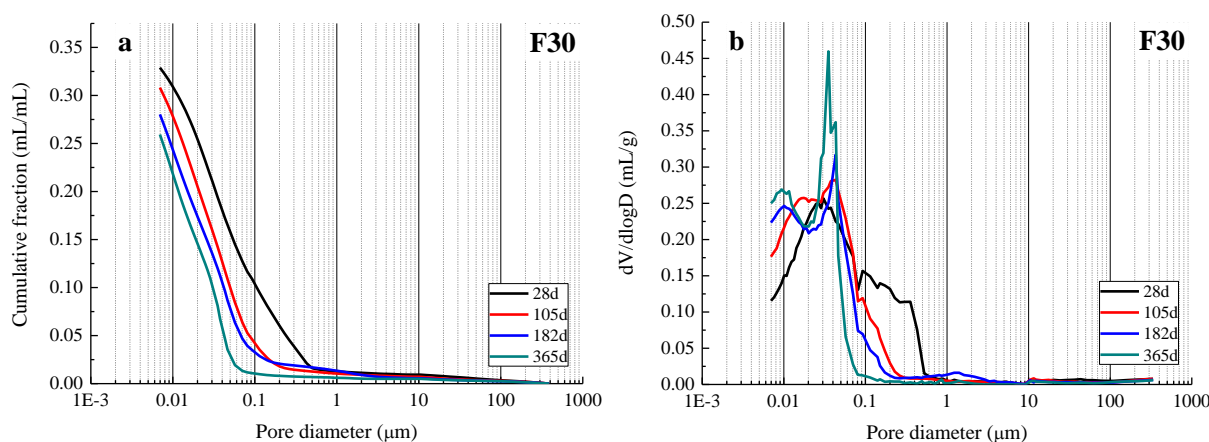


*Figure 3-32* Pore size distribution of F30 hydrated for from 28d up to 1 year

In the differential curves of P100 (*Figure 3-31b*) and F30 (*Figure 3-32b*), both the two peaks indicating the “threshold” pore diameters can be observed, which will disappear with increasing hydration time. This is also found in studies of other researchers [5, 50].

The first peak in the differential curves indicates the capillary pores with an average diameter larger than 0.01  $\mu\text{m}$ . With the development of hydration, the larger capillary pore will gradually be filled with hydration products and become disconnected. This is the reason why the first peak becomes weak and moves to a smaller pore diameter area with increasing hydration time.

The second peak indicates the gel pores. The threshold pore diameter of this peak is around 0.02-0.04  $\mu\text{m}$  for all the mixture in this study. This value is higher than the size of the gel pores defined by Powers (< 0.01  $\mu\text{m}$ ) [52] and Jennings (3-30 nm) [53].

From *Figure 3-31b* to *Figure 3-32b*, the second peaks in OPC paste and in the paste blended with only 30% of FA both show growth in intensity, but become narrow with increasing hydration time.

Based on the above-mentioned MIP test results, the total porosity and effective porosity of different FA blended pastes together with OPC paste are calculated with the procedure illustrated with *Figure 3-29*. The calculated porosities of pastes hydrated for the same age are plotted against the replacement level of FA. The hydration time varies from 28 days to 1 year. Effects of the FA content on the total porosity is shown in *Figure 3-33*.

For the same age, the use of FA will increase the total porosity of cement paste blended with FA. Especially at the earlier age, the total porosity of blended cement paste has a nearly positive linear relation with the replacement level of FA, as shown in *Figure 3-33*. At later ages, i.e. 182 days or 1 year, the above-mentioned relation is not exactly linear. The total porosity of OPC paste decreases slowly or even increases slightly from 105 days to 1 year compared to FA blended cement pastes (i.e. F10 and F30).

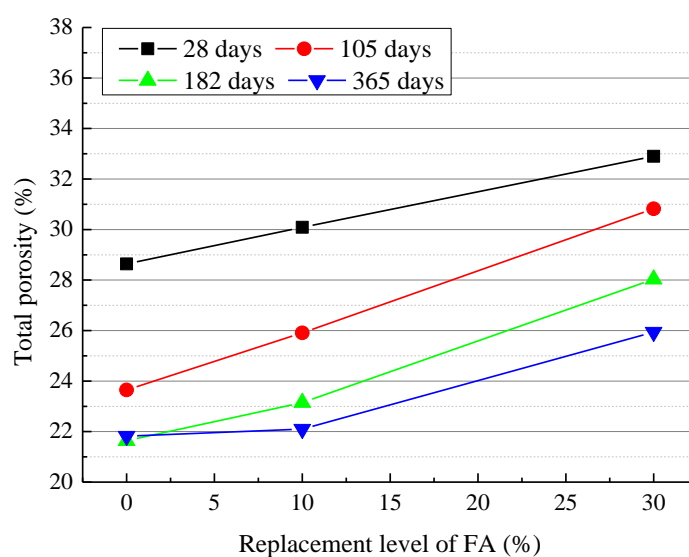


*Figure 3-33 Effects of FA amount on the total porosity of blended cement paste hydrated for 28 days, 105 days, 182 days or 1 year*

*Table 3-17 Normalized total porosity of FA blended cement paste (% , normalized to the total porosity of OPC paste at the same age) (Mixture composition: see Table 3-8)*

Hydration time [days]	Normalized total porosity [%] of different mixtures		
	P100	F10	F30
28	100.0	105.1	114.9
105	100.0	109.6	130.3
182	100.0	107.0	129.5
365	100.0	101.3	118.9

It is known that the degree of pozzolanic reaction of FA is much lower than the degree of hydration of cement at the same age. Less reaction products are generated in blended cement paste, resulting in a higher total porosity compared to pure Portland cement paste [54]. The higher the replacement level of FA, the higher the total porosity compared to that of mixtures F10 and F30.

Total (MIP) porosities of different FA blended cement pastes are normalized to the total (MIP) porosity of OPC paste with the same age. The normalized values are listed in *Table 3-17*. Comparing with P100 hydrated for 28 days, the total porosity of F10 and F30 are increased by 5.1% and 14.9% respectively, approximately half of the related replacement level of FA. When hydrated for 105 days, the total porosity reaches the highest values for both F10 and F30, i.e. 9.6% and 30.3%, respectively. These two increments are nearly the same as the replacement levels of FA in the related blended cement pastes. With further hydration, the increase of the total porosity of blended cement pastes due to the incorporating of FA decreases with hydration time.

From 28 days to 105 days, there are more hydration products produced in P100 than in F10 and F30 because of the lower reaction rate of the pozzolanic reaction and dilution effects. Therefore, the total porosity of P100 is reduced more than that of F10 and F30.

From 105 days to 182 days or 1 year, the hydration of cement is slowed down, resulting the less changes of the total porosity of P100. Meanwhile, the pozzolanic reaction of FA is not slowed down in F10 and F30. The total porosities of these mixtures decrease further with hydration time and the difference of the total porosities between P100 and F10 or F30 decreases. In summary, the increase in total porosity of FA blended cement paste is highest at 105 days.

Effects of the FA content on the effective porosity is shown in *Figure 3-34*. The normalized effective porosities of FA blended cement pastes are listed in *Table 3-18*. Apparently, the replacement level of FA affects the effective porosity of blended cement paste in the same trend as the total porosity.

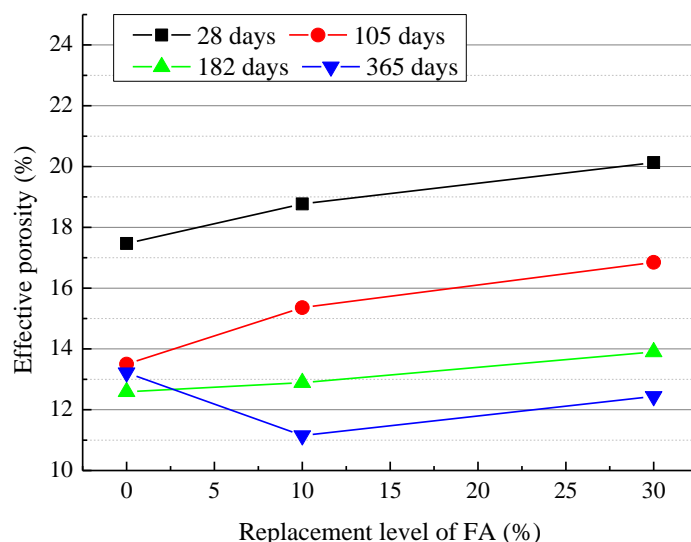


Figure 3-34 Effects of FA amount on the effective porosity (MIP) of blended cement paste hydrated for 28 days, 105 days, 182 days or 1 year

Table 3-18 Normalized effective porosity of FA blended cement paste (% , normalized to the effective porosity of OPC paste at the same age) (Mixture composition: see Table 3-8)

Hydration time [days]	Normalized effective porosity [%] of different mixtures		
	P100	F10	F30
28	100.0	107.4	115.2
105	100.0	113.8	124.8
182	100.0	102.4	110.4
365	100.0	84.3	94.0

### 3.3.3.2 Effects of BFS on the porosity of blended cement paste

Pore size distributions of cement pastes blended with BFS (B70) are illustrated in *Figure 3-35*. Hydration time of B70 paste varies from 28 days up to 1 year.

The total pore volume of B70 decreases with hydration time. Unlike OPC (P100) and FA blended paste (F30) shown in *Figure 3-31b* and *Figure 3-32b*, the pore size distribution differential curve of B70 has no peak indicating the “threshold” pore diameter between 0.1 and 1  $\mu\text{m}$  (first peak). Most of the pores in B70 have a pore diameter less than 0.1  $\mu\text{m}$ . Furthermore, it is hard to find the second peak. Only a ‘shoulder peak’ of the second peak can be observed in the differential curve of B70 paste hydrated for 28 days. After 28 days, the second peak totally disappears. This means that the hydration of BFS produces more C-S-H, which contributes to a much finer pore structure of BFS blended cement paste.

Based on the above-mentioned MIP test results, the total porosity and effective porosity of different BFS blended pastes together with OPC paste are calculated according to the procedure illustrated in *Figure 3-29*. The calculated porosities of pastes hydrated for the same age are plotted against the replacement level of BFS. The hydration time varies from 28 days to 1 year.

Effects of BFS content on the total porosity of blended cement paste is shown in *Figure 3-36*. The curves in *Figure 3-36* show that the total porosity of cement paste blended with BFS decreases with the increasing replacement level of BFS under the same hydration time. The total porosity of BFS blended cement paste has a nearly negative linear relation with the replacement level of BFS, especially for the data measured from samples hydrated for 182 days.

Total porosities of different BFS blended cement pastes are normalized to the total porosity of OPC paste with the same age. The normalized values are listed in *Table 3-19*. Apparently, the introduction of BFS in cement will cause a reduction of the total porosity of BFS blended cement paste. This effect will become more obvious when increasing the amount of BFS or hydration time.

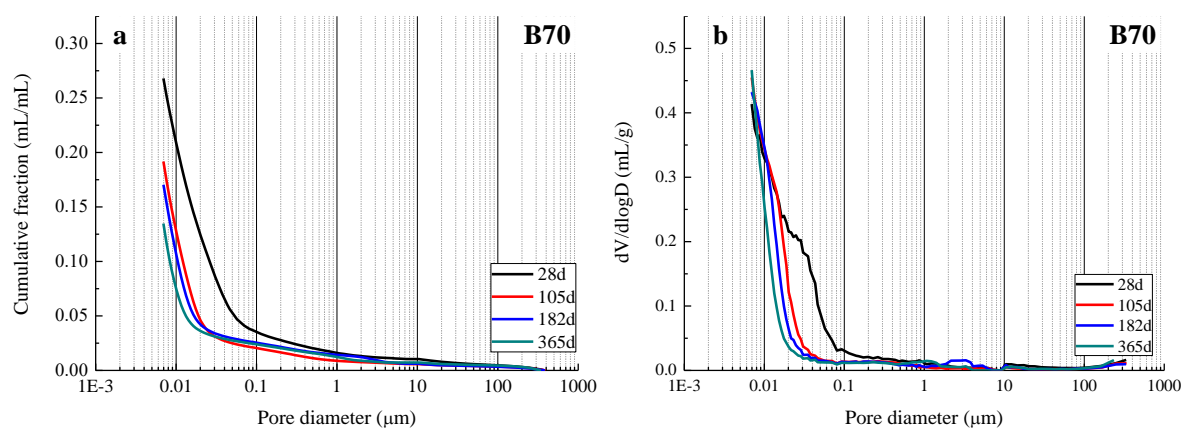


*Figure 3-35* Pore size distribution of B70 hydrated for from 28d up to 1 year

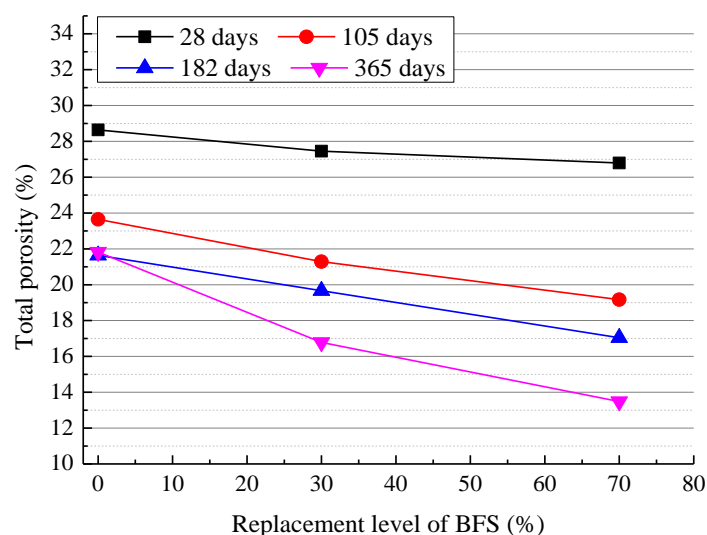


*Figure 3-36* Effects of BFS amount on the total porosity of blended cement paste hydrated for 28 days, 105 days, 182 days or 1 year

Table 3-19 Normalized total porosity of BFS blended cement paste (% , normalized to the total porosity of OPC paste at the same age). (Mixture composition: see Table 3-8)

Hydration time [days]	Normalized total porosity of different mixtures		
	P100	B30	B70
28	100.0	83.2	93.5
105	100.0	72.5	81.1
182	100.0	70.7	78.7
365	100.0	56.2	61.8

Unlike FA, the fineness of BFS is even higher than OPC in this study. Moreover, the pozzolanic reaction of BFS develops faster than that of FA, although it is slower than the hydration of OPC. Therefore, the use of BFS will cause a dramatic decrease of the total porosity of cement paste blended with BFS. Due to the reaction of BFS at later ages, this effect increases with hydration time.

The porosity of paste, mortar or concrete blended with BFS has already been measured by many researchers in the past with different methods, such as MIP, BSE imaging analysis and water sorption etc. To compare the results of this study with the references, only the data measured by MIP are discussed here. It appears, however, that the conclusions regarding the effects of BFS amount on the porosity are ambiguous. Some studies conclude that incorporating BFS will cause a reduction of the porosity of paste [55-57], mortar [58] or concrete [59-62] blended with BFS, whereas other researchers draw an opposite conclusions [63-66].

By comparing study of above-mentioned references, three major factors are found to affect the conclusions related to the porosity, which are the fineness of BFS, drying method of sample and age of the sample. Even with the same w/b and cured under the same conditions, different conclusions were made for the effects of BFS on the total porosity of blended cement paste (mortar or concrete) when the three factors are different.

When using BFS with fineness higher than OPC, the total porosity of BFS blended cement paste (mortar or concrete) is normally lower than that of OPC paste (mortar or concrete). On the contrary, the researchers [63] [66] found that the addition of BFS would increase the total porosity of blended cement paste when using BFS with a fineness less than OPC.

The drying method of the specimens prepared for MIP tests also affects the test results and conclusions. The specimens in this study were freeze-dried before the MIP test. The details are described in elsewhere [5]. In some studies, the specimens are oven-dried before the MIP test [64] [62]. In the latter case the results show that using BFS will increase the total porosity of blended paste or concrete. Other reseachers found that the conclusion will be different when measurements are performed at different ages. Ortega [67] compared the porosities of OPC and slag cement (with a content of GGBS between 66-80% of total binder) mortars cured under different conditions. The w/b ratios were 0.40 and 0.50. Under normal laboratory curing condition ( RH of 100%, 20°C), the slag cement mortar showed higher total porosity at early age (7 days), but less total porosity at later age (28, 90, 180 days) compared with OPC mortar.

Choi [56] investigated the micropore structures of high-strength cement pastes (w/b of 0.20) blended with high volume of BFS (replacing OPC up to 80% by mass). With increasing replacement level of BFS, the porosity of blended cement paste increased at early ages (3 days), but decreased at later ages (7, 28, and 91 days).

Leemann [68] compared the total pore volumes (ml/g) of OPC (CEM I 42.5) and slag cement (CEM III/B, 70% of slag by mass) mortar with the same w/b of 0.50. The specimens were crushed and freeze-dried before the MIP test. The results showed that the slag cement mortar has higher total pore volume in the early age (7 days or 28 days), but lower total pore volume in the later age (182 days) compared with the OPC mortar.

Yio[57] investigated the pore structure and mass transport properties of cement paste blended with SCMs (SF, FA and BFS), with average particle sizes lower than that of OPC. The cement paste blended with 60% of BFS had a higher total porosity at early age (7 days), but a lower total porosity at later age (90 days) than OPC paste.

Based on the results measured in this research and discussion about the reference data, the use of BFS in cement paste will normally cause the reduction of the porosity of the paste, and hence a reduction of the porosity of mortar or concrete made with this paste.

### 3.3.3.3 Situation in OPC-FA-BFS ternary system

Total porosity and effective porosity of F30 and B30 are compared in *Figure 3-37a* and *Figure 3-37b*, respectively. The addition of FA will increase the porosity of cement paste blended with FA, whereas the addition of BFS will bring a reduction to the porosity of BFS blended cement paste. Apparently, FA and BFS have totally opposite effects on the porosities of blended cement paste. Therefore, the ternary mixture is compared and studied with binary mixture in this section, in order to find if it has a better behavior from the porosity point of view.

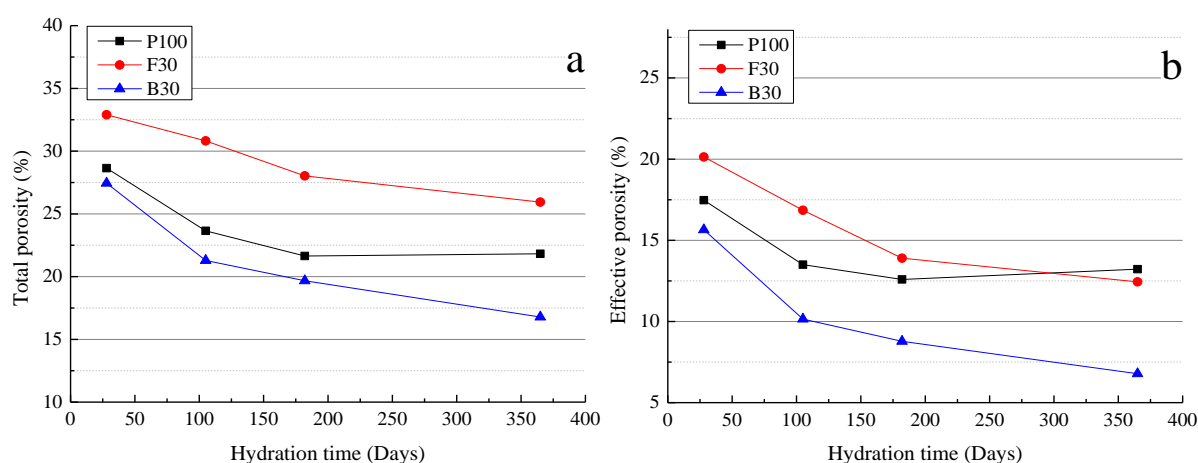


Figure 3-37 Comparison of total and effective porosity of F30 and B30



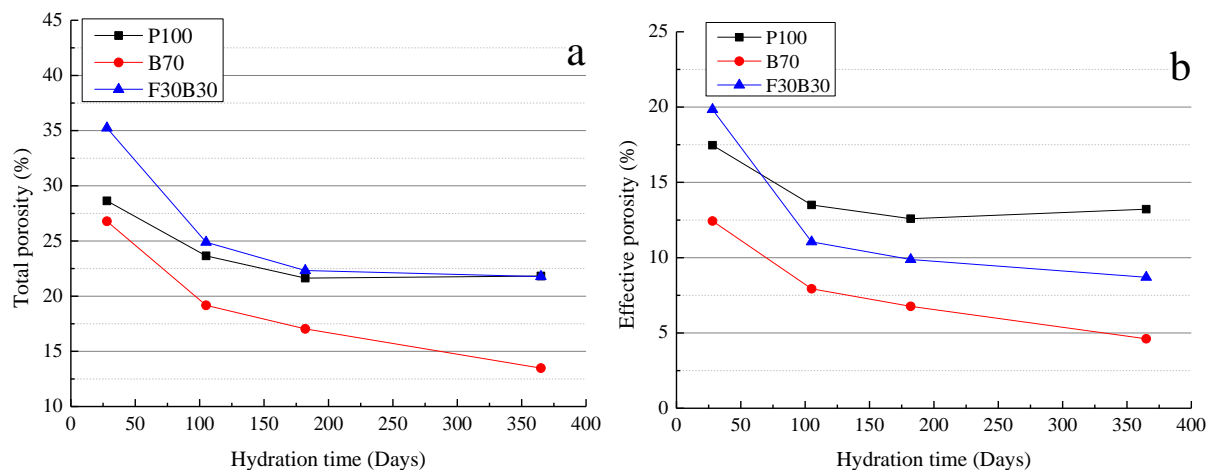


Figure 3-38 Comparison of total and effective porosity of B70 and F30B30

Total porosity and effective porosity of B70 and F30B30 are compared in *Figure 3-38a* and *Figure 3-38b*, respectively. The total porosity of F30B30 is higher than that of B70, but is getting closer to that of OPC paste (P100), with increasing hydration time. In *Figure 3-17*, the amount of portlandite in F30B30 is relatively higher than that of B70. Considering both the amount of portlandite and porosity, F30B30 may show better resistance to  $\text{CO}_2$  attack than B70 which contains the similar amount of SCMs. Therefore, an optimized ternary mixture can be designed to fulfill three requirements of blended cement concrete: economic, low- $\text{CO}_2$  emission and better carbonation resistance.

### 3.4 Conclusion

Effects of SCMs (FA and BFS) on the development of portlandite and C-S-H, together with the porosities of blended cement paste, are studied both experimentally and by numerical simulation. Some general conclusions are drawn below.

- ◆ Using FA and BFS can both cause reduction of the amount of portlandite in blended cement paste. The amount of portlandite has a negative linear relation with the replacement level of FA or BFS. The intercept value of this linear relation is close to the maximum amount of portlandite that will be produced in case of fully hydrated cement paste, given the same w/b of the mixtures.
- ◆ Partial replacement of OPC by FA and BFS will cause production of C-S-H gels with a lower C/S than that produced by hydration of OPC. With increasing replacement level of FA or BFS, the amount of C-S-H gel with lower C/S will increase. The average C/S of C-S-H gels produced by the pozzolanic reaction of FA varies from 1.0 to 1.30. Meanwhile, the average C/S of C-S-H gels produced by the pozzolanic reaction of BFS is slightly higher, varies from 1.1 to 1.30 in paste hydrated for 1 year.

- ◆ Using FA will increase the total and effective porosities of FA blended cement paste. This effect will be highest in pastes hydrated for 105 days. BFS will cause a reduction to the total and effective porosities of BFS blended cement paste.
- ◆ Optimized concrete mixture by considering the price, lower CO<sub>2</sub> emission and carbonation resistance can be designed by using both FA and BFS, or combinations of these two materials, in the concrete.

### 3.5 References

- [1] P. Gao, Simulation of hydration and microstructure development of blended cements, Delft University of Technology, 2018.
- [2] R. Allmann, R. Hinek, The introduction of structure types into the Inorganic Crystal Structure Database ICSD, *Acta Crystallogr A*, 63 (2007) 412-417.
- [3] H. Rietveld, A profile refinement method for nuclear and magnetic structures, *Journal of applied Crystallography*, 2 (1969) 65-71.
- [4] N. Doebelin, R. Kleeberg, Profex: a graphical user interface for the Rietveld refinement program BGMN, *Journal of applied crystallography*, 48 (2015) 1573-1580.
- [5] G. Ye, Experimental study and numerical simulation of the development of the microstructure and permeability of cementitious materials, TU Delft, Delft University of Technology 2003.
- [6] K. Van Breugel, Simulation of hydration and formation of structure in hardening cement-based materials, (1991).
- [7] E.A.B. Koenders, Simulation of volume changes in hardening cement-based materials, (1997).
- [8] N. Richard, Structure et propriétés élastiques des phases cimentières base de mono-aluminate de calcium, 1999.
- [9] A. Noumowé, Effet des hautes températures (20 °C–600 °C) sur le béton, Institut National des Sciences Appliquées, 1995.
- [10] E. Nonnet, N. Lequeux, P. Boch, Elastic properties of high alumina cement castables from room temperature to 1600 C, *Journal of the European Ceramic Society*, 19 (1999) 1575-1583.
- [11] 杨南如, 无机非金属材料测试方法, 武汉工业大学出版社 1990.
- [12] Q. Zhou, F. Glasser, Thermal stability and decomposition mechanisms of ettringite at < 120 C, *Cement Concrete Res*, 31 (2001) 1333-1339.
- [13] B. Lothenbach, G. Le Saout, M. Ben Haha, R. Figi, E. Wieland, Hydration of a low-alkali CEM III/B-SiO<sub>2</sub> cement (LAC), *Cement Concrete Res*, 42 (2012) 410-423.
- [14] B. Lothenbach, G. Le Saout, E. Gallucci, K. Scrivener, Influence of limestone on the hydration of Portland cements, *Cement Concrete Res*, 38 (2008) 848-860.
- [15] J.T. Klopoggea, J. Kristófb, R.L.J.C.O. Frosta, Thermogravimetric analysis-mass spectrometry (TGA-MS) of hydrotalcites containing CO<sub>3</sub><sup>2-</sup>, NO<sub>3</sub><sup>-</sup>, Cl<sup>-</sup>, SO<sub>4</sub><sup>2-</sup> or ClO<sub>4</sub><sup>-</sup>, 1 (2001) 451.
- [16] T. Stanimirova, N. Piperov, N. Petrova, G. Kirov, Thermal Evolution of Mg–Al–CO<sub>3</sub> Hydrotalcites, *Clay Minerals*, 39 (2004).
- [17] G. Platret, Suivi de l'hydratation du ciment et de l'évolution des phases solides dans les bétons par analyse thermique, Caractéristiques microstructurales et propriétés relatives à la durabilité des bétons. Méthodes de mesure et d'essai de laboratoire. Méthodes d'essai, (2002).
- [18] T. Kato, K. Murakami, K. Sugawara, Carbon Reduction of Gypsum Produced from Flue Gas Desulfurization, *CHEMICAL ENGINEERING*, 29 (2012).
- [19] R. Kuusik, P. Salkkonen, L. Niinistö, Thermal decomposition of calcium sulphate in carbon monoxide, *J Therm Anal*, 30 (1985) 187-193.
- [20] B.K. Marsh, R.L. Day, Pozzolanic and cementitious reactions of fly ash in blended cement pastes, *Cement Concrete Res*, 18 (1988) 301-310.
- [21] Z. Yu, Microstructure development and transport properties of portland cement-fly ash binary systems: in view of service life predictions, (2015).
- [22] E.W. Washburn, The Dynamics of Capillary Flow, *Physical Review*, 17 (1921) 273-283.
- [23] R.A. Cook, K.C. Hover, Experiments on the contact angle between mercury and hardened cement paste, *Cement Concrete Res*, 21 (1991) 1165-1175.
- [24] C.A. León y León, New perspectives in mercury porosimetry, *Advances in Colloid and Interface Science*, 76-77 (1998) 341-372.
- [25] R.A. Cook, K.C. Hover, Mercury porosimetry of hardened cement pastes, *Cement Concrete Res*, 29 (1999) 933-943.
- [26] B. Kolani, L. Buffo-Lacarrière, A. Sellier, G. Escadeillas, L. Boutillon, L. Linger, Hydration of slag-blended cements, *Cement and Concrete Composites*, 34 (2012) 1009-1018.
- [27] E. Sakai, S. Miyahara, S. Ohsawa, S.-H. Lee, M. Daimon, Hydration of fly ash cement, *Cement Concrete Res*, 35 (2005) 1135-1140.

- [28] J.F. Young, W. Hansen, Volume relationships for CSH formation based on hydration stoichiometries, MRS Online Proceedings Library Archive, 85 (1986).
- [29] D.P. Bentz, P.V. Coveney, E.J. Garboczi, M.F. Kleyn, P.E. Stutzman, Cellular automaton simulations of cement hydration and microstructure development, *Modelling and Simulation in Materials Science and Engineering*, 2 (1994) 783.
- [30] T. Merzouki, M. Bouasker, N.E.H. Khalifa, P. Mounanga, Contribution to the modeling of hydration and chemical shrinkage of slag-blended cement at early age, *Constr Build Mater*, 44 (2013) 368-380.
- [31] D.P. Bentz, S. Remond, Incorporation of fly ash into a 3-D cement hydration microstructure model, US Department of Commerce, Technology Administration, National Institute of ...1997.
- [32] J.M. Richardson, J.J. Biernacki, P.E. Stutzman, D.P. Bentz, Stoichiometry of Slag Hydration with Calcium Hydroxide, *J Am Ceram Soc*, 85 (2002) 947-953.
- [33] R. Castaing, Application of electron probes to local chemical and crystallographic analysis, Ph. D. Thesis (University of Paris), (1951).
- [34] J. Labberigue-Frolow, P. Radvanyi, Le rendement de fluorescence de la couche K. Mesures spectrométriques sur  $^{4399}\text{Tc}^*(6, 04 \text{ h})$  et  $^{49} 115\text{In}^*(4, 5 \text{ h})$ , *Journal de Physique et le Radium*, 17 (1956) 944-949.
- [35] H. Uchikawa, S. Uchida, S. Hanehara, Effect of character of glass phase in blending components on their reactivity in calcium hydroxide mixture, 1986.
- [36] T. Sato, I. Furuhashi, Review of the 36th General Meeting, Cement Association of Japan, (1982) 42.
- [37] A. Harrisson, An Examination of Some Pore and Composite Portland Cement Pastes Using Scanning Electron Microscopy with X-ray Analytical Capability, *Proceedings of the 8th International Congress on the Chemistry of Cement*, 1986, 1986, pp. 170-175.
- [38] H.F.W. Taylor, A. Turner, Reactions of tricalcium silicate paste with organic liquids, *Cement Concrete Res*, 17 (1987) 613-623.
- [39] G. Groves, P. Le Sueur, W. Sinclair, Transmission Electron Microscopy and Microanalytical Studies of Ion-Beam-Thinned Sections of Tricalcium Silicate Paste, *J Am Ceram Soc*, 69 (1986) 353-356.
- [40] I. Odler, H. Dörr, Early hydration of tricalcium silicate I. Kinetics of the hydration process and the stoichiometry of the hydration products, *Cement Concrete Res*, 9 (1979) 239-248.
- [41] L. SUEUR, Chemical and morphological studies of the hydration of tricalcium silicate, *Proc. Br. Ceram. Soc.*, 1984, pp. 177.
- [42] D.L. Kantro, C.H. WEISE, Hydration of Various Beta-Dicalcium Silicate Preparations, *J Am Ceram Soc*, 62 (1979) 621-626.
- [43] K. Fujii, W. KONDO, Rate and Mechanism of Hydration of  $\beta$ -Dicalcium Silicate, *J Am Ceram Soc*, 62 (1979) 161-167.
- [44] S. Shibata, K. Kishi, K. Asaga, M. Daimon, P. Shrestha, Preparation and hydration of  $\beta$ -C2S without stabilizer, *Cement Concrete Res*, 14 (1984) 323-328.
- [45] A. Harrisson, N. Winter, H.F. Taylor, Microstructure and microchemistry of slag cement pastes, MRS Online Proceedings Library Archive, 86 (1986).
- [46] R. Snellings, T. Paulhiac, K. Scrivener, The Effect of Mg on Slag Reactivity in Blended Cements, *Waste and Biomass Valorization*, 5 (2014) 369-383.
- [47] I. Richardson, G. Groves, Microstructure and microanalysis of hardened cement pastes involving ground granulated blast-furnace slag, *J Mater Sci*, 27 (1992) 6204-6212.
- [48] S. Mindess, J.F. Young, D. Darwin, *Concrete* Prentice-Hall, Englewood Cliffs, NJ, 481 (1981).
- [49] P. Navi, C. Pignat, Simulation of cement hydration and the connectivity of the capillary pore space, *Adv Cem Based Mater*, 4 (1996) 58-67.
- [50] Z. Yu, G. Ye, The pore structure of cement paste blended with fly ash, *Constr Build Mater*, 45 (2013) 30-35.
- [51] M.M.Y. Delmi, A. Ai't-Mokhtar, O. Amiri, Modelling the coupled evolution of hydration and porosity of cement-based materials, *Constr Build Mater*, 20 (2006) 504-514.
- [52] T.C. Powers, T.L. Brownyard, Studies of the Physical Properties of Hardened Portland Cement Paste, *Journal Proceedings*, 43.

- [53] H.M. Jennings, Refinements to colloid model of CSH in cement: CM-II, *Cement Concrete Res*, 38 (2008) 275-289.
- [54] Z. Yu, *Microstructure Development and Transport Properties of Portland Cement-fly Ash Binary Systems*, Technical University Delft, (2015).
- [55] J. Yang, J. Huang, X. He, Y. Su, H. Tan, W. Chen, X. Wang, B. Strnadel, Segmented fractal pore structure covering nano- and micro-ranges in cementing composites produced with GGBS, *Constr Build Mater*, 225 (2019) 1170-1182.
- [56] Y.C. Choi, J. Kim, S. Choi, Mercury intrusion porosimetry characterization of micropore structures of high-strength cement pastes incorporating high volume ground granulated blast-furnace slag, *Constr Build Mater*, 137 (2017) 96-103.
- [57] M.H.N. Yio, H.S. Wong, N.R. Buenfeld, 3D pore structure and mass transport properties of blended cementitious materials, *Cement Concrete Res*, 117 (2019) 23-37.
- [58] M.A. Megat Johari, J.J. Brooks, S. Kabir, P. Rivard, Influence of supplementary cementitious materials on engineering properties of high strength concrete, *Constr Build Mater*, 25 (2011) 2639-2648.
- [59] P. Duan, Z. Shui, W. Chen, C. Shen, Enhancing microstructure and durability of concrete from ground granulated blast furnace slag and metakaolin as cement replacement materials, *Journal of Materials Research and Technology*, 2 (2013) 52-59.
- [60] M. Han-Young, H.-S. Kim, D.-S. Choi, Pore Size Distribution and Chloride Diffusivity of Concrete Containing Ground Granulated Blast Furnace Slag, *Journal of the Korea Concrete Institute*, 16 (2004) 277-282.
- [61] L. Zheng, M.R. Jones, Z. Song, Concrete pore structure and performance changes due to the electrical chloride penetration and extraction, *Journal of Sustainable Cement-Based Materials*, 5 (2016) 76-90.
- [62] H.Y. Moon, H.S. Kim, D.S. Choi, Relationship between average pore diameter and chloride diffusivity in various concretes, *Constr Build Mater*, 20 (2006) 725-732.
- [63] E. Berodier, K. Scrivener, Evolution of pore structure in blended systems, *Cement Concrete Res*, 73 (2015) 25-35.
- [64] K. Li, Q. Zeng, M. Luo, X. Pang, Effect of self-desiccation on the pore structure of paste and mortar incorporating 70% GGBS, *Constr Build Mater*, 51 (2014) 329-337.
- [65] F.d.C.R. Almeida, A.J. Klemm, Evaluation of hardened state properties of GGBS-PC mortars modified by superabsorbent polymers (SAP), *Proc., Int. RILEM Conf. on Materials, Systems and Structures in Civil Engineering Conf. Segment on Concrete with Supplementary Cementitious Materials*, 2016, pp. 11-20.
- [66] A. Hadj-sadok, S. Kenai, L. Courard, A. Darimont, Microstructure and durability of mortars modified with medium active blast furnace slag, *Constr Build Mater*, 25 (2011) 1018-1025.
- [67] J.M. Ortega, I. Sánchez, M.A. Climent, Impedance spectroscopy study of the effect of environmental conditions in the microstructure development of OPC and slag cement mortars, *Archives of Civil and Mechanical Engineering*, 15 (2015) 569-583.
- [68] A. Leemann, R. Loser, P. Trtik, B. Münch, Blending of cements-influence on porosity and chloride resistance, *First Middle East Conference on Smart Monitoring Assessment and Rehabilitation of Civil Structures*, 2011.

## Accelerated Carbonation of Blended Cement Paste

---

### 4.1 Introduction

In Chapter 3, the amount of hydration products and the microstructure of cement paste blended with SCMs were studied. Effects of SCMs on the assemblage of hydrates and microstructure were discussed. In the chapter cement pastes studied in Chapter 3 will be used in accelerated carbonation experiments.

In this chapter the focus is on the transformation of calcium-bearing phases and evolution of microstructure of cement paste blended with SCMs during carbonation. Influences of the variety and content of SCMs are discussed. Carbonation of C-S-H gel and the effects on the microstructure development are investigated.

#### 4.1.1 Mixture composition and sample pre-treatment

Mixtures for samples used for carbonation test were prepared from the same materials and cured by using the same methods mentioned in Chapter 3. After curing for 1 year, plastic bottles were cut into two pieces, i.e. part A and part B, in order to obtain two cylinders (height = 40 mm,  $\phi = 50$  mm, as shown in *Figure 4-1a*). The cutting surface was grinded by the sandpaper # 800, in order to achieve a uniform surface roughness. The condition of the polished surface exposed to CO<sub>2</sub> is shown in *Figure 4-1b*. The water on the surface was removed by cloth. Both top surface rims and bottom surface of part B were re-sealed with silicon sealant in order to obtain one - dimensional carbonation condition. *Figure 4-1c* shows the well-sealed sample, ready for the accelerated carbonation test.

#### 4.1.2 Accelerated carbonation test in the lab

Under ambient conditions carbonation in concrete develops slowly and even slower in cement paste. In order to obtain enough data for different mixtures in a relatively short time, accelerated carbonation tests can be performed in the lab. After pre-treatment, the samples for the carbonation tests were moved into the carbonation chamber. In the carbonation chamber,

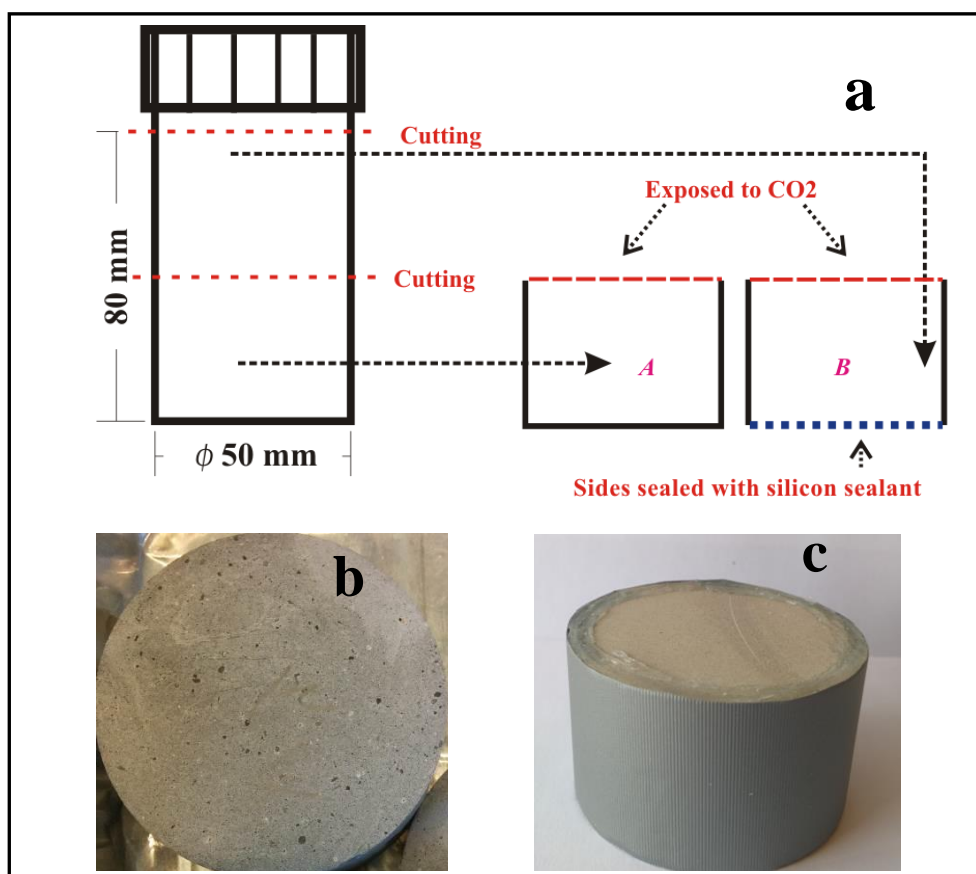


*Figure 4-1* Preparing and pre-treatment of samples used for carbonation: a. cutting; b. after surface grinding; c. the well-sealed sample

the CO<sub>2</sub> concentration is maintained at  $3\% \pm 0.2$ , automatically regulated by the solenoid valve connected to a CO<sub>2</sub> sensor. The temperature is regulated at 20°C and the relative humidity is controlled at around 75% by using the saturated NaCl solution. The carbonation exposure periods were 28 days to 84 days and 224 days. A part of the recorded relative humidity and temperature data are illustrated in *Figure 4-2*. The fluctuation in the humidity was caused by removing samples or adding water to the NaCl solution.

#### 4.1.3 Test methods

During carbonation hydration products, such as portlandite (CH) and calcium silicate hydrates (C-S-H), are transformed into CaCO<sub>3</sub> and silicate gel. These transformations also lead to changes of the microstructure, including changes of the gel pore and capillary pore structure of the cement paste. Since the pH value of the pore solution decreases with ongoing carbonation, the carbonation depths were determined using the phenolphthalein spray test. Thermogravimetric analysis (TGA) was used to determine the amounts of portlandite and CaCO<sub>3</sub> of samples after carbonation. The gel pore volume and pore size distribution of carbonated paste were determined from nitrogen adsorption tests. Meanwhile, Mercury Intrusion Porosimetry (MIP) was used to determine porosity, the capillary pore volume and pore size distribution of cement paste after carbonation.

**Phenolphthalein spray test** -- The carbonation depth ( $X_c$ ) was determined by phenolphthalein spray test. Phenolphthalein is a pH indicator. When the pH value increases from 8.2 to 12.0, the color changes from pink to fuchsia. It becomes colorless when the pH

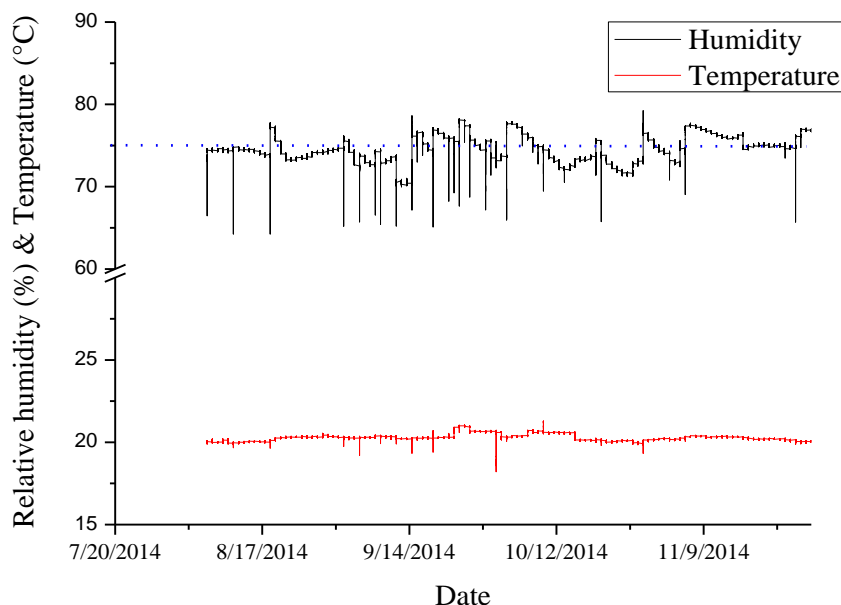


*Figure 4-2 Monitored data of relative humidity and temperature in the carbonation chamber*



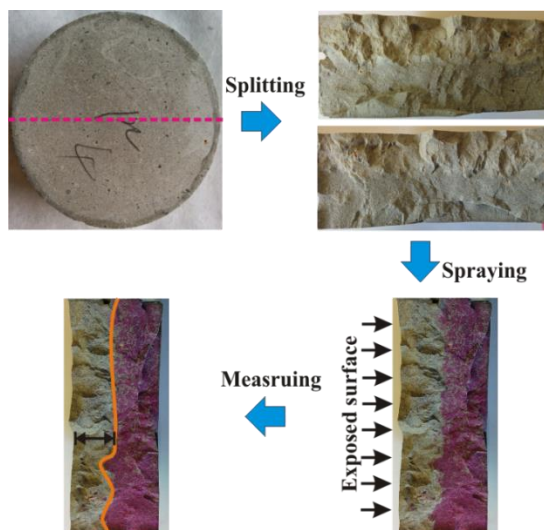


Figure 4-3 Procedure of the carbonation depth measurement by phenolphthalein spray test

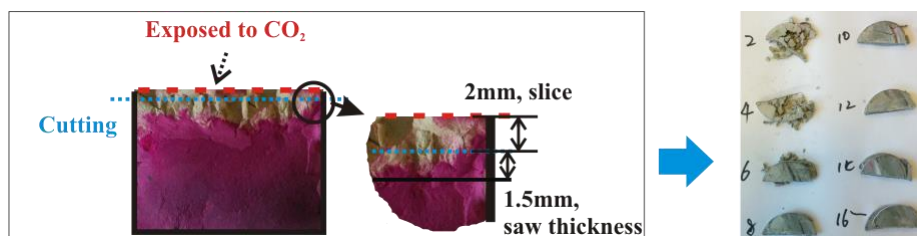


Figure 4-4 Schematic diagram of the cutting of slice specimens

value is lower than 8.2. For the spray test a solution of 1% (w/v) phenolphthalein in 95% (v/v) ethanol was used. After carbonation, the cylindrical specimens were split into two half-cylinders. Phenolphthalein solution was sprayed on both exposed fresh surfaces. About 10 points, 0.5 mm intervals between test points, were chosen to measure the carbonation depth. Final carbonation depth was the average of 10 measurements. The procedure of the phenolphthalein spray test is illustrated in *Figure 4-3*.

**Slice cutting** -- In order to draw the carbonation profiles of phases involved in the carbonation process and the porosity of the cement paste, slices were sawn from the two half-cylinders after the spray test, step by step from the exposed surface to deeper inside area of the sample. The thickness of the slices was approximately 2 mm. The cutting procedure for obtaining the slices is shown in *Figure 4-4*.

After cutting, these slices were immersed in liquid nitrogen and freeze-dried until the samples were ready for the TGA, MIP and nitrogen adsorption test. The details of drying procedure and treatment of samples used for the above tests were described in section 3.2.2.

**Nitrogen adsorption** -- The gel pore structure, i.e. pores 2-37 nm, was inferred from nitrogen adsorption isotherms. Based on the nitrogen adsorption data, the gel pore volume and size distribution can be calculated by using the BJH model [1].

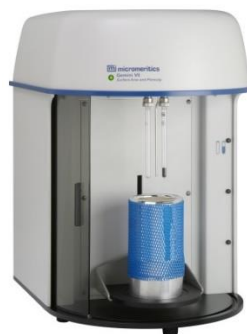


Figure 4-5 Gemini VII 2390 instrument used for nitrogen adsorption test.

Nitrogen adsorption tests were performed by using Gemini VII 2390, shown in *Figure 4-5*. The relative pressure used in the measurement was in the range of 0.05-0.98.

**TGA & MIP** -- The details of TGA and MIP test were described in section 3.2.3.

## 4.2 Experimental results and discussions

### 4.2.1 Development of the carbonation depth ( $X_c$ )

The measured carbonation depths  $X_c$  in mm are listed in *Table 4-1*. *Figure 4-6* shows the time evolution of  $X_c$  for different cement pastes. A square root of time relation passing through the origin has been used to fit  $X_c$  data. The carbonation depth illustrated in the figure is the median value of the measured data. The rate of carbonation in unidimensional is also calculated with the following equation:

$$X_c (mm) = A \cdot \sqrt{t} \quad \text{Eq. 4-1}$$

In Portland cement concrete the carbonation rate is - in a first approximation -, proportional to the porosity of the concrete, but inversely proportional to the content of calcium-bearing phases if the environmental effects are the same. As shown in *Figure 4-6*, the

Table 4-1 Carbonation depths of samples carbonated for different days measured by phenolphthalein

Mixture	Carbonation depth $X_c$ (mm)								
	Carbonated for 28 days			Carbonated for 84 days			Carbonated for 224 days		
	Average	Median	Max.	Average	Median	Max.	Average	Median	Max.
P100	2.9	2.9	3.5	3.5	3.5	5.7	8.3	8.3	10.6
F30	6.2	6.1	9.2	7.7	7.3	10.6	14.1	14.3	15.7
B70	4.9	4.9	8.3	8.2	8.2	11.4	13.5	13.5	16.1
F30B30	7.4	7.3	9.0	11.7	11.9	13.2	17.2	17.2	20.4
F10B54	6.2	5.8	8.8	8.5	8.3	10.9	13.1	13.3	13.9

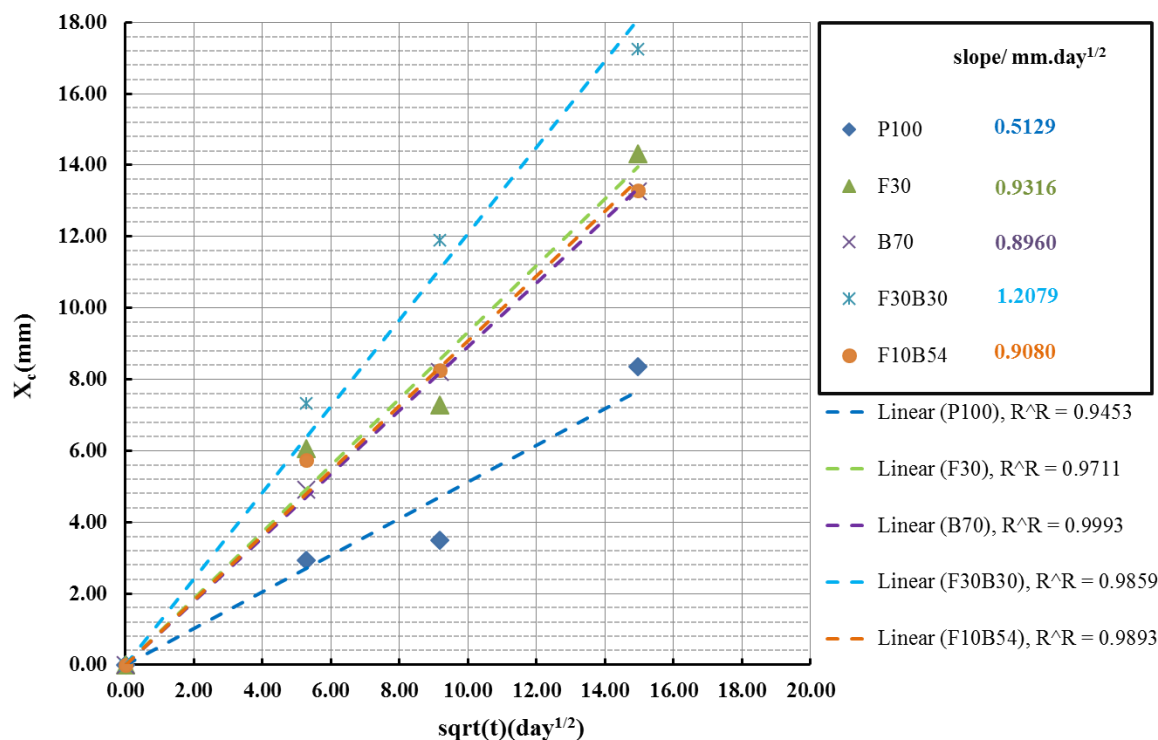


Figure 4-6 Relations between carbonation depth  $X_c$  and square root of time (Eq. 4-1)

carbonation rate in the FA-blended cement paste F30 is higher than in BFS-blended cement paste B70, even though the BFS content in B70 is more than twice the FA amount in F30. For mixtures, the carbonation rate in F10B54 is closer to that in B70. F30B30 has the highest carbonation rate.

For an explanation of afore mentioned findings, at least two factors have to be considered. On one hand, partial replacement of Portland cement by SCMs will cause a dramatic reduction of portlandite concentration in blended cement paste. On the other hand, some types of SCMs, like BFS, will lead to a lower total porosity of blended cement paste. The carbonation rate is determined by these two major factors. In general, the carbonation rate is higher in blended cement paste compared to Portland cement (see *Table 4-1*). Carbonation develops more quickly in FA-blended cement paste than BFS-blended cement paste. For example, F30 contains a higher amount of portlandite, but also has higher total porosity compared to B70. The carbonation develops faster in F30, even though the SCMs content in B70 is twice that in F30. Comparing with BFS in this study, FA is found to have more negative effects on the carbonation resistance of blended cement paste. This is also found in the ternary system. Compared to B70, the BFS was partially replaced by FA to prepare the ternary mixtures F10B54 and F30B30. Even though the total amount of SCMs in these two ternary mixtures is lower, the carbonation rates are higher than that of B70. Especially, F30B30 exhibits a high carbonation rate. *Table 4-2* gives a summary of the total porosities and the amounts of portlandite of different mixtures. The conclusions are in good agreement with those published by other researchers [2-4].

Table 4-2 Total porosity and the amount of portlandite in cement paste

Characteristic	Unit	Mixture				
		P100	F30	B70	F30B30	F10B54
Content of portlandite	g/cm <sup>3</sup>	0.276	0.11	0.025	0.046	0.045
Total porosity before carbonation	%	0.216	0.256	0.132	0.218	0.154
Total porosity after carbonation	%	0.132	0.195	0.178	0.225	0.187

#### 4.2.2 Phase assemblages in blended cement paste after carbonation

The typical TGA-MS results for cement paste after carbonation are shown in *Figure 4-7*. It includes the DTG curves (solid line) and mass spectroscopy curves (dot line) indicating the gas released. The decomposition of CaCO<sub>3</sub> mainly happens in the range of 600-900°C [5, 6].

Further, in the DTG curve in *Figure 4-7*, two obvious peaks in CO<sub>2</sub> MS curve appear, which are due to the de-carbonation of  $\gamma$ -CaCO<sub>3</sub> (aragonite) and  $\beta$ -CaCO<sub>3</sub> (calcite), respectively. In the DTG curve of carbonated blended cement paste, there is one more peak at lower temperature, which is not obvious in the DTG curve of carbonated Portland cement paste. This indicates the decomposition of  $\mu$ -CaCO<sub>3</sub> (vaterite). Both aragonite and vaterite are metastable calcium

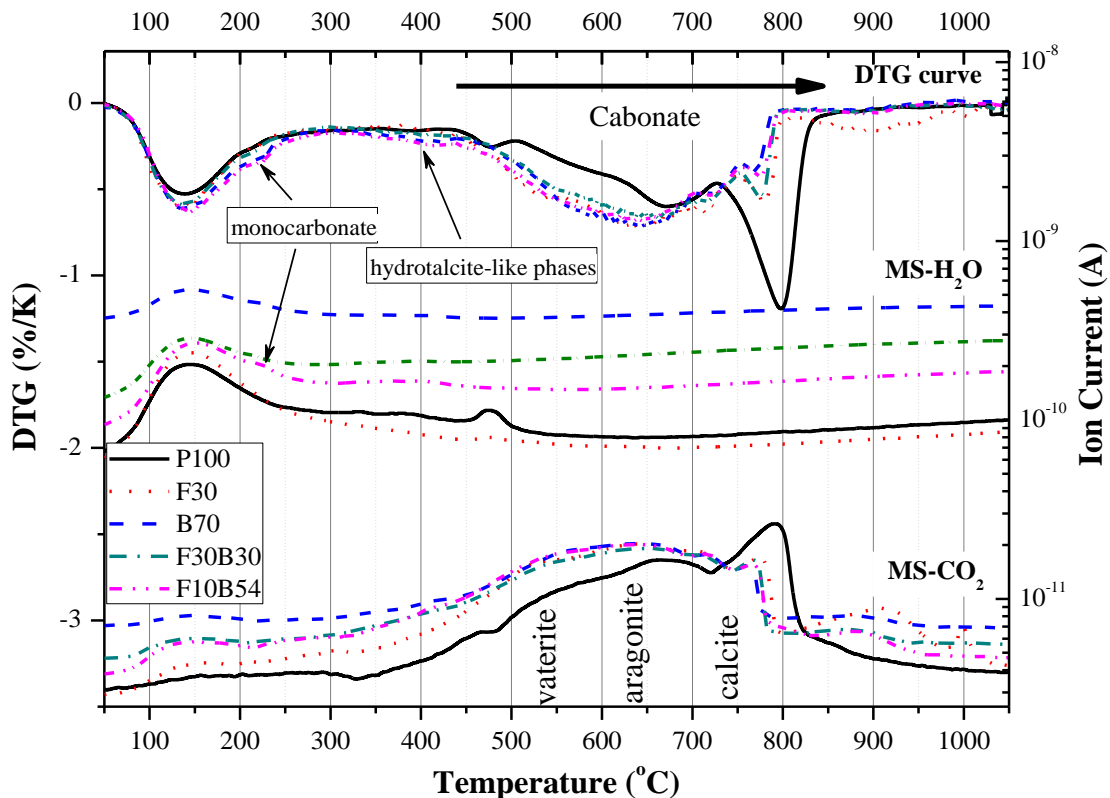


Figure 4-7 TGA-MS coupled test results of cement paste w/b = 0.5: Hydrated for 1 year, then carbonated for 84 days, the outermost surface part with a depth of 2mm.

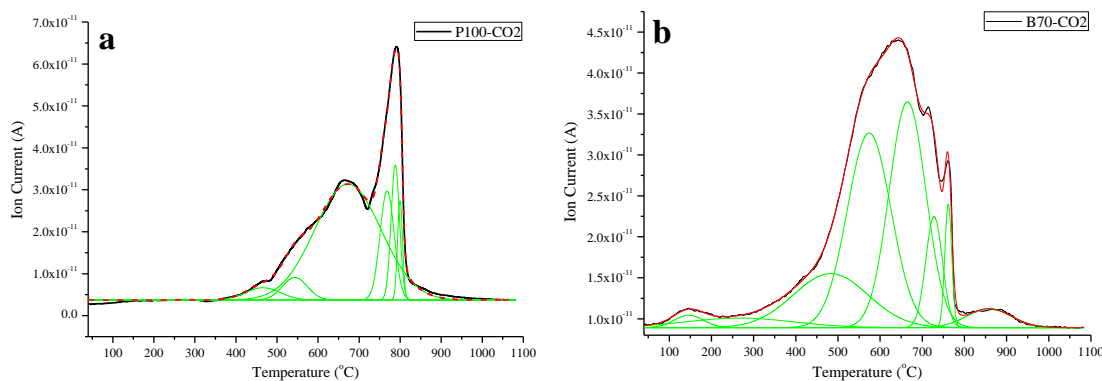


Figure 4-8 Gaussian multi-peaks fitting of CO<sub>2</sub> mass spectrum of cement paste (red line – original mass spectroscopy, green line – fitted peaks): (a) Portland cement paste P100; (b) BFS cement paste B70

Table 4-3 Decomposition temperature of different types of calcium carbonate

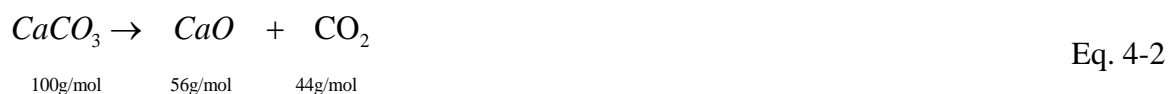
	Amorphous CaCO <sub>3</sub>	Vaterite	Aragonite	Calcite
P100	424 - 508 °C	510 - 621 °C	592 - 754 °C	750 - 806 °C
F30	327 - 500 °C	493 - 597 °C	601 - 754 °C	760 - 784 °C
B70	394 - 572 °C	522 - 626 °C	622 - 748 °C	754 - 770 °C
F30B30	352 - 504 °C	505 - 619 °C	615 - 755 °C	757 - 775 °C
F10B54	358 - 452 °C	494 - 635 °C	619 - 750 °C	756 - 776 °C

carbonate formation, and are particularly formed from carbonation of C-S-H gel with low Ca/Si ratio [7]. MS patterns also confirm that CO<sub>2</sub> starts to be released in the same temperature range as CH. This is due to the presence of amorphous forms of calcium carbonate [8-13].

In order to figure out the proportion of CO<sub>2</sub> released from different polymorphs of calcium carbonate, the CO<sub>2</sub> mass spectrum of P100 and B70 are picked from Figure 4-7 and fitted by multi-Gaussian peaks. The fitting schematic diagram is shown in Figure 4-8. Each peak is a sign of CO<sub>2</sub> emission during the heating. For example, the peak in the range of 750-800°C is indicating CO<sub>2</sub>, which is produced from decomposition of calcite. The decomposition temperatures of different CaCO<sub>3</sub> polymorphs are determined from the fitting results, which are listed in Table 4-3.

From the relevant TG curve, the relative weight loss [%] due to decomposition can be determined as follows:

According to the decomposition reaction of CaCO<sub>3</sub>, viz.:



the CaCO<sub>3</sub> concentration in cement paste can be calculated by Eq. 4-3.

$$[C\bar{C}] \text{ (mol / L)} = \frac{w_c^{c\bar{c}}}{100} \times \frac{\rho_{bulk}}{M_c} \quad \text{Eq. 4-3}$$

where,  $w_c^{c\bar{c}}$  (%) is the relative weight loss [%] of  $\text{CO}_2$  from the decomposition of  $\text{CaCO}_3$  in the TG curve.  $M_c$  is the molar weight (g/mol) of  $\text{CO}_2$ .  $\rho_{bulk}$  is the bulk density (g/L), measured by MIP.

The concentration of calcium carbonate on the surface of cement pastes specimen were calculated and compared in *Figure 4-9*. The surface part has a depth of 2 mm and the cement pastes were carbonated for 28 and 84 days. The values of the bulk density  $\rho_{bulk}$  are listed in *Table 4-4*.

Comparing with Portland cement paste, the concentration of calcite in blended cement pastes decreases, but the concentration of vaterite increases with increasing SCMs content. The reason is that calcite is mainly formed from carbonation of portlandite, which is abundant in OPC paste; other metastable carbonates are mainly produced from the carbonation of C-S-H. The concentrations of aragonite and calcite are almost unchanged when the carbonation

*Table 4-4 Bulk density  $\rho_{bulk}$  of carbonated cement paste (g/ml)*

Carbonation time	Mixture composition				
	P100	F30	B70	F30B30	F10B54
28 days	1787	1752	1662	1573	1613
84 days	1828	1695	1701	1610	1669

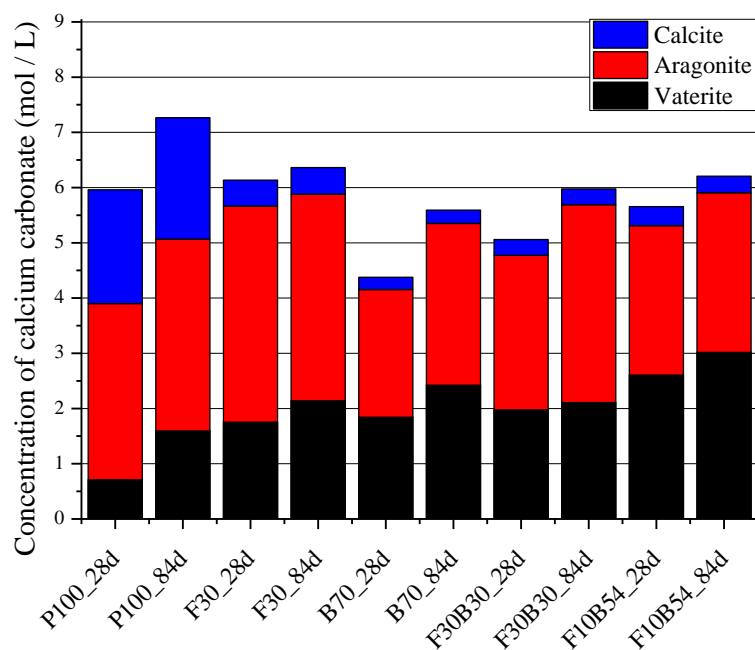


*Figure 4-9 Concentration of different forms of carbonates in cement paste: hydrated for 1 year, then carbonated for 28 days and 84 days*

time increased from 28 days to 84 days, but the concentration of vaterite increases with carbonation time. Compared with F30, more vaterite but less aragonite and calcite were formed in B70 due to carbonation.

#### 4.2.3 Profiles of the portlandite and the amounts of $\text{CaCO}_3$

In order to obtain the phase concentration profile in cement paste after carbonation, the TGA test was performed for slices taken from different depths along the carbonation front of the paste sample. Based on the weight loss from TG curve, the portlandite concentration was calculated with Eq. 3-5 (see section 3.2.3).

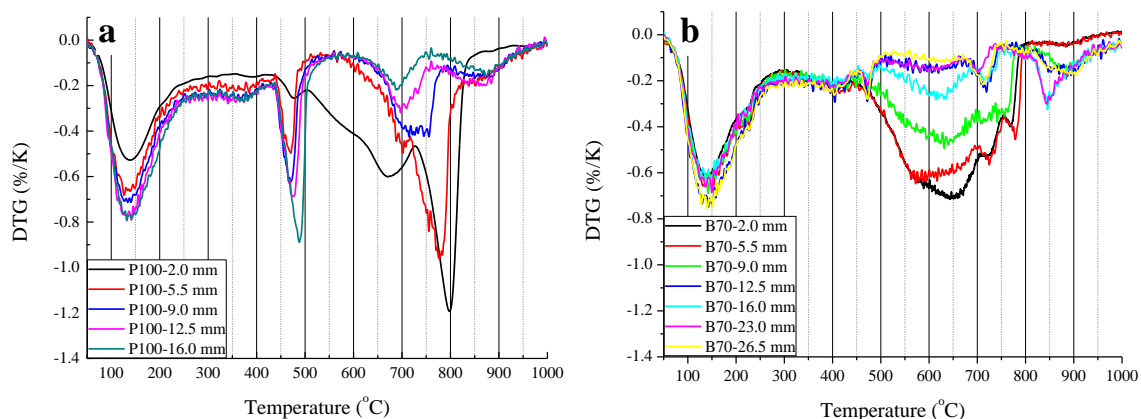


Figure 4-10 DTG curves of slices cut from: (a) Portlandite cement paste; (b) BFS-blended cement paste; '2 mm' is the depth of the slice away from the exposed surface.

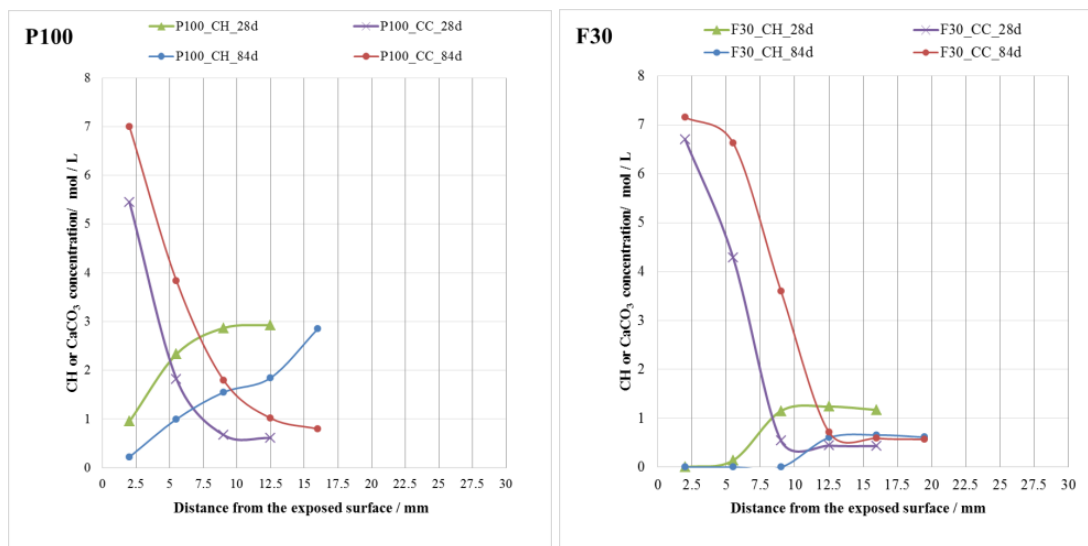


Figure 4-11 Profiles of the amounts of portlandite and  $\text{CaCO}_3$  in cement paste after carbonation, calculated based on the TGA data (Hydrated for 1 year, carbonated for 28 and 84 days, carbonation condition: 70% RH and 3%  $\text{CO}_2$  concentration).

To be continued on next page →

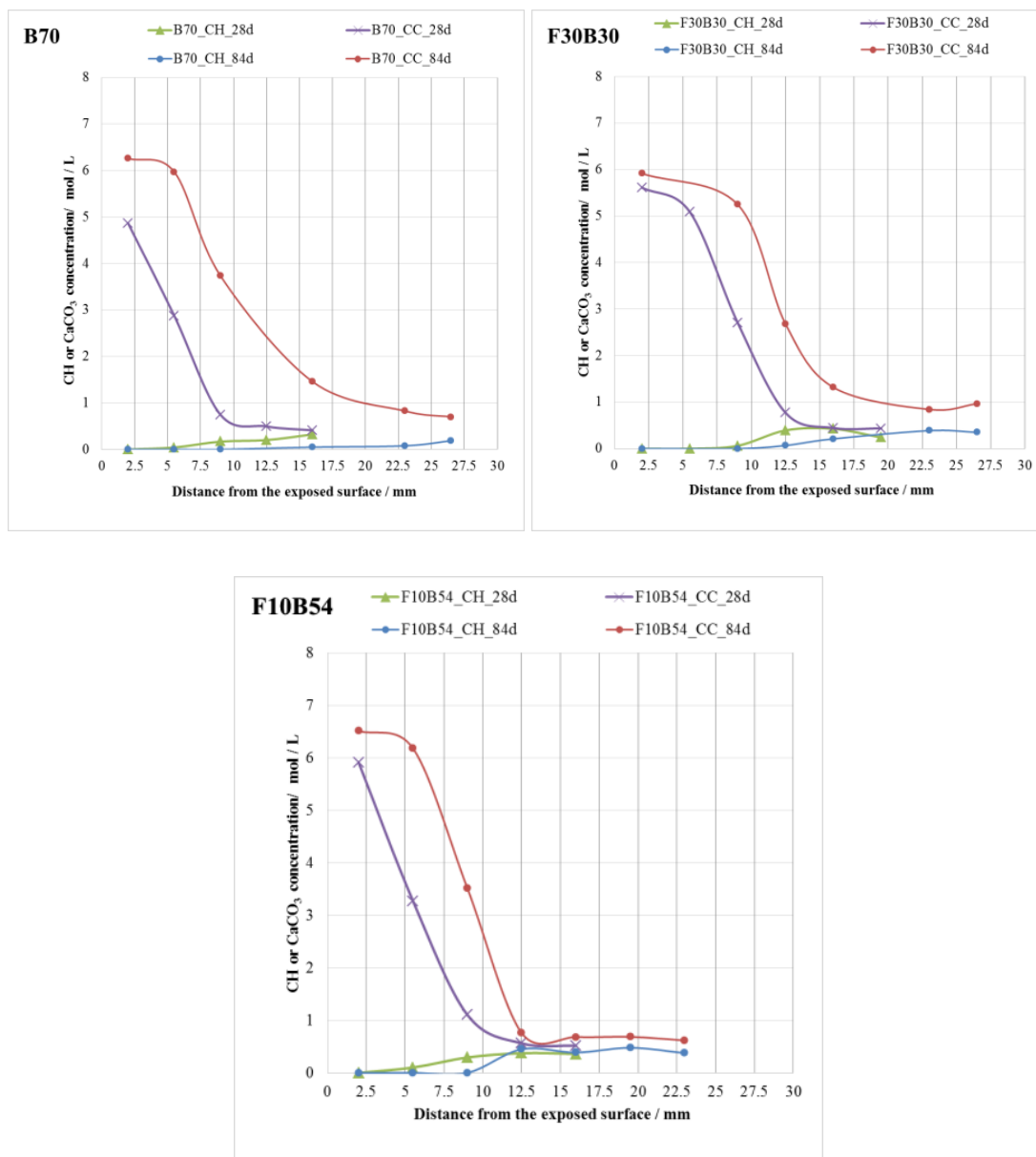


Figure 4-11 - continued - Profiles of the amounts of portlandite and  $\text{CaCO}_3$  in cement paste after carbonation, calculated based on the TGA data (Hydrated for 1 year, carbonated for 28 and 84 days, carbonation condition: 70% RH and 3%  $\text{CO}_2$  concentration).

As discussed in section 4.2.2, calcite is not the only type of  $\text{CaCO}_3$  formed during carbonation. Due to these polymorphs, the temperature of the decomposition of  $\text{CaCO}_3$  can vary from 400-825°C. Moreover, this temperature range is different from mixture to mixture and also different from slice to slice in the same sample, as shown in *Figure 4-10*. Considering both the MS of  $\text{CO}_2$  and DTG curve, the weight loss related to the decomposition of  $\text{CaCO}_3$  was determined for each slice and used in the calculation. The concentration of  $\text{CaCO}_3$  in the blended cement paste was calculated by using Eq. 4-3. The concentrations of portlandite and  $\text{CaCO}_3$  are calculated for each slice. Concentration profiles were drawn and compared in *Figure 4-11*.



Table 4-5 Comparison of carbonation depth tested by two methods (carbonation for 84 days)

	Carbonation depth for different mixtures [mm]				
	P100	F30	B70	F30B30	F10B54
TG	12.5	12.5	22.5	22.5	12.5
phenolphthalein spray	3.45	7.27	8.35	11.9	8.25

Using SCMs in cement paste results in a lower portlandite content, due to the dilution effect and pozzolanic reaction. Normally, the higher amount of SCMs, the lower amount of portlandite. During carbonation, the portlandite is converted into  $\text{CaCO}_3$ . Therefore, from the exposed surface to the non-carbonated part, the amount of portlandite increases from zero, together with the decrease of the amount of  $\text{CaCO}_3$ . Profiles of portlandite and  $\text{CaCO}_3$  move towards inside of the cement paste specimen with increasing carbonation time. These phase profiles can be used to determine the carbonation front or depth. The depth where the amounts of both portlandite and  $\text{CaCO}_3$  become almost unchanged is considered as the carbonation depth. The carbonation depth inferred from phase profile is compared with that measured by phenolphthalein test. The results are presented in Table 4-5. The carbonation depth determined by TGA-MS turns out to be much higher than that determined by the phenolphthalein.

It should be noticed that the increasing amount of  $\text{CaCO}_3$  with the extension of carbonation time is mainly contributed by the carbonation of C-S-H in cement paste blended with a high amount of SCMs, such as B70, F10B54 and F30B30.

#### 4.2.4 Effects of carbonation on the capillary pore-MIP test

MIP test was performed on each slice sawed from the sample of blended cement paste which was carbonated for 84 days. Pore volume and pore size distribution of each slice were calculated from MIP test results. Final results of each mixture are summarized and illustrated in Figure 4-12 and Figure 4-13, in which the test results of binary and ternary mixtures are compared, respectively. It should be noted that the labels of the curve (i.e. 2 mm) are indicating the cutting position of the slice referring to the exposure surface. It means slice cut at 2 mm represents the totally carbonated area and slice cut at the maximum distance (i.e. 12.5 mm for P100) indicates the totally non-carbonated zone. The meaning of label is applicable to all the mixtures studied.

In general, the pore size distribution differential curve of cement paste measured by MIP shows two ‘critical peak’ [14]. The first critical peak is in the range of 0.1 to 1  $\mu\text{m}$ , corresponding to large capillary pores. The second critical peak is in the range of 0.01 to 0.1  $\mu\text{m}$ , corresponding to medium capillary pores, according to the classification of pores in cement paste by Minders and Young [15]. Although there are different definitions of capillary pores [16], the classification and definition by Minders and Young will be used here.

For Portland cement paste the pore volume in the range of 0.01-0.1  $\mu\text{m}$  decreases during the carbonation (Figure 4-12a), together with the intensity of the second critical peak which

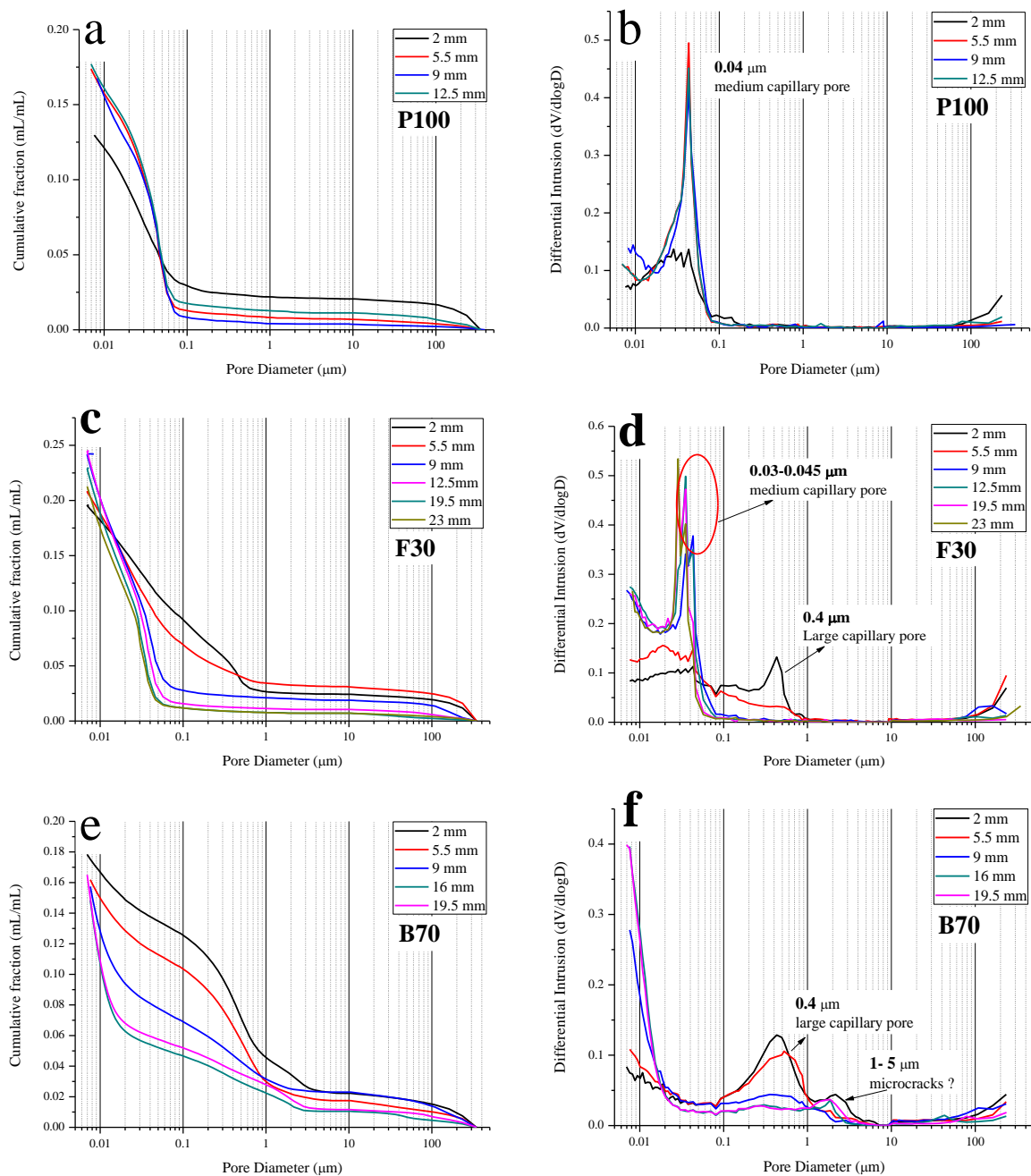


Figure 4-12 Capillary pore volume and pore size distribution of Portland cement and binary mixture: a & b: Portland cement paste (P100); c & d: blended with 30% of FA (F30); e & f: blended with 70% of BFS (B70) (Hydrated for 1 year, then carbonated for 84 days)

corresponds to the medium capillary pore (Figure 4-12b). The pore volume in the range of 0.1-1.0  $\mu\text{m}$  is approximately the same before and after carbonation. For the non-carbonated part of Portland cement paste, there is no first critical peak in the pore size distribution differential curve (Figure 4-12b).

Normally, carbonation in Portland cement is only responsible for a clogging of the microstructure between 0.01-0.1  $\mu\text{m}$ , corresponding to medium capillary pores attributed to the voids among outer C-S-H clusters, which is confirmed by many studies [17-21]. It is due

to the formation of  $\overline{CC}$  in the pores, with a greater molar volume than the initial component CH. However, carbonation is also capable of producing larger capillary pores of 100-200 nm size if the w/c ratio or CO<sub>2</sub> concentration is high enough (i.e. w/c > 0.5 or CO<sub>2</sub> > 50%), claimed by some other researchers [12, 22-24]. Chaussadent et al [25] studied the relationship between w/c ratio and size of hydrates in cement pastes. Hydrates with a bigger size can be developed well in capillary pores of concretes with high w/c ratio. During carbonation, the CH dissolves, leaving bigger pores while carbonation products preferably develop in the smaller pores. This is one of the possible reasons for the appearance of pores around 100-200 nm and at the same time filling of smaller 30 nm pores. Whatever the effects of carbonation on the capillary pore structure, i.e. making it coarser or finer, the total porosity of Portland cement paste (mortar, or concrete) decreases due to carbonation (natural or accelerated).

For cement paste blended with 30% of FA, the pore volume in the range of 0.02-1  $\mu\text{m}$ , which includes the medium and large capillary pores, increases during carbonation (*Figure 4-12c*). In the relevant differential curve (*Figure 4-12d*), there is a shift of the second critical peak, corresponding to the medium capillary pore, towards greater pore radii during carbonation, together with a decline in intensity. Moreover, the “first peak” indicating large capillary pores appears after carbonation (2.0 mm - line in *Figure 4-12d*). And the intensity of the “first peak” increases with the carbonation time (from 5.5 mm - line to 2.0 mm - line). The totally carbonated cement paste blended with 30% of FA (2 mm part) exhibits a coarser capillary pore structure.

For cement paste blended with 70% of BFS, the pore volume in the range of 0.01-1  $\mu\text{m}$  increases dramatically (*Figure 4-12e*). There are no critical peaks observed in the differential curve of BFS blended cement paste (19.5 mm - line in *Figure 4-12f*). However, the peak corresponding to large capillary pores appears during the carbonation (2.0 & 5.5 mm - line in *Figure 4-12f*). A new critical peak in the range of 1-5  $\mu\text{m}$  arises after carbonation. It means a much coarser capillary pore structure of B70, compared to the FA blends, was formed.

*Figure 4-13* shows the pore volume and pore size distribution curves of the ternary mixtures. F10B54 and F30B30. For both ternary mixtures, the pore volume in the range of 0.01-1  $\mu\text{m}$  increases dramatically (*Figure 4-13a* and *Figure 4-13c*). There are no critical peaks observed in the differential curve of both mixtures (16.0 mm - line in *Figure 4-13b* and 26.5 mm - line in *Figure 4-13d*). However, the peak corresponding to large capillary pores appears during the carbonation (2.0 mm - line in *Figure 4-13b* and *Figure 4-13d*). Like in the curves of B70, a new critical peak in the range of 1-5  $\mu\text{m}$  arises after carbonation. The MIP test results of B70, F10B54 and F30B30 are showing the similar changes of the microstructure of these three mixtures during the carbonation.

The total porosity and effective capillary porosity calculated from MIP test data are shown in *Figure 4-14*. Apparently, both the total and effective capillary porosity of Portland cement (P100) and FA blended cement paste (F30) paste decrease due to carbonation. For cement paste blended with a relatively high amount of BFS, like B70 and F10B54, the total porosity and effective capillary porosity increase. This is consistent with the results tested on the concrete under natural carbonation up to 20 years [26]. For mixture F30B30 the effective capillary porosity increases, although the total porosity decreases due to carbonation.

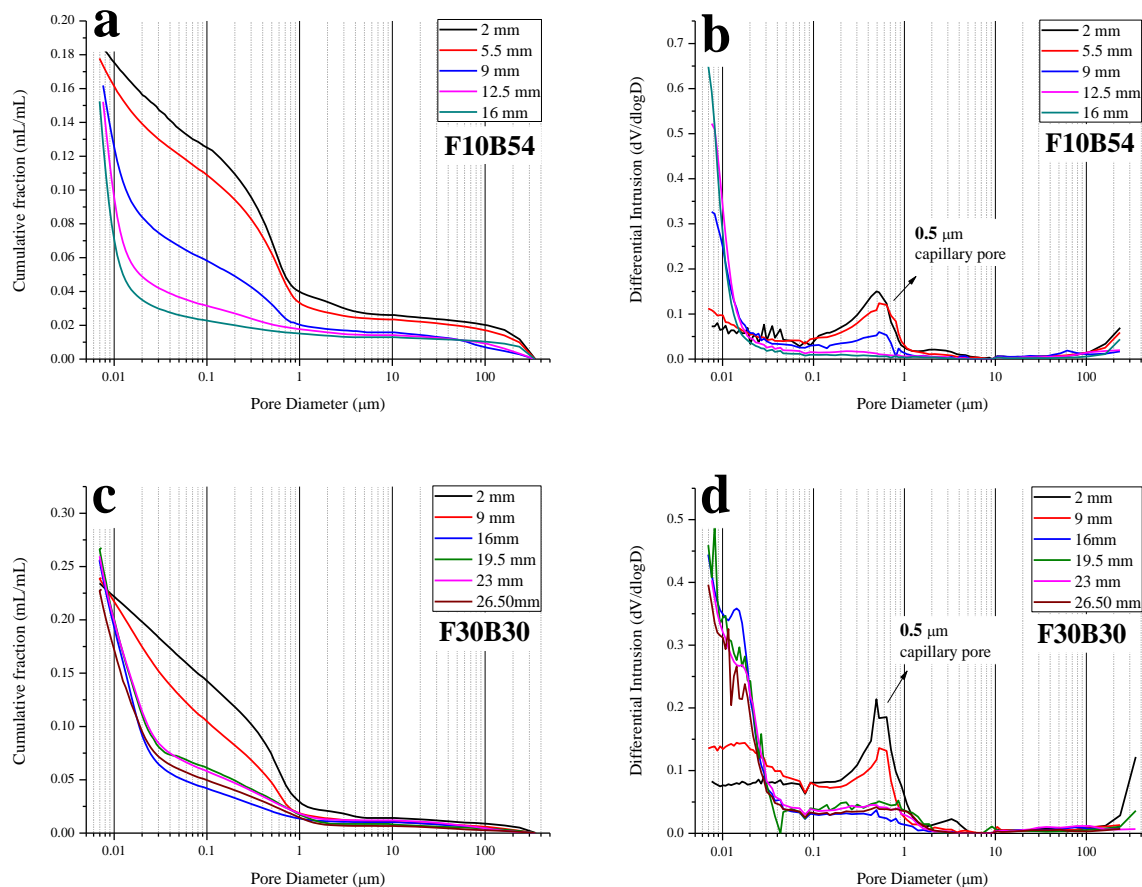


Figure 4-13 Capillary pore volume and pore size distribution for ternary mixture: cement paste blended with 10% of FA and 54% of BFS (F10B54), blended with 30% of FA and 30% of BFS (F30B30) (hydrated for 1 year, then carbonated for 84 days).

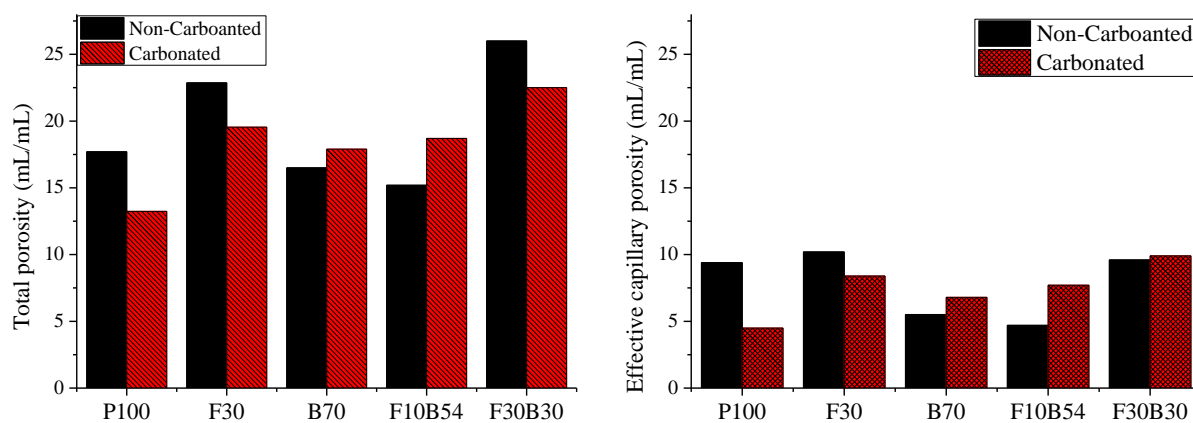


Figure 4-14 Total porosity and effective capillary porosity of blended cement paste before and after carbonation (hydrated for 1 year, then carbonated for 84 days).

It is known that carbonation of portlandite causes a decrease of porosity. However, the porosity of B70 and F10B54 increases after the carbonation (see Figure 4-14). The only

reason is that the carbonation of CSH may increase the porosity, especially the carbonation of C-S-H with low Ca/Si ratio produced from the pozzolanic reactions.

Calculated on the basis of the TGA test results, the amounts of calcium carbonate contributed by the carbonation of portlandite, or C-S-H were calculated separately and shown in *Figure 4-15a*. Apparently, the proportion of  $\text{CaCO}_3$  contributed by the carbonation of C-S-H is significantly higher than that produced from the carbonation of portlandite, in the three mixtures blended with a high amount of SCMs such as B70, F10B54 and F30B30. This is consistent with the results found in the fly ash blended paste, when the replacement level of FA increases higher than 40% [24].

As discussed, the carbonation of C-S-H contributes an increase of the porosity of carbonated cement paste. And most of the  $\text{CaCO}_3$  are formed from the carbonation of C-S-H in blended cement paste. Therefore, the carbonation of C-S-H has a dominant effect on the evolution of total porosity in cement paste blended with the high amount of SCMs. Combined with the total porosity tested by MIP, the relationship between the changes of total porosity in cement paste and the amount of C-S-H being carbonated are drawn and illustrated in *Figure 4-15b*.

Total porosities of B70 and F10B54 increase with the increasing amount of C-S-H involving in the carbonation; total porosities of P100 and F30 decrease with the increase of the amount of carbonated C-S-H. The total porosity of F30B30 increases after carbonation, however the increment in porosity decreases when the amount of C-S-H being carbonated increases.

It should be noticed that the property of low Ca C-S-H in FA blended cement paste is quite different from that produced from the pozzolanic reaction of BFS. They may have the opposite effects on the porosity development in blended cement paste, see in *Figure 4-15b*. The combined effect from the carbonation of these two types of C-S-H results in the particular development of the total porosity in F30B30.

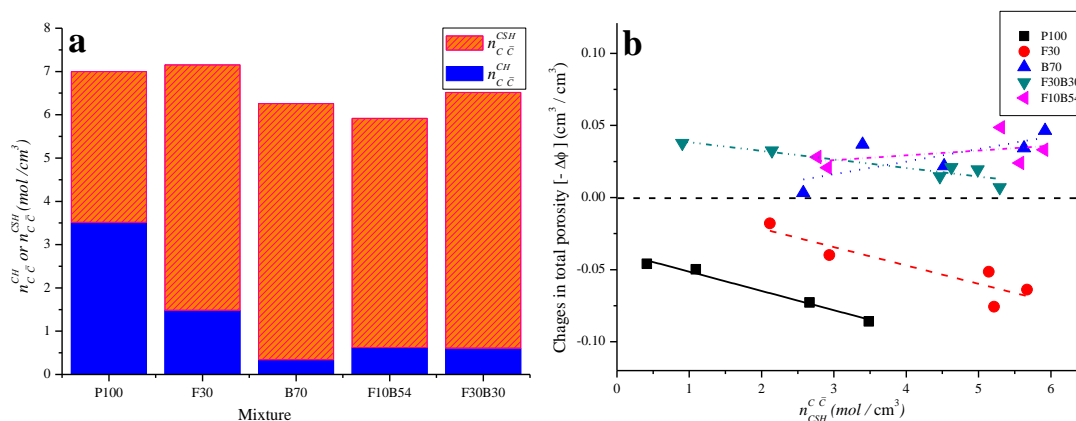


*Figure 4-15 (a) The amounts of  $\text{CaCO}_3$  contributed by the carbonation of CH ( $n_{C \bar{C}}^{CH}$ ) or CSH ( $n_{C \bar{C}}^{CSH}$ ) (Hydrated for 1 year, then carbonated for 84 days; the surface part). (b) Relationship between the changes of total porosity in cement paste and the amount of C-S-H being carbonated during carbonation*

#### 4.2.5 Effects of carbonation on the gel pore-Nitrogen adsorption test

By using BJH method, the pore size distributions in the range of 2-37 nm are calculated from the nitrogen adsorption test results performed on the blended cement paste carbonated for 84 days, as shown in *Figure 4-16*.

As mentioned in Jennings' work, the low density (LD) C-S-H structure has a significant internal porosity accessible to nitrogen, while the high density (HD) C-S-H has not. Therefore, the pores in this scale range are mainly gel pores of LD C-S-H. These pores can be divided into two categories: small gel pores (SGP = 1-3 nm) and large gel pores (LGP = 3-12 nm), according to the Globule C-S-H model [27], schematically shown in *Figure 4-17a*. The definition of gel pores and the schematic will be used for the discussion of the gel pore structure development during carbonation, measured by nitrogen adsorption test and shown in *Figure 3-16*.

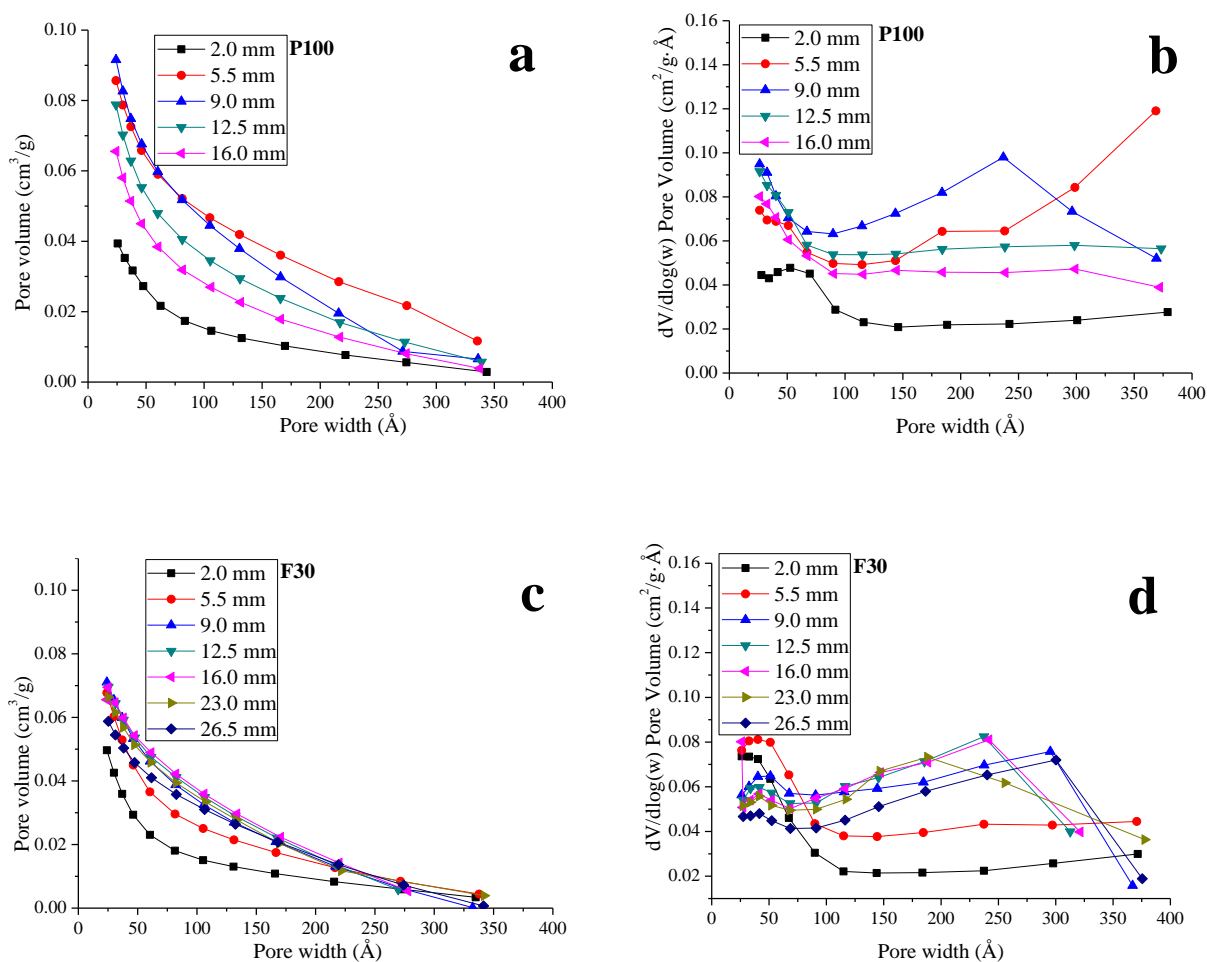


*Figure 4-16 Evolution of accumulative pore volume and pore size distributions (2-37 nm) of different mixture. (Hydrated for 1 year, then carbonated for 84 days).*

*To be continued on next page →*

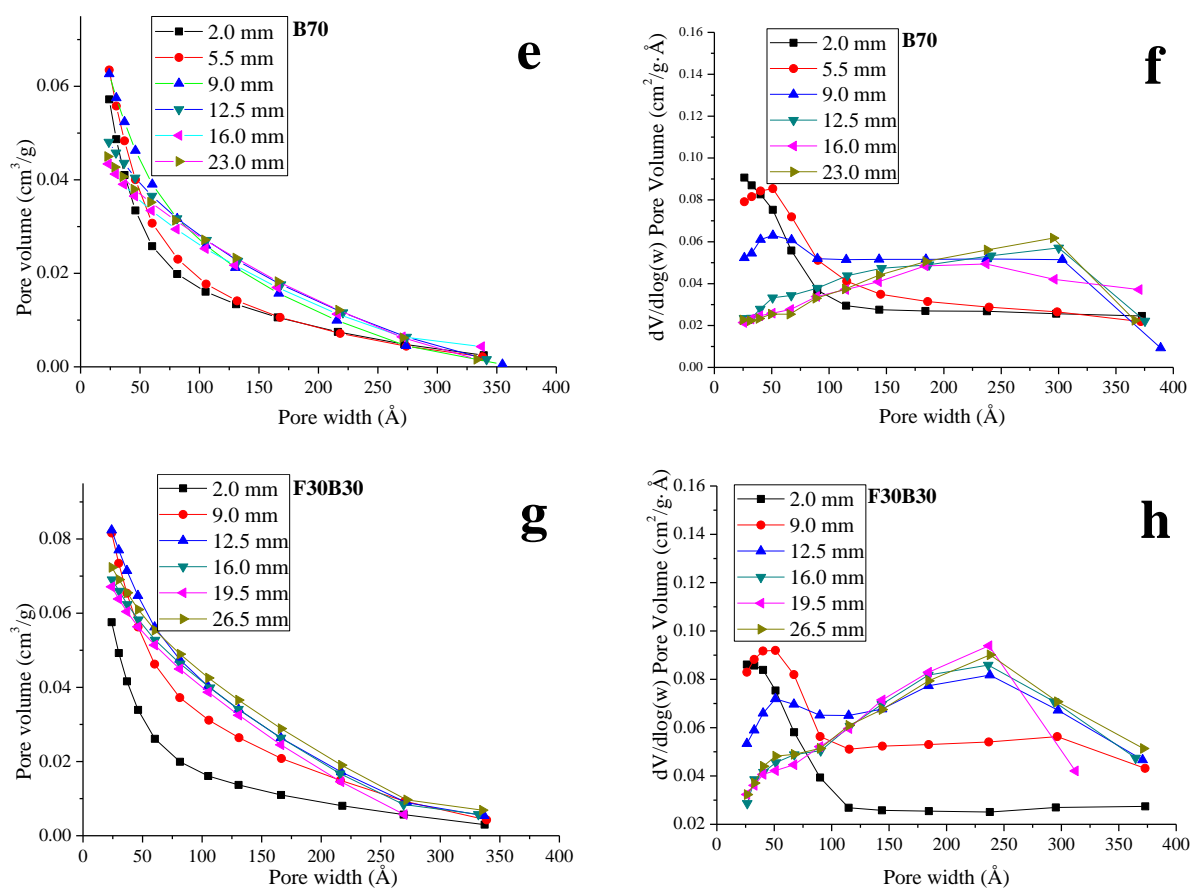


Figure 4-16 - continued - Evolution of accumulative pore volume and pore size distributions (2-37 nm) of different mixture. (Hydrated for 1 year, then carbonated for 84 days).

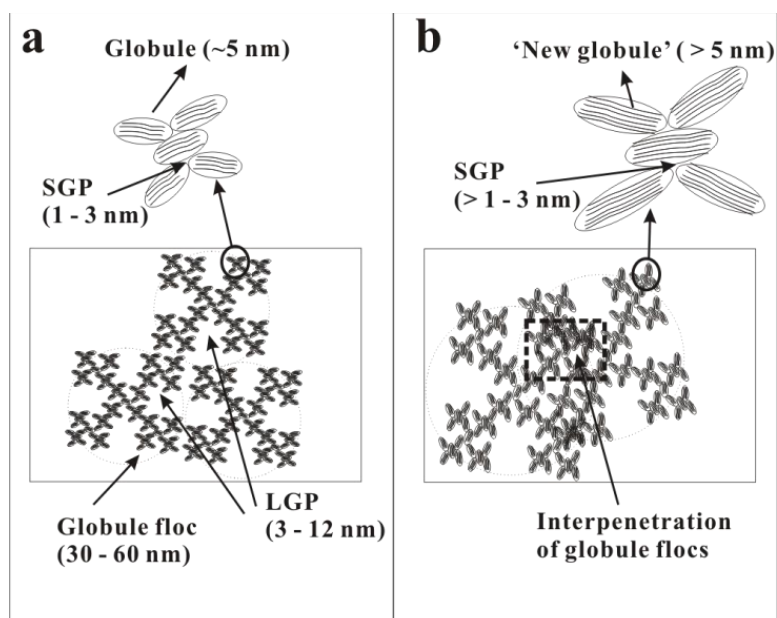


Figure 4-17 Evolution of the gel pore structure of C-S-H based on the Colloid model: a before carbonation; b after carbonation (re-draw after Jennings [32]).

For all mixtures shown in *Figure 4-16*, the pore volume in the range from 2-37 nm (see *Figure 4-16a, c, e, g*) decrease due to carbonation. In the relevant differential curves (*Figure 4-16b, d, f, h*), the critical peak at around 5 nm appears, whereas the critical peak at around 22-30 nm disappears. The first peak at around 5 nm indicates the small gel pores, and the second peak at around 22-30 nm corresponds to the pore space between the globule flocs, which have a size between 30-60 nm. During carbonation, the polymerization of silicate chains will develop in three dimensions after the decalcification. The globule will grow (*Figure 4-17b*). Therefore, the pore space between globules (size of the SGP) increases and contributes to the appearance of the first critical peak. The polymerization of silicate chains can also happen between the adjacent chains from different globule flocs, which will cause the interpenetration of globule flocs. The interpenetration of globule flocs will reduce the size of LGP (see *Figure 4-17a*) and the volume of the pore space between globule flocs (see *Figure 4-17b*). This is the other reason why the critical peak around 5 nm appears, whereas the critical peak at about 22-30 nm disappears due to carbonation, together with the decrease of the gel pore volume. These changes can be observed more obvious in the mixtures with a high replacement level of SCMs, like B70 and F30B30 (see *Figure 4-16f* and *Figure 4-16h*).

### 4.3 Conclusions

In this chapter, the reaction products of the carbonation process and microstructural changes in cement paste blended with SCMs have been studied by using TGA, MIP and nitrogen adsorption. The evolution of capillary pores and the gel pore structure caused by the carbonation of C-S-H are discussed. The main conclusions are the following.

- ◆ The carbonation rate increases dramatically in cement paste blended with SCMs, especially in FA blended paste. The carbonation rate in ternary mixture F10B54 is quite close to that in B70, F30B30, has the highest carbonation rate. All the samples discussed were hydrated for 365 days before the carbonation test.
- ◆ There are four types of calcium carbonate formed in the cement paste during carbonation, i.e. amorphous calcium carbonate, vaterite, aragonite and calcite. Calcite is the most observed form of calcium carbonate in carbonated Portland cement paste. Vaterite and aragonite are the main carbonates in blended cement paste, such as F30 and B70. With increasing carbonation time (from 28 days to 84 days), the proportion of vaterite in blended cement paste increases dramatically.
- ◆ The carbonation of C-S-H increases the pore volume of pores with radius close to the small gel pores but causes the reduction of the volume of gel pores.
- ◆ Both the total porosity and effective capillary porosity increases in cement paste B70 and F10B54 due to carbonation. The effective capillary porosity of mixture F30B30 increases, whereas the total porosity decreases. Carbonation leads to a coarser capillary pore structure in blended cement paste with a high amount of SCMs.
- ◆ Calculation results based on the TGA data show that the dominant amounts of  $\text{CaCO}_3$  are produced from the carbonation of C-S-H in these three pastes blended with high amounts



of SCMs (B70, F10B54 and F30B30). It indicates that the carbonation of C-S-H will increase the porosity of blended cement paste after carbonation.

## 4.4 References

- [1] L.G. Joyner, E.P. Barrett, R. Skold, The determination of pore volume and area distributions in porous substances. II. Comparison between nitrogen isotherm and mercury porosimeter methods, *Journal of the American Chemical Society*, 73 (1951) 3155-3158.
- [2] V.G. Papadakis, Effect of supplementary cementing materials on concrete resistance against carbonation and chloride ingress, *Cement Concrete Res*, 30 (2000) 291-299.
- [3] C.D. Atiş, Accelerated carbonation and testing of concrete made with fly ash, *Constr Build Mater*, 17 (2003) 147-152.
- [4] K. Sisomphon, L. Franke, Carbonation rates of concretes containing high volume of pozzolanic materials, *Cement Concrete Res*, 37 (2007) 1647-1653.
- [5] P. Grattan-Bellew, Microstructural investigation of deteriorated Portland cement concretes, *Constr Build Mater*, 10 (1996) 3-16.
- [6] A. Noumowé, Effet des hautes températures (20 °C–600 °C) sur le béton, Institut National des Sciences Appliquées, 1995.
- [7] L. Black, C. Breen, J. Yarwood, K. Garbev, P. Stemmermann, B. Gasharova, Structural features of C–S–H (I) and its carbonation in air—a Raman spectroscopic study. Part II: carbonated phases, *J Am Ceram Soc*, 90 (2007) 908-917.
- [8] E. Stepkowska, M.A. Aviles, J.M. Blanes, J.L. Perez-Rodriguez, Gradual transformation of Ca(OH)<sub>2</sub> into CaCO<sub>3</sub> on cement hydration, *J Therm Anal Calorim*, 87 (2007) 189-198.
- [9] E.T. Stepkowska, J.M. Blanes, F. Franco, C. Real, J.L. Pérez-Rodríguez, Phase transformation on heating of an aged cement paste, *Thermochim Acta*, 420 (2004) 79-87.
- [10] L. Brečević, A.E. Nielsen, Solubility of amorphous calcium carbonate, *Journal of Crystal Growth*, 98 (1989) 504-510.
- [11] W. Cole, B. Kroone, Carbon dioxide in hydrated Portland cement, *ACI Journal Proceedings*, ACI, 1960.
- [12] D.R. Moorehead, Cementation by the carbonation of hydrated lime, *Cement Concrete Res*, 16 (1986) 700-708.
- [13] T. Baird, A.G. Cairns-Smith, D.S. Snell, Morphology and CO<sub>2</sub> uptake in tobermorite gel, *Journal of Colloid And Interface Science*, 50 (1975) 387-391.
- [14] R.A. Cook, K.C. Hover, Mercury porosimetry of hardened cement pastes, *Cement Concrete Res*, 29 (1999) 933-943.
- [15] S. Mindess, J.F. Young, D. Darwin, *Concrete*, Prentice Hall, Englewood Cliffs, NJ, (1981) 481.
- [16] H.M. Jennings, Colloid model of C–S–H and implications to the problem of creep and shrinkage, *Mater Struct*, 37 (2004) 59-70.
- [17] S.E. Pihlajavaara, Some results of the effect of carbonation on the porosity and pore size distribution of cement paste, *Matériaux et Constructions*, 1 (1968) 521-527.
- [18] H.-W. Song, S.-J. Kwon, Permeability characteristics of carbonated concrete considering capillary pore structure, *Cement Concrete Res*, 37 (2007) 909-915.
- [19] M. Auroy, S. Poyet, P. Le Bescop, J.-M. Torrenti, T. Charpentier, M. Moskura, X. Bourbon, Impact of carbonation on unsaturated water transport properties of cement-based materials, *Cement Concrete Res*, 74 (2015) 44-58.
- [20] F. Puertas, M. Palacios, T. Vázquez, Carbonation process of alkali-activated slag mortars, *J Mater Sci*, 41 (2006) 3071-3082.
- [21] H. Matsusato, K. Ogawa, M. Funato, T. Sato, Studies on the carbonation of hydrated cement and its effect on microstructure and strength, 9th International Congress on the Chemistry of Cement, 1992, pp. 363-369.
- [22] R.M. Lawrence, T.J. Mays, S.P. Rigby, P. Walker, D. D'Ayala, Effects of carbonation on the pore structure of non-hydraulic lime mortars, *Cement Concrete Res*, 37 (2007) 1059-1069.
- [23] G. Villain, M. Thiery, Impact of carbonation on microstructure and transport properties of concrete, *Proceedings of*, 2005, pp. 1-8.
- [24] M. Thiéry, P. Faure, A. Morandea, G. Platret, J.-F. Bouteloup, P. Dangla, V. Baroghel-Bouny, Effect of carbonation on the microstructure and moisture properties of cement-based materials, XII DBMC (12th International Conference on Building Materials and Components, 2011, pp. 1-8.

- [25] T. Chaussadent, V. Baroghel-Bouny, H. Hornain, N. Rafäi, A. Ammouche, Effect of water-cement ratio of cement pastes on microstructural characteristics related to carbonation process, *ACI Special Publication*, 192 (2000).
- [26] G.G. Litvan, A. Meyer, Carbonation of granulated blast furnace slag cement concrete during twenty years of field exposure, *ACI SP*, 91 (1986) 1445-1462.
- [27] H.M. Jennings, Refinements to colloid model of CSH in cement: CM-II, *Cement Concrete Res*, 38 (2008) 275-289.

## Synthesis of C-S-H gel with Different Ca/Si Ratio

### 5.1 Introduction

In Chapter 4, the study was focused on transformation of calcium-bearing phases and evolution of the microstructure due to carbonation of cement paste blended with SCMs. That study included the carbonation of, among other phases, C-S-H gel. However, the C-S-H phases in the blended cement pastes consist of different types of C-S-H, confirmed by the EDAX mapping test results in Chapter 3. The C/S ratio of C-S-H gel produced by cement hydration is ranging from 1.50 to 2.30 in this study. The C/S ratio of C-S-H gel produced from the pozzolanic reaction of FA and BFS are in the range of 1.0 to 1.3 and 1.1 to 1.3 respectively.

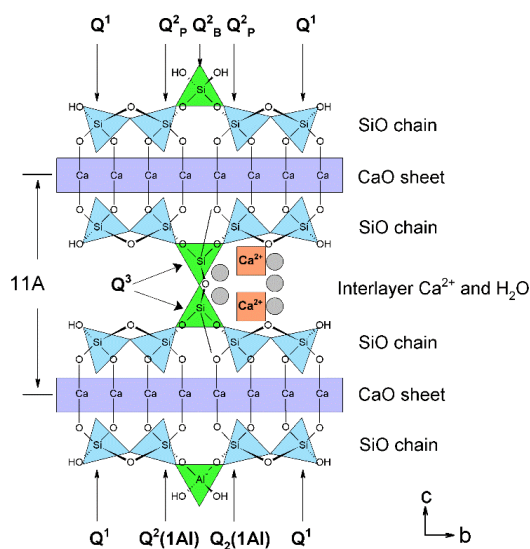


Figure 5-1 Schematic of the layer crystal structure for the 11 Å tobermorite

The C-S-H phases (including all the C-S-H gels mentioned above and natural phases) share a similar layer structure, which can be inferred from the refined structure of 11Å tobermorite ( $\text{Ca}_{4.5}\text{Si}_6\text{O}_{16}(\text{OH})\cdot 5\text{H}_2\text{O}$ ) [1]. This refined structure consists of three parts:  $\text{CaO}_2$  sheets, a ‘dreierkette’ SiO-chain and the interlayer, as illustrated in *Figure 5-1*. The C/S ratio of C-S-H in the (blended) concrete is normally higher than 0.83. From tobermorites to C-S-H phases with higher C/S ratio found in concrete, the main change in the structure is that the chains of  $\text{SiO}_4$  tetrahedra are broken by removing of the bridge tetrahedra ( $Q_B^2$ ). Meanwhile, extra  $\text{Ca}^{2+}$  is incorporated into the interlayer and even into the bridge site with further increasing of C/S ratio. The variations in the molecular structure of C-S-H with different C/S ratio can be reflected in the spectrum of XRD or  $^{29}\text{Si}$  NMR.

In the layer structure of C-S-H, Ca is expected to appear in three different chemical sites: the  $\text{CaO}_2$  sheet layer, a bridging site, and the interlayer, shown in *Figure 5-1*. The proportions of Ca located in different sites vary among C-S-H with different Ca/Si ratio. Therefore, it is expected that C-S-H gels with different C/S ratio perform differently when exposed to carbonation. In the carbonation studies in previous chapters, only the average effect of the mixed C-S-H phases on carbonation was considered. In this chapter the focus will be on carbonation of only C-S-H gels with different C/S ratios.

In Chapter 5, C-S-H with C/S ratios ranging from 0.66 to 2.0 are synthesized in a water solution, covering the C/S ratios of C-S-H identified in blended cement paste in Chapter 3. The synthetic products are measured by different methods, including XRD, TGA-MS,  $^{29}\text{Si}$  NMR and FTIR, to characterize the synthesized C-S-H gels. C-S-H phases with the targeted C/S ratios will be used for accelerated carbonation tests as discussed in Chapter 6.

## 5.2 Materials and experiments

### 5.2.1 Materials

Raw materials used to synthesize C-S-H gels in the  $\text{CO}_2$ -free water are CaO and fumed silica. CaO is freshly prepared by calcination of  $\text{CaCO}_3$  under  $1000^\circ\text{C}$  for at least 4 hours before synthesis. Fumed silica with the surface area of 175-225  $\text{m}^2/\text{g}$  is produced by Sigma-Aldrich.  $\text{CO}_2$ -free deionized water is obtained by boiling the deionized water in the narrow mouth Erlenmeyer flask sealed with a rubber cork. The rubber cork is pierced by a glass tube used for cooling water and discharging  $\text{CO}_2$ . The glass tube is connected to the stem of a glass funnel, of which the other side is soaked in saturated  $\text{Ca}(\text{OH})_2$  water to absorb the  $\text{CO}_2$ .

### 5.2.2 Synthesis of C-S-H gels

C-S-H gels were prepared by using stoichiometric amounts of CaO and fumed silica, aiming at C/S ratios ranging between 0.66 and 2.0. The mix design for preparing C-S-H with different C/S ratios is described in *Table 5-1*. Solid agents were mixed with  $\text{CO}_2$ -free water with a water/solid ratio of 50:1.

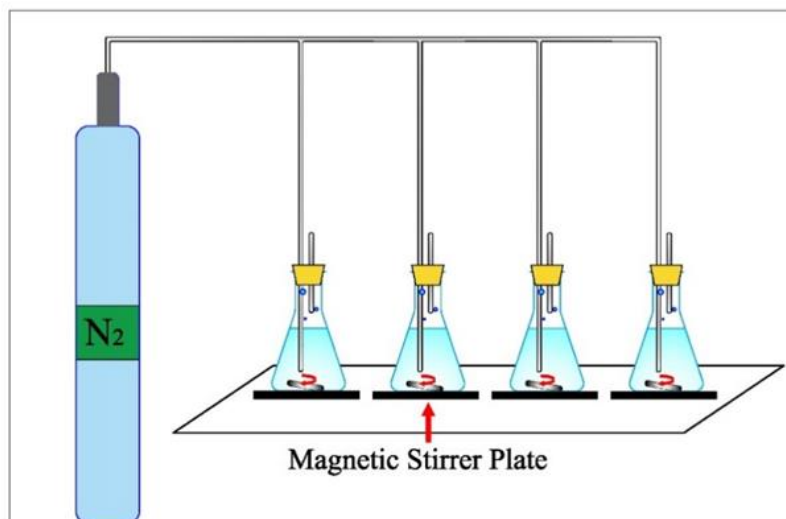


Figure 5-2 Schematic diagram of the set-up for synthesis of C-S-H gels

The solution was stirred with a magnetic stirrer at around 20°C. The whole synthesis procedure was under the N<sub>2</sub> protection to minimize carbonation. After 1-, 2- or 4-weeks reaction, the slurry with products were extracted, washed and filtered through a Balston No. 45 paper. Then they were moved as quick as possible into a vacuum drying chamber. After drying under 35°C for 24 h, the above-mentioned samples were transferred and stored in the desiccator with the relative humidity of 30%, regulated by a standard saturated CaCl<sub>2</sub>·6H<sub>2</sub>O solution. The set-up of the synthesis device is shown in Figure 5-2.

Table 5-1 Mass fraction of raw materials for preparing different C-S-H and C-A-S-H

Sample NO.	Ca/Si ratio	Al/Si ratio	CaO (g)	SiO <sub>2</sub> (g)	H <sub>2</sub> O (g)
1	0.66	--	3.0	4.9	400
2	0.86	--	3.6	4.4	400
3	1.18	--	4.2	3.8	400
4	1.40	--	4.5	3.5	400
5	1.70	--	4.9	3.1	400
6	2.00	--	5.2	2.8	400

### 5.2.3 Characteristic methods of C-S-H gels

Characteristic methods used for identification of synthetic products were X-ray diffraction (XRD), Thermogravimetric analysis (TGA), Fourier transform infrared spectroscopy (FTIR) and Nuclear magnetic resonance (NMR). For executing the above-mentioned tests, well-dried synthetic products were ground into powders with an average particle size less than 75 μm. The details of these methods were described as follows.

**XRD** -- XRD test were performed by a Philips PW 1830 diffractometer (see *Figure 5-3* ) using CuK $\alpha$  radiation ( $\lambda = 0.154056$  nm, 40 mA, 40 KV). The scanning rate was set as a step size of  $0.03^\circ$ , 3 s per step. The scanning covers the 2-Theta range between  $5^\circ$  and  $70^\circ$ . The test results are analyzed with the software X'Pert HighScore<sup>®</sup> version 1.0b.

**TGA-MS** -- Thermogravimetric analysis (TGA) was also carried out with the Netzsch STA 449 F3 Jupiter<sup>®</sup> instrument, coupled with a mass spectrometer (MS) Netzsch QMS 403 C Quadrupole<sup>®</sup> (see *Figure 3-4*) under a dry argon atmosphere. More technical details of this test method together with the requirements for sample, are described in section 3.2.3 of Chapter 3.

**FTIR** -- Fourier transform infrared spectroscopy (FTIR), coupled with attenuated total reflectance (ATR) technique, enables examination of samples in the solid or liquid state without

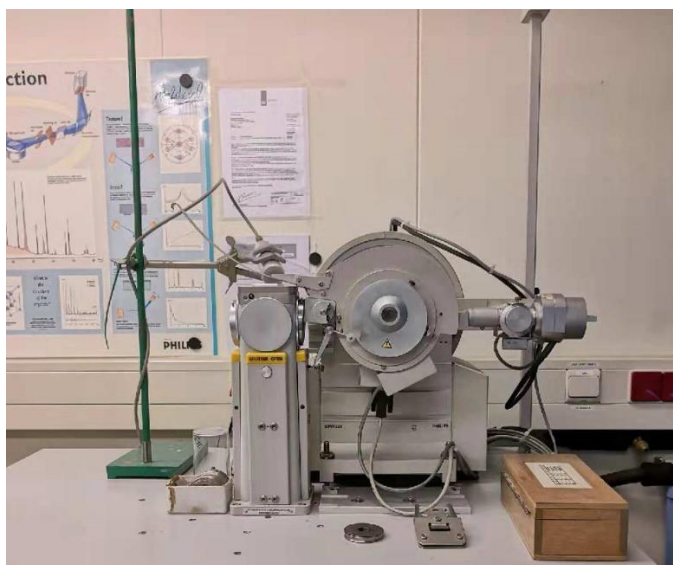


*Figure 5-3 Philips PW 1830 diffractometer used for X-ray diffraction test*



*Figure 5-4 TM 100 Optical ATR-FTIR spectrometer*

further preparation. In this research, the FTIR spectra were collected over the wavelength range from 4000 to 400  $\text{cm}^{-1}$  at a resolution of 4  $\text{cm}^{-1}$  using TM 100 Optical ATR-FTIR spectrometer, shown in *Figure 5-4*. The well-grinded samples were spread on the testing plate (ATR crystal) and pressed to obtain good contact.

**NMR** -- Solid state  $^{29}\text{Si}$  single pulse magic angle spinning (MAS) NMR spectra were acquired using a BrukerMSL-400 spectrometer (magnetic field 9.8 T; operating frequencies of 79.5 MHz for  $^{29}\text{Si}$ ). C-S-H samples were ground and packed into the zirconia rotor sealed at either end with Teflon end plugs, and spun at 6 kHz in a Varian 7 mm wide-body probe. The spectra were acquired using a pulse recycle delay of 5 s, a pulse width of 4.97  $\mu\text{s}$ , and an acquisition time of 20 ms; 2002 scans were collected for each sample.  $^{29}\text{Si}$  chemical shifts are given relative to tetrakis (trimethylsilyl) silane (TMMSS) at -9.8 ppm, with kaolinite as an external standard at -91.2 ppm.

Quantitative information of the fractions of silicate tetrahedra with different connectivity was obtained by deconvolution of the single pulse spectra measured by  $^{29}\text{Si}$ NMR. The tetrahedra unit  $Q^1$ ,  $Q^2$  and  $Q^3$  are described in *Figure 5-1*.  $Q^4$  indicates the silicate tetrahedron is directly connected to adjacent four tetrahedra. The spectra were fitted to Gaussian/Lorentzian mixed function using the open-source software package dmfit2015.

## 5.3 Experimental results and discussions

### 5.3.1 Effects of synthesis time on the formation of C-S-H gels

Firstly, the effects of synthesis time on the final products, i.e. the synthesized C-S-H, were studied. The products synthesized for different weeks were examined by XRD and X-ray fluorescence (XRF) to figure out the appropriate duration for the synthesis of C-S-H with different target C/S ratio.

#### 5.3.1.1 XRD test results of C-S-H gels synthesized for different weeks

The XRD test results of products synthesized for 1-, 2- and 4-week are compared in *Figure 5-5* to *Figure 5-8*. In *Figure 5-5*, four main peaks with a d-spacing ( $\text{\AA}$ ) value of 3.04 ( $29.27^\circ$  in  $2\theta$ ), 2.79 ( $32.16^\circ$  in  $2\theta$ ), 1.82 ( $50.05^\circ$  in  $2\theta$ ), 1.66 ( $55.39^\circ$  in  $2\theta$ ) respectively can be found in the XRD spectra of products synthesized for only 1 week. These four peaks are the characteristic peaks of C-S-H(I) [2], which is one of the C-S-H phases found in Portland cement concrete. Moreover, nearly no changes can be observed in the XRD spectra when the synthesis time are increased from 1 week to 2 or 4 weeks. No traces of any reflection indicating unreacted CaO,  $\text{Ca}(\text{OH})_2$  and  $\text{CaCO}_3$  polymorphs were visible in the diffraction patterns, regardless of synthesis time. Therefore, the main solid phase in the synthetic products is C-S-H(I) and the C-S-H gel can be formed in one week.

From *Figure 5-6* to *Figure 5-8*, the same conclusion as mentioned above can be drawn for the synthesis of C-S- H gels with designed C/S ratios of 0.86, 1.18 and 1.40. That is C-S-H can be produced with the synthesis time of one week.



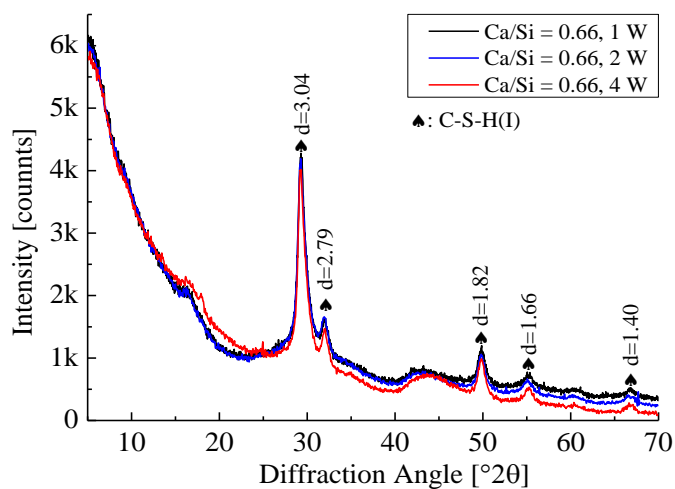


Figure 5-5 XRD test results of products with designed C/S of 0.66, synthesized for 1-, 2- and 4-week

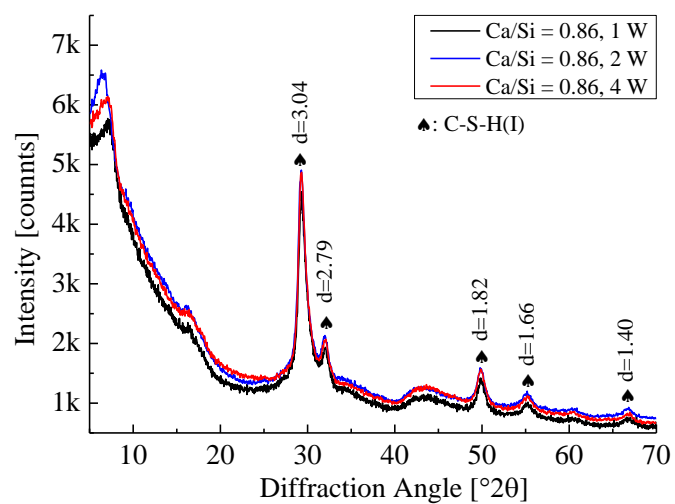


Figure 5-6 XRD test results of products with designed C/S of 0.86, synthesized for 1-, 2- and 4-week

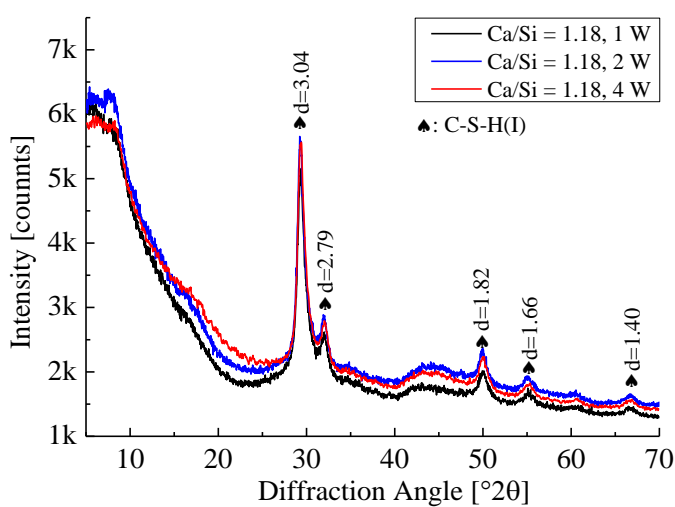


Figure 5-7 XRD test results of products with designed C/S of 1.18, synthesized for 1-, 2- and 4-week

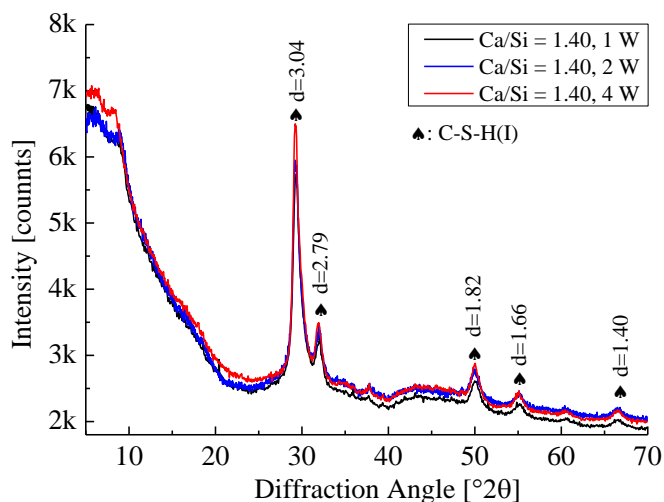


Figure 5-8 XRD test results of products with designed C/S of 1.40, synthesized for 1-, 2- and 4-week

### 5.3.1.2 XRF test results of C-S-H gels synthesized for different weeks

According to the XRD results discussed in section 5.3.1.1, the main solid phase found in the synthetic products is C-S-H(I), regardless of synthesis time and initial C/S ratio. Therefore, the C/S ratio of synthesized C-S-H gels can be calculated based on the bulk weight percentage of CaO and SiO<sub>2</sub>, measured by XRF. The calculated C/S ratio of C-S-H gels synthesized for different time, are described, and compared with the designed C/S ratio of the related mixture in Figure 5-9.

Apparently, for all designed mixtures, the C/S ratio of synthetic C-S-H gels are decreasing with synthesis time and getting closer to the designed C/S ratio. The appropriate synthesis time is 4 weeks in this study. In the following sections, the test results of C-S-H gels synthesized for 4 weeks will be presented and discussed.

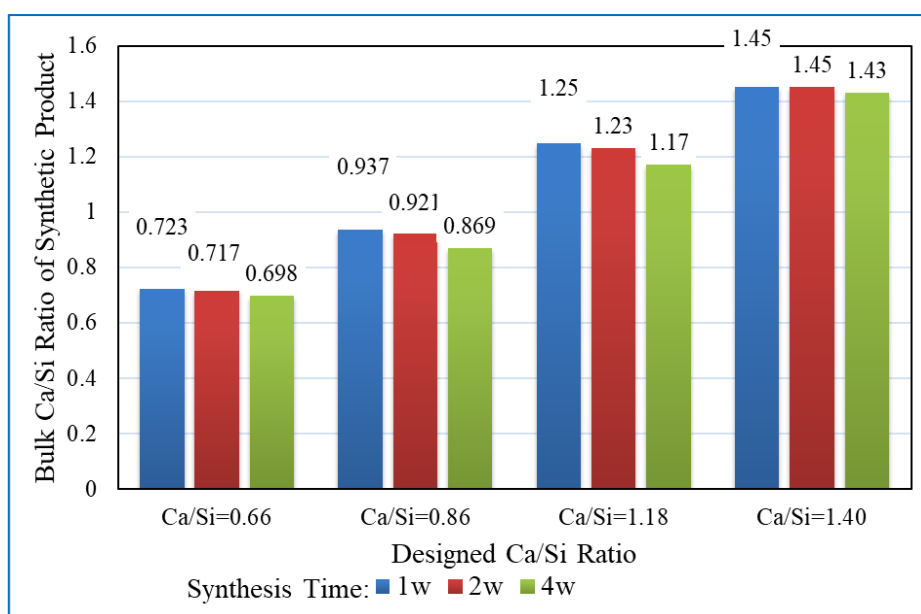


Figure 5-9 Bulk C/S ratio of synthetic products synthesized for 1, 2 and 4 weeks

### 5.3.2 Identification of C-S-H gels with different C/S ratio

As discussed in section 5.3.1.1, the C-S-H gels synthesized from CaO and fumed silica in the solution are showing the same identical peaks as C-S-H(I) [2] in XRD spectrum. However, those data are not sufficient to confirm that products are exactly the C-S-H with the target C/S ratio. Some other identities of C-S-H(I), which can be revealed in the XRD, TGA,  $^{29}\text{Si}$  NMR and FTIR spectrum, will be described and discussed in the flowing sections, to further identify the C-S-H gels with different C/S ratio.

#### 5.3.2.1 XRD test results of C-S-H gels with different C/S ratio

The XRD test results of C-S-H gels synthesized for 4 weeks are compared in *Figure 5-10*. In the XRD patterns of C-S-H gels with a lower targeted C/S (0.66, 0.86, 1.18 and 1.40), only diffraction peaks related to the C-S-H(I) phase can be found.

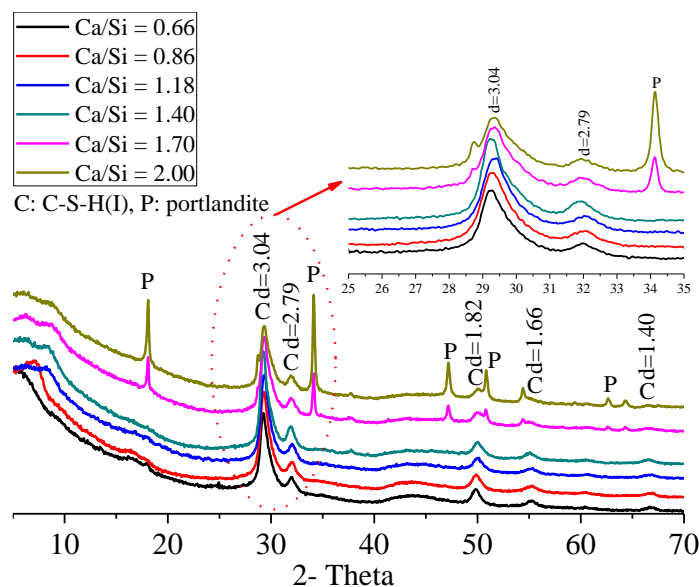


Figure 5-10 XRD test results of C-S-H with different C/S (0.66 - 2.0), synthesis for 4 weeks.

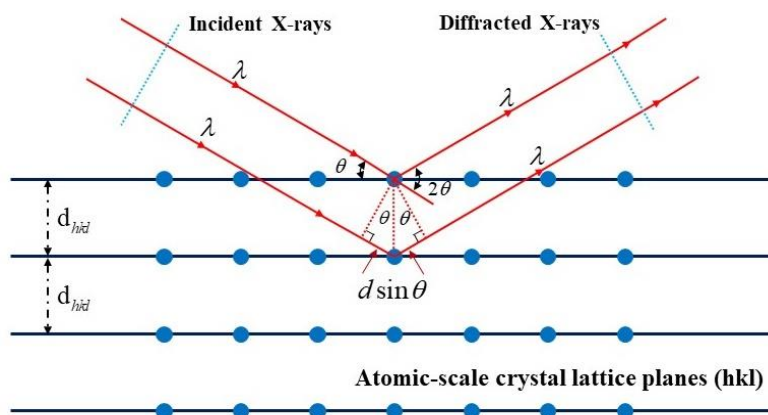
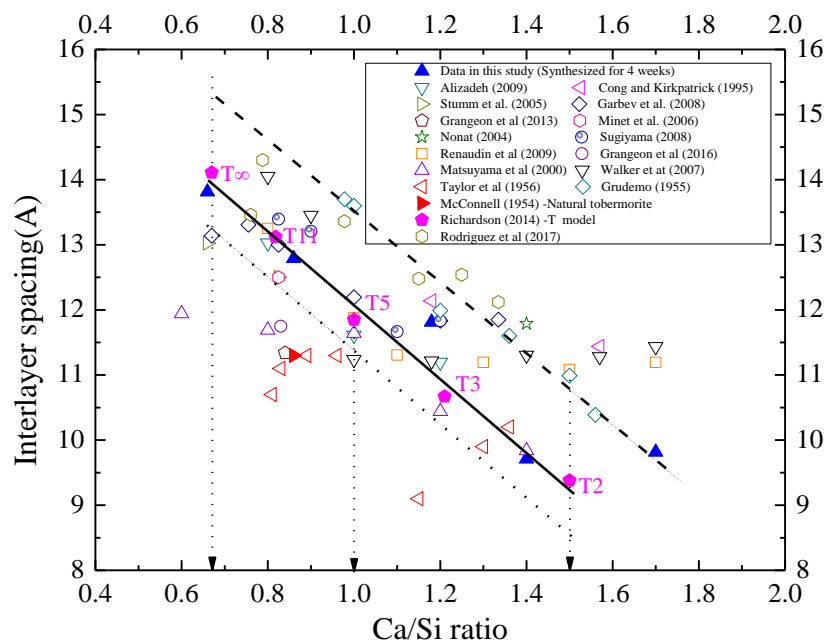


Figure 5-11 Schematic of constructive interference of X-rays, Bragg's law (modified based on the image in Wikipedia)

However, in the XRD patterns of C-S-H gels with a higher designed C/S ratio, i.e. 1.70 and 2.00, some other peaks with diffraction angles of 34.11, 47.14 and 50.80 can be observed (see *Figure 5-10*). These peaks are related to portlandite ( $\text{Ca}(\text{OH})_2$ ). Apparently, it is better to limit the C/S ratio of the raw mixture to 1.40 (value found in this study) when trying to get C-S-H only. Otherwise, portlandite will appear in the products. This is in agreement with results of other researchers [3-5].

The X-ray diffraction pattern is obtained by measuring the intensity of scattered X-rays as a function of scattering angle. Very strong peaks in the diffraction pattern are obtained at the points where the scattering angle and the interplane spacing  $d$  satisfy Bragg's law[6], described in *Figure 5-11*. The X-axis of the X-ray diffraction pattern can either be expressed as  $2\theta$  or interplane spacing  $d$ .

In the XRD spectrum of C-S-H(I), an identical peak at around  $7.4^\circ$  ( $2\theta$ ,  $\text{Cu K}\alpha$ ) appears. This peak is formed when the incident X-rays is approaching and scattered by the atomics in the crystal lattice plane 001(Miller index) of C-S-H (perpendicular to  $c$  direction as indicated in *Figure 5-1*). which is exactly the Ca-O sheet layer in the C-S-H crystal structure. Therefore, the spacing of the (001) lattice plane of C-S-H is equal to the interlayer spacing or the basal spacing, which has the most conspicuous variations, both in position and in intensity. It shifts towards lower  $d$  spacing (higher diffraction angles) with increasing C/S ratio, which can be considered as a characteristic to distinguish C-S-H gels with different C/S ratio. The interlayer spacings were extracted from the XRD patterns of C-S-H gels with different C/S ratio, synthesized for 4 weeks. They were plotted versus C/S ratio in *Figure 5-12* and compared



*Figure 5-12* Variation in the interlayer spacing in C-S-H versus C/S. Published XRD patterns having too weak peaks or showing the presence of portlandite were excluded. Magenta full-filled pentagons indicate the model structure developed by Richardson[7].

with the data published by other researchers [3, 7-20]. It should be noted that only the data of C-S-H synthesized in water solution at room temperature were collected and compared in this figure.

Apparently, the interlayer spacing of synthesized C-S-H gels decided from the XRD patterns, shifts to lower  $d$  spacing when increasing the C/S ratio from 0.66 to 1.50. It indicates that C-S-H gels with different C/S ratio were synthesized successfully. Although there is quite a large scatter in the data, attributed to the degree of drying or the intermixing of C-S-H with the second phase (e.g.  $\text{Ca}(\text{OH})_2$ ), most of the data lie in between the two dashed trend lines. The upper (dashed) and the lower (dotted) trend-line represent the samples which were dried lightly and strongly respectively, before the XRD test. The distance of the two parallel lines is approximately  $2 \text{ \AA}$  and is not affected by the C/S ratio. For the C-S-H gel with a certain C/S ratio, this  $2 \text{ \AA}$  difference is caused by adding or removing one water molecule in the interlayer. Comparing the positions of the data points with other experimental data or hypothetical data in *Figure 5-12*, the C/S ratio of synthesized C-S-H gels satisfy the targeted value.

The data calculated from the XRD patterns of synthesized C-S-H gels lays in between the two parallel trend lines of *Figure 5-12*. The solid line, containing data points notified as  $T_n$ , are the values calculated from the patterns of hypothetical crystal structures of C-S-H proposed by Richardson. The experimental data of this research are scattered around this solid trend line. This means the crystal structure of synthesized C-S-H can be interpreted by the structure model proposed by Richardson, which will be discussed further in the following section 5.3.3.

### 5.3.2.2 TGA test results of C-S-H gels with different C/S ratio

The typical TGA test results of C-S-H with the C/S of 0.86 is shown in *Figure 5-13*, including TG, DTG and DSC curves.

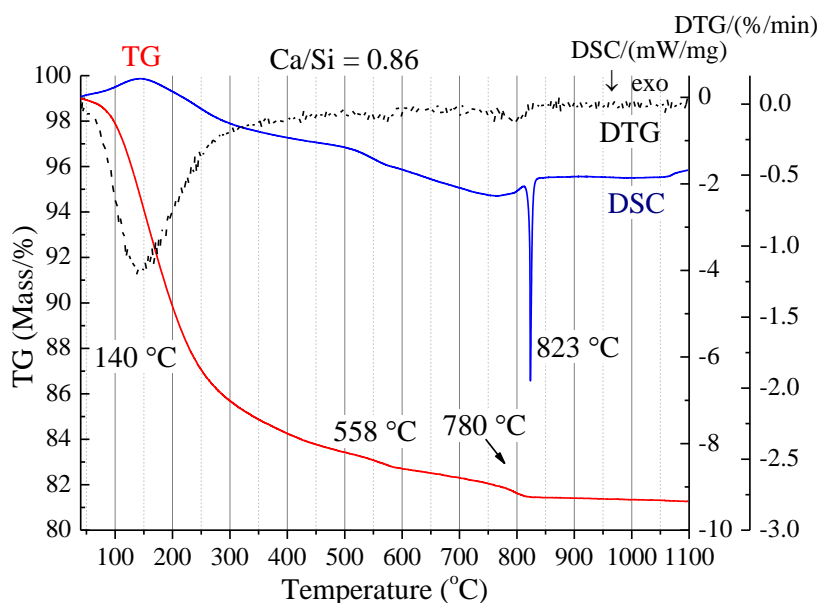


*Figure 5-13* Test results of TGA coupled with gas analysis for C-S-H (C/S = 0.86, synthesized over 4 weeks)

As shown in *Figure 5-13*, there is an endotherm peak in the DSC curve of C-S-H at around 100-200°C and an exothermic peak at around 835-900°C. The latter is related to the transformation of C-S-H into  $\beta$ -wollastonite, which shifts to the higher temperature with increasing C/S ratio [3, 21-25]. This feature is used to identify different C-S-H phases synthesized.

The temperature values of the exothermic peaks are extracted from the DSC curves of the C-S-H gels synthesized over 4 weeks (see *Figure 5-14*). These values are plotted versus the targeted C/S ratio in *Figure 5-15*, and compared with the data from other literatures.

The exotherm peak (at around 835°C) shifts toward the higher temperature when increasing the C/S ratio of C-S-H gel from 0.66 to 1.40 (see *Figure 5-15*). However, this peak will not shift further when the C/S ratio is higher than 1.40. Shifting of the exotherm peaks

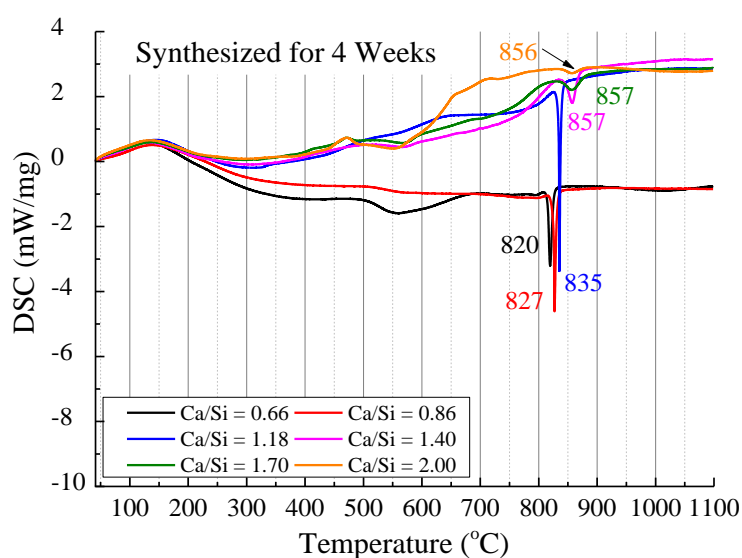


Figure 5-14 DSC curves of C-S-H synthesized over 4 weeks

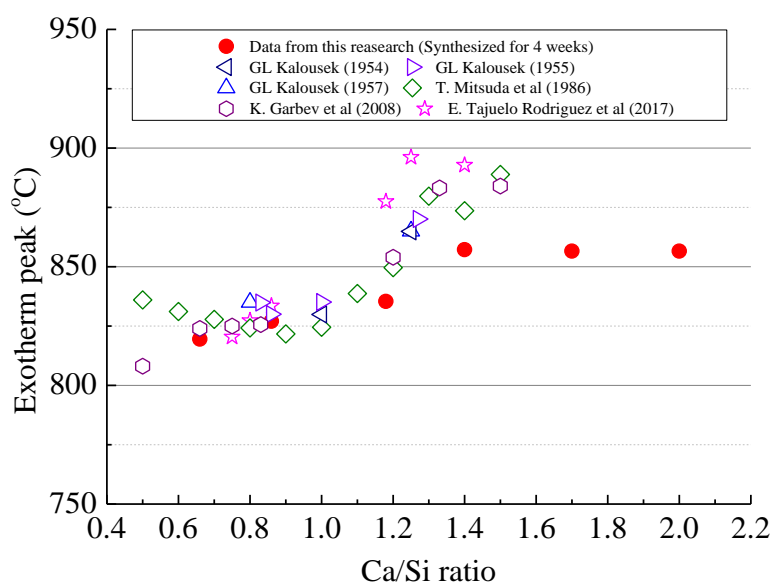


Figure 5-15 Relations between the exotherm peak position and C/S ratios

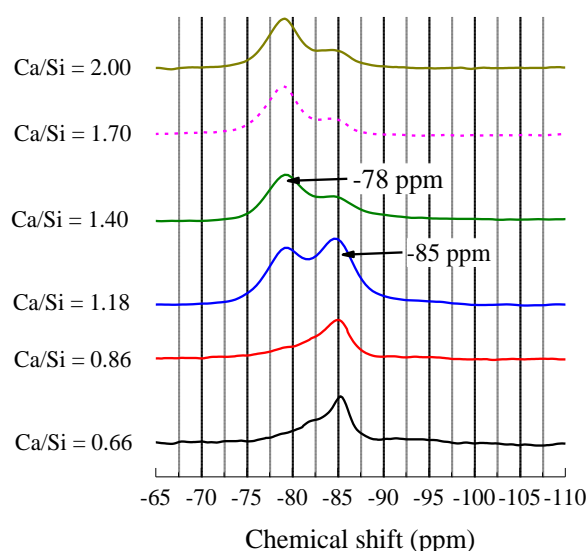


Figure 5-16  $^{29}\text{Si}$  NMR test results of C-S-H with different C/S (0.66 - 2.0), synthesized for 4 weeks.

(at around  $835^\circ\text{C}$ ) of synthetic C-S-H gels proves that the C-S-H gels have different C/S ratios. Comparing the positions of data points tested in this study with the reference data, the final C/S ratio of the synthesized C-S-H gels satisfy the initial designed values.

### 5.3.2.3 $^{29}\text{Si}$ NMR test results of C-S-H gels with different C/S ratio

The  $^{29}\text{Si}$  NMR test results of C-S-H gel synthesized over 4 weeks are described in *Figure 5-16*. The peaks around -78 ppm and -85 ppm indicates the  $\text{Q}^1$  and  $\text{Q}^2$  type of  $\text{SiO}_4$  tetrahedra, respectively [26, 27].

Normally, notation  $\text{Q}^n$  is used in  $^{29}\text{Si}$  NMR spectroscopy to describe different types of  $\text{SiO}_4$  tetrahedra according to the surroundings of the silicon atom. The number  $n$  (0 - 4) denotes the number of  $\text{SiO}_4$  units connected to the silicon atom by “Si-O-Si” chain.

*Figure 5-1*, shown at the very beginning of this chapter, illustrates the pentameric unit, in which a bridging  $\text{SiO}_4$  ( $\text{Q}_B^2$ ) connects two dimers, resulting in two  $\text{SiO}_4$  end-groups ( $\text{Q}^1$ ) and two “paired”  $\text{SiO}_4$  sites ( $\text{Q}_P^2$ ). Normally, the  $\text{Q}_3$  or  $\text{Q}_4$   $\text{SiO}_4$  tetrahedra is absent in the C-S-H phases produced by the hydration of Portland cements.

In *Figure 5-16*, the intensity of the peak indicating  $\text{Q}^1$  increases with the increase of the C/S ratio, whereas the intensity of the peak indicating  $\text{Q}^2$  decreases.

The increase of the C/S ratio in C-S-H based on the tobermorite structure can be caused by: omission of the bridge tetrahedra and incorporation of additional calcium in the interlayer. Removing the bridge tetrahedra will cause the breaking of the silicate chain, the fractions of different bridge tetrahedra and paired tetrahedra will be changed as well according to the layer structure illustrated in *Figure 5-1*. The mean length of the silicate chain and the fractions of different types of silicate tetrahedra have a strong relation with the C/S ratio of the C-S-H. Especially, the mean silicate chain length can be considered as an identical property to distinguish the C-S-H gels with different C/S ratio.

The mean silicate chain length (MCL), fraction of bridging tetrahedra (BT %) and the fraction of paired tetrahedra (PT %) can be calculated with Eq. 5-1 to Eq. 5-3 as follows [28]:

Mean silicate chain length:

$$MCL = \frac{2(Q^1 + Q^2)}{Q^1} \quad \text{Eq. 5-1}$$

Fraction of bridging tetrahedra:

$$BT\% = \frac{Q^2}{3(Q^1 + Q^2)} \quad \text{Eq. 5-2}$$

Fraction of paired tetrahedra:

$$PT\% = \frac{Q^1 + 2/3Q^2}{Q^1 + Q^2} \quad \text{Eq. 5-3}$$

in which  $Q^1$  and  $Q^2$  are the fractions of Si present in  $Q^1$  and  $Q^2$  tetrahedra, respectively. Quantitative information of the Si fraction was obtained by the deconvolution of the single pulse  $^{29}\text{Si}$  NMR spectra. The spectra were fitted to Gaussian/Lorentzian mixed function by using the dmfit2015 software package. An example of the fitting result is shown in *Figure 5-17*.

The deconvolution process is performed on the  $^{29}\text{Si}$  NMR test results of C-S-H gels with C/S varied from 0.66 to 2.0, synthesized for 4 weeks. The relative fraction of  $Q^n$ , MCL and other properties related to the evolution of the silicate chain were calculated based on the deconvolution results, which are listed in *Table 5-2*.

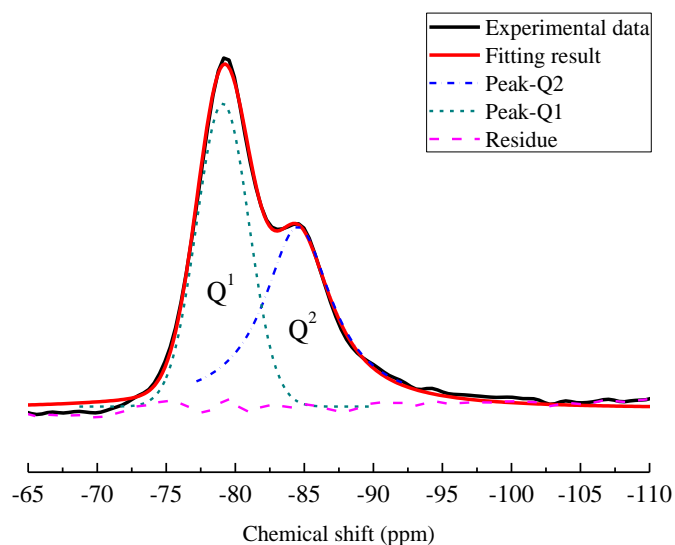


*Figure 5-17 Fitting results of  $^{29}\text{Si}$  NMR spectrum, Ca/Si = 1.4, synthesis for 4 weeks.*



Table 5-2 Relative fraction of  $Q^n$  (%), mean chain length (MCL), fraction of bridging tetrahedra (BT %) and fraction of paired tetrahedra (PT %) in C-S-H with different C/S ratio, synthesized over 4 weeks

Ca/Si	Synthesis time [weeks]	$Q^1$ [%]	$Q^2$ [%]	MCL tetrahedron unit	BT [%]	PT [%]	BT/PT
0.66	4	14.41	85.59	13.88	0.29	0.71	0.40
0.86	4	19.21	80.79	10.41	0.27	0.73	0.37
1.18	4	42.02	57.97	4.76	0.19	0.81	0.24
1.40	4	66.72	33.28	3.00	0.11	0.89	0.12
1.70	4	80.79	19.22	2.48	0.06	0.94	0.07
2.00	4	66.96	33.03	2.99	0.11	0.89	0.12

Fractions of bridging tetrahedra (BT) decrease with the increasing of C/S ratio of C-S-H gels synthesized, which indicates removal of BT from the silicate chain as discussed above. The consequence is the production of more PT- and  $Q^1$ -type of tetrahedra. The amount of  $Q^2$ -type of tetrahedra will decrease as well, also shown in *Figure 5-16*.

MCL of C-S-H with different C/S ratio were also calculated and plotted against the C/S ratio, compared with the data of C-S-H gel synthesized from the water solution [2, 27, 29-32] (see *Figure 5-18*).

The MCL of the C-S-H decreases with increasing C/S ratios when the C/S ratio is lower than 1.4. Then the MCL stays at around 2~3 tetrahedron units long. The variation of the MCL shown in *Figure 5-18* indicates that C-S-H gels with different C/S ratio were synthesized. Comparing the MCL with the data from references, the final C/S ratio of synthetic C-S-H gels satisfies the initial targeted value.

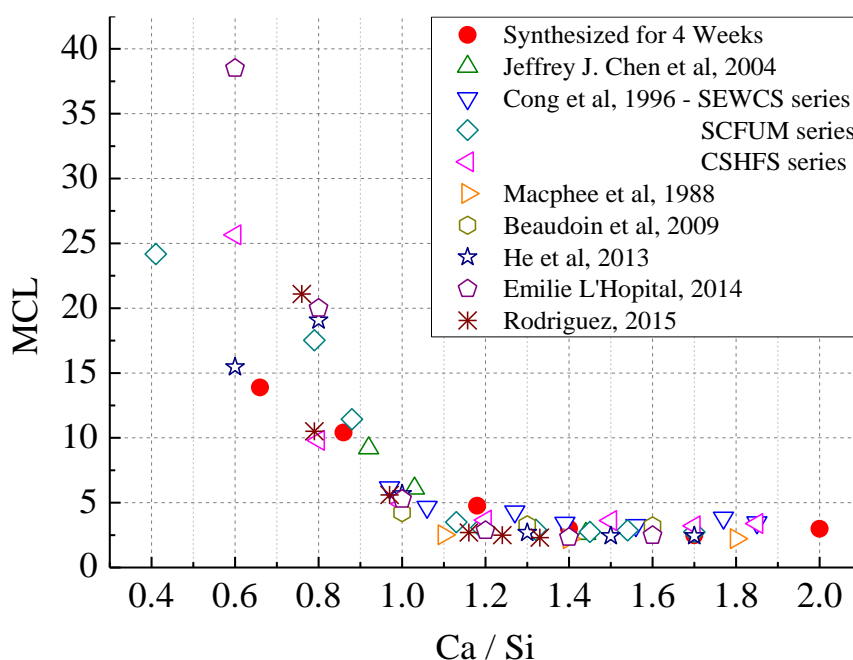


Figure 5-18 Calculated mean silicate chain length (MCL) of C-S-H with different C/S ratio.

### 5.3.2.4 FTIR test results of C-S-H gels with different C/S ratio

Similarly, some features found in the FTIR spectra of C-S-H gels will be used to identify the synthesized C-S-H gels. FTIR tests were performed on the C-S-H gels with C/S ratios 0.66 to 2.0 and synthesized over 4 weeks. The test results are compared in *Figure 5-19*.

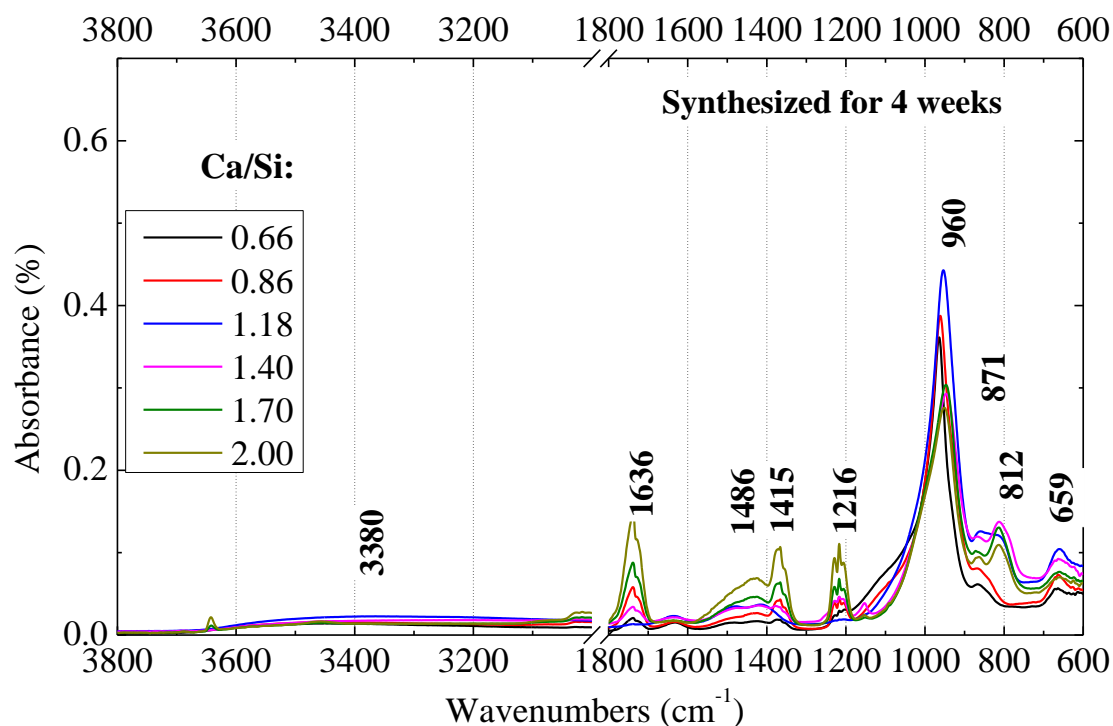


Figure 5-19 FTIR test results of C-S-H with different C/S (0.66 - 2.0), synthesized for 4 weeks

Table 5-3 Relative assignments of major bands observed in the FTIR spectra of synthesized C-S-H

Peak wavenumbers (cm <sup>-1</sup> )	Primary assignment	Reference
~659	Si-O-Si bending	[27]
~812	Si-O stretching of Q <sup>1</sup>	[33]
~871	Bending ( $\nu_2$ ) of CO <sub>3</sub> <sup>2-</sup>	[33-45]
~960	Si-O stretching vibrations of Q <sup>2</sup> tetrahedra; Shifting to lower frequency with increasing of Ca/Si	[33, 40, 42, 45-49]
~1216	Si-O stretching vibration in Q3 sites (only in 1.1nm T)	[33]
~1400 to 1500	stretching ( $\nu_3$ ) of CO <sub>3</sub> <sup>2-</sup> (carbonation)	[33-44, 50-52]
~1636	H-O-H bending vibration of water (OH in 1.4nm T)	[33-38]
~1730	H-O-H bending vibration of bound water	[49]
~3380	water molecules	[33-38]
~3640	O-H stretching vibration in Ca(OH) <sub>2</sub>	[39, 42, 50, 51]

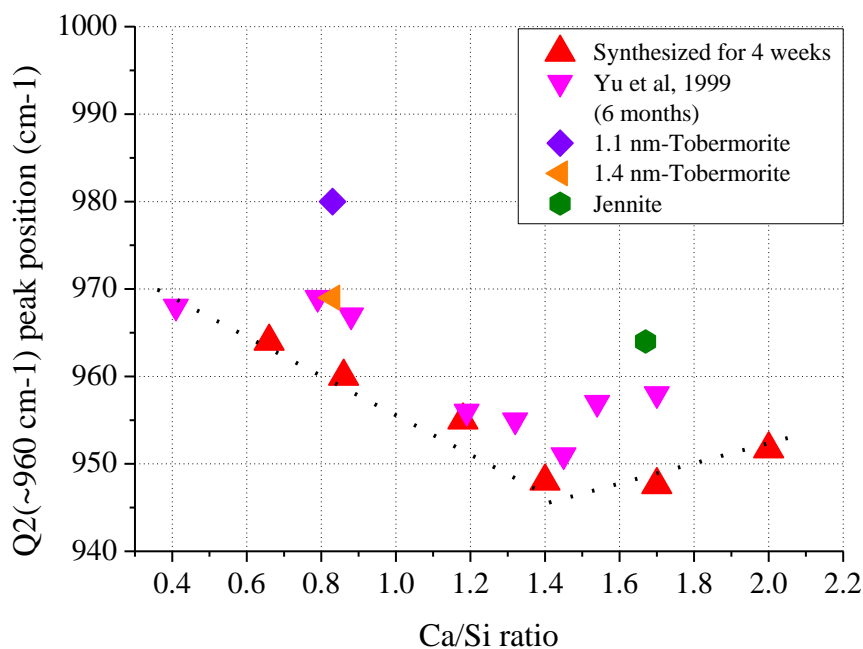


Figure 5-20 Relationships between the position of peaks indicating  $Q^2$  ( $\sim 960\text{cm}^{-1}$ ) and C/S ratio

There are some identical peaks observed in the absorbance spectrum of synthesized C-S-H. The chemical bond vibrations related to these peaks are listed in *Table 5-3*.

The peaks at around 659, 812, 960 and 1212 are related to the bands in the silicate chain, which confirm the existence of  $Q^1$  and  $Q^2$  tetrahedra. The characteristic peak at approximately  $970\text{ cm}^{-1}$  corresponds to the Si-O stretching vibrations of  $Q^2$  tetrahedra, which shifts to a lower frequency with increasing C/S ratio [33, 47, 53].

The positions of peak  $\sim 970\text{ cm}^{-1}$  in the FTIR spectra of synthesized C-S-H are plotted versus the designed C/S ratio in *Figure 5-20*, and compared with data collected from other researchers.

Apparently, the peak  $\sim 960\text{ cm}^{-1}$  shifts toward lower wavenumbers when the C/S ratio increases from 0.66 to 1.40. However, the peak will shift by following the opposite rule when the C/S ratio increases further. The variations of the peak  $\sim 960\text{ cm}^{-1}$  among the synthesized C-S-H gels show that the C-S-H gels with different C/S ratio were synthesized. By comparing with the reference data points, the final C/S ratio of the synthesized C-S-H is consistent with the initial targeted value.

### 5.3.3 Structure of nano-crystalline C-S-H gels

In Chapter 6, the carbonation rate of C-S-H gels with different C/S ratio will be calculated based on the amounts of products and remaining C-S-H gels after exposure to accelerated carbonation. The amounts of these phases will be determined with the Rietveld refinement of XRD test results. It is known that the crystal information file of each phase involved is necessary for the Rietveld analysis. Therefore, the appropriate crystal structure file of C-S-H will be discussed and selected for the study in Chapter 6.

### 5.3.3.1 Effects of crystal size on the XRD pattern

C-S-H is normally considered as an amorphous or poorly crystalline phase due to its short-range order feature and lack of structure order in the long range. The short range is in nanometer scale, so the C-S-H is also named as nanocrystalline C-S-H. The smallest size of the nano-crystallites is in the order of 3-6 nm [3, 54]. For the nanocrystalline C-S-H in OPC-pastes, the largest dimension is typically in the range of 6-15 nm [3, 54]. Other researchers also found that the largest dimension can be over 100 nm [55, 56], which may be either corresponding to a partially continuous structure [57] or to a colloidal state [58]. Nevertheless, the general crystal size of C-S-H phases is in nanoscale. It is known that the peak in the XRD pattern is affected by the size of the crystals as well. Therefore, it is necessary to figure out the size effect before performing the Rietveld refinement of synthesized C-S-H gels.

For studying the crystal structure of nanocrystalline C-S-H, Richardson[7] proposed a series of T-models for the description of the structure of C-S-H(I), which were modified based on tobermorite crystal structure, which cover C/S ratios in the range of 0.66 - 1.50. The related crystallographic information files (CIF) were proposed as well. These CIFs will be used to study the effects of crystal size on the XRD pattern.

Theoretical XRD patterns were simulated based on the above-mentioned CIFs by using *CrystalDiffract* (CrystalMaker Software Ltd). Assuming the crystals are isotropic, the calculated patterns of C-S-H phases with different isotropic crystal sizes are compared in *Figure 5-21* to *Figure 5-24*.  $T_n$  in the figures is the label of the T-model, in which, “T” denotes “tobermorite-based structure”; a number or “ $\infty$ ” denotes the mean length of the silicate chains.

The characteristic peaks in the calculated XRD patterns are widening if the assumed crystal size decreases. Patterns in *Figure 5-23* and *Figure 5-24* are more like the normal powder diffraction spectrum of crystal phases. Compared to the real XRD patterns of synthesized C-S-H(I) in *Figure 5-10*, the peak shape of calculated patterns shown in *Figure 5-21* and *Figure 5-22* are much more suitable to describe the crystal structure of C-S-H. The setting of crystal sizes will be considered in the following Rietveld refinement.

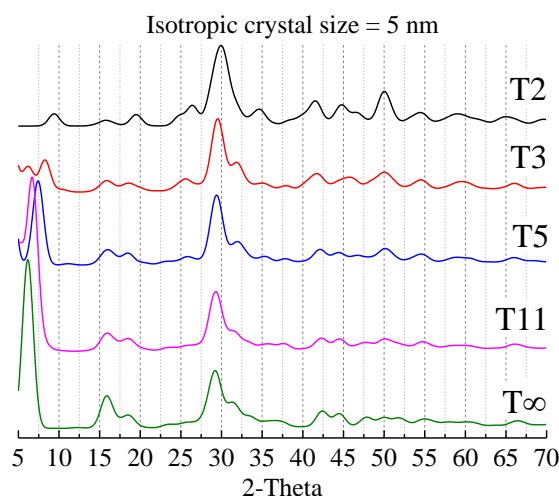


*Figure 5-21* Calculated XRD patterns for the model structures of C-S-H(I) proposed by Richardson (monochromatic Cu  $K_\alpha$  radiation,  $\lambda = 1.5406 \text{ \AA}$ ), assuming the crystal size of 5 nm

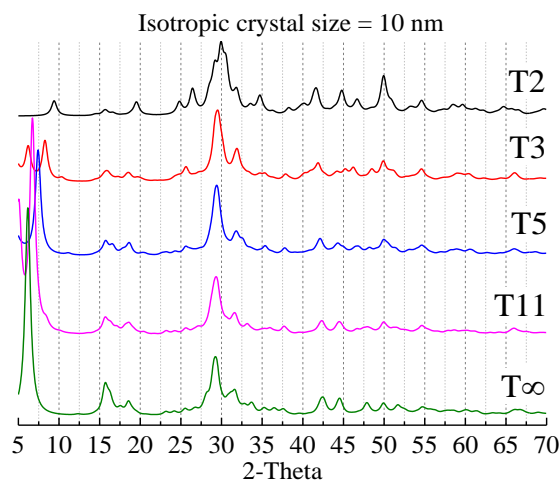


Figure 5-22 Calculated XRD patterns for the model structures of C-S-H(I) proposed by Richardson (monochromatic Cu K $\alpha$  radiation,  $\lambda = 1.5406 \text{ \AA}$ ), assuming the crystal size of 10 nm

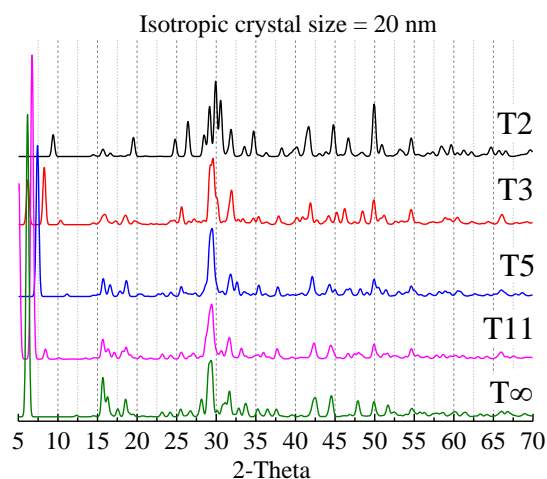


Figure 5-23 Calculated XRD patterns for the model structures of C-S-H(I) proposed by Richardson (monochromatic Cu K $\alpha$  radiation,  $\lambda = 1.5406 \text{ \AA}$ ), assuming the crystal size of 20 nm

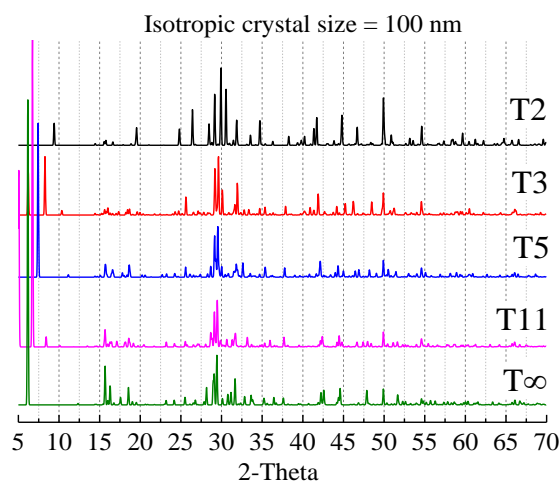


Figure 5-24 Calculated XRD patterns for the model structures of C-S-H(I) proposed by Richardson (monochromatic Cu K $\alpha$  radiation,  $\lambda = 1.5406 \text{ \AA}$ ), assuming the crystal size of 100 nm

### 5.3.3.2 T-series structure model of C-S-H

In section 5.3.3.1, the effects of crystal size on the shape of XRD pattern of C-S-H are discussed. The T-series structure models of C-S-H are introduced and used as examples. The T-series structure models are the hypothetical C-S-H crystal structures developed by Richardson, which will provide the CIFs of the C-S-H in the Rietveld refinement. These structure models are listed in *Table 5-4* with explanation of the notation.

*Table 5-4 Notation of structure models used in the Rietveld refinement*

Structure Model	Ca/Si	MCL	Position Relation of the Neighbor Bridging Tetrahedra		Based Tobermorite Structure	Approximate Layer Spacing	
			Staggered	Adjacent	Clino-T	11 Å	14 Å
T2_ac	1.25	2	-	√	√	-	-
T2_sc_LS1	1.50	2	√	-	√	-	-
T2_sc_LS2	1.50	2	√	-	√	-	-
T3_14sc	1.22	3	√	-	√	-	√
T5_14sc	1.10	5	√	-	√	-	√
T5_11sc	1.10	5	√	-	√	√	-
T11_14sc	0.82	11	√	-	√	-	√
Tinf_11ac	0.83	Infinite-chain	-	√	√	√	-
Tinf_14ac	0.83	Infinite-chain	-	√	√	-	√
Tinf_14sc	0.83	Infinite-chain	√	-	√	-	√
*Tinf_sc_noCa_LS1	0.66	Infinite-chain	√	-	√	-	-
Tinf_sc_noCa_LS2	0.66	Infinite-chain	√	-	√	-	-

\* noCa means no interlayer  $Ca^{2+}$  ions.

In the name of the structure model, “T” is the abbreviation of Tobermorite; the number or “inf” behind “T” indicates the mean silicate chain length (MCL) in this C-S-H. The bridging tetrahedral sites (vacancies in the silicate chain of T2) are either adjacent to one another or staggered by  $b/2$ . The two features of the structure model are labelled as “a” and “s” in their name, respectively, and are illustrated in *Figure 5-25* and *Figure 5-26*. “LS1” and “LS2” indicate the first and second of two alternative layer spacings in the hypothetical dimer with the staggered chain. For example, in the first version (T2\_sc\_LS1), the interlayer Ca is placed close to the vacant tetrahedral bridging site, whereas the second version, i.e. T2\_sc\_LS2, involves two Ca atoms.

The schematic of the structures of T2\_sc\_LS1 and T2\_sc\_LS2 are illustrated in *Figure 5-26* and *Figure 5-27*. It should be noticed that structure models originated from ortho-tobermorite are not used in the refinement, because it is not possible to generate the dimeric models, i.e. T2\_so\_LS1 and T2\_so\_LS2, which are crystal-chemically consistent with known calcium silicate hydrates by using an ortho-tobermorite starting structure, concluded by Richardson [7].

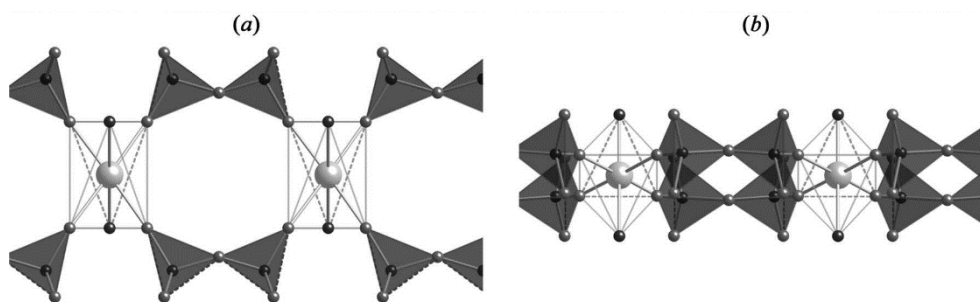


Figure 5-25 A hypothetical dimer ( $T2_{ac}$ ) derived from a clinotobermorite with the bridging tetrahedral sites adjacent to one another. (a) Viewed along the **a** axis, and (b) viewed along the **b** axis (after Richardson [7])

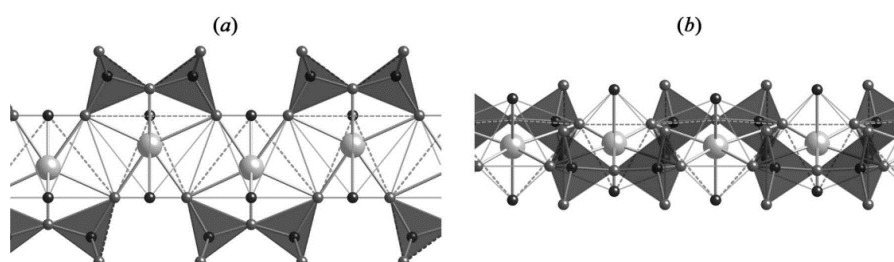


Figure 5-26 A hypothetical dimer ( $T2_{sc-LS1}$ ) derived from a clinotobermorite with the bridging tetrahedral sites staggered by  $b/2$ . (a) Viewed along the **a** axis, and (b) viewed along the **b** axis (after Richardson [7])

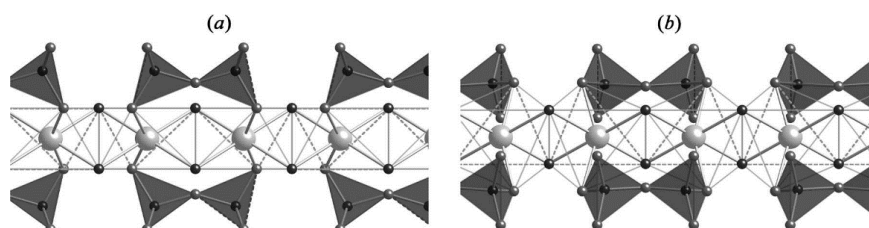


Figure 5-27 A hypothetical dimer ( $T2_{sc-LS2}$ ) derived from a clinotobermorite with the bridging tetrahedral sites staggered by  $b/2$ . (a) Viewed along the **a** axis, and (b) viewed along the **b** axis (after Richardson [7])

### 5.3.3.3 Rietveld refinement of synthetic C-S-H gels with different C/S ratio

In section 5.3.3.2, the hypothetical T-series crystal structure models are briefly introduced. Their CIFs will be used in the Rietveld refinement in this section. With the CIFs of C-S-H phases the Rietveld refinement was performed for the XRD results of synthesized C-S-H gels by using *Profex* software [59].

Several combinations of structure models were considered in the refinement program. The optimized combinations for each sample with C/S ratios 0.66 - 2.00, synthesized over 4 weeks, were described in *Figure 5-28* to *Figure 5-33*. In each figure, part *a* and *b* indicate the refinement results for the anisotropic and isotropic grain sizes of crystals, respectively.

Rietveld refinement results, including the accuracy of fit, are listed in *Table 5-5*. There are two Rietveld reliability factors:  $R_{exp}$  and  $\chi^2$ . The lower these two factors, the better the refinement result.

The results show that the crystal structure of each type of synthesized C-S-H (with certain C/S ratio) can be described by one or two-mixed hypothetical structures. For example, the crystal structure of synthesized C-S-H with C/S ratios 0.66 and 1.18 can be interpreted by the crystal structure model Tinf\_sc\_noCa\_LS2 and T3\_14sc, respectively. As for the synthesized C-S-H with C/S ratio of 0.86, its crystal structure can be described by the mix-structures of T5\_14sc and Tinf\_11ac. The crystal structure of synthesized C-S-H with C/S ratios even higher than 1.40, can be interpreted by the mix-structures of T2\_sc\_LC1 and T3\_14sc, plus  $\text{Ca}(\text{OH})_2$ , if there is. Furthermore, the refinement result is always better regardless of the C/S when considering the C-S-H as anisotropic crystals, if checking the Rietveld reliability factors, i.e.  $R_{exp}$  and  $\chi^2$ .

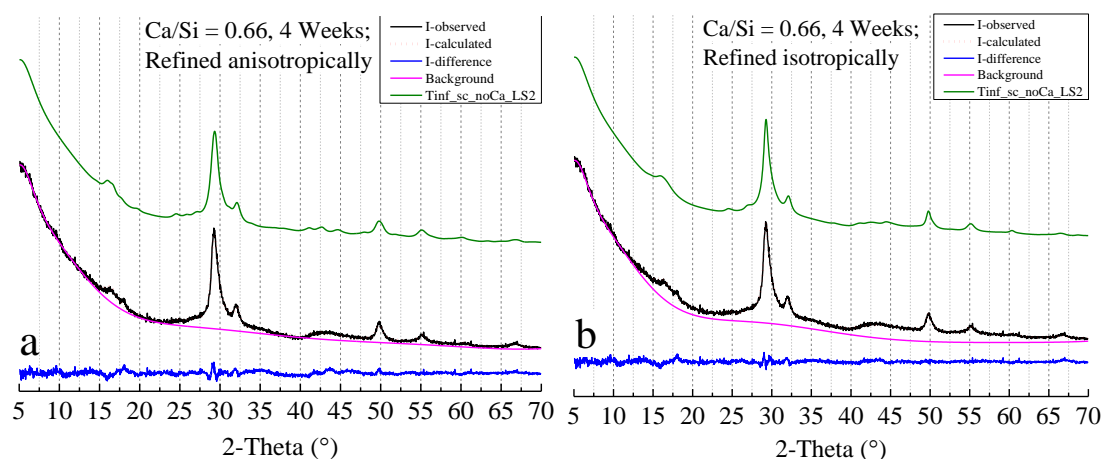


Figure 5-28 Rietveld refinement for the powder pattern of sample C/S = 0.66; a - refinement considering the anisotropic crystal size, b - refinement considering the isotropic crystal size.

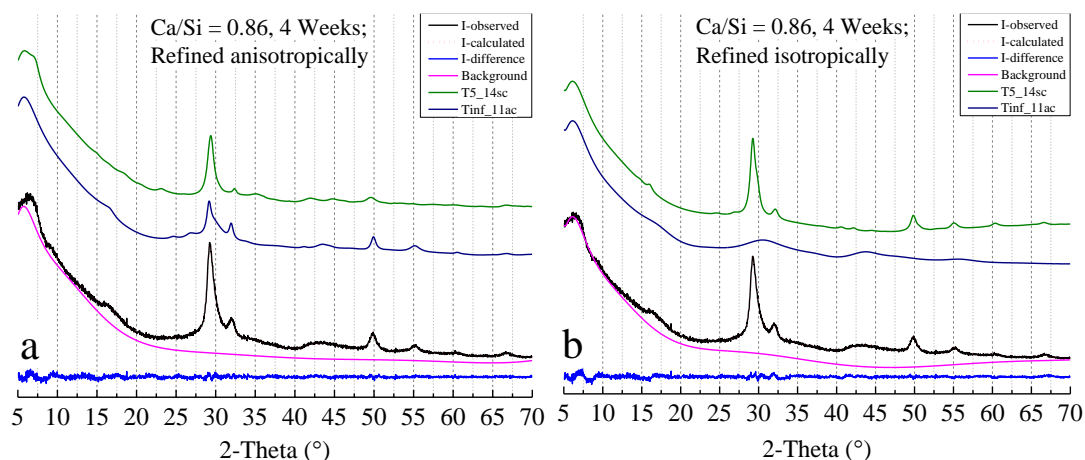


Figure 5-29 Rietveld refinement for the powder pattern of sample C/S = 0.86; a - refinement considering the anisotropic crystal size, b - refinement considering the isotropic crystal size.



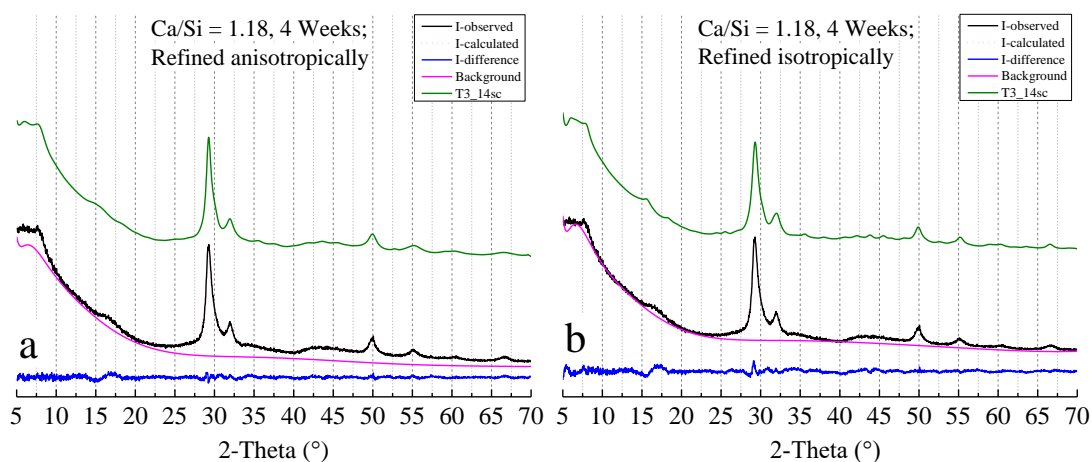


Figure 5-30 Rietveld refinement for the powder pattern of sample  $C/S = 1.18$ ; a - refinement considering the anisotropic crystal size, b - refinement considering the isotropic crystal size.

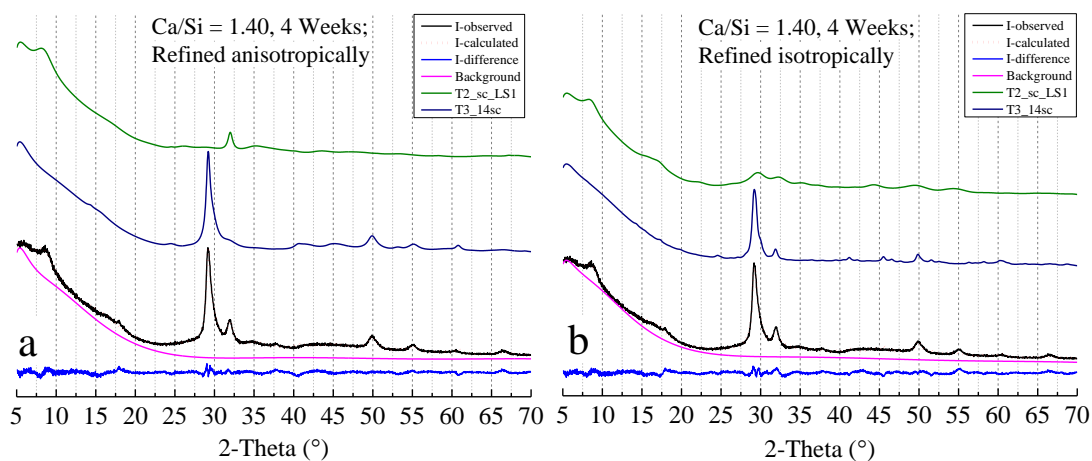


Figure 5-31 Rietveld refinement for the powder pattern of sample  $C/S = 1.40$ ; a - refinement considering the anisotropic crystal size, b - refinement considering the isotropic crystal size.

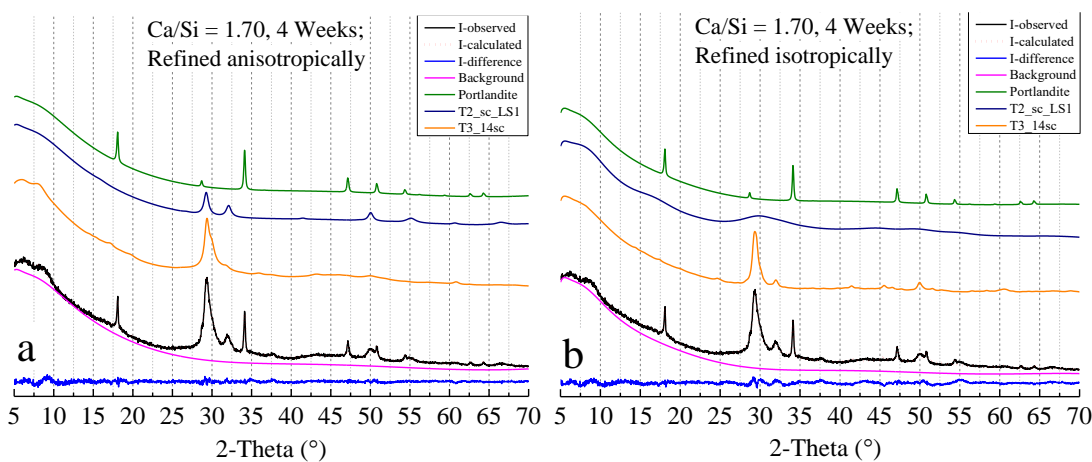


Figure 5-32 Rietveld refinement for the powder pattern of sample  $C/S = 1.70$ ; a - refinement considering the anisotropic crystal size, b - refinement considering the isotropic crystal size.

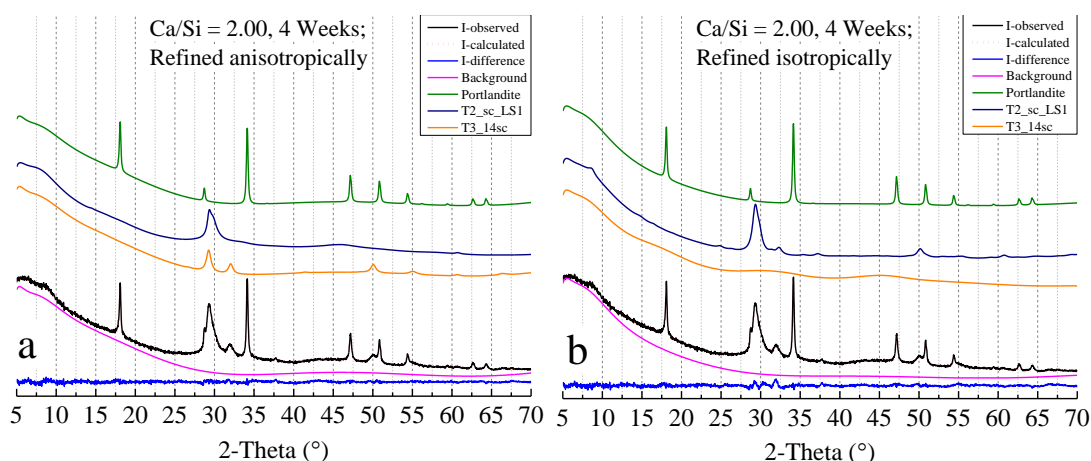


Figure 5-33 Rietveld refinement for the powder pattern of sample  $C/S = 2.00$ ; a - refinement considering the anisotropic crystal size, b - refinement considering the isotropic crystal size.

In Figure 5-12, the interlayer spacings of synthesized C-S-H gel were compared with those data from references and the T-series structure models. The locations of the data points from this research are either close to a certain T model ( $C/S = 0.66$  or  $1.18$ ) or lie in between two T models ( $C/S = 0.86$  or  $1.40$ ). For example, the data of the C-S-H gel with  $C/S$  ratios  $0.66$  and

Table 5-5 Rietveld refinement results of the C-S-H gel series, synthesized for 4 weeks

C/S	Crystal Size Condition	Refine Result Evaluation			Refined Bulk C/S	Weight Percentage of Possible Phases					
		* $R_{wp}$	* $R_{exp}$	* $\chi^2$		T2_sc_LS1	T3_14_sc	T5_14_sc	Tinf_1_lac	Tinf_sc_noC_a_LS2	Ca(OH) <sub>2</sub>
0.66	Isotropic	4.5	2.6	3.00	0.67	-	-	-	-	1.00	-
	Anisotropic	3.64	2.59	1.98	0.67	-	-	-	-	1.00	-
0.86	Isotropic	3.58	2.65	1.83	0.86	-	-	0.16	0.84	-	-
	Anisotropic	3.22	2.65	1.47	0.91	-	-	0.47	0.53	-	-
1.18	Isotropic	4.67	2.67	3.06	1.22	-	1.00	-	-	-	-
	Anisotropic	3.62	2.66	1.85	1.22	-	1.00	-	-	-	-
1.40	Isotropic	5.62	2.74	4.21	1.4	0.68	0.32	-	-	-	-
	Anisotropic	4.81	2.73	3.10	1.34	0.46	0.54	-	-	-	-
1.70	Isotropic	5.11	2.64	3.75	1.5	0.75	0.21	-	-	-	0.04
	Anisotropic	3.57	2.63	1.84	1.34	0.11	0.84	-	-	-	0.06
2.00	Isotropic	4.13	2.58	2.56	1.33	0.10	0.85	-	-	-	0.05
	Anisotropic	3.46	2.58	1.79	1.37	0.05	0.87	-	-	-	0.08
CIFs ref.									[7]		ICSD 64950

\* Rietveld reliability factors, including weighted profile R-factor ( $R_{wp}$ ), expected R factor ( $R_{exp}$ ) and goodness of fit or Chi squared,  $\chi^2 = (R_{wp}/R_{exp})^2$  [60].

1.18 are near to Tinf and T3 respectively. The data of the C-S-H gel with C/S ratio 0.86 is located on the solid trend line but in between T11 and T5. As for the C-S-H with the C/S of 1.40, the data lie in between T3 and T2 in *Figure 5-12*. This means the crystal structures of C-S-H gels synthesized in this study can be described from refined T-series structure models, which is confirmed by the optimized refinement results for each synthesized C-S-H gel, shown in *Table 5-5*.

## 5.4 Conclusion

In Chapter 5, C-S-H gels with different C/S ratios are synthesized in a water solution for the accelerated carbonation study. The synthetic products are studied by using XRD,  $^{29}\text{Si}$  NMR, TGA and FTIR. The crystal structure of synthesized C-S-H are discussed. The main conclusions are as follows:

- ◆ C-S-H(I) with different C/S ratios are synthesized successfully under the applied experimental conditions, identified by the test results from different measurement methods.
- ◆ When the designed C/S ratio is over 1.40, portlandite will appear in the synthetic products.
- ◆ The results confirm again that the “defect-tobermorite” model is an appropriate one to explain the structure of C-S-H(I) (C/S = 0.66~1.40). C-S-H(I) with higher C/S ratio can be derived from tobermorite by removing the bridge tetrahedra and incorporating extra  $\text{Ca}^{2+}$  in the interlayer. It yields C-S-H with a C/S ratio up to 1.50. By incorporating nanocrystalline portlandite in the interlayer of the structure, C-S-H can be formed with even higher C/S ratio.
- ◆ The crystal structure of synthesized C-S-H(I) can be refined and well described using T-series structure models.

## 5.5 References

- [1] S. Merlino, E. Bonaccorsi, T. Armbruster, The real structure of tobermorite 11Å normal and anomalous forms, OD character and polytypic modifications, *Eur J Mineral*, 13 (2001) 577-590.
- [2] J.J. Chen, J.J. Thomas, H.F. Taylor, H.M. Jennings, Solubility and structure of calcium silicate hydrate, *Cement Concrete Res*, 34 (2004) 1499-1519.
- [3] G. Renaudin, J. Russias, F. Leroux, F. Frizon, C. Cau-dit-Coumes, Structural characterization of C–S–H and C–A–S–H samples—part I: long-range order investigated by Rietveld analyses, *Journal of Solid State Chemistry*, 182 (2009) 3312-3319.
- [4] K. Garbev, G. Beuchle, M. Bornefeld, L. Black, P. Stemmermann, Cell Dimensions and Composition of Nanocrystalline Calcium Silicate Hydrate Solid Solutions. Part 1: Synchrotron-Based X-Ray Diffraction, *J Am Ceram Soc*, 91 (2008) 3005-3014.
- [5] K. Garbev, M. Bornefeld, G. Beuchle, P. Stemmermann, Cell Dimensions and Composition of Nanocrystalline Calcium Silicate Hydrate Solid Solutions. Part 2: X-Ray and Thermogravimetry Study, *J Am Ceram Soc*, 91 (2008) 3015-3023.
- [6] W.H. Bragg, W.L. Bragg, The reflection of X-rays by crystals, *Proceedings of the Royal Society of London. Series A, Containing Papers of a Mathematical and Physical Character*, 88 (1913) 428-438.
- [7] I.G. Richardson, Model structures for C-(A)-SH (I), *Acta Crystallographica Section B: Structural Science, Crystal Engineering and Materials*, 70 (2014) 903-923.
- [8] R.A. Alizadeh, Nanostructure and engineering properties of basic and modified calcium-silicate-hydrate systems, University of Ottawa (Canada), 2009.
- [9] X. Cong, R.J. Kirkpatrick, Effects of the temperature and relative humidity on the structure of C S H gel, *Cement Concrete Res*, 25 (1995) 1237-1245.
- [10] A. Stumm, K. Garbev, G. Beuchle, L. Black, P. Stemmermann, R. Nüesch, Incorporation of zinc into calcium silicate hydrates, Part I: formation of CSH (I) with C/S= 2/3 and its isochemical counterpart gyrolite, *Cement Concrete Res*, 35 (2005) 1665-1675.
- [11] S. Grangeon, F. Claret, C. Lerouge, F. Warmont, T. Sato, S. Anraku, C. Numako, Y. Linard, B. Lanson, On the nature of structural disorder in calcium silicate hydrates with a calcium/silicon ratio similar to tobermorite, *Cement Concrete Res*, 52 (2013) 31-37.
- [12] J. Minet, S. Abramson, B. Bresson, A. Franceschini, H. Van Damme, N. Lequeux, Organic calcium silicate hydrate hybrids: a new approach to cement based nanocomposites, *J Mater Chem*, 16 (2006) 1379-1383.
- [13] A. Nonat, The structure and stoichiometry of C-S-H, *Cement Concrete Res*, 34 (2004) 1521-1528.
- [14] D. Sugiyama, Chemical alteration of calcium silicate hydrate (C–S–H) in sodium chloride solution, *Cement Concrete Res*, 38 (2008) 1270-1275.
- [15] K. Garbev, G. Beuchle, M. Bornefeld, L. Black, P. Stemmermann, Cell Dimensions and Composition of Nanocrystalline Calcium Silicate Hydrate Solid Solutions. Part 1: Synchrotron - Based X - Ray Diffraction, *J Am Ceram Soc*, 91 (2008) 3005-3014.
- [16] H. Matsuyama, J. Young, Effects of pH on precipitation of quasi-crystalline calcium silicate hydrate in aqueous solution, *Adv Cem Res*, 12 (2000) 29-33.
- [17] C.S. Walker, D. Savage, M. Tyrer, K.V. Ragnarsdottir, Non-ideal solid solution aqueous solution modeling of synthetic calcium silicate hydrate, *Cement Concrete Res*, 37 (2007) 502-511.
- [18] S. Grangeon, F. Claret, C. Roosz, T. Sato, S. Gaboreau, Y. Linard, Structure of nanocrystalline calcium silicate hydrates: insights from X - ray diffraction, synchrotron X - ray absorption and nuclear magnetic resonance, *Journal of applied crystallography*, 49 (2016) 771-783.
- [19] H. Taylor, J. Howison, Relationships between calcium silicates and clay minerals, *Clay Minerals Bull*, 3 (1956) 98-111.
- [20] Å. Grudemo, An electronographic study of the morphology and crystallization properties of calcium silicate hydrates, Svenska forskningsinstitutet för cement och betong vid Kungl. Tekniska högskolan 1955.
- [21] G.L. Kalousek, Crystal chemistry of hydrous calcium silicates: I, Substitution of aluminum in lattice of tobermorite, *J Am Ceram Soc*, 40 (1957) 74-80.

- [22] G. Kalousek, Application of differential thermal analysis in a study of the system lime-silica-water, Proc. 3rd Int. Symp. on Chemistry of cements, London, 1952, 1952.
- [23] G.L. Kalousek, Tobermorite and related phases in the system CaO-SiO<sub>2</sub>-H<sub>2</sub>O, Journal Proceedings, 1955, pp. 989-1011.
- [24] T. Mitsuda, S. Kobayakawa, H. Toraya, Characterization of hydrothermally formed CSH, The 8th international congress on the chemistry of cement, Rio de Janeiro, 1986, pp. 176.
- [25] E. Tajuelo Rodriguez, K. Garbev, D. Merz, L. Black, I.G. Richardson, Thermal stability of C-S-H phases and applicability of Richardson and Groves' and Richardson C-(A)-S-H(I) models to synthetic C-S-H, Cement Concrete Res, 93 (2017) 45-56.
- [26] I. Richardson, G. Groves, The structure of the calcium silicate hydrate phases present in hardened pastes of white Portland cement/blast-furnace slag blends, J Mater Sci, 32 (1997) 4793-4802.
- [27] X.D. Cong, R.J. Kirkpatrick, Si-29 MAS NMR study of the structure of calcium silicate hydrate, Adv Cem Based Mater, 3 (1996) 144-156.
- [28] I. Richardson, G. Groves, Models for the composition and structure of calcium silicate hydrate (C-S-H) gel in hardened tricalcium silicate pastes, Cement Concrete Res, 22 (1992) 1001-1010.
- [29] D. Macphee, E. Lachowski, F.P. Glasser, Polymerization effects in CSH: implications for Portland cement hydration, Adv Cem Res, 1 (1988) 131-137.
- [30] J.J. Beaudoin, L. Raki, R. Alizadeh, A<sup>29</sup>Si MAS NMR study of modified C-S-H nanostructures, Cement and Concrete Composites, 31 (2009) 585-590.
- [31] Y. He, L. Lu, L.J. Struble, J.L. Rapp, P. Mondal, S. Hu, Effect of calcium-silicon ratio on microstructure and nanostructure of calcium silicate hydrate synthesized by reaction of fumed silica and calcium oxide at room temperature, Mater Struct, (2013) 1-12.
- [32] É.M. L'Hôpital, Aluminium and alkali uptake in calcium silicate hydrates (C-S-H), EPFL, 2014.
- [33] P. Yu, R.J. Kirkpatrick, B. Poe, P.F. McMillan, X. Cong, Structure of Calcium Silicate Hydrate (C-S-H): Near-, Mid-, and Far-Infrared Spectroscopy, J Am Ceram Soc, 82 (1999) 742-748.
- [34] M. Handke, Vibrational Spectra, Force Constants, and Si-O Bond Character in Calcium Silicate Crystal Structure, Applied Spectroscopy, 40 (1986) 871-877.
- [35] J. Russell, A. Fraser, Infrared methods, Clay Mineralogy: Spectroscopic and chemical determinative methods, Springer 1994, pp. 11-67.
- [36] P.F. McMillan, R.L. Remmele, Hydroxyl sites in SiO<sub>2</sub> glass; a note on infrared and Raman spectra, Am Mineral, 71 (1986) 772-778.
- [37] I. Richardson, G. Groves, A. Brough, C. Dobson, The carbonation of OPC and OPC/silica fume hardened cement pastes in air under conditions of fixed humidity, Adv Cem Res, 5 (1993) 81-86.
- [38] D. Williams, Frequency Assignments in Infra-red Spectrum of Water, Nature, 210 (1966) 194.
- [39] R. Hanna, P. Barrie, C. Cheeseman, C. Hills, P. Buchler, R. Perry, Solid state <sup>29</sup>Si and <sup>27</sup>Al NMR and FTIR study of cement pastes containing industrial wastes and organics, Cement Concrete Res, 25 (1995) 1435-1444.
- [40] S. Barnett, D.E. Macphee, E.E. Lachowski, N. Crammond, XRD, EDX and IR analysis of solid solutions between thaumasite and ettringite, Cement Concrete Res, 32 (2002) 719-730.
- [41] D. Gastaldi, F. Canonico, E. Boccaleri, Ettringite and calcium sulfoaluminate cement: investigation of water content by near-infrared spectroscopy, J Mater Sci, 44 (2009) 5788-5794.
- [42] M.Y. Mollah, M. Kesmez, D.L. Cocks, An X-ray diffraction (XRD) and Fourier transform infrared spectroscopic (FT-IR) investigation of the long-term effect on the solidification/stabilization (S/S) of arsenic (V) in Portland cement type-V, Sci Total Environ, 325 (2004) 255-262.
- [43] H.H. Adler, P.F. Kerr, Infrared spectra, symmetry and structure relations of some carbonate minerals, American Mineralogist: Journal of Earth and Planetary Materials, 48 (1963) 839-853.
- [44] S. Teleb, D.E.-S. Nassr, E. Nour, Synthesis and infrared spectra of alkaline earth metal carbonates formed by the reaction of metal salts with urea at high temperature, Bulletin of Materials Science, 27 (2004) 483-485.
- [45] J. Piasta, Z. Sawicz, L. Rudzinski, Changes in the structure of hardened cement paste due to high temperature, Matériaux et Constructions, 17 (1984) 291-296.
- [46] J.F. Stebbins, P.F. McMillan, D.B. Dingwell, Structure, dynamics, and properties of silicate melts, Walter de Gruyter GmbH & Co KG 2019.
- [47] D. Sykes, J.D. Kubicki, A model for H<sub>2</sub>O solubility mechanisms in albite melts from infrared spectroscopy and molecular orbital calculations, Geochim Cosmochim Acta, 57 (1993) 1039-1052.

- 
- [48] J. Bensted, S.P. Varma, Some applications of infrared and Raman spectroscopy in cement chemistry. Part 3-hydration of Portland cement and its constituents, *Cement Technology*, 5 (1974) 440-445 448-450.
- [49] V.C. Farmer, *Infrared spectra of minerals*, Mineralogical society 1974.
- [50] X. Gao, Y. Lo, C. Tam, C. Chung, Analysis of the infrared spectrum and microstructure of hardened cement paste, *Cement Concrete Res*, 29 (1999) 805-812.
- [51] M. Mollah, W. Yu, R. Schennach, D.L. Cocke, A Fourier transform infrared spectroscopic investigation of the early hydration of Portland cement and the influence of sodium lignosulfonate, *Cement Concrete Res*, 30 (2000) 267-273.
- [52] W.B. White, Infrared characterization of water and hydroxyl ion in the basic magnesium carbonate minerals, *American Mineralogist: Journal of Earth and Planetary Materials*, 56 (1971) 46-53.
- [53] P.F. McMillan, G.H. Wolf, B.T. Poe, Vibrational spectroscopy of silicate liquids and glasses, *Chemical Geology*, 96 (1992) 351-366.
- [54] L. Skinner, S. Chae, C. Benmore, H. Wenk, P. Monteiro, Nanostructure of calcium silicate hydrates in cements, *Physical review letters*, 104 (2010) 195502.
- [55] I. Richardson, Tobermorite/jennite-and tobermorite/calcium hydroxide-based models for the structure of CSH: applicability to hardened pastes of tricalcium silicate,  $\beta$ -dicalcium silicate, Portland cement, and blends of Portland cement with blast-furnace slag, metakaolin, or silica fume, *Cement Concrete Res*, 34 (2004) 1733-1777.
- [56] A. Bazzoni, S. Ma, Q. Wang, X. Shen, M. Cantoni, K.L. Scrivener, The effect of magnesium and zinc ions on the hydration kinetics of C3S, *J Am Ceram Soc*, 97 (2014) 3684-3693.
- [57] E.M. Gartner, A proposed mechanism for the growth of C-S-H during the hydration of tricalcium silicate, *Cement Concrete Res*, 27 (1997) 665-672.
- [58] H.M. Jennings, Refinements to colloid model of CSH in cement: CM-II, *Cement Concrete Res*, 38 (2008) 275-289.
- [59] N. Doebelin, R. Kleeberg, Profex: a graphical user interface for the Rietveld refinement program BGMN, *Journal of applied crystallography*, 48 (2015) 1573-1580.
- [60] B.H. Toby, R factors in Rietveld analysis: How good is good enough?, *Powder diffraction*, 21 (2006) 67-70.

## **Accelerated Carbonation of Synthesized C-S-H gels with Different C/S Ratio**

### **6.1 Introduction**

In Chapter 5, C-S-H gel with different Ca/Si ratios (C/S) were prepared successfully from water solution. Several methods including XRD, XRF, TGA, FTIR and  $^{29}\text{Si}$  NMR are used to identify the C-S-H phases. Crystal structures of nanocrystalline C-S-H were discussed as well in Chapter 5. C-S-H gels synthesized for 4 weeks were selected for the accelerated carbonation study in this Chapter 6. The C/S ratio of C-S-H used in the accelerated carbonation test ranges from 0.66 to 2.00.

The selected C-S-H gels are exposed to the accelerated carbonation:  $\text{CO}_2$  concentration of 3% (V/V), temperature of  $20^\circ\text{C}$  and the relative humidity of 75%. Carbonation products of C-S-H gels are characterized to with the aim to understand the carbonation mechanism of C-S-H. Especially, the carbonation rates of C-S-H with different C/S ratio are compared and investigated. The results of this study will provide input for modelling of C-S-H carbonation in Chapter 7.

## 6.2 Materials and experiments

### 6.2.1 Accelerated carbonation experiment of C-S-H gels

C-S-H gels synthesized for 4 weeks were used for accelerated carbonation tests. C/S ratios of the C-S-H gels are listed in *Table 6-1*. As mentioned earlier in section 5.2.2, these samples were stored in a desiccator with relative humidity of 30%, regulated by standard saturated  $\text{CaCl}_2 \cdot 6\text{H}_2\text{O}$  solution, before exposed to accelerated carbonation. Before placing the samples in the carbonation chamber, these specimens were grinded into powders.  $\text{CO}_2$  concentration in the chamber was maintained at  $3\% \pm 0.2$  (V/V) by the solenoid valve connected with a  $\text{CO}_2$  sensor. The temperature inside the carbonation chamber was  $20^\circ\text{C}$  and the relative humidity around 75% by using the saturated NaCl solution. The samples were exposed to carbonation for several hours (from 0.5 h to 24 h) and days (from 1 day to 7 days). Samples exposed for hours will be used to study the early-age behavior of C-S-H gels under accelerated carbonation. The other samples exposed for days will be used for the study of final products of C-S-H gels after carbonation and the carbonation rate of C-S-H with different C/S ratio.

### 6.2.2 Test methods of C-S-H gels after carbonation

Carbonation process and related carbonation products of C-S-H have been studied by many authors [1-3]. From their studies, it has been learned that carbonation of C-S-H is a complex decalcification-polymerization process and the formation of amorphous silica gel. The carbonation reaction of C-S-H can be described as follows (Eq. 6-1).



in which  $C = \text{CaO}$ ,  $H = \text{H}_2\text{O}$ ,  $S = \text{SiO}_2$ , and  $\bar{C} = \text{CO}_2$ .  $x$ ,  $y$  and  $t$  are the molecular numbers.  $x$  stands for the C/S ratio of C-S-H. As indicated in Eq. 6-1, the Ca will be removed from the C-S-H layer structure during decalcification and reacts with  $\text{CO}_2$  to form carbonates. Meanwhile, the adjacent Si-tetrahedra in different silicate chains will be linked together to form a 2- or 3-dimensional network, illustrated in *Figure 6-1*.

*Table 6-1 C-S-H gels selected for the accelerated carbonation test*

Sample NO.	Ca/Si ratio	Synthesis Time
1	0.66	4 weeks
2	0.86	4 weeks
3	1.18	4 weeks
4	1.40	4 weeks
5	1.70	4 weeks
6	2.00	4 weeks



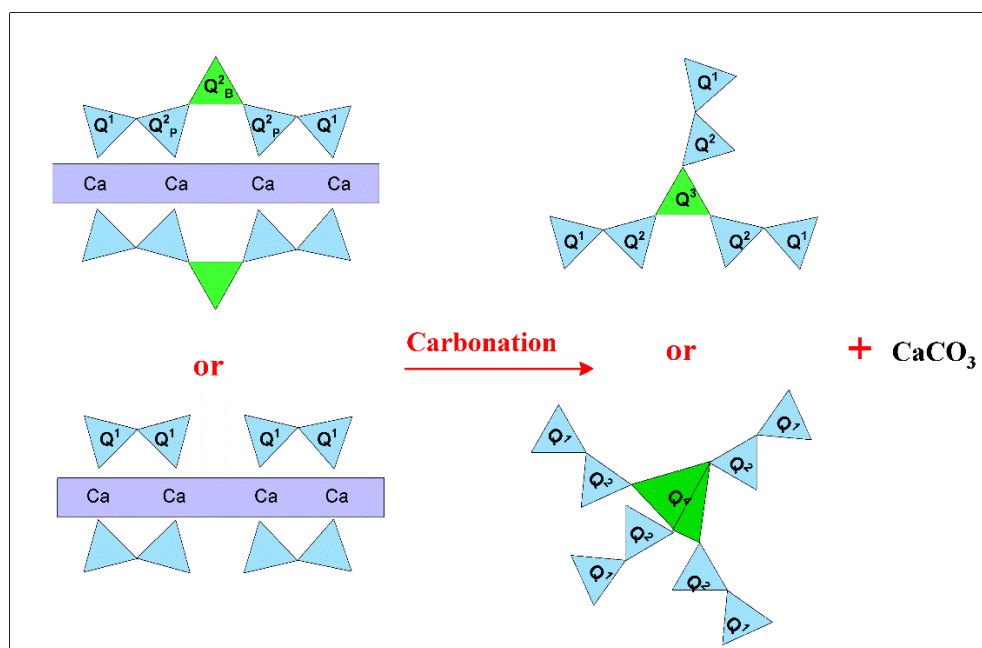


Figure 6-1 Schematic of polymerization of silicate chain

Table 6-2 The arrangements of accelerated carbonation experiments and related test methods

Sample NO.	Exposure Time	Test Method	Test Purpose
1 - 6	Hours, 0.5 h to 24 h	FTIR	Early-age behaviour
	Days, 1 day to 7 days	XRD and Rietveld analysis, $^{29}\text{Si}$ NMR	Final carbonation products and average carbonation rate

Different test methods were applied in this study to investigate the changes of C-S-H gels after different accelerated carbonation periods. The purpose of the test method is summarized in *Table 6-2*.

X-ray diffraction (XRD) was mainly used to investigate the amounts of carbonates. Rietveld refinement was performed on the XRD test result to quantify the amounts of carbonation products of synthesized C-S-H. Before the XRD test, the samples were mixed with approximate 12-13% of corundum ( $\text{Al}_2\text{O}_3$ , PDF 00-10-0173) as an internal standard. Average carbonation rates of C-S-H with different C/S ratio were calculated based on the Rietveld analysis results.

$^{29}\text{Si}$  Nuclear magnetic resonance (NMR), and Fourier transform infrared spectroscopy (FTIR) were used to study the changes of silicate chains in the C-S-H when exposed to accelerated carbonation. FTIR was specially used to study the changes of the layer structure of C-S-H gels after accelerated carbonation for several hours. The accelerated carbonation arrangements and related test methods are listed in *Table 6-2*. More details of the above-mentioned test methods were described already in section 5.2.3.

## 6.3 Experimental results and discussions

### 6.3.1 Carbonation of C-S-H gels

#### 6.3.1.1 XRD test results of C-S-H gels after carbonation

After accelerated carbonation for several days, the C-S-H gels with C/S ratios of 0.66 to 2.00 were measured by XRD to identify the carbonates and other possible crystal phases. Exposure time varied from 1 day to 7 days. The test results are presented in *Figure 6-2* to *Figure 6-7*.

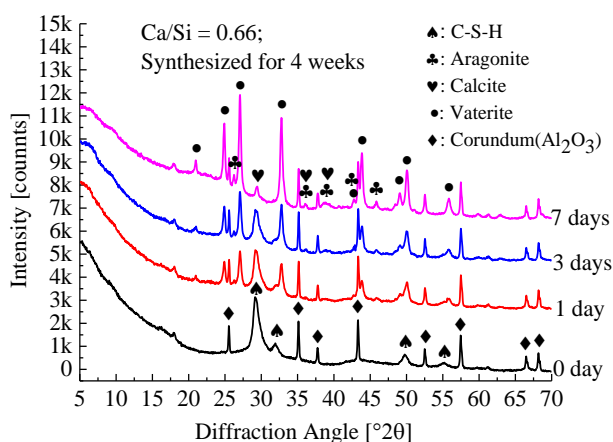


Figure 6-2 XRD test results of C-S-H (C/S = 0.66, age 4 weeks), exposed to carbonation from 0 day to 7 days

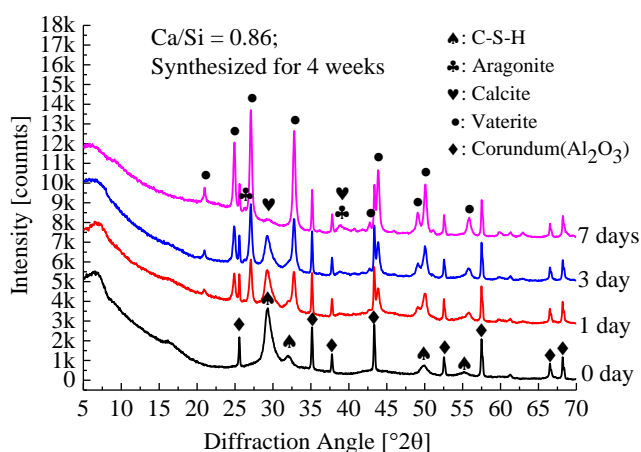


Figure 6-3 XRD test results of C-S-H (C/S = 0.86, age 4 weeks), exposed to carbonation from 0 day to 7 days

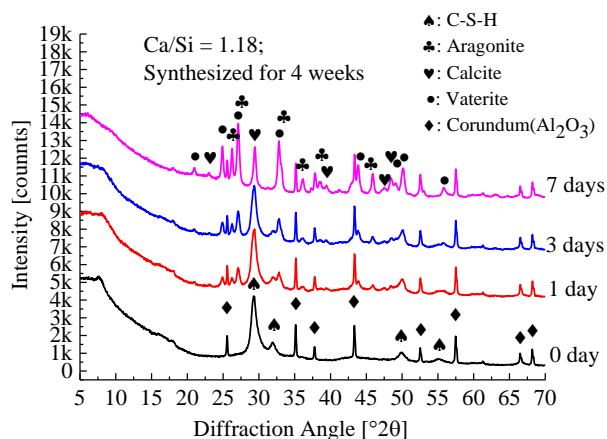


Figure 6-4 XRD test results of C-S-H ( $C/S = 1.18$ , age 4 weeks), exposed to carbonation from 0 day to 7 days

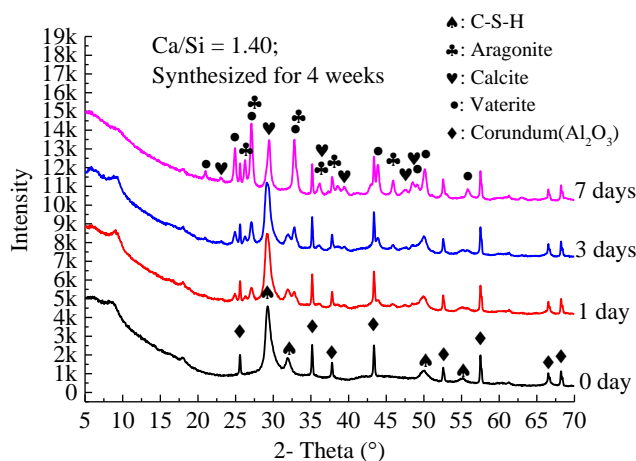


Figure 6-5 XRD test results of C-S-H ( $C/S = 1.40$ , age 4 weeks), exposed to carbonation from 0 day to 7 days

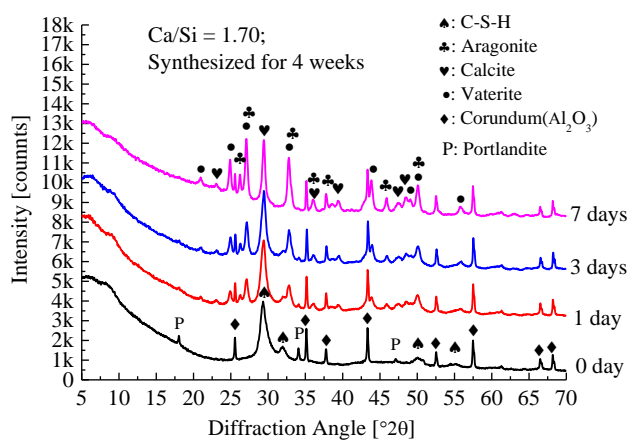


Figure 6-6 XRD test results of C-S-H ( $C/S = 1.70$ , age 4 weeks), exposed to carbonation from 0 day to 7 days

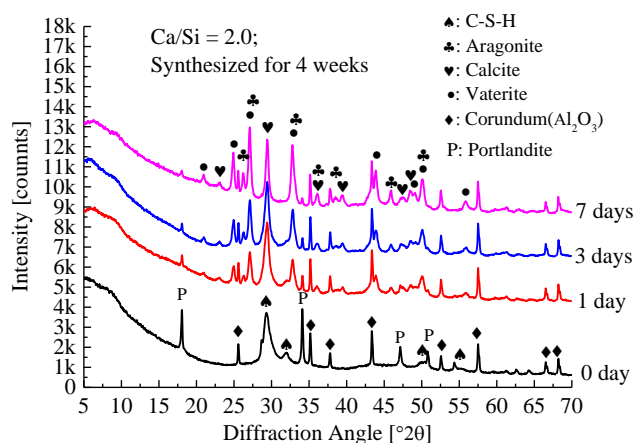


Figure 6-7 XRD test results of C-S-H ( $C/S = 2.0$ , age 4 weeks), exposed to carbonation from 0 day to 7 days

In general, before exposure to carbonation, the phases identified in XRD patterns are C-S-H(I) and portlandite, together with the internal standard Corundum. When exposed to carbonation, the diffraction peaks related to C-S-H(I) and portlandite show a decrease in intensity and even disappear with the increasing exposure time.

It is noticed that new diffraction peaks appear in the XRD pattern after carbonation. For example, peaks with the diffraction angle ( $^{\circ} 2\theta$ ) of 23.07, 29.44 and 39.37 are indicating calcite. The peaks at 26.22, 36.10 and 45.91 denote aragonite. The peaks at 24.91, 27.09 and 32.79 are related to vaterite. Details of the identified phases and their related diffraction peaks are listed in Table 6-3. These carbonates are the three polymorphs of  $\text{CaCO}_3$ . The latter two are metastable phases of calcium carbonate. Apparently, the characteristic peaks of all the three polymorphs are found in the XRD patterns after carbonation. The intensities of the major peaks indicating these carbonates are increasing with increasing exposure time.

As discussed above, three polymorphs of  $\text{CaCO}_3$  are identified in the carbonation products of all C-S-H-gels with different C/S ratio. However, the amounts of different polymorphs varied from case to case. Figure 6-2 and Figure 6-3 show that the carbonation product of

Table 6-3 Phases identified and related diffraction peaks in the XRD spectra

Phases Identified	C-S-H	Portlandite	Corundum	Polymorphs of $\text{CaCO}_3$		
		( $\text{Ca}(\text{OH})_2$ )	( $\text{Al}_2\text{O}_3$ )	Calcite	Vaterite	Aragonite
		PDF NO.	PDF NO.	PDF NO.	PDF NO.	PDF NO.
		00-044-1481	00-010-0173	00-05-0586	04-011-5985	00-041-1475
Diffraction Angle ( $^{\circ}$ ) of identical peaks	29.27	18.04	25.57	23.07	20.95	26.22
	32.16	34.11	35.17	29.44	24.91	27.22
	50.05	47.14	37.78	39.37	27.09	33.16
	55.39	50.80	43.38	47.52	32.79	36.10
	-	-	52.57	48.45	42.82	38.55
	-	-	57.52	-	43.87	45.91
	-	-	66.52	-	50.08	-
	-	-	68.20	-	55.87	-

C-S-H with C/S ratios of 0.66 or 0.86 are mainly aragonite and vaterite, after 7 days' exposure. But in the XRD patterns of C-S-H gel with C/S ratios of 1.18 or 1.40 after 7 days' exposure, the peak number and intensity related to calcite increase dramatically (*Figure 6-4* and *Figure 6-5*). It is well known that calcite is normally formed from the carbonation of portlandite in concrete. Calcite is also the main carbonation product of C-S-H with a relatively high C/S ratio, i.e. 1.18 to 2.00. Therefore, obvious peaks related to calcite can also be observed in the XRD patterns of carbonated C-S-H gel with the C/S ratios 1.70 and 2.00, which are not pure C-S-H gel but mixed with portlandite, see *Figure 6-6* and *Figure 6-7*.

### 6.3.1.2 $^{29}\text{Si}$ NMR test results of C-S-H gels after carbonation

$^{29}\text{Si}$  NMR test is a mature technique to identify different types of Si tetrahedra in a molecular structure. In this research, it is used to study the evolution of Si structure in C-S-H during the carbonation.  $^{29}\text{Si}$  NMR test results of C-S-H gels with different C/S ratio exposed for 3 and 7 days are shown in *Figure 6-8*. The characteristic peaks at around -101 and -111 ppm indicate the  $\text{Q}^3$  and  $\text{Q}^4$  types of tetrahedra, respectively. These peaks for  $\text{Q}^3$  and  $\text{Q}^4$  appear after exposed to carbonation for 3 or 7 days. Meanwhile the peaks related to the  $\text{Q}^1$  and  $\text{Q}^2$  tetrahedra disappear.

*Table 6-4 Relative fraction of  $\text{Q}^n$  (%) in C-S-H gels with different C/S ratio before and after exposure to accelerated carbonation*

Ca/Si	Exposure time (days)	$\text{Q}^1$	$\text{Q}^2$	$\text{Q}^3$	$\text{Q}^4$
0.66	0	14.41	85.59	-	-
	3	-	3.3	21.19	75.51
	7	-	1.46	24.53	74.01
0.86	0	19.21	80.79	-	-
	3	-	1.94	17.31	80.77
	7	-	-	16.17	83.82
1.18	0	42.02	57.97	-	-
	3	-	-	22.66	77.34
	7	-	-	32.32	67.69
1.40	0	66.72	33.28	-	-
	3	-	2.42	48.57	79.0
	7	-	-	27.77	72.23
1.70	0	71.42	28.57	-	-
	3	-	-	21.0	79.0
	7	-	-	22.25	77.75
2.00	0	71.69	28.3	-	-
	3	-	-	26.74	73.36
	7	-	-	18.3	81.7

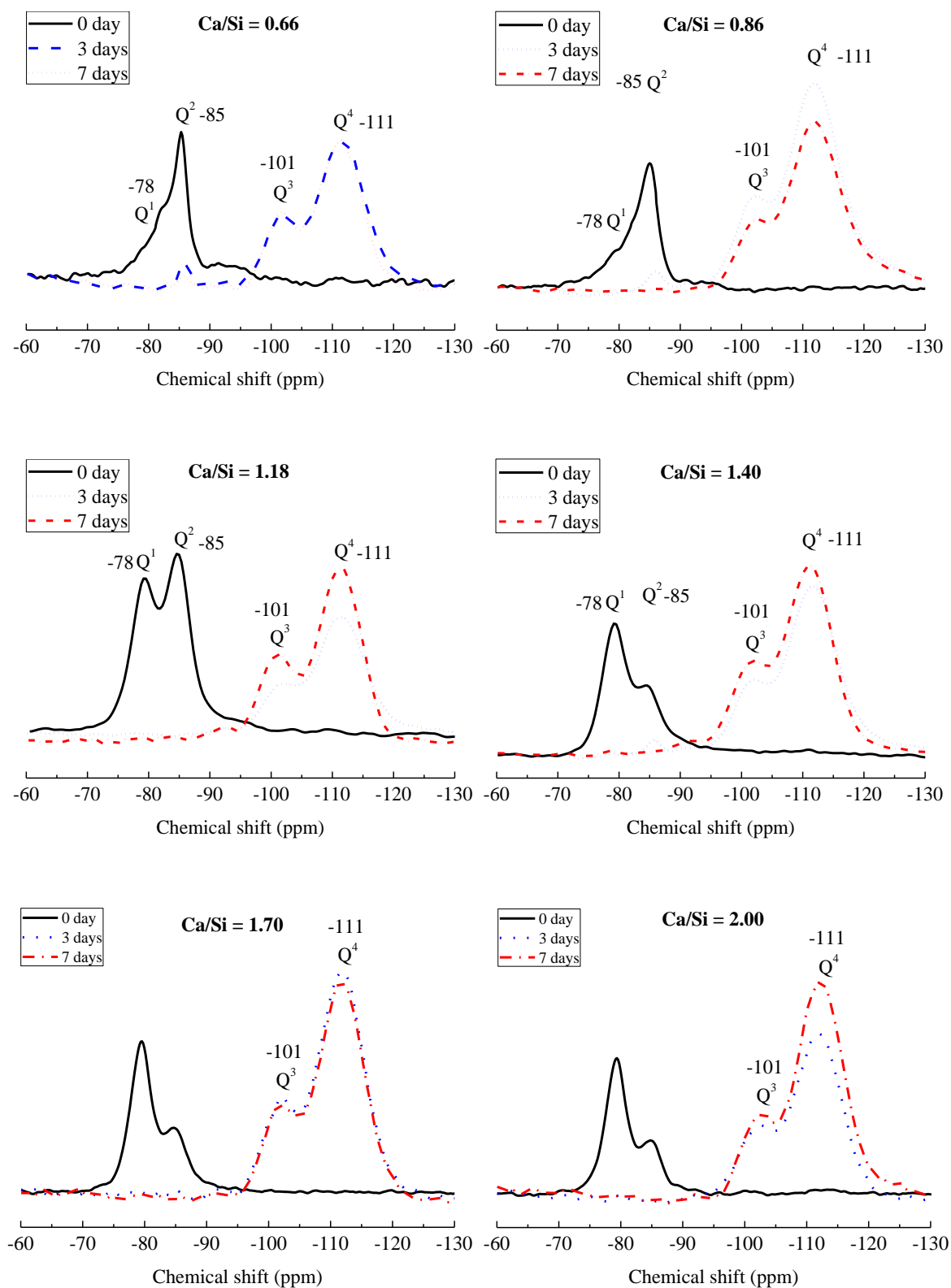


Figure 6-8  $^{29}\text{Si}$  NMR test results of C-S-H, C/S ratio = 0.66 - 2.00, carbonated for 3 and 7 days

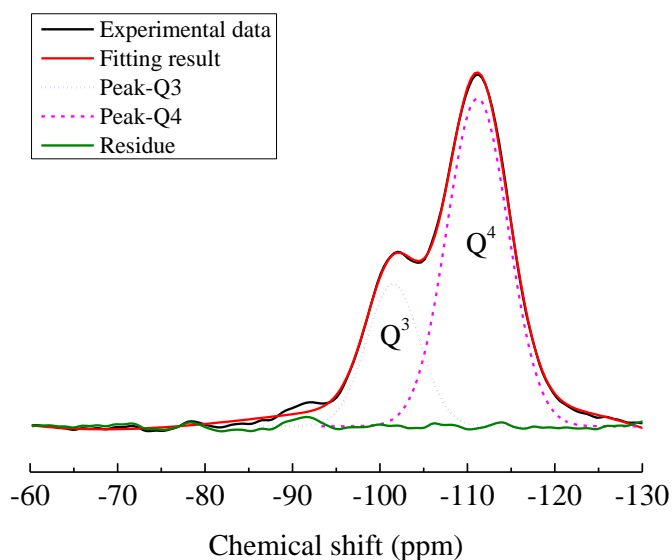


Figure 6-9 Fitting results of  $^{29}\text{Si}$  NMR spectrum,  $\text{Ca}/\text{Si} = 1.4$ , synthesis for 4 weeks, exposed to carbonation for 7 days

In order to find the quantitative information of different types of Si tetrahedra ( $\text{Q}^1$ ,  $\text{Q}^2$ ,  $\text{Q}^3$  and  $\text{Q}^4$ ) in the C-S-H gels after exposure to carbonation, the deconvolution process was performed on all the  $^{29}\text{Si}$  NMR spectra shown in Figure 6-8. One of the deconvolutions (or fitting) results is presented in Figure 6-9. The relative percentages of different types of Si tetrahedra ( $\text{Q}^n$ ) were calculated based on the deconvolution results and listed in Table 6-4.

Obviously, the fractions of  $\text{Q}^3$  and  $\text{Q}^4$  type of tetrahedra in the C-S-H gels (regardless the C/S ratio) dramatically increase after carbonation. Meanwhile, the fractions of  $\text{Q}^1$  and  $\text{Q}^2$  type of tetrahedra decrease to zero. The evolution of the fractions of four  $\text{Q}^n$  types of tetrahedra observed from the  $^{29}\text{Si}$  NMR results reveals the polymerization of the silicate chain structure. This is illustrated schematically in Figure 6-1. The appearance of  $\text{Q}^3$  and  $\text{Q}^4$  indicate that the silicates on the neighboring silicate chain are interlinked with each other to form the silicate network in three directions.  $\text{Q}^3$ - and  $\text{Q}^4$ -type tetrahedra are usually found in quartz or silica gel. However, the characteristic peaks of quartz are not observed in the XRD test results. Therefore, these peaks are related to silica gel, which is also formed during carbonation of C-S-H gels.

### 6.3.2 Rietveld analysis of XRD test results

It is known that only crystalline phases create the distinct diffraction patterns, and the amorphous phase is absent in the XRD patterns. By using the Rietveld refinement as illustrated in Figure 3-2, the phase quantifications are usually reported by their weight percentage, relative to the total weight of all crystalline phases (see Step 3 in Figure 3-2). If a crystalline phase with known quantity is added in the sample, the relative quantities can be normalized to absolute values (see Step 4 in Figure 3-2). The added crystalline phase should be stable and inert and is also called as the internal standard. In this research, the internal standard used is corundum ( $\text{Al}_2\text{O}_3$ ).

Table 6-5 Weight percentage (%) of the internal standard  $Al_2O_3$  added in C-S-H gels with different C/S ratios before exposure to accelerated carbonation

Ca/Si	0.66	0.86	1.18	1.40	1.70	2.00
$Al_2O_3$	10.85	13.47	11.59	10.68	11.02	11.69

Table 6-6 Crystallographic information file (CIF) of  $Al_2O_3$  and calcium carbonates

Crystal Phases	Corundum	Vaterite	Aragonite	Calcite
CIF No.	ICSD 31546	ICSD 15879	ICSD 32100	ICSD 16710

The weight percentages of  $Al_2O_3$  in the initial mixtures are listed in Table 6-5. Calculations of the relative and absolute quantities is performed with the Profex software [4].

Rietveld refinement was performed on the XRD test results shown from Figure 6-2 to Figure 6-7, to calculate the relative amounts of crystal phases, in particular the different polymorphs of calcium carbonates. The crystallographic information files (CIFs) of corundum and calcium carbonates used in the Rietveld refinement are listed as follow in Table 6-6.

The CIF used to simulate the pattern of C-S-H can be found in the section 5.3.3.3 of Chapter 5, Table 5-5.

The refinement results of C-S-H gels with a C/S ratio of 1.18, carbonated for different days, are illustrated from Figure 6-10 to Figure 6-13.

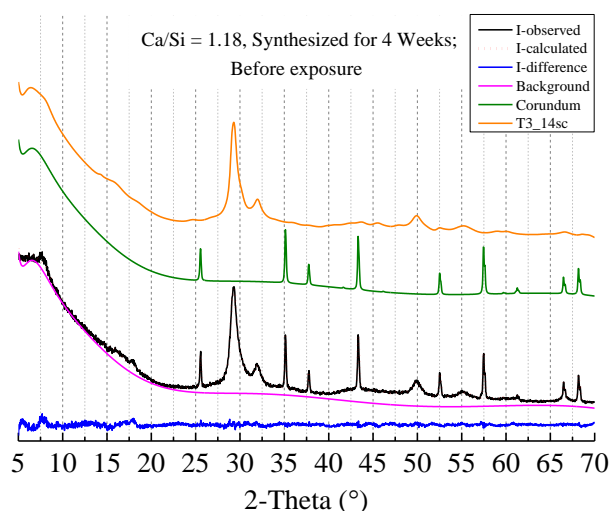


Figure 6-10 Rietveld refinement result of C-S-H (C/S = 1.18) before exposure to carbonation



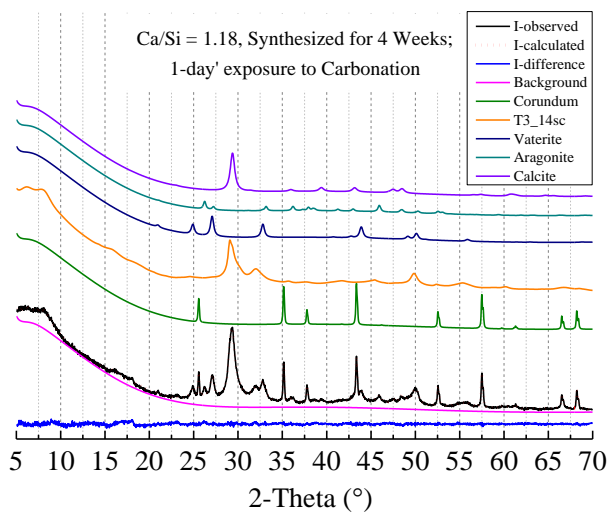


Figure 6-11 Rietveld refinement result of C-S-H ( $C/S = 1.18$ ) after 1-day's exposure to carbonation

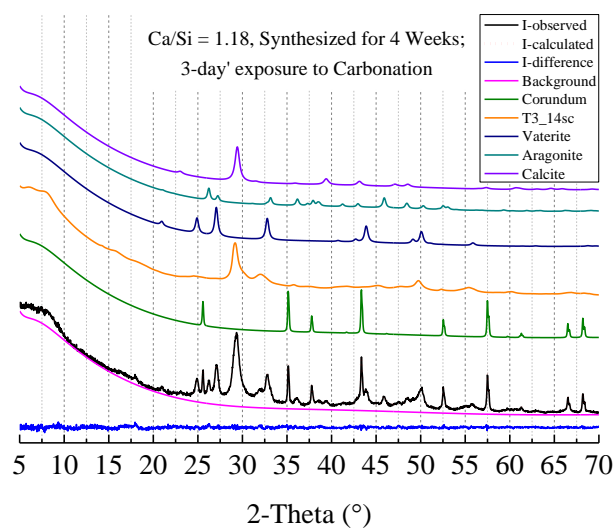


Figure 6-12 Rietveld refinement result of C-S-H ( $C/S = 1.18$ ) after 3-day's exposure to carbonation

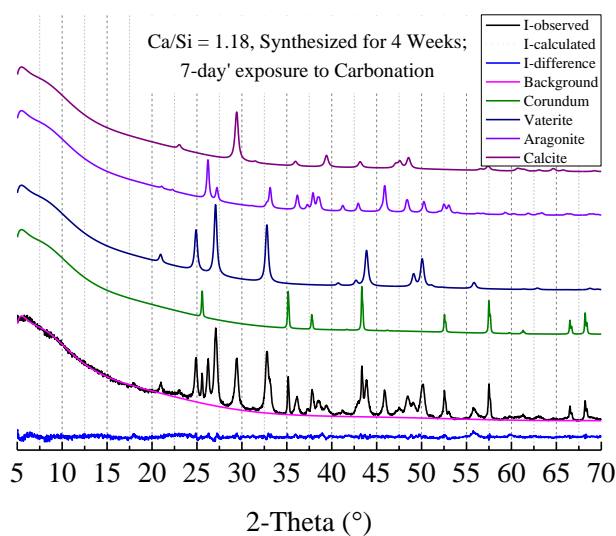


Figure 6-13 Rietveld refinement result of C-S-H ( $C/S = 1.18$ ) after 7-days exposure to carbonation

From the Rietveld refinement results, the relative quantities of different crystal phases in the C-S-H gels with C/S ratios of 0.66, 0.86, 1.18, 1.40, 1.70 and 2.00 before and after carbonation are calculated and listed in *Table 6-7* to *Table 6-12*.

*Table 6-7 Relative quantities (wt %) of different phases in the C-S-H gel (C/S = 0.66) exposed to the carbonation for different days*

C/S	Exposure Time (Day)	Refine Result Evaluation			Relative Quantities (wt %)				
		*R <sub>wp</sub>	*R <sub>exp</sub>	* $\chi^2$	Al <sub>2</sub> O <sub>3</sub>	Tinf_sc_noCa_LS2	Vaterite	Aragonite	Calcite
0.66	0	3.54	2.54	1.94	17.03	82.90	0.00	0.00	0.00
	1	3.58	2.45	2.14	15.80	36.20	44.65	1.79	1.64
	3	4.20	2.48	2.87	15.76	19.50	60.35	2.35	2.08
	7	4.68	2.35	3.97	13.73	0	80.10	3.80	2.37

*Table 6-8 Relative quantities (wt %) of different phases in the C-S-H gel (C/S = 0.86) exposed to the carbonation for different days*

C/S	Exposure Time (Day)	Refine Result Evaluation			Relative Quantities (wt %)					
		*R <sub>wp</sub>	*R <sub>exp</sub>	* $\chi^2$	Al <sub>2</sub> O <sub>3</sub>	Tinf_11ac	T5_14sc	Vaterite	Aragonite	Calcite
0.86	0	3.33	2.61	1.63	17.51	31.10	36.60	0.00	0.00	0.00
	1	3.28	2.29	2.05	15.79	35.10	47.40	39.30	0.31	1.16
	3	3.35	2.48	1.82	14.39	25.80	17.60	45.24	0.88	1.46
	7	5.78	2.41	5.75	15.65	22.20	15.80	81.34	0.99	2.02

*Table 6-9 Relative quantities (wt %) of different phases in the C-S-H gel (C/S = 1.18) exposed to the carbonation for different days*

C/S	Exposure Time (Day)	Refine Result Evaluation			Relative Quantities (wt %)				
		*R <sub>wp</sub>	*R <sub>exp</sub>	* $\chi^2$	Al <sub>2</sub> O <sub>3</sub>	T3_14sc	Vaterite	Aragonite	Calcite
1.18	0	3.93	2.70	2.12	13.84	86.16	0.00	0.00	0.00
	1	4.05	2.56	2.50	15.45	43.70	24.21	7.75	8.88
	3	3.69	2.49	2.20	15.20	31.14	35.60	8.43	9.62
	7	4.25	2.49	2.91	13.45	0.00	56.98	17.81	11.76

*Table 6-10 Relative quantities (wt %) of different phases in the C-S-H gel (C/S = 1.40) exposed to the carbonation for different days*

C/S	Exposure Time (Day)	Refine Result Evaluation			Relative Quantities (wt %)					
		*R <sub>wp</sub>	*R <sub>exp</sub>	* $\chi^2$	Al <sub>2</sub> O <sub>3</sub>	T3_14sc	T2_sc_LS1	Vaterite	Aragonite	Calcite
1.40	0	4.31	2.62	2.71	11.69	23.40	64.90	0.00	0.00	0.00
	1	4.48	2.54	3.11	13.40	15.41	44.50	16.28	2.40	7.98
	3	4.67	2.55	3.35	14.56	12.78	28.00	30.40	4.32	9.95
	7	4.27	2.52	2.87	13.42	0.00	0.00	59.08	12.71	14.79

Table 6-11 Relative quantities (wt %) of different phases in the C-S-H gel ( $C/S = 1.70$ ) exposed to the carbonation for different days

C/S	Exposure Time (Day)	Refine Result Evaluation			Relative Quantities (wt %)						
		* $R_{wp}$	* $R_{exp}$	* $\chi^2$	Al <sub>2</sub> O <sub>3</sub>	T3_14sc	T2_sc_LS1	Ca(OH) <sub>2</sub>	Vaterite	Aragonite	Calcite
1.70	0	3.60	2.62	1.89	12.59	21.10	64.40	1.87	0.00	0.00	0.00
	1	3.27	2.56	1.63	12.21	16.20	17.10	1.30	35.66	4.55	12.98
	3	3.59	2.53	2.01	11.21	2.61	25.40	0.34	39.40	5.61	15.48
	7	4.09	2.44	2.81	11.61	0.00	0.00	0.00	59.24	11.26	17.89

Table 6-12 Relative quantities (wt %) of different phases in the C-S-H gel ( $C/S = 2.00$ ) exposed to the carbonation for different days

C/S	Exposure Time (Day)	Refine Result Evaluation			Relative Quantities (wt %)						
		* $R_{wp}$	* $R_{exp}$	* $\chi^2$	Al <sub>2</sub> O <sub>3</sub>	T3_14sc	T2_sc_LS1	Ca(OH) <sub>2</sub>	Vaterite	Aragonite	Calcite
2.00	0	3.48	2.62	1.76	12.43	27.10	54.00	6.48	0.00	0.00	0.00
	1	3.37	2.45	1.89	13.47	14.42	13.47	2.14	40.55	5.91	9.77
	3	3.93	2.63	2.23	11.99	7.31	8.55	1.14	48.49	6.76	15.76
	7	4.10	2.33	3.10	11.88	0.00	0.00	0.39	60.56	10.26	16.87

\* Rietveld reliability factors, including weighted profile R-factor( $R_{wp}$ ), expected R factor( $R_{exp}$ ) and goodness of fit or Chi squared,  $\chi^2 = (R_{wp}/R_{exp})^2$  [5].

Polymorph compositions of CaCO<sub>3</sub> found in the C-S-H gels with different C/S ratios exposed to carbonation are illustrated in Figure 6-14.

Based on the refinement results, the vaterite is the major carbonate produced from the carbonation of C-S-H, regardless the C/S ratio. Only small amounts of aragonite and calcite will be formed during the carbonation of C-S-H with lower C/S ratio ( $C/S = 0.66$  or  $0.86$ ). The amount of aragonite and calcite increased a lot for C/S ratios 1.18 or even higher.

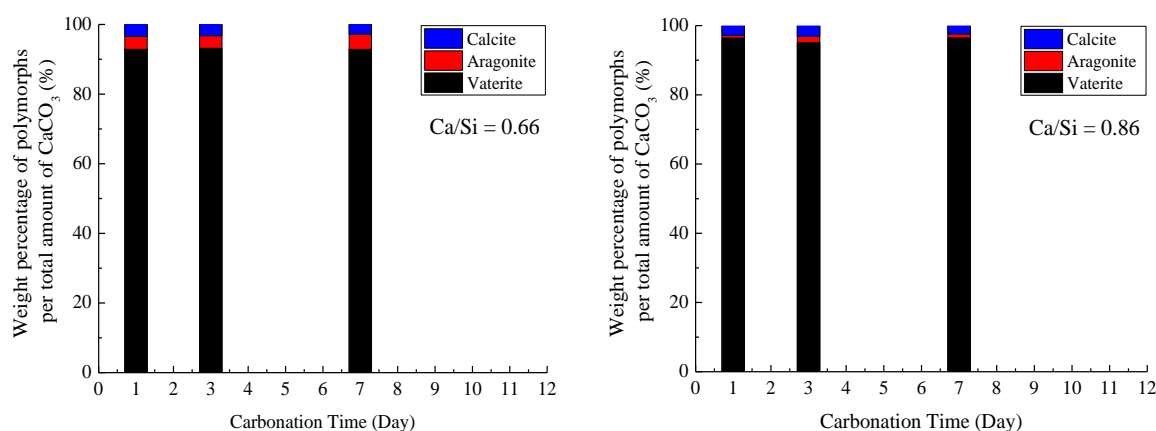


Figure 6-14 Polymorph amounts of calcium carbonates in the carbonation products of C-S-H,  $C/S = 0.66 - 2.00$

To be continued on next page →

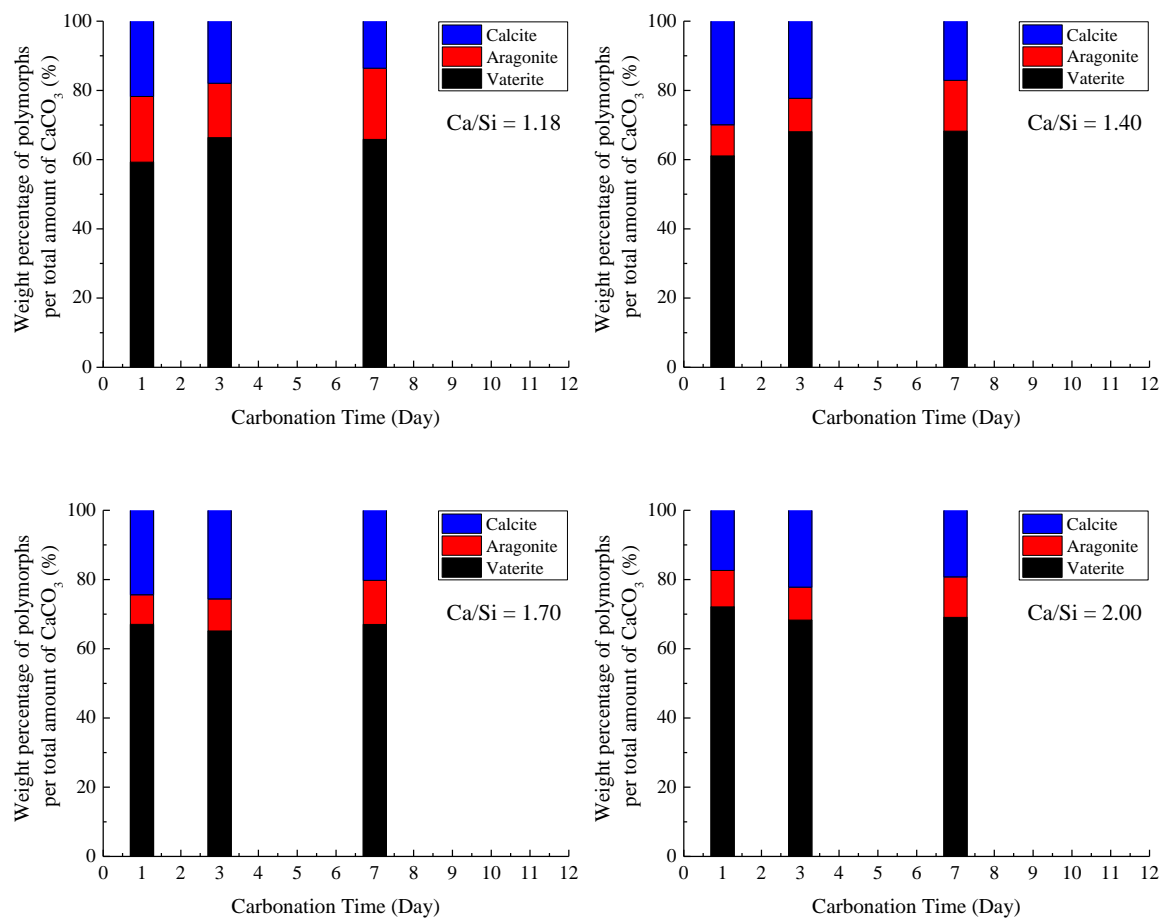


Figure 6-14 - continued - Polymorph amounts of calcium carbonates in the carbonation products of C-S-H, C/S = 0.66 - 2.00

### 6.3.3 Carbonation rate of C-S-H gels with different C/S

As mentioned in section 6.2.2, the carbonation of C-S-H is a complex decalcification-polymerization process of the C-S-H, which can be described with Eq. 6-1. The average carbonation rate (if not specially specified, the carbonation rate in the following discussion is indicating the average carbonation rate of the C-S-H gel) can be calculated based on the amounts of  $\text{CaCO}_3$  formed and changes with exposure time. The relative amounts of  $\text{CaCO}_3$  formed in the C-S-H gel after each carbonation time, were discussed in section 6.3.2 and are listed in Table 6-7 to Table 6-12.

As the total weight of the solid is changed with the carbonation, the relative quantities of  $\text{CaCO}_3$  shall be normalized to the initial weight of C-S-H gels and expressed as the unit of g per g of initial C-S-H gels. The carbonation rate will be calculated based on the normalized amount. The calculation of the carbonation rate of C-S-H runs as follows.

Since  $\text{Al}_2\text{O}_3$  (corundum) is not involved in the reaction, the amount of this internal standard  $m_{\text{Al}_2\text{O}_3}(t)$  [g] can be calculated with Eq. 6-2 and Eq. 6-3:

$$m_{Al_2O_3}(t)(g) = m_{cr}(t) \times w_{Al_2O_3}^{rel}(t) \quad \text{Eq. 6-2}$$

or

$$m_{Al_2O_3}(t_0)(g) = m_{cr}(t_0) \times w_{Al_2O_3}^{rel}(t_0) \quad \text{Eq. 6-3}$$

in which  $m_{Al_2O_3}(t)$  [g] is the weight of  $Al_2O_3$  in the carbonation products of C-S-H gel after the carbonation time  $t$  [day];  $m_{cr}(t_0)$  [g] is the initial weight of crystal phases identified by XRD in the C-S-H gel;  $m_{cr}(t)$  [g] is the total weight of crystals in the C-S-H gel after carbonation time of  $t$  [day].  $w_{Al_2O_3}^{rel}(t_0)$  and  $w_{Al_2O_3}^{rel}(t)$  are the relative weight percentage of  $Al_2O_3$  in the crystals at the beginning and after carbonation of  $t$  [day].

The total crystal weight  $m_{cr}(t)$  [g] can be normalized to the initial crystal weight  $m_{cr}(t_0)$  [g]. The normalized total crystal weight  $m_{cr}^{nor}(t)$  [g] is indicated in Eq. 6-4:

$$m_{cr}^{nor}(t)(g/g) = \frac{m_{cr}(t)}{m_{cr}(t_0)} = \frac{w_{Al_2O_3}^{rel}(t_0)}{w_{Al_2O_3}^{rel}(t)} \quad \text{Eq. 6-4}$$

Following the same method, the weight of  $CaCO_3$  at exposure time  $t$  (day) can be normalized to the initial total weight of crystal phases and expressed in Eq. 6-5:

$$m_{cc}^{nor-cr}(t)(g/g) = \frac{m_{cc}(t)}{m_{cr}(t_0)} = \frac{m_{cc}(t)}{m_{cr}(t)} \times \frac{m_{cr}(t)}{m_{cr}(t_0)} = \frac{m_{cc}(t)}{m_{cr}(t)} \times \frac{w_{Al_2O_3}^{rel}(t_0)}{w_{Al_2O_3}^{rel}(t)} = w_{cc}^{rel}(t) \times \frac{w_{Al_2O_3}^{rel}(t_0)}{w_{Al_2O_3}^{rel}(t)} \quad \text{Eq. 6-5}$$

in which  $m_{cc}^{nor-cr}(t)(g/g)$  and  $w_{cc}^{rel}(t)$  are the normalized weight (to the initial crystal weight) and relative weight percentage of  $CaCO_3$  at exposure time  $t$  (day) respectively. This equation is used for the calculation of the normalized weight of three polymorphs of  $CaCO_3$  and other crystals listed in *Table 6-7* to *Table 6-12*.

Following the illustration in *Figure 3-2*, the initial composition of C-S-H phases mixed with internal standard  $Al_2O_3$  can be described as follow in *Figure 6-15*.

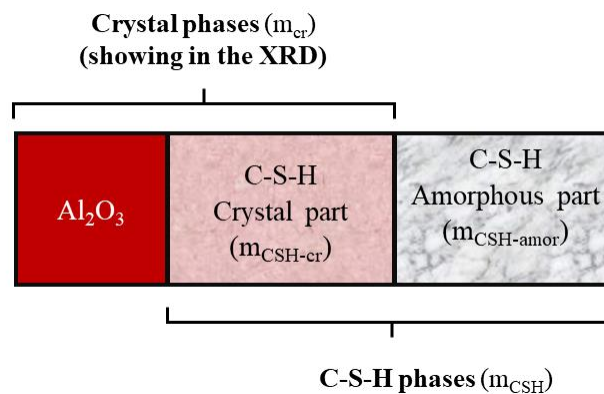


*Figure 6-15 Schematic of initial phase compositions of C-S-H gel mixed with internal standard ( $Al_2O_3$ )*

The weight of  $\text{CaCO}_3$ , i.e.  $m_{\text{c}\bar{\text{c}}}(t)$ , at exposure time  $t$  (day) will be normalized to the initial total weight of C-S-H gel and described in Eq. 6-6:

$$m_{\text{c}\bar{\text{c}}}^{\text{nor-CSH}}(t)(g/g) = \frac{m_{\text{c}\bar{\text{c}}}(t)}{m_{\text{CSH}}(t_0)} = \frac{m_{\text{c}\bar{\text{c}}}(t)}{m_{\text{cr}}(t_0)} \times \frac{m_{\text{cr}}(t_0)}{m_{\text{CSH-cr}}(t_0)} \times \frac{m_{\text{CSH-cr}}(t_0)}{m_{\text{CSH}}(t_0)} \quad \text{Eq. 6-6}$$

where  $(m_{\text{c}\bar{\text{c}}}(t))/(m_{\text{cr}}(t_0))$  is the weight normalized to initial total crystal weight, described in Eq. 6-5. The terms  $(m_{\text{cr}}(t_0))/(m_{\text{CSH-cr}}(t_0))$  and  $(m_{\text{CSH-cr}}(t_0))/(m_{\text{CSH}}(t_0))$  are related to the weight percentage of the crystal portion in C-S-H to the total initial weight of crystal phases identified by XRD and to the total initial weight of C-S-H gel, respectively. They are expressed in Eq. 6-7 and Eq. 6-8.

$$\frac{m_{\text{cr}}(t_0)}{m_{\text{CSH-cr}}(t_0)} = \frac{1}{w_{\text{CSH-cr}}^{\text{rel}}(t_0)} \quad \text{Eq. 6-7}$$

$$\frac{m_{\text{CSH-cr}}(t_0)}{m_{\text{CSH}}(t_0)} = \frac{w_{\text{CSH-cr}}^{\text{rel}}(t_0) \times \frac{w_{\text{Al}_2\text{O}_3}^{\text{abs}}(t_0)}{w_{\text{Al}_2\text{O}_3}^{\text{rel}}(t_0)}}{1 - w_{\text{Al}_2\text{O}_3}^{\text{abs}}(t_0)} \quad \text{Eq. 6-8}$$

where  $w_{\text{CSH-cr}}^{\text{rel}}(t_0)$ ,  $w_{\text{Al}_2\text{O}_3}^{\text{rel}}(t_0)$  denote the relative weight percentage of the crystal phases and internal standard  $\text{Al}_2\text{O}_3$  in the initial C-S-H gel mixed with  $\text{Al}_2\text{O}_3$ . These two values can be found from the Rietveld refined results listed in *Table 6-7* to *Table 6-12*.  $w_{\text{Al}_2\text{O}_3}^{\text{abs}}(t_0)$  is the absolute weight percentage of  $\text{Al}_2\text{O}_3$  in the initial C-S-H gel mixed with  $\text{Al}_2\text{O}_3$ , which is listed in *Table 6-5*.

After calculation of the normalized weight of  $\text{CaCO}_3$  produced during exposure to  $\text{CO}_2$ , the carbonation rate (reaction rate) can be calculated by Eq. 6-9.

$$r_{\text{c}\bar{\text{c}}} = -\frac{d[C_xSH_y]}{dt} = \frac{1}{x} \times \frac{d[C\bar{C}]}{dt} (g/g/day) \quad \text{Eq. 6-9}$$

where  $[C_xSH_y]$ ,  $[C\bar{C}]$  denotes the concentration of the  $C_xSH_y$ , or  $C\bar{C}$ . The concentration of  $\text{CaCO}_3$  is expressed as the weight per the initial weight of C-S-H ( $g/g$ ), which is the normalized weight mentioned in Eq. 6-6.

Based on the relative quantities, the normalized weight of different polymorphs of  $\text{CaCO}_3$  produced are calculated for different C-S-H gels when carbonated for different time. The calculated normalized weights of  $\text{CaCO}_3$  polymorphs are listed in *Table 6-13*.

Table 6-13 Normalized weight (g/g) of different  $\text{CaCO}_3$  polymorphs produced in the C-S-H gel (C/S = 0.66 to 2.00) exposed to the carbonation for different days

C/S	Exposure Time (Day)	Normalized Weights (g / 1 g of initial C-S-H gel)		
		Vaterite	Aragonite	Calcite
0.66	0	0.00	0.00	0.00
	1	0.929	0.037	0.034
	3	0.932	0.036	0.032
	7	0.928	0.044	0.027
0.86	0	0.00	0.00	0.00
	1	0.964	0.008	0.028
	3	0.951	0.018	0.031
	7	0.964	0.012	0.024
1.18	0	0.00	0.00	0.00
	1	0.593	0.190	0.217
	3	0.664	0.157	0.179
	7	0.658	0.206	0.136
1.40	0	0.00	0.00	0.00
	1	0.611	0.090	0.299
	3	0.681	0.097	0.223
	7	0.682	0.147	0.171
1.70	0	0.00	0.00	0.00
	1	0.670	0.086	0.244
	3	0.651	0.093	0.256
	7	0.670	0.127	0.202
2.00	0	0.00	0.00	0.00
	1	0.721	0.105	0.174
	3	0.683	0.095	0.222
	7	0.691	0.117	0.192

Especially, the normalized amount of portlandite was calculated for C-S-H gels before the exposure. Then, the amount of  $\text{CaCO}_3$  produced by the carbonation of portlandite in some C-S-H gels (C/S ratio of 1.7 or 2.0) was subtracted from the total amount of carbonates, to calculate the amount of  $\text{CaCO}_3$  produced from the carbonation of C-S-H gels. Total normalized weight of  $\text{CaCO}_3$  is plotted versus the carbonation time in *Figure 6-16*.

By fitting the data in *Figure 6-16*, a liner relation is built between the total amount  $\text{CaCO}_3$  and carbonation time. Apparently, the total normalized amount of  $\text{CaCO}_3$  (divided by the C/S of C-S-H) formed from the carbonation of C-S-H is in a linear relation with the carbonation time. The slope is indicating the carbonation rate ( $\text{g} / \text{g} / \text{day}$ ) of  $\text{CaCO}_3$  referring to Eq. 6-9.

The carbonation rate of C-S-H is constant for all the studied C-S-H gels. Carbonation rate expressed here actually is the general crystal growth rate of  $\text{CaCO}_3$ . Formation of  $\text{CaCO}_3$  crystal consists of two processes: crystal nucleation and growth. In the initial nucleation stage, crystal nucleus with different particle sizes are simultaneously nucleated and then growing with the time. According to the crystal growth rate dispersion (GRD) model [6], which is describing the variation in the crystal growth rates within a population of crystals. In this

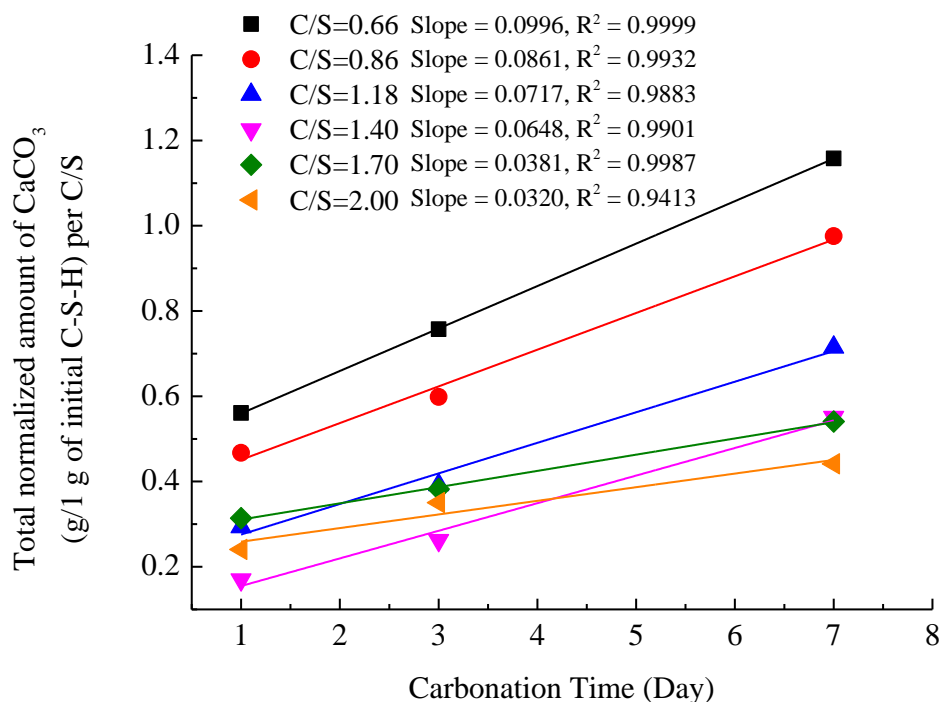


Figure 6-16 Development of total  $\text{CaCO}_3$  amount produced from the carbonation of C-S-H with exposure time

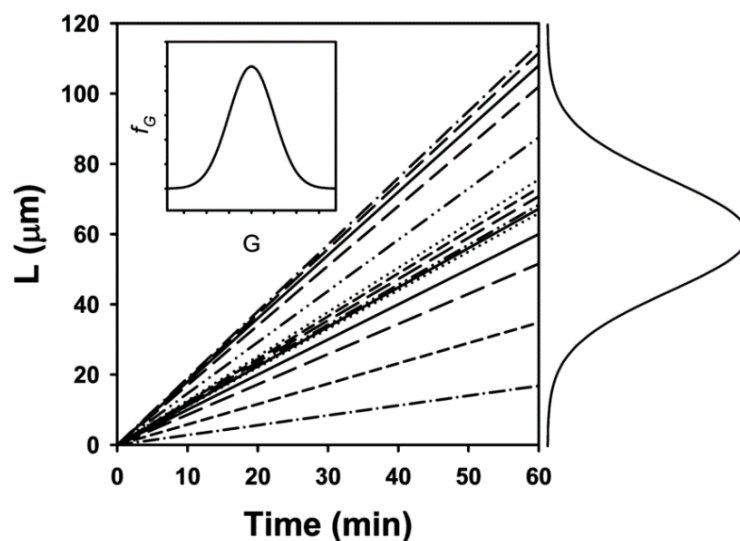


Figure 6-17 Expected sizes of individual particles in a batch growth cell vs time; the growth rate distribution is shown in the inset, after [6]

model, each individual crystal is growing with a unique constant rate (see Figure 6-17). The crystal growth rate dispersion is the assembling of all the growth rates of every individual crystal in the population. And the particle size distribution at any time is a linear expansion of the growth rate distribution, shown in Figure 6-17. Thus, the overall crystal growth rate of the whole population should be a constant as well. This is exactly what is observed in Figure 6-16.



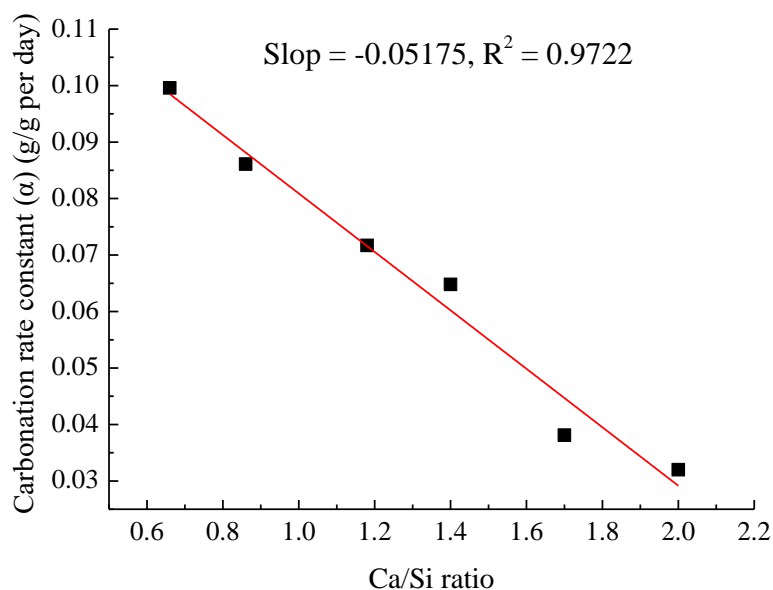


Figure 6-18 Relation between carbonation rate related constant and C/S of C-S-H powder

Furthermore, the carbonation rate constant of C-S-H powder calculated by the above-mentioned method and are plotted against the C/S ratio in *Figure 6-18*. Apparently, the carbonation rate constant of C-S-H gels in powder status has a good negative linear correlation with the C/S ratio. The higher the C/S ratio, the lower the carbonation rate constant. It can be concluded that the C-S-H with relative higher C/S ratio has a higher resistance to carbonation.

### 6.3.4 Carbonation of C-S-H gels in the early stage

#### 6.3.4.1 Carbonation rate tested by FTIR

In section 6.3.1, the XRD and  $^{29}\text{Si}$  NMR test results of C-S-H gels exposed to accelerated carbonation for days were discussed. However, the carbonation process was developed so fast, that only the final carbonation products were found. In order to observe the changes of the silicate chain structure in the early exposure stage, FTIR tests were performed on the C-S-H gels with different C/S ratio, exposed to accelerated carbonation for hours, varying from 0.5 h to 24 h. The FTIR test results are shown in *Figure 6-19*.

In the FTIR spectra of C-S-H, there is a characteristic peak at around  $970\text{ cm}^{-1}$ . This peak indicates the Si-O stretching vibrations of  $\text{Q}^2$  tetrahedra. It shifts to the lower frequency (higher wavenumber in FTIR spectra) with the increasing of C/S [7-9]. On the contrary, it shifts to higher frequency (lower wavenumber in FTIR spectra) after carbonation, see *Figure 6-19*. Meanwhile, the intensity of the peak at around  $970\text{ cm}^{-1}$  decreases dramatically.

The shoulder peak at around  $1066\text{ cm}^{-1}$ , indicating the Si-O stretching vibrations of  $\text{Q}^2$  tetrahedra, is showing an obvious growth in the intensity after carbonation. This peak only appears in the FTIR spectrum of C-S-H with low C/S ratio or in the tobermorite. The changes of these two peaks during carbonation reveal the progressive polymerization of silicate chains.

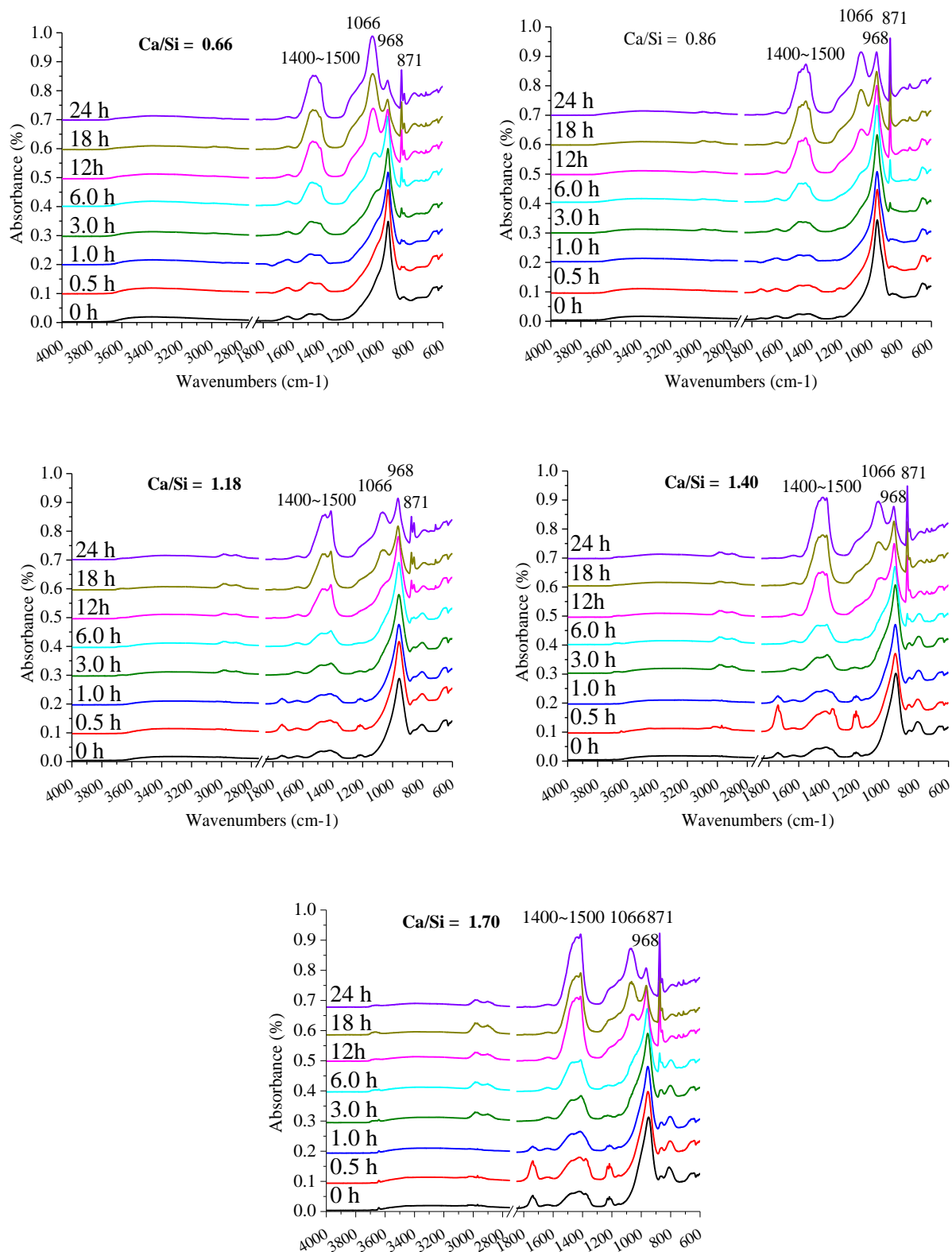


Figure 6-19 FTIR test of C-S-H, C/S = 0.66 - 1.70, exposed to carbonation for hours, from 0.5 to 24 hours

The peak at around 875 and 1400-1500 cm<sup>-1</sup> represents the bending of CO<sub>3</sub><sup>2-</sup> ( $\nu_2$ ) and the stretching of CO<sub>3</sub><sup>2-</sup> ( $\nu_3$ ), respectively. Both have a dramatic increase in the intensity when the

shoulder peak ( $1066\text{ cm}^{-1}$ ) grows into an obvious and independent peak. For example, it can be observed in the spectrum of C-S-H with the C/S ratio of 0.66, carbonated for 3 h. This ‘critical’ time is 6 h for the C-S-H with C/S ratios 0.86 and 12 h for the rest three C-S-H phases (C/S = 1.18, 1.40 and 1.70). The changes of these peaks in the FTIR spectra indicate that the destruction of the silicate chain in the C-S-H is starting under carbonation. Comparing the ‘critical’ time identified for different C-S-H gels, it can be concluded that C-S-H with a higher C/S ratio decomposed at a lower rate than that of C-S-H with a lower C/S ratio.

## 6.4 Conclusions

In this chapter, the accelerated carbonation was performed on the C-S-H gels with different C/S ratio. The  $\text{CO}_2$  concentration in the carbonation chamber was maintained at  $3\% \pm 0.2$  (V/V), which is relatively higher than that in ambient condition. The carbonation products are identified by means of XRD,  $^{29}\text{Si}$  NMR, and FTIR. Both qualitative and quantitative information related to the carbonation rate of different C-S-H gels are collected and compared. The main conclusions are as follow:

- ◆ Carbonation products of C-S-H are calcium carbonate ( $\text{CaCO}_3$ ) and silica gel.
- ◆ Three polymorphs of  $\text{CaCO}_3$  are found in the carbonation products of C-S-H with different C/S ratio, i.e., Calcite, Aragonite and Vaterite ( $\mu\text{-CaCO}_3$ ), but in different amounts.
- ◆ Vaterite is the major carbonate in carbonation products of C-S-H. Limited amount of aragonite and calcite can be observed in the carbonation products of C-S-H with relatively lower C/S ratio (0.66 or 0.86). A dramatic increase of the amount of aragonite and calcite is only found in carbonation product of C-S-H with relatively high C/S ratio, i.e.,  $\text{C/S} > 0.86$ .
- ◆ Carbonation rate of C-S-H powder is calculated in this study, based on the changes of calcium carbonate amount with the carbonation time, which represents the average carbonation rate of the C-S-H powder. This carbonation rate is a constant value for each C-S-H gel studied.
- ◆ The carbonation rate constant of C-S-H is decreasing with increasing C/S ratio; it has a negative linear correlation with the C/S ratio (*Figure 6-18*).
- ◆ C-S-H gel with relatively high C/S ratio has a lower carbonation rate, confirmed by both the calculated carbonation rate constant of C-S-H powder and by the test results of FTIR, which has a better resistance to carbonation under the same conditions.
- ◆ Although the carbonation rate is determined for C-S-H powder in this study, the relative carbonation rate of C-S-H with different C/S ration can be introduced in the calculation of carbonation depth developed in the concrete, when modelling the depth from the chemical reaction point of view.

## 6.5 References

- [1] L. Black, C. Breen, J. Yarwood, K. Garbev, P. Stemmermann, B. Gasharova, Structural features of C–S–H (I) and its carbonation in air—a Raman spectroscopic study. Part II: carbonated phases, *J Am Ceram Soc*, 90 (2007) 908-917.
- [2] V.r.L. Zdeněk Šauman, Long-term carbonization of the phases  $3\text{CaO}\cdot\text{Al}_2\text{O}_3\cdot 6\text{H}_2\text{O}$  and  $3\text{CaO}\cdot\text{Al}_2\text{O}_3\cdot\text{SiO}_2\cdot 4\text{H}_2\text{O}$ , *Cement Concrete Res*, 2 (1972) 12.
- [3] A. Morandea, M. Thiery, P. Dangla, Investigation of the carbonation mechanism of CH and CSH in terms of kinetics, microstructure changes and moisture properties, *Cement Concrete Res*, 56 (2014) 153-170.
- [4] N. Doebelin, R. Kleeberg, Profex: a graphical user interface for the Rietveld refinement program BGMN, *Journal of applied crystallography*, 48 (2015) 1573-1580.
- [5] B.H. Toby, R factors in Rietveld analysis: How good is good enough?, *Powder diffraction*, 21 (2006) 67-70.
- [6] S. Srisanga, A.E. Flood, S.C. Galbraith, S. Rugmai, S. Soontaranon, J. Ulrich, Crystal Growth Rate Dispersion versus Size-Dependent Crystal Growth: Appropriate Modeling for Crystallization Processes, *Crystal Growth & Design*, 15 (2015) 2330-2336.
- [7] P. Yu, R.J. Kirkpatrick, B. Poe, P.F. McMillan, X. Cong, Structure of Calcium Silicate Hydrate (C - S - H): Near -, Mid -, and Far - Infrared Spectroscopy, *J Am Ceram Soc*, 82 (1999) 742-748.
- [8] D. Sykes, J.D. Kubicki, A model for H<sub>2</sub>O solubility mechanisms in albite melts from infrared spectroscopy and molecular orbital calculations, *Geochim Cosmochim Ac*, 57 (1993) 1039-1052.
- [9] P.F. McMillan, G.H. Wolf, B.T. Poe, Vibrational spectroscopy of silicate liquids and glasses, *Chemical Geology*, 96 (1992) 351-366.

## Implementation

In practice, a well-known square-root empirical equation is used for the prediction of carbonation depth developed in Portland cement concrete (see also Ch. 2). However, the experimental studies in this thesis revealed that the carbonation of C-S-H phases plays a very important role in the carbonation of blended cement paste, which is not considered in the empirical equation used in practice for predicting the rate of carbonation in Portland cement concrete. Therefore, the improved empirical equation will be developed for the blended cement concrete in this chapter.

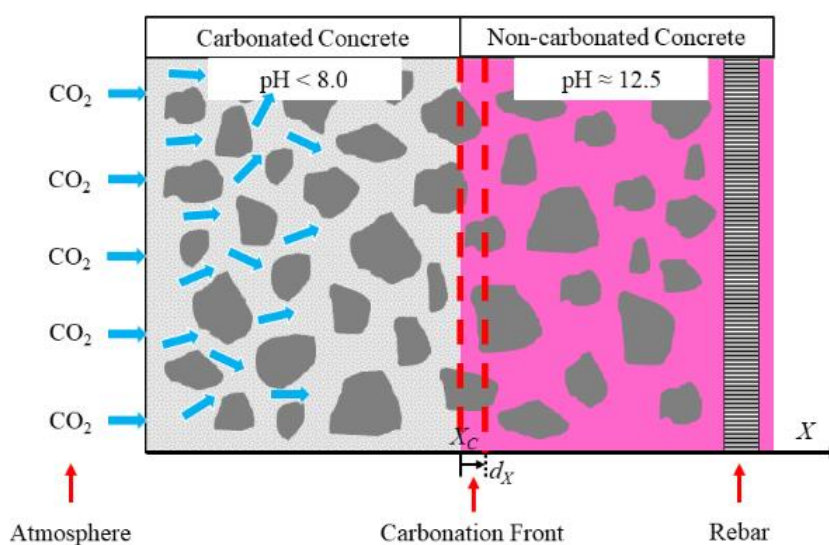


Figure 7-1 Illustration of an arbitrary stage of the carbonation process in concrete.

## 7.1 Modelling strategy

The desired improved predictive formula focuses on the mass balances of the major phases involved in the physico-chemical processes happening in the carbonation front, illustrated in *Figure 7-1*.

At the carbonation front, hydration, carbonation and CO<sub>2</sub> diffusion happen simultaneously. For each phase involved, the equation related to mass balance is built. In the end they are combined into the mass balance of CO<sub>2</sub> as basis for an improved equation for predicting the carbonation depth, which is the function of phase concentration, diffusion coefficient of CO<sub>2</sub> and time. The final equation will be validated by the experimental data from Chapter 3 and 4.

In Chapter 3, a few mixtures of cement paste were designed. For a certain mixture, the concentration of phases present prior to carbonation are measured and are used as input. After accelerated carbonation tests (Chapter 4), the porosities of totally carbonated samples are measured and used to calculate the CO<sub>2</sub> diffusion coefficient. In the end, the calculated improved equation will be validated by the carbonation depth data measured in Chapter 4. The modelling strategy is described in *Figure 7-2*.

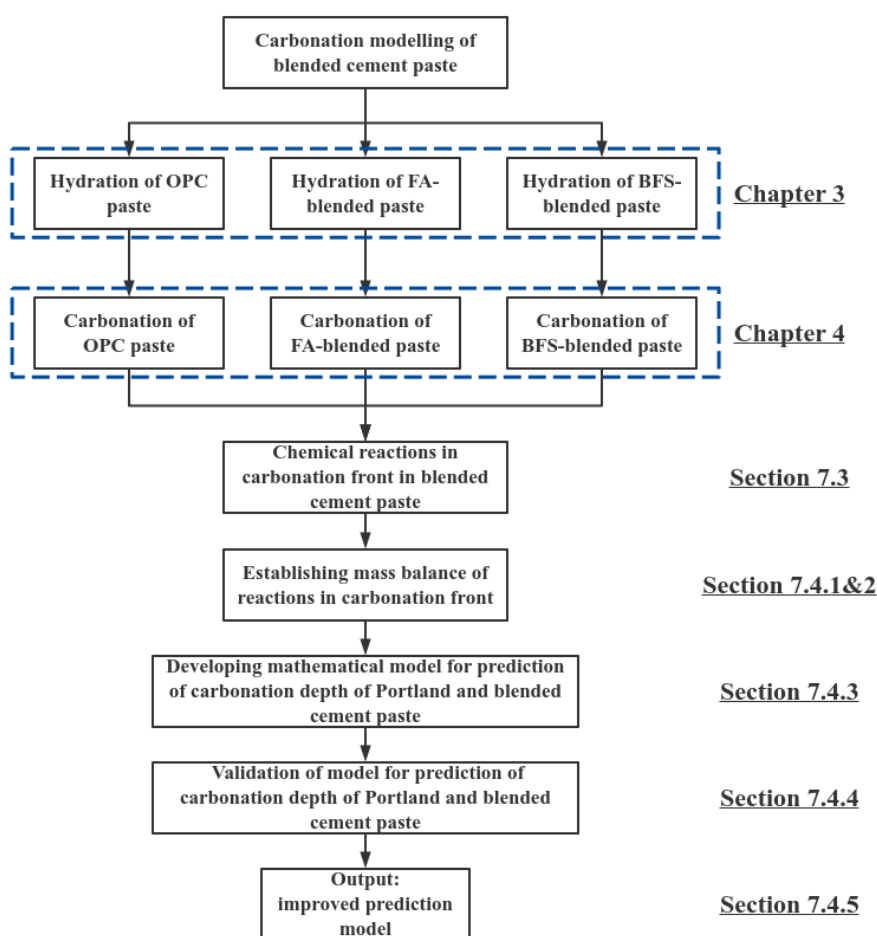


*Figure 7-2 Schematic of modelling strategy*

## 7.2 Physicochemical processes involved in carbonation

The physico-chemical processes involved in the carbonation of blended concrete are:

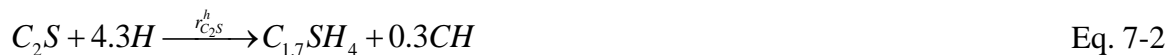
- The chemical reactions including hydration and pozzolanic reactions from where calcium-bearing phases are formed.
- The diffusion of atmospheric CO<sub>2</sub> in the gaseous phases in the concrete pores.
- The dissolution and diffusion of solid Ca(OH)<sub>2</sub> in the pore water.
- The dissolution of CO<sub>2</sub> and its reaction with dissolved Ca(OH)<sub>2</sub> in the pore water.
- The reaction of CO<sub>2</sub> with other solid calcium-bearing phases, e.g. unhydrated C<sub>3</sub>S and C<sub>2</sub>S.
- The reduction of the pore volume due to the production of solid phases during the hydration and carbonation.
- The condensation of water vapour on the walls of concrete pores, in equilibrium to the ambient temperature and relative humidity conditions.

In the following study, these processes are quantitatively described by a mathematical model in details.

## 7.3 Chemical reactions in blended cement paste

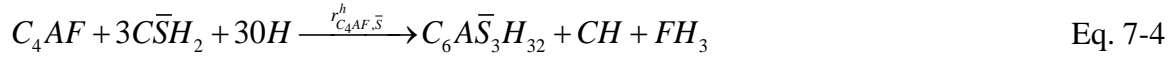
### 7.3.1 Hydration reactions in Portland cement and blended cement pastes

In blended cement pastes, chemical reactions include the hydration of Portland cement and pozzolanic reaction of SCMs. Calcium-bearing phases are produced from both. The major calcium-bearing phases involved in the carbonation of concrete are Ca(OH)<sub>2</sub> (CH or portlandite), calcium silicate hydrate (C-S-H) and still unhydrated silicates, i.e. tricalcium silicate, 3CaO·SiO<sub>2</sub> (C<sub>3</sub>S) and dicalcium silicate, 2CaO·SiO<sub>2</sub> (C<sub>2</sub>S). CH and C-S-H are the products of hydration of C<sub>3</sub>S and C<sub>2</sub>S [1-3]. The chemical composition of C-S-H is assumed to be C<sub>1.7</sub>SH<sub>4</sub> [4]:

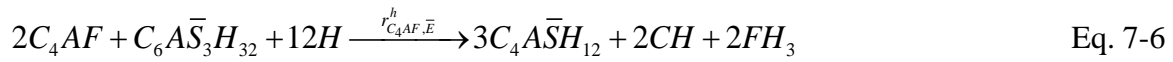


For the other two major minerals in cement clinker, i.e. C<sub>3</sub>A and C<sub>4</sub>AF, the chemical reactions are determined by the actual amounts of gypsum (C $\bar{S}$ H<sub>2</sub>) and ettringite (C<sub>6</sub>A $\bar{S}$ <sub>3</sub>H<sub>32</sub>) in the system [2, 3]. In formula form:

1. If gypsum is present in the system:



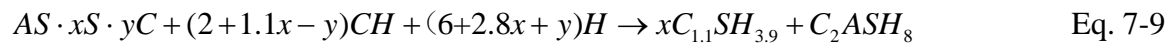
2. If gypsum is totally consumed and ettringite is present in the system:



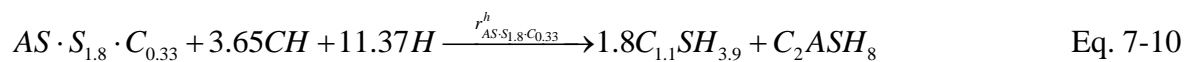
3. If both gypsum and ettringite are used up in the system:



C-S-H with relatively low Ca/Si ratio is produced from the pozzolanic reaction of fly ash (FA) and blast furnace slag (BFS), during which CH is consumed. The stoichiometry of pozzolanic reaction of FA is described in Eq. 7-9 (Bentz [5]):

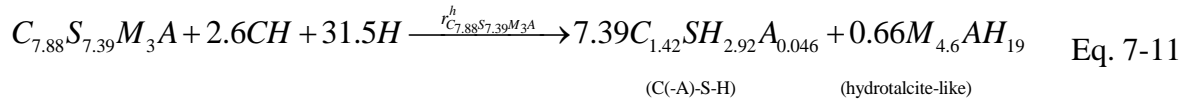


in which  $AS \cdot xS \cdot yC$  is the chemical formula of FA.  $x$  and  $y$  are stoichiometry coefficients, which can be calculated from the chemical composition of FA. For the chemical compositions of FA, listed earlier *Table 3-1*, the values of  $x$  and  $y$  are 1.80 and 0.33, respectively. The pozzolanic reaction of FA is rewritten accordingly as follows:



where  $C_{1.1}SH_{3.9}$  and  $C_2ASH_8$  are the C-S-H gel and strätlingite produced from the pozzolanic reaction of FA. According to Richardson [6] the stoichiometry in the pore solution of the reaction between BFS and portlandite can be described by Eq. 7-11:





The above-mentioned chemical reactions occur at molar rates  $r_i^h$  (in moles of reactant  $i$ , [m<sup>3</sup>/s]), in which the index  $i$  indicates the reacting constituent of Portland cement and SCMs, i.e.  $C_3S$ ,  $C_2S$  etc.. The superscript  $h$  denotes 'hydration'.

In the blended system, the molar rates (in moles of product  $i$ , [m<sup>3</sup>/s]) of production of C-S-H and CH, denoted by  $r_{CSH}^h$  and  $r_{CH}^h$  respectively, are:

$$r_{C_{1.7}SH}^h = r_{C_3S}^h + r_{C_2S}^h \quad \text{Eq. 7-12}$$

$$r_{C_{1.1}SH}^h = 1.8r_{AS_{51.8}C_{0.33}}^h \quad \text{Eq. 7-13}$$

$$r_{C_{1.42}SH}^h = 7.39r_{C_{7.88}S_{7.39}M_3A}^h \quad \text{Eq. 7-14}$$

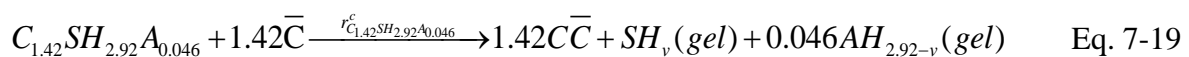
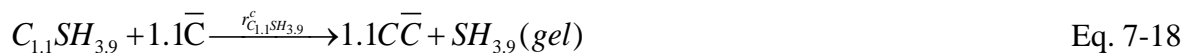
$$r_{CH}^h = 1.3r_{C_3S}^h + 0.3r_{C_2S}^h + 1.0r_{C_4AF}^h - 2.03r_{C_{1.1}SH}^h - 0.35r_{C_{1.42}SH}^h \quad \text{Eq. 7-15}$$

### 7.3.2 Carbonation reactions in Portland and blended cement pastes

The carbonation of portlandite in the cement paste happens, at a rate of  $r_{CH}^c$  (in moles of CH, solid, or dissolved [m<sup>3</sup>/s]):



The carbonation of C-S-H and unhydrated silicates takes place according to the following reactions:





The above-mentioned carbonation reactions occur at molar rates  $r_i^c$  (in moles of reactant  $i$ , [m<sup>3</sup>/s]), in which  $i$  refers to reacting constituent involved in the carbonation process. i.e.  $CH$ ,  $CSH$  etc.. The superscript  $c$  denotes ‘carbonation’.

### 7.3.3 Pore structure formation and diffusivity – Introductory comments

During the chemical reactions solid phases dissolve while forming a porous microstructure. The porosity  $\varepsilon$  of concrete changes with time according to:

$$\varepsilon(t) = \varepsilon_0 - \Delta\varepsilon_h(t) - \Delta\varepsilon_c(t) \quad \text{Eq. 7-22}$$

in which  $\varepsilon_0$  is the ratio of the volume of mixing water to the total volume of fresh concrete, and  $\Delta\varepsilon_h(t)$ ,  $\Delta\varepsilon_c(t)$  are the changes in porosity due to hydration and carbonation, respectively.

Diffusion of CO<sub>2</sub> takes place in the gas phase of the concrete pores, while the dissolved CH and CO<sub>2</sub> react in the pore solution. To compute the fraction of the pore volume filled with water, it is assumed that the amount of water in the pores is constant in time at constant ambient relative humidity and temperature, regardless the amount of water consumed or produced by hydration and carbonation. For a given relative humidity (RH), the pores with diameter less than the Kelvin diameter  $d_k$ , corresponding to RH, will be filled with water [7], whereas the walls of remaining pore will be covered with a thin film of water. The thickness  $w_T$  of the water film is determined by the prevailing relative humidity [7]. If the pore size distribution is known, the volume fraction  $f_K$  of the pores filled with water can be calculated, as well as the volume fraction  $f_w$  occupied by the film of water. The sum  $f = f_K + f_w$  is the volume fraction of the pores corresponding to the liquid phase and the rest,  $1 - f$ , is that of the gas phase. The magnitudes both  $f_w$  and  $f$  are necessary for the mathematical model described in the following paragraphs.

## 7.4 Mathematical model for predicting the carbonation depth

### 7.4.1 Mass balance at the reaction front of phases involved in carbonation

The mathematical model for predicting the carbonation depth is based on the mass-balances of phases involved in chemical and physical reactions happening at the carbonation front. Calculation of mass balance will be applied for CO<sub>2</sub>, CH, C-S-H and unhydrated C<sub>3</sub>S, C<sub>2</sub>S.

### Mass balance of CO<sub>2</sub>

In the carbonation front, the CO<sub>2</sub> is consumed during the chemical reactions between CO<sub>2</sub> and carbonatable phases. Meanwhile, fresh CO<sub>2</sub> is supplied continuously by the CO<sub>2</sub> diffusion. The instantaneous change of CO<sub>2</sub> amount can be expressed in the following equation.

$$\begin{aligned} \frac{d}{dt} [\varepsilon(1-f)[CO_2]] = \frac{d}{dx} \left( D_{e,CO_2} \frac{d[CO_2]}{dx} \right) \\ - \varepsilon^0 f_w r_{CH}^c - 1.7 r_{C_{1.7}SH}^c - 1.1 r_{C_{1.1}SH_{3.9}}^c - 1.42 r_{C_{1.42}SH_{2.92}A_{0.046}}^c \\ - 3r_{C_3S}^c - 2r_{C_2S}^c \end{aligned} \quad \text{Eq. 7-23}$$

in which  $x$  indicates the distance from the surface of the concrete and  $t$  denotes time.

### Mass balance of CH (solid or dissolved)

In the carbonation front, CH is consumed during the carbonation. Meanwhile, fresh CH is produced from hydration. The instantaneous change of CH amount can be expressed in the following equation.

$$\frac{d}{dt} [Ca(OH)_2] = r_{CH}^h - \varepsilon^0 f_w r_{CH}^c \quad \text{Eq. 7-24}$$

in which, the Ca(OH)<sub>2</sub> (aq) diffusion term is not considered, because it is negligibly small for relative humidity less than about 90% [8].

### Mass balance of C-S-H

In the carbonation front, C-S-H is consumed during the carbonation. Meanwhile, fresh C-S-H is produced from hydration. The instantaneous change of C-S-H amount can be expressed in the following equation.

$$\frac{d}{dt} [C_{1.7}SH] = r_{C_{1.7}SH}^h - r_{C_{1.7}SH}^c \quad \text{Eq. 7-25}$$

$$\frac{d}{dt} [C_{1.1}SH_{3.9}] = r_{C_{1.1}SH_{3.9}}^h - r_{C_{1.1}SH_{3.9}}^c \quad \text{Eq. 7-26}$$

$$\frac{d}{dt} [C_{1.42}SH_{2.92}A_{0.046}] = r_{C_{1.42}SH_{2.92}A_{0.046}}^h - r_{C_{1.42}SH_{2.92}A_{0.046}}^c \quad \text{Eq. 7-27}$$

Mass balance of unhydrated silicates

In the carbonation front, unhydrated silicates are consumed by both carbonation and hydration. The instantaneous change of C-S-H amount can be expressed in the following equation.

$$\frac{d}{dt}[C_3S] = -r_{C_3S}^h - r_{C_3S}^c \quad \text{Eq. 7-28}$$

$$\frac{d}{dt}[C_2S] = -r_{C_2S}^h - r_{C_2S}^c \quad \text{Eq. 7-29}$$

Considering Eq. 7-12 to Eq. 7-15, Eq. 7-24 through Eq. 7-29 in Eq. 7-23, mass balance of CO<sub>2</sub> can be described as follows:

$$\begin{aligned} 0 = & \frac{d}{dx} \left( D_{e,CO_2} \frac{d[CO_2]}{dx} \right) \\ & \text{(part 1)} \\ & + \frac{d}{dt} ([CH] + 1.7[C_{1.7}SH] + 1.1[C_{1.1}SH_{3.9}] + 1.42[C_{1.42}SH_{2.92}A_{0.046}] + 3[C_3S] + 2[C_2S]) \\ & \text{(part 2)} \\ & + (1.674r_{AS-S_{1.8}C_{0.33}}^h - 7.91r_{C_{7.88}S_{7.39}M_3A}^h - 1.0r_{C_4AF}^h) \\ & \text{(part 3)} \end{aligned} \quad \text{Eq. 7-30}$$

Assuming that the carbonation front is sharp and with no transition zone, the following conditions can be obtained:

$$\begin{aligned} [CO_2] = 0, [Ca(OH)_2] = [Ca(OH)_2]^0, [C_{1.7}SH] = [C_{1.7}SH]^0, \\ [C_{1.1}SH_{3.9}] = [C_{1.1}SH_{3.9}]^0, [C_{1.42}SH_{2.92}A_{0.046}] = [C_{1.42}SH_{2.92}A_{0.046}]^0 \\ [C_3S] = [C_3S]^0, [C_2S] = [C_2S]^0, x > x_c \end{aligned} \quad \text{Eq. 7-31}$$

whereas, in the completely carbonated area it holds:

$$[Ca(OH)_2] = [C_{1.7}SH] = [C_{1.1}SH_{3.9}] = [C_{1.42}SH_{2.92}A_{0.046}] = [C_3S] = [C_2S] = 0, 0 \leq x \leq x_c \quad \text{Eq. 7-32}$$

#### 7.4.2 Diffusion coefficient of CO<sub>2</sub> – $D_{e,CO_2}^c$

In the later region of totally carbonated zone, the diffusion coefficient of CO<sub>2</sub> is constant and

equal to the value that related to the completely carbonated area,  $D_{\epsilon,CO_2}^c$ . Therefore, there also exists in this region:

$$\frac{d^2[CO_2]}{dx^2} = 0, \text{ i. e., } [CO_2] = [CO_2]^0 \left(1 - \frac{x}{x_c}\right), 0 \leq x \leq x_c \quad \text{Eq. 7-33}$$

The diffusion coefficient of CO<sub>2</sub> (in m<sup>2</sup>/sec) can be calculated with [9]:

$$D_{\epsilon,CO_2}^c \approx 1.64 \times 10^{-5} (\epsilon^c)^{2.74} (1 - S_{SR})^{4.2} \quad \text{Eq. 7-34}$$

in which  $S_{SR}$  is the degree of saturation of the pore system,  $\epsilon^c$  is the porosity of total carbonated cement paste.

### 7.4.3 Prediction of carbonation depth of Portland and blended cement paste

#### 7.4.3.1 General predictive equation

All terms in Eq. 7-30 are multiplied by  $dx_c$  which is illustrated in *Figure 7-1*. The third part of Eq. 7-30, which describes the reaction rate kinetics, i.e.  $r_{C_4AF}^H$ , is small and assumed zero. Moreover, a study of the competition among different carbonation reactions [10] shows that the carbonation of  $C_3S$  and  $C_2S$  will consume only 1/50 and 1/20, respectively, of CO<sub>2</sub> consumed by the carbonation of CH for the same carbonation time. Therefore, the carbonation of  $C_3S$  and  $C_2S$  can be ignored in this equation. The final equation can then be described as follows:

$$x_c \frac{dx_c}{dt} = \frac{D_{\epsilon,CO_2} [CO_2]^0}{\left([CH]^0 + 1.7[C_{1.7}SH]^0 + 1.1[C_{1.1}SH_{3.9}]^0 + 1.42[C_{1.42}SH_{2.92}A_{0.046}]^0\right)} \quad \text{Eq. 7-35}$$

By integrating and satisfying the initial condition  $x_c = 0$  at  $t = 0$ , leads to:

$$x_c = \sqrt{\frac{2[CO_2]^0 D_{\epsilon,CO_2}^c}{\left([CH]^0 + 1.7[C_{1.7}SH]^0 + 1.1[C_{1.1}SH_{3.9}]^0 + 1.42[C_{1.42}SH_{2.92}A_{0.046}]^0\right)}} t \quad \text{Eq. 7-36}$$

#### 7.4.3.2 Carbonation depth of Portland cement and blended pastes

When applying Eq. 7-36 for different mixtures, the rate of the carbonation front (depth) in Portland cement paste ( $x_c^{PC}$ ) and FA ( $x_c^{FA}$ ) or BFS ( $x_c^{BFS}$ ) blended cement paste can be

obtained with the following formulae (note: for comparison Papadakis' equation, i.e. Eq. 7-38, for carbonation of Portland cement paste is shown as well; see also section 7.4.5):

$$x_c^{PC} = \sqrt{\frac{2[CO_2]^0 D_{e,CO_2}^c}{([CH]^0 + 1.7[C_{1.7}SH]^0)} t} \quad \text{Eq. 7-37}$$

$$x_c^{PC} = \sqrt{\frac{2[CO_2]^0 D_{e,CO_2}^c}{([CH]^0 + 3.0[C_3S_2H_3]^0)} t} \quad (\text{Papadakis' equation}) \quad \text{Eq. 7-38}$$

$$x_c^{FA} = \sqrt{\frac{2[CO_2]^0 D_{e,CO_2}^c}{([CH]^0 + 1.7[C_{1.7}SH]^0 + 1.1[C_{1.1}SH_{3.9}]^0)} t} \quad \text{Eq. 7-39}$$

$$x_c^{BFS} = \sqrt{\frac{2[CO_2]^0 D_{e,CO_2}^c}{([CH]^0 + 1.7[C_{1.7}SH]^0 + 1.42[C_{1.42}SH_{2.92}A_{0.046}]^0)} t} \quad \text{Eq. 7-40}$$

#### 7.4.4 Determination of model parameters of prediction formula

The formulas presented in section 7.4.3 contain several components, c.q. parameters, of which the values still need to be determined. The unknowns are the diffusion coefficient of CO<sub>2</sub> and initial concentrations (at the start of the carbonation process) of different constituents involved in the carbonation process, viz.:

- Diffusion coefficient of CO<sub>2</sub>
- Concentration of CH
- Concentration of (different types of) C-S-H

The values of these unknowns are determined by the composition of the binders and stage of the hydration process. The concentration of CH and C-S-H are calculated based on the TGA data tested in Chapter 3. The diffusion coefficient of CO<sub>2</sub> is calculated based on the porosity of fully carbonated paste by using Eq. 7-34. Apart from the above-mentioned quantities, the CO<sub>2</sub> concentration has to be known. This concentration is determined by the ambient conditions at the concrete surface.

In the following sub-sections the Eq. 7-37 to Eq. 7-40 will be used for predicting the carbonation depth in three cement pastes, i.e. Portland cement paste P100 and blended cement pastes F30 and B70. The mixture compositions were presented already in *Table 3-8*. The samples were hydrated for 1 year (365 days) before the accelerated carbonation test started. The CO<sub>2</sub> concentration ( $[CO_2]^0$ ) and relative humidity (RH) are 3% (V/V) and 75%, respectively, as specified in section 4.1.2 of Chapter 4. The samples of different mixtures,

chosen for the determination of porosity, were carbonated for 84 days. Predicted carbonation depths will be compared with measured carbonation depths shown in *Figure 4-6*.

Table 7.1 summarizes the results and calculations, as well as other parameter values for determination of the carbonation depth. The details of the calculations of these parameters for the mixtures P100, F30 and B70 will be described in the following sections.

*Table 7-1 Parameters used in Eq. 7-37, Eq. 7-39 and Eq. 7-40*

Component	Symbol	Unit	Mixture		
			P100	F30	B70
Porosity	$\varepsilon^c$	%	13.24	19.54	17.90
Saturation degree	$S_{SR}$	%	38.0	38.0	38.0
Diffusion coefficient	$D_{e,CO_2}^c$	$\times 10^{-8}, m^2/s$	0.8647	2.5120	1.9756
*CO <sub>2</sub> concentration	$[CO_2]^0$	$\times 10^{-3}, mol/L$	1.25	1.25	1.25
Water released from CH	$w_h^{CH}$	%	4.19	1.8	0.42
Bulk density	$\rho_{bulk}$	g/L	1606.5	1482.3	1456.8
CH-concentration	$[CH]^0$	mol/L	3.74	1.48	0.34
Released water from C-S-H	$w_h^{C-S-H}$	%	9.87	9.21	11.31
H <sub>2</sub> O concentration	$[H]_{C-S-H}^0$	mol/L	8.81	7.58	9.15
	$[C_{1.7}SH]^0$	mol/L	2.20	1.07	0.58
C-S-H concentration	$[C_{1.1}SH_{3.9}]^0$	mol/L	-	0.84	-
	$[C_{1.42}SH_{2.92}A_{0.046}]^0$	mol/L	-	-	2.33

\* The temperature and CO<sub>2</sub> concentration in the carbonation chamber are 20°C and 3%(V/V) respectively. Under 20°C, the molar volume of gas is 24 L/mol. Therefore, the calculated  $[CO_2]^0$  is 0.00125 mol/L.

#### 7.4.4.1 Determination of diffusion coefficient of CO<sub>2</sub>

The saturation degree  $S_{SR}$  of the pore system is determined by the ambient relative humidity  $RH$ , the relation of which was built by Papadakis and verified by experimental data [7]. From his studies, the relation of  $S$  and  $RH$  (%) is independent of the presence of aggregates, but obviously affected by the w/c ratio and carbonation. From *Figure 6-a* in his study [7], the Saturation degree  $S_{SR}$  is confirmed as 0.38 in this figure, when the ambient RH equals to 75%. The total porosity  $\varepsilon^c$  of completely carbonated (blended) cement pastes are taken from the same MIP test data shown in *Figure 4-14*. These data are re-listed in *Table 7-1*. The diffusion coefficients  $D_{e,CO_2}^c$  of different mixtures are calculated with Eq. 7-34 and also listed in *Table 7-1*.

#### 7.4.4.2 Determination of initial concentration of CH

The initial concentration of CH ( $[CH]^0$ , mol/L) in the (blended) cement paste can be calculated with the modified equation based on Eq. 3-5 in Chapter 3:

$$[CH]^0 (\text{mol} / \text{L}) = \frac{w_h^{CH}}{100} \times \frac{\rho_{bulk}}{M_{H_2O}} \quad \text{Eq. 7-41}$$

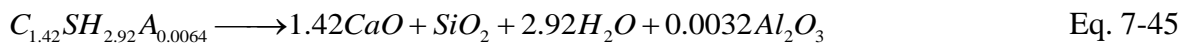
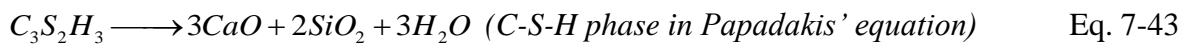
where  $w_h^{CH}$  is the relative mass percentage of water due to the dehydration of CH, calculated by the tangential method (see *Figure 3-6*);  $\rho_{bulk}$  (g / L) is the bulk density of cement paste before carbonation, calculated from the MIP test result discussed in section 3.3.3;  $M_{H_2O}$  (g / mol) = 18 is the molar weight of H<sub>2</sub>O. Based on the TG test results shown in *Figure 3-5*, the values of  $w_h^{CH}$  for different mixtures are calculated and listed in *Table 7-1*.

The bulk density  $\rho_{bulk}$  (g / L) of the cement pastes before carbonation are taken from the same MIP test data shown in *Chapter 3*, listed in *Table 7-1*.

By inserting the data for the amount of released water  $w_h^{CH}$  and the bulk density  $\rho_{bulk}$  to Eq. 7-41, the initial concentration of  $[CH]^0$  [mol/L] of different (blended) cement pastes are calculated and listed in *Table 7-1*.

#### 7.4.4.3 Determination of initial concentration of C-S-H

As mentioned before, the chemical formula of C-S-H produced from the hydration of Portland cement and the pozzolanic reactions of FA or BFS are expressed as  $C_{1.7}SH_4$ ,  $C_{1.1}SH_{3.9}$  and  $C_{1.42}SH_{2.92}A_{0.0064}$ , respectively. The amounts of different types of C-S-H can be obtained from dehydration data. The dehydration of different types of C-S-H can be described as follows:



Based on the above equations, the amount of C-S-H can be calculated from the amount of water released in the dehydration of C-S-H during the heating process in TG tests:



In Portland cement paste:

$$[C_{1.7}SH_4]^0 (mol / L) = \frac{1}{4} \times [H]_{CSH}^0 = \frac{1}{4} \times \frac{w_h^{CSH}}{100} \times \frac{\rho_{bulk}}{M_{H_2O}} \quad \text{Eq. 7-46}$$

In FA blended cement paste:

$$[C_{1.7}SH_4]^0 (mol / L) = \frac{1}{4} \times [H]_{C_{1.7}SH_4}^0 = \frac{1}{4} \times \frac{w_h^{C_{1.7}SH_4}}{100} \times \frac{\rho_{bulk}}{M_{H_2O}} \quad \text{Eq. 7-47}$$

$$[C_{1.1}SH_{3.9}]^0 (mol / L) = \frac{1}{3.9} \times [H]_{C_{1.1}SH_{3.9}}^0 = \frac{1}{3.9} \times \frac{w_h^{C_{1.1}SH_{3.9}}}{100} \times \frac{\rho_{bulk}}{M_{H_2O}} \quad \text{Eq. 7-48}$$

$$[H]_{C-S-H}^0 (mol / L) = \frac{w_h^{C-S-H}}{100} \times \frac{\rho_{bulk}}{M_{H_2O}} = [H]_{C_{1.7}SH_4}^0 + [H]_{C_{1.1}SH_{3.9}}^0 \quad \text{Eq. 7-49}$$

in BFS blended cement paste:

$$[C_{1.42}SH_{2.92}A_{0.0064}]^0 (mol / L) = \frac{1}{2.92} \times [H]_{C_{1.42}SH_{2.92}A_{0.0064}}^0 = \frac{1}{2.92} \times \frac{w_h^{C_{1.42}SH_{2.92}A_{0.0064}}}{100} \times \frac{\rho_{bulk}}{M_{H_2O}} \quad \text{Eq. 7-50}$$

$$[H]_{C-S-H}^0 (mol / L) = \frac{w_h^{C-S-H}}{100} \times \frac{\rho_{bulk}}{M_{H_2O}} = [H]_{C_{1.7}SH_4}^0 + [H]_{C_{1.42}SH_{2.92}A_{0.0064}}^0 \quad \text{Eq. 7-51}$$

where  $w_h^{CSH}$  is the relative mass percentage of water due to the dehydration of certain C-S-H, which can be calculated from the same TG test data used for the determination of  $w_h^{CH}$ .

In the TG curve of cement pastes prior to carbonation (see Figure 3-5), the weight loss in the range of 40-400°C is normally related to the dehydration of C-S-H [11, 12], part of the carboaluminate hydrates [13], AFm and AFt [14] [15] phases, monocarbonate [16], as well as to the emission of physically-bound water [12]. Further considering the TGA-MS results shown in Figure 3-5, the weight loss in the range of 105 – 350°C is considered as the water released from the C-S-H during the heating. The  $w_h^{C-S-H}$  for different mixtures are calculated and listed in Table 7-1.

The concentration of water  $[H]_{C-S-H}^0$  [mol/L] released from the dehydration of C-S-H in different cement pastes, are calculated with Eq. 7-46, Eq. 7-49 and Eq. 7-51. The results are listed in Table 7-1.

#### 7.4.4.3a Determination of initial concentration of $C_{1.7}SH_4$

The initial concentration of  $C_{1.7}SH_4$  in Portland cement paste is determined by Eq. 7-46. The calculation result of  $[C_{1.7}SH_4]^0$  is listed in *Table 7-1*.

#### 7.4.4.3b Determination of initial concentration of $C_{1.1}SH_{3.9}$ and $C_{1.42}SH_{2.92}A_{0.0064}$

It should be emphasized that  $[H]_{CSH}^0$ , calculated for blended cement pastes F30 and B70, indicates the *total* amount of water. It includes both the water released from  $C_{1.7}SH_4$  and the water released from  $C_{1.1}SH_{3.9}$  (in F30) or  $C_{1.42}SH_{2.92}A_{0.0064}$  (in B70), as described in Eq. 7-49 or Eq. 7-51. The initial concentration of different C-S-H phases in the blended paste will be calculated separately.

The ratio of the initial concentrations of different C-S-H gels formed in blended cement paste can be calculated with:

$$\frac{[C_{1.7}SH_4]^0}{[C_{1.1}SH_{3.9}]^0} = \frac{v_{C_{1.7}SH_4}}{v_{C_{1.1}SH_{3.9}}} \times \frac{V_{C_{1.1}SH_{3.9}}}{V_{C_{1.7}SH_4}} \quad \text{Eq. 7-52}$$

$$\frac{[C_{1.7}SH_4]^0}{[C_{1.42}SH_{2.92}A_{0.0064}]^0} = \frac{v_{C_{1.7}SH_4}}{v_{C_{1.42}SH_{2.92}A_{0.0064}}} \times \frac{V_{C_{1.42}SH_{2.92}A_{0.0064}}}{V_{C_{1.7}SH_4}} \quad \text{Eq. 7-53}$$

where  $v_{C-S-H}$  (L) is the volume of C-S-H and  $V_{C-S-H}$  (L/mol) the molar volume of C-S-H. The molar volumes of different C-S-H gels are listed in *Table 7-2*.

*Table 7-2 Molar volume of C-S-H ( $V_{C-S-H}$ ,  $10^{-3}$  L/mol)*

Minerals	$V_{C-S-H}$ ( $10^{-3}$ L/mol)	ref.
$C_{1.7}SH_4$	112.9	[17, 18]
$C_{1.1}SH_{3.9}$	60.4	[19]
$C_{1.42}SH_{2.92}A_{0.0064}$	68.2	[19]

*Table 7-3 Volume ratio of different types of C-S-H formed in specific mixtures*

Mixture	$\frac{v_{C_{1.7}SH_4}}{v_{C_{1.1}SH_{3.9}}}$	$\frac{v_{C_{1.7}SH_4}}{v_{C_{1.42}SH_{2.92}A_{0.0064}}}$
F30	2.38	-
B70	-	0.41

The volume ratio of different C-S-H gels formed in the blended cement paste is taken from the modeling results described in *Figure 3-22* (for FA blended) and *Figure 3-28* (for BFS blended). For specific mixture F30 and B70, these values are listed in *Table 7-3*.

By applying the data in *Table 7-2* and *Table 7-3* in Eq. 7-52 and Eq. 7-53, the ratio of initial concentration of different C-S-H formed in the specific blended cement paste can be calculated and listed in *Table 7-4*.

Applying the data given in *Table 7-1* ( $[H]_{C-S-H}^0$ ) and *Table 7-4* to the equations Eq. 7-46 to Eq. 7-51, the initial concentration of different types of C-S-H are calculated and listed in *Table 7-1*.

*Table 7-4 Ratio of initial concentration of different types of C-S-H formed in the specific mixtures*

Mixture	$\frac{[C_{1.7}SH_4]^0}{[C_{1.1}SH_{3.9}]^0}$	$\frac{[C_{1.7}SH_4]^0}{[C_{1.42}SH_{2.92}A_{0.0064}]^0}$
F30	1.27	-
B70	-	0.25

#### 7.4.4.4 Final prediction model for cement paste P100, F30 and B70

After inputting these data listed in *Table 7-1*, the equations Eq. 7-37, Eq. 7-39 and Eq. 7-40 are further expressed respectively as follows:

For Portland cement paste (Eq. 7-54):

$$x_c^{PC} = 0.4997\sqrt{t(\text{day})} \quad (\text{mm} / \text{day}^{\frac{1}{2}}) \quad \text{Eq. 7-54}$$

For FA blended cement paste (Eq. 7-55):

$$x_c^{FA} = 1.1335\sqrt{t(\text{day})} \quad (\text{mm} / \text{day}^{\frac{1}{2}}) \quad \text{Eq. 7-55}$$

For BFS blended cement paste (Eq. 7-56):

$$x_c^{BFS} = 0.9596\sqrt{t(\text{day})} \quad (\text{mm} / \text{day}^{\frac{1}{2}}) \quad \text{Eq. 7-56}$$

The equations for predicting carbonation depth developed for different blended pastes will be plotted in the figures and compared with the carbonation depth shown in *Figure 4-6*.

The carbonation depth in mixture P100 predicted with Eq. 7-54 is plotted in *Figure 7-3*, and compared with the experimental data shown earlier in *Figure 4-6*.

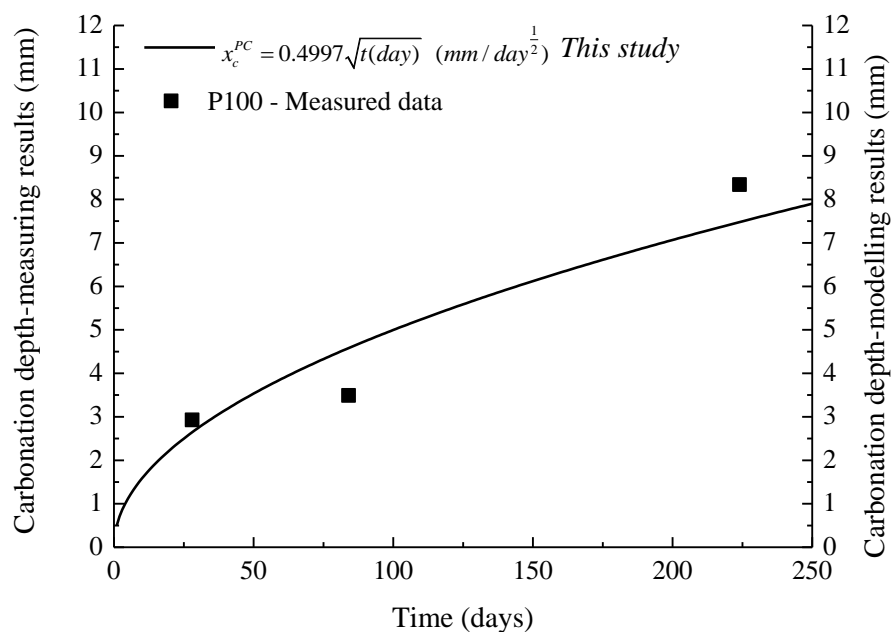


Figure 7-3 Carbonation depth predicted with Eq. 7-54 and measured carbonation depth -- Portland cement paste P100 (Hydrated for 365 days, carbonated for 84 days)

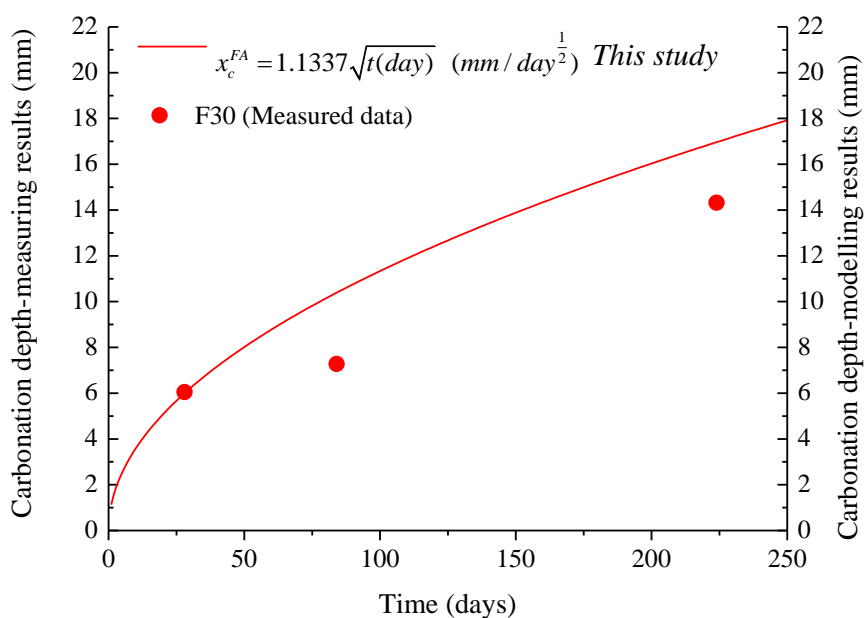


Figure 7-4 Carbonation depth predicted with Eq. 7-55 and measured carbonation depth -- Blended cement paste F30 (Hydrated for 365 days, carbonated for 84 days)

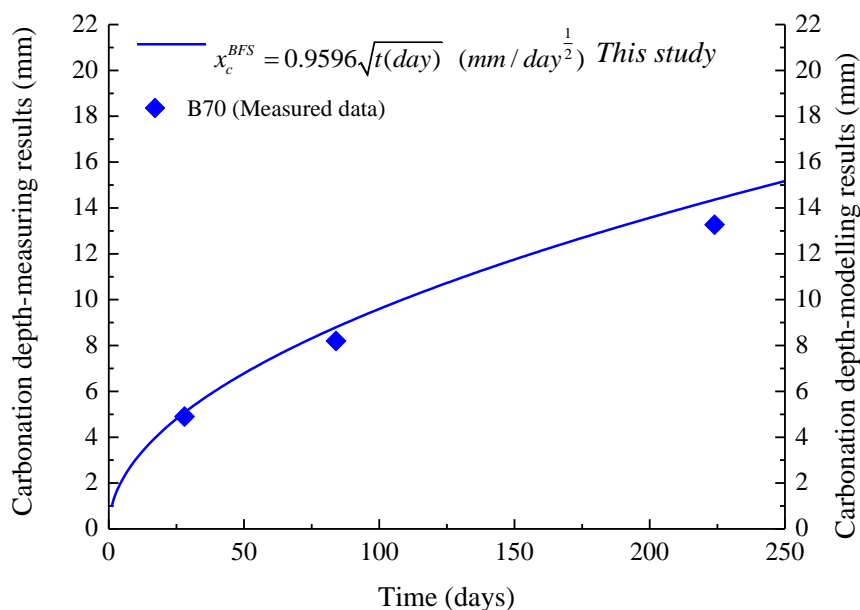


Figure 7-5 Carbonation depth predicted with Eq. 7-56 and measured carbonation depth -- Blended cement paste B70 (Hydrated for 365 days, carbonated for 84 days)

Apparently, the model developed in this study gives a good prediction for Portland cement paste P100, certainly applicable for the practice.

Prediction models for fly ash blended cement paste (Eq. 7-55) is plotted in *Figure 7-4*. For F30, the model developed in this study is over-estimating the carbonation depth, but it is still applicable for the practice. More experimental data is needed for the improvement of the model for fly ash blended cement paste.

Prediction models for blast furnace slag blended cement paste (Eq. 7-56) is plotted in *Figure 7-5*. It is clear that the predictions with the model developed in this study is in good agreement with the measured carbonation depth for the slag-blended cement paste B70.

#### 7.4.5 Case study by application of Papadakis' equation

The original equation for prediction of the carbonation depth proposed by Papadakis is Eq. 7-38. This equation, however, has been developed for the prediction of carbonation depth in Portland cement concrete. In this study, this original equation is 'extended' for the prediction of the carbonation depth developed in blended cement concrete. The Papadakis' equation is applied for the three mixtures considered in this study, i.e. P100, F30 and B70. Note that this exercise is only done with the aim of seeing how the Papadakis equation performs if the input is adjusted to allow for the actual values of model parameters.

The parameters used in the calculation by Papadakis' equation are listed in *Table 7-5*. Most of the values of the parameters are the same as those used for the equations developed in this study (*Table 7-1*). The only difference is the initial concentration of C-S-H, which will be calculated separately.

Table 7-5 Parameters used in Eq. 7-38 (Papadakis' equation)

Component	Symbol	Unit	Mixture		
			P100 - Papadakis' equation	F30 - Papadakis' equation	B70 - Papadakis' equation
Porosity	$\varepsilon^c$	%	13.24	19.54	17.90
Saturation degree	$S_{SR}$	%	38.0	38.0	38.0
Diffusion coefficient	$D_{e,CO_2}^c$	$\times 10^{-8}$ , m <sup>2</sup> /s	0.8647	2.5120	1.9756
*CO <sub>2</sub> concentration	$[CO_2]^0$	$\times 10^{-3}$ , mol/L	1.25	1.25	1.25
Water released from CH	$w_h^{CH}$	%	4.19	1.8	0.42
Bulk density	$\rho_{bulk}$	g/L	1606.5	1482.3	1456.8
CH-concentration	$[CH]^0$	mol/L	3.74	1.48	0.34
Released water from C-S-H	$w_h^{C-S-H}$	%	9.87	9.21	11.31
H <sub>2</sub> O concentration	$[H]_{C-S-H}^o$	mol/L	8.81	7.58	9.15
C-S-H concentration	$[C_3S_2H_3]^0$	mol/L	2.20	2.53	3.05

\* The temperature and CO<sub>2</sub> concentration in the carbonation chamber are 20°C and 3%(V/V) respectively. Under 20°C, the molar volume of gas is 24 L/mol. Therefore, the calculated  $[CO_2]^0$  is 0.00125 mol/L.

Especially, for the blended cement paste (F30, B70), only one type of C-S-H, produced from the hydration of cement, is considered in the calculation. The total amount of water (listed in Table 7-5) are all considered as the water released from the dehydration of  $C_3S_2H_3$ .

The initial concentration of C-S-H in Papadakis' equation is calculated for three same mixtures by using the following equation.

$$[C_3S_2H_3]^0 (\text{mol} / \text{L}) = \frac{1}{3} \times [H]_{CSH}^0 = \frac{1}{3} \times \frac{w_h^{CSH}}{100} \times \frac{\rho_{bulk}}{M_{H_2O}} \quad (\text{Papadakis' equation}) \quad \text{Eq. 7-57}$$

The initial concentrations of C-S-H of three cases are calculated listed in Table 7-5.

After inputting the data listed in Table 7-5, Eq. 7-38 can be further worked out for different cement pastes as follows:

For Portland cement paste (Eq. 7-58):

$$x_c^{PC} = 0.4250 \sqrt{t(\text{day})} \quad (\text{mm} / \text{day}^{\frac{1}{2}}) \quad (\text{P100-Papadakis' equation}) \quad \text{Eq. 7-58}$$

For FA blended cement paste (Eq. 7-59):

$$x_c^{FA} = 0.7738\sqrt{t(\text{day})} \quad (\text{mm} / \text{day}^{\frac{1}{2}}) \quad (\text{F30-Papadakis' equation}) \quad \text{Eq. 7-59}$$

For BFS blended cement paste (Eq. 7-60):

$$x_c^{BFS} = 0.6706\sqrt{t(\text{day})} \quad (\text{mm} / \text{day}^{\frac{1}{2}}) \quad (\text{B70-Papadakis' equation}) \quad \text{Eq. 7-60}$$

The equations for predicting carbonation depth developed for different blended pastes have been inserted in *Figure 7-3* to *Figure 7-5* and are presented below as *Figure 7-6* to *Figure 7-8*.

*Figure 7-6* presents the results for mixture P100. The curves obtained with Eq. 7-54 and Eq. 7-58 are both plotted and compared with the experimental data of *Figure 4-6*. Apparently, the model developed in this study gives a better prediction for Portland cement paste, compared with the prediction with the extended Papadakis's equation. With his extended equation the measured carbonation depth is a bit underestimated.

Predicted carbonation curves for fly ash blended cement paste F30 are presented in *Figure 7-7* (Eq. 7-55, Eq. 7-59). Also for F30 the extended Papadakis' equation underestimates the carbonation depth when applying for blended cement paste directly, whereas the model developed in this study tends to overestimate the measured carbonation depth.

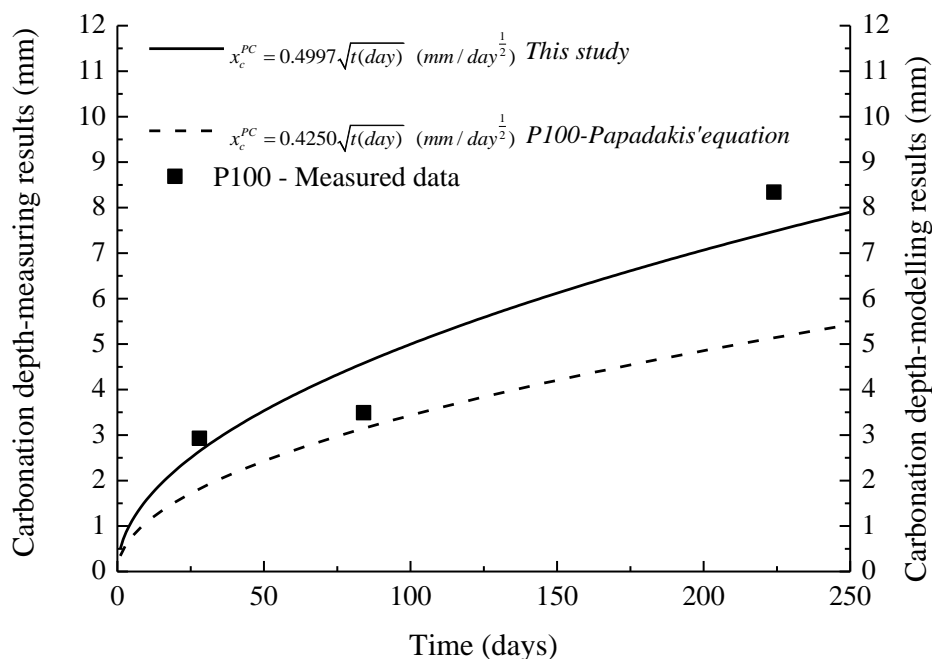


*Figure 7-6 Predicted and measured carbonation depth in Portland cement paste -- P100 (Hydrated for 365 days, carbonated for 84 days)*

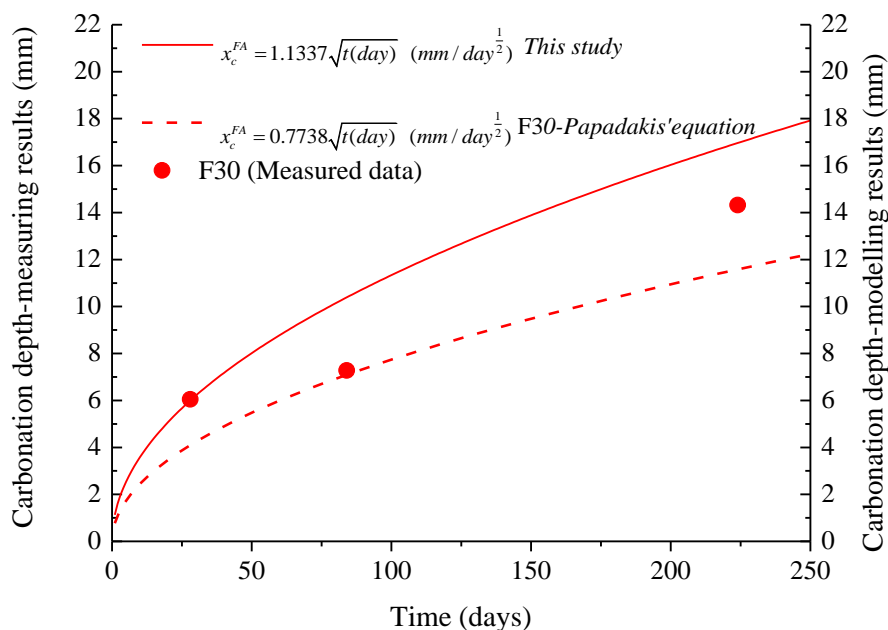


Figure 7-7 Predicted and measured carbonation depth in blended cement paste -- F30 (Hydrated for 365 days, carbonated for 84 days)

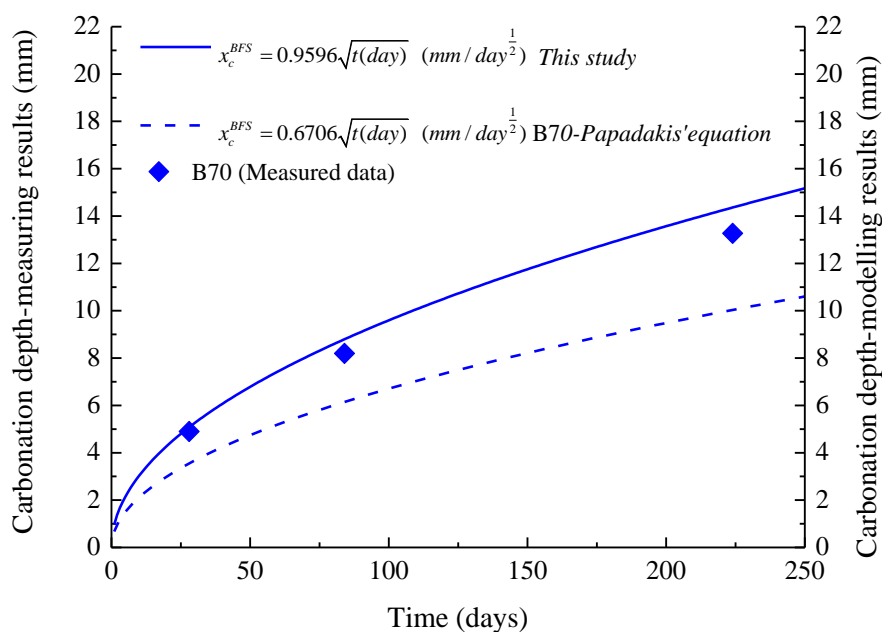


Figure 7-8 Predicted and measured carbonation depth in blended cement paste -- B70 (Hydrated for 365 days, carbonated for 84 days)

Predicted carbonation depths for blast furnace slag blended cement paste are plotted in Figure 7-8. (Eq. 7-56, Eq. 7-60). It is clear to see that values predicted with the model developed in this study is in good agreement with the measurement data of B70, whereas the extended Papadakis equation underestimates the measured carbonation depth.



## 7.5 Conclusion

In summary: the model developed in this study for predicting the evolution of the carbonation depth in Portland cement paste and blended cement pastes (fly ash-based pastes and blast furnace slag paste) performs satisfactorily. Although the value is over-estimating the carbonation depth of fly ash blended paste, the model is still applicable for the practice. With more experimental data, the model can be improved further in future study.

A comparison of predictions with the model developed in this study with predictions with an 'extended' Papadakis equation shows that the former model really is an improvement.

## 7.6 References

- [1] J.F. Young, W. Hansen, Volume relationships for CSH formation based on hydration stoichiometries, MRS Online Proceedings Library Archive, 85 (1986).
- [2] D.P. Bentz, P.V. Coveney, E.J. Garboczi, M.F. Kleyn, P.E. Stutzman, Cellular automaton simulations of cement hydration and microstructure development, *Modelling and Simulation in Materials Science and Engineering*, 2 (1994) 783.
- [3] T. Merzouki, M. Bouasker, N.E.H. Khalifa, P. Mounanga, Contribution to the modeling of hydration and chemical shrinkage of slag-blended cement at early age, *Constr Build Mater*, 44 (2013) 368-380.
- [4] P. Gao, Simulation of hydration and microstructure development of blended cements, Delft University of Technology, 2018.
- [5] D.P. Bentz, S. Remond, Incorporation of fly ash into a 3-D cement hydration microstructure model, US Department of Commerce, Technology Administration, National Institute of ...1997.
- [6] J.M. Richardson, J.J. Biernacki, P.E. Stutzman, D.P. Bentz, Stoichiometry of Slag Hydration with Calcium Hydroxide, *J Am Ceram Soc*, 85 (2002) 947-953.
- [7] V.G. Papadakis, C.G. Vayenas, M.N. Fardis, Physical and chemical characteristics affecting the durability of concrete, *Aci Mater J*, 88 (1991).
- [8] V.G. Papadakis, C.G. Vayenas, M.N. Fardis, Fundamental modeling and experimental investigation of concrete carbonation, *Aci Mater J*, 88 (1991).
- [9] M. Thiery, G. Villain, P. Dangla, G. Platret, Investigation of the carbonation front shape on cementitious materials: Effects of the chemical kinetics, *Cement Concrete Res*, 37 (2007) 1047-1058.
- [10] M. Peter, A. Muntean, S. Meier, M. Böhm, Competition of several carbonation reactions in concrete: a parametric study, *Cement Concrete Res*, 38 (2008) 1385-1393.
- [11] N. Richard, Structure et propriétés élastiques des phases cimentières base de mono-aluminate de calcium, 1999.
- [12] A. Noumowé, Effet des hautes températures (20 °C–600 °C) sur le béton, Institut National des Sciences Appliquées, 1995.
- [13] E. Nonnet, N. Lequeux, P. Boch, Elastic properties of high alumina cement castables from room temperature to 1600 C, *Journal of the European Ceramic Society*, 19 (1999) 1575-1583.
- [14] B. Lothenbach, G. Le Saout, M. Ben Haha, R. Figi, E. Wieland, Hydration of a low-alkali CEM III/B-SiO<sub>2</sub> cement (LAC), *Cement Concrete Res*, 42 (2012) 410-423.
- [15] Q. Zhou, F. Glasser, Thermal stability and decomposition mechanisms of ettringite at < 120 C, *Cement Concrete Res*, 31 (2001) 1333-1339.
- [16] B. Lothenbach, G. Le Saout, E. Gallucci, K. Scrivener, Influence of limestone on the hydration of Portland cements, *Cement Concrete Res*, 38 (2008) 848-860.
- [17] H.M. Jennings, A model for the microstructure of calcium silicate hydrate in cement paste, *Cement Concrete Res*, 30 (2000) 101-116.
- [18] H.M. Jennings, J.W. Bullard, J.J. Thomas, J.E. Andrade, J.J. Chen, G.W. Scherer, Characterization and modeling of pores and surfaces in cement paste: correlations to processing and properties, *J Adv Concr Technol*, 6 (2008) 5-29.
- [19] C. Roosz, P. Vieillard, P. Blanc, S. Gaboreau, H. Gailhanou, D. Braithwaite, V. Montouillout, R. Denoyel, P. Henocq, B. Madé, Thermodynamic properties of C-S-H, C-A-S-H and M-S-H phases: Results from direct measurements and predictive modelling, *Appl Geochem*, 92 (2018) 140-156.

## Retrospection, Conclusions and Recommendations

---

### 8.1 Retrospection

In the introduction of this thesis, the environmental benefits of using supplementary cementitious materials (SCMs) were mentioned. Partial replacement of clinker with SCMs in cement production, so called clinker substitution, is a mature technique that contributes greatly to the reduction of CO<sub>2</sub> emissions. However, the addition of SCMs affects the hydration process of cement on the one hand and leads pozzolanic reactions on the other. This ultimately changes the hydration products and microstructure of concrete. This brings new challenges for the durability of concrete, especially the resistance to carbonation, which is the focus of this thesis.

Carbonation of concrete is a complex process involving CO<sub>2</sub> diffusion, dissolution and reactions with different carbonatable phases produced from the hydration and pozzolanic reactions. In the literature review (Chapter 2), the mechanism of carbonation of concrete is described, as well as the variations involved in the addition of SCMs. The study shows that the carbonation of C-S-H plays the key role in the carbonation of concrete with mixed-in SCMs, which is not considered in the current empirical prediction models. The aim of this research is to study the carbonation mechanism of different types of C-S-H and its effects on the chemistry of the reaction products and the development of the microstructure of cement paste blended with SCMs, such as fly ash (FA) and ground granulated blast-furnace slag (GGBS).

In Chapter 3, several mixtures were designed to study the effects of SCMs on the formation of major calcium-containing phases (CH and C-S-H) and the microstructure of blended cement paste. In Chapter 4, accelerated carbonation experiments were performed on the same pastes prepared and studied in Chapter 3. The effects of SCMs on the development of carbonation depth were investigated, as well as the carbonation profiles of portlandite / calcium carbonate, which represent the real carbonation front. The microstructures of above-mentioned blended cement pastes were analyzed after carbonation. The porosity of carbonated paste, which determines CO<sub>2</sub> diffusion, was compared with that of the same paste before carbonation. The changes in porosity were related to the amounts of carbonated C-S-H phases, to investigate the effects of C-S-H carbonation on the development of the microstructure of blended cement paste during carbonation. The experimental data collected in chapters 3 and 4 were used to develop an improved empirical prediction tool for the carbonation depth.

In Chapter 5, C-S-H phases with different Ca/Si ratios (designed based on the results found in Chapter 3) were synthesized from solution reactions. These C-S-H phases were identified by different test methods. In Chapter 6, accelerated carbonation experiments were performed on the synthesized C-S-H phases identified in Chapter 5. Based on the collected data, the carbonation rates of different C-S-H phases were studied both qualitatively and half-quantitatively. The results found in Chapter 6 were considered in the development of an improved empirical prediction tool for estimating the carbonation depth in real concrete structures. The development of such a prediction tool was described in Chapter 7.

## 8.2 Conclusions

The general conclusions of this thesis are summarized below.

- *Effects of SCMs on the formation of calcium-bearing phases and microstructure of blended cement paste*

The use of FA and BFS leads to a reduction in the amount of portlandite in blended cement paste. The amount of portlandite has a negative linear relationship with the replacement level of FA or BFS. Partial replacement of OPC by FA and BFS leads to the production of C-S-H gels with lower C/S ratio than hydration of OPC. With increasing replacement of FA or BFS, the amount of C-S-H gels with lower C/S ratio increases. The average C/S ratio of C-S-H gels produced by the pozzolanic reaction of FA ranges from 1.0 to 1.30. Meanwhile, the average C/S ratio of C-S-H gels produced by the pozzolanic reaction of BFS is slightly higher, ranging from 1.1 to 1.30 in paste hydrated for 1 year. The use of FA increases the total and effective porosity of FA-blended cement paste. This effect is greatest in pastes hydrated for 105 days. BFS causes a reduction of the total and effective porosity of BFS-blended cement paste. BFS and FA affect the concrete porosity in opposite ways. The diffusion rate of hazardous components, such as CO<sub>2</sub> in the concrete, is normally determined by the porosity. From a porosity point of view, concrete

mixtures with ternary system (combining both FA and BFS with OPC) is a better option when facing durability problems.

- *Effects of carbonation of C-S-H on microstructure of blended cement paste*

The carbonation of C-S-H increases the pore volume of pores with a radius close to the small gel pores, but causes the reduction in the volume of gel pores. Both total porosity and effective capillary porosity increase in cement paste B70 and F10B54 as a result of carbonation. The effective capillary porosity of mixture F30B30 increases, whereas the total porosity decreases. Carbonation of blended cement paste with a large amount of SCMs leads to a coarser capillary pore structure. Calculation results based on the TGA data show that in these three pastes the dominant amount of  $\text{CaCO}_3$  comes from the carbonation of C-S-H. This indicates that the carbonation of C-S-H will increase the porosity of blended cement paste after carbonation.

- *Mechanism of carbonation of C-S-H*

Carbonation products of C-S-H are calcium carbonate ( $\text{CaCO}_3$ ) and silica gel. Three polymorphs of  $\text{CaCO}_3$  are found in the carbonation products of C-S-H with different C/S ratio, i.e. Calcite, Aragonite and Vaterite ( $\mu\text{-CaCO}_3$ ). Vaterite is the major carbonate in carbonation products of C-S-H. A limited amount of aragonite and calcite was observed in the carbonation products of C-S-H with a relatively low C/S ratio (0.66 or 0.86). A dramatic increase of the amount of aragonite and calcite is only found in carbonation product of C-S-H with a relatively high C/S ratio, i.e.,  $\text{C/S} > 0.86$ . The rate of carbonation of C-S-H decreases with increasing C/S ratio. An almost linear correlation was found between the rate of carbonation and the C/S ratio. C-S-H gels with a relatively high C/S ratio have a better resistance to carbonation.

- *Modelling carbonation depth*

Improved empirical models are developed for estimating the carbonation depth in concrete made with different blended cements. Modelling data are plotted and validated by experimental data. The improved empirical model has a good prediction for the carbonation depth development in Portland cement paste and BFS blended cement paste (with 70% of BFS) in this study. When applied to FA-blended cement paste (with 30% of FA), the predicted carbonation depth is over-estimated, but still close to the measurement depth. Overall, the improved empirical model is applicable for practical and engineering applications.

### 8.3 Recommendations

Based on the experimental and modelling results, some recommendations about carbonation modelling for blended cement concrete are given below:

- *Assumption for carbonation front*

The carbonation front in the model is assumed to be a perfect and clear reaction front with no “transition zone”. This means that there are only two zones in the concrete under carbonation: a completely carbonated zone and a zone which is undergoing carbonation. However, in the experimental study of Chapter 4, a “transition zone”, or partially carbonated zone, was observed in both Portland cement paste and blended paste. In future research, the carbonation front will be considered as a partially carbonated area, for example assuming that 50% or even 75% of the carbonatable phases are consumed. Furthermore, the modelling and prediction will take into account concentration gradients of each phase involved in the carbonation process.

- *Input of the concentration of calcium-bearing phases*

In the improved empirical model, the concentration of each phase involved in the carbonation should be confirmed, along with the porosity of concrete prior to carbonation. These data are functions of the degree of hydration. Thermodynamic modelling of the reactions at the carbonation front can provide a comprehensive source of related data as well. It is necessary to combine the modelling with thermodynamic or improved hydration modelling in the future prediction of carbonation depth.

- *Carbonation rate of C-S-H phases*

The improved empirical model for blended cement concrete deals with different types of C-S-H phase. However, a mass balance-based model does not take into account the rate kinetics of C-S-H carbonation. This varies in different C-S-H phases, as is confirmed in the experimental study in Chapter 6. For some blended mixtures, the carbonation process may no longer be controlled by CO<sub>2</sub>-diffusion, but determined by the reaction rates of the phases involved in the chemical reactions in the carbonation front. This should be considered and studied in the future.

# Curriculum Vitae

## Personal information

Name Bei Wu  
 Date of Birth Jan. 1986  
 Email b.wu@live.cn

<https://www.linkedin.com/in/bei-wu-73684765/>



## Education Background

Oct. 2011 - May 2023	PhD Delft University of technology, Delft, Netherlands
Sep. 2008 - Jun. 2011	M. E. Materials Physics and Chemistry Wuhan University of Technology, Wuhan, China
Sep. 2004 - Jun. 2008	B.E. Materials Science and Engineering Wuhan University of Technology, Wuhan, China

## Working Experiences

Feb. 2016 - Feb. 2018	Senior Consulting Engineer Advanced Construction Technology Services, Jeddah, KSA
Apr. 2019 - Mar. 2020	Researcher Delft University of technology, Delft, Netherlands

## Publications

Vanoutrive, H., Van den Heede, P., Alderete, N., Andrade, C., Bansal, T., Camões, A., ... & Gruyaert, E. (2022). Report of RILEM TC 281-CCC: outcomes of a round robin on the resistance to accelerated carbonation of Portland, Portland-fly ash and blast-furnace blended cements. *Materials and structures*, 55(3), 1-29.

von Greve-Dierfeld, S., Lothenbach, B., Vollpracht, A., Wu, B., Huet, B., Andrade, C., ... & De Belie, N. (2020). Understanding the carbonation of concrete with supplementary

---

cementitious materials: a critical review by RILEM TC 281-CCC. *Materials and structures*, 53(6), 1-34.

Wu B, Ye G. Study of carbonation rate of synthetic CSH by XRD, NMR and FTIR[J]. *Heron*, 2019, 64(1-2).

Wu B, Ye G. Yunpeng Liu and Wenqin Zhang, Study of carbonation rate of synthesized C-S-H by NMR and FTIR. In: Guang Ye, Yong Yuan, editors. 4<sup>th</sup> International Conference on Service Life Design for Infrastructures, Proceedings. 2018, p. 167-170 (RILEM Pro 125)

Wu B, Ye G. Carbonation of C-S-H and the effects on the porosity development of blended cement paste. In: Guang Ye, editor. Workshop on Concrete Modelling and Materials Behaviour in honor of Professor Klass van Breugel, Proceedings. 2018, p. 256-259 (RILEM Pro 126)

Wu B, Ye G. "Development of porosity of cement paste blended with supplementary cementitious materials after carbonation." *Construction and Building Materials* 145 (2017): 52-61.

Wu B, Ye G. Carbonation mechanism of different kind of C-S-H: rate and products. In: Jensen OM, Kovler K, De Belie N, editors. *Concrete with Supplementary Cementitious Materials*. Paris, France: RILEM; 2016. p. 163–272. (RILEM Pro 113)

Wu B, Ye G. Development of porosity of cement paste blended with supplementary cementitious materials after carbonation. In: Shi C, Yao Y, editors. 14th International Congress on the Chemistry of Cement, Proceedings. 2015. p. 1-18.

Wu B, Zhang Y, Ye G. The influences of CSH on the carbonation resistance of cement blended with supplementary cementitious materials. In: K. van Breugel, E.A.B. Koenders, editors. 1st International Conference on Ageing of Materials & Structures, Proceedings. 2014. p. 187-194.

Wu B, Ye G. Comparative studies of carbonation fronts of cement paste blended with supplementary cementitious materials. 3rd international conference on service life design for infrastructure, Proceedings. 2014

Li, XG, Lv, Y, Ma, BG, Jian, SW, Tan, HB, Wu, B (2014). Utilization of oil well-derived drilling waste in shale-brick production., *Environmental Engineering and Management Journal*, 13 (1), 173-180.

Wu B, Li, XG, Ma, BG, Zhang, ML (2012). Solidification of heavy metals in ettringite and its stability research. In: Guang Ye, K. van Breugel, editors. 2nd International conference on Microstructural-related Durability of Cementitious Composites, Proceedings. 2012. p. 1596-1605. (RILEM Pro 083)